STUDY AND ANALYSIS OF SAR IMAGES USING UNSUPERVISED CLASSIFICATION

A THESIS

Submitted in partial fulfilment of the
requirements for the award of the degree
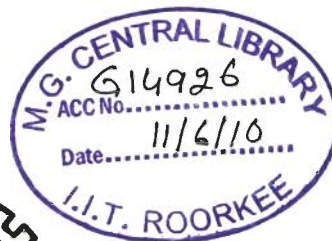*of*
DOCTOR OF PHILOSOPHY
in
ELECTRONICS AND COMPUTER ENGINEERING

by

VIJAYA CHAMUNDEESWARI V

DEPARTMENT OF ELECTRONICS AND COMPUTER ENGINEERING
INDIAN INSTITUTE OF TECHNOLOGY ROORKEE
ROORKEE - 247 667 (INDIA)
FEBRUARY, 2009

INDIAN INSTITUTE OF TECHNOLOGY ROORKEE
ROORKEE

CANDIDATE'S DECLARATION

I hereby certify that the work which is being presented in the thesis entitled **STUDY AND ANALYSIS OF SAR IMAGES USING UNSUPERVISED CLASSIFICATION** in partial fulfilment of the requirements for the award of the Degree of Doctor of Philosophy and submitted in the Department of Electronics and Computer Engineering of the Indian Institute of Technology Roorkee, Roorkee is an authentic record of my own work carried out during a period from July 2005 to February 2009 under the supervision of Dr. Dharmendra Singh, Associate Professor, and Dr. Kuldip Singh, Professor, Department of Electronics and Computer Engineering, Indian Institute of Technology Roorkee, Roorkee.

The matter presented in this thesis has not been submitted by me for the award of any other degree of this or any other Institute.

(Vijaya Chamundeeswari V)

This is to certify that the above statement made by the candidate is correct to the best of our knowledge.

(Dharmendra Singh)
Supervisor

(Kuldip Singh)
Supervisor

Date: 16|02|09

The Ph.D. Viva-Voce Examination of **Vijaya Chamundeeswari V**, Research Scholar has been held on ……………..

Signature of Supervisors

Signature of External Examiner

i

Abstract

Land cover and land use classification on a huge scale, e.g. national or continental scale, have become more and more important in wide range of applications like urban planning, farming, study of human impacts on environment, and study of damages caused by natural disasters like landslides, hurricanes, erosion or earthquakes. Earth observation using satellite imagery is a challenging tool for land cover monitoring that may offer a wide coverage efficiently. Automated classification of image into various land covers like water, urban and agriculture is an imminent necessity for large scale landscape monitoring. Land cover classification of the image is the process of segmenting the image into clusters according to desired parameters and labeling each cluster as various land covers according to characteristics of pixels within clusters. Therefore, there is a need to analyze satellite images and explore possibilities of using these images for classification purposes more efficiently.

Radar sensors have specific advantages for land cover classification due to their operating frequency range: (1) Sensitive to surface characteristics like surface roughness and dielectric property, (2) Independent of sun illumination, and (3) Capable of providing all time (day and night) and all weather acquisitions. It's another advantage is its relatively high spatial resolution. Therefore, by seeing the advantages of Synthetic Aperture Radar (SAR) image, it is required to explore its applications for various land cover classification.

Land cover classification of SAR image can be approached as (i) Clustering the pixels and labeling clusters into various land covers like water, urban and agriculture, and (ii) classifying land cover in to 'change' and 'no change' areas by comparing SAR image that are obtained at different time with quantitative assessment of changes. For classification of single polarized SAR image, backscattering coefficient and texture are the only information available. Hence, analyzing single polarized SAR image is still a big challenge.

The present dissertation work is an effort to obtain unsupervised land cover classification in one hand and on the other hand, to classify 'change' and 'no change' areas with quantitative measurement of changes. The main aim of this dissertation is

to study and develop suitable algorithm for unsupervised classification of single polarized SAR image by (i) identifying textural features that should be most effective for land cover discrimination and devising techniques to measure features, (ii) defining algorithm to integrate the features for clustering, (iii) labeling of clusters with minimum *apriori* information and (iv) application of image analysis and interferometry for quantitative and qualitative analysis of changes on land surfaces (i.e., subsidence).

To test and critically analyze the various land cover classification algorithms, three imagesets of ERS-2 SAR C-band images (5.3 GHz frequency and VV polarization) at a spatial resolution of ~12.5 m are used. The test site selected for this study is Haridwar region, India (Latitude: 77° 51′E to 77°55′12″E; Longitude: 29°54′N and 29°50′50″ N). New Orleans city of USA (Latitude: 30°3′27″N to 29°54′43″N; Longitude: 90°15′12″W to 89°53′36″W) is taken as the study area for application of image analysis and interferometric techniques to observe qualitative and quantitative changes on land surface (i.e., subsidence). For this purpose, 84 Single look complex (SLC) RADARSAT-1 images were acquired from 15 April, 2002 to 15 March, 2007 with 24 day repeat interval.

First chapter presents the introduction of the thesis which includes motivation, major research gaps, and details about the study area and satellite image used.

In chapter II of thesis, brief review of related works is presented.

Chapter III explores the analysis of role of various intensity and textural measures for their discriminative ability for land cover classification (i.e., water, urban and agriculture areas) of SAR data. In this chapter, suitable algorithm by which various texture measures can be combined for unsupervised SAR data classification was proposed and the study of their combined effect on classification accuracy was presented. Texture, being an important property for describing various land covers in SAR data has led to analysis of various texture measures for its classification. Till now, texture measures have been applied individually or combined by K-means for classification purposes but gave less accuracy (approximately 50%, Dekker, 2003). There is a need to study the role of various texture measures in classification and to improvise the algorithm of combining texture measures. In this chapter, various texture measures namely mean, variance, semivariogram, lacunarity, weighted rank

fill ratio and wavelet components, and their combined effects for classification, were analyzed by applying them to synthetic images as well as to SAR data. The focus of this chapter was to increase classification accuracy by fusion of maximum information obtained by single polarized SAR data. Individual texture measures have been analyzed for improving classification accuracy in one hand, whereas in another hand, to obtain combined effect of these textural measures on classification accuracy, PCA has been applied and selected principal components were used for further classification. Because it is well known that PCA has its own advantage of fusing information from number of various input features, and giving output in terms of eigen vectors which are orthogonal, capturing information from the input features (Bajwa and Hyder, 2005; Joliffe, 2002). It was observed that feature set comprising of mean, variance, wavelet components, semivariogram, lacunarity and weighted rank fill ratio provided good classification accuracy up to 90.4% than by using individual textural measures (with individual texture measure, maximum classification accuracy achievable is approximately 76%) and this increased accuracy justified the complexity involved in the process (Chamundeeswari et al., 2006a; 2006b; 2009).

An effort of devising adaptive unsupervised classification technique with the help of wavelets for multi resolution analysis of SAR image has been explored in chapter IV. Till now, most of the developed research works requires either ancillary image such as elevation model, ground truth or involves user interaction to decide parameters involved in classification algorithm. Hence, there is a need to develop user independent algorithm with minimum *apriori* information. For multi resolution analysis, wavelet transform is an excellent tool (Mallat, 1989) and its ability to capture different textures in SAR image has not yet been fully explored (Leporini and Pesquet, 1997). Therefore, in this task, an attempt to critically analyze multi resolution texture by wavelet decomposition has been carried out. Four band wavelet decomposition is applied on SAR image and textural features are extracted from wavelet coefficients corresponding to each of these sub-bands. Integrated feature vector corresponding to every sub-band chosen, is obtained by integrating textural features corresponding to that band and backscattering coefficient. Adaptive neuro-fuzzy algorithm ranks and selects important feature vectors for classification process. This algorithm helps in removing redundant feature bands and choosing relevant feature vectors for classification. Then, K-means classification is applied on

chosen feature vectors. The proposed classification process involves three user defined parameters namely (i) window size of local estimator 1, (ii) window size of local estimator 2 (Local estimator 1 & 2 are used to compute textural features from sub-bands obtained by wavelet decomposition at level 1 and 2 respectively), and (iii) number of feature vectors to be chosen for K-means classification from adaptive neuro-fuzzy algorithm. To make the algorithm adaptive and optimum, user dependency has to be removed and above mentioned user defined parameters are to be identified for maximum achievable classification accuracy. For this purpose, an algorithm is proposed for classification accuracy in terms of the parameters involved in segmentation process. This will be very helpful to develop automated land cover monitoring system with SAR image, where optimized parameters are to be developed only once and these parameters can be applied to SAR image of the scene year after year for a particular region. Single polarized SAR image is classified into water, and urban areas using the proposed method and overall classification accuracy is obtained in the range of 85.92%–93.70% by comparing with ground truth image (Chamundeeswari et al., 2007a; Chamundeeswari and Singh, 2006).

Labeling of different clusters on SAR image is quite a challenging task. Therefore in chapter V, the task of how to label these clusters is critically analyzed and studied. Earlier researchers have used backscattering coefficient for labeling the different clusters. But it is difficult to get unique value of backscattering coefficient for different clusters (i.e., major land covers namely water, urban and agriculture areas). Therefore, roughness parameters, along with backscattering coefficient may be used for labeling of clusters in SAR image. In this chapter, we have proposed an algorithm that includes surface roughness as one of the criteria along with backscattering coefficient, for labeling various clusters. Surface roughness measures RMS height,'s' (i.e., vertical roughness) and correlation length '*l*' (i.e., horizontal roughness). This surface roughness may directly indicate the various major land covers like water, urban and agriculture areas. First to check the sensitivity of textural measures on roughness, effect of eight different textural measures namely of mean, variance, wavelet components, semivariogram, lacunarity and weighted rank fill ratio on surface roughness is critically analyzed. This analysis has been carried out on developed synthetic images (approximately 300 images for various combinations of *s* and *l*). Semivariogram, weighted rank fill ratio and wavelet components are found to

be suitable texture measures for retrieving surface roughness parameters. An empirical relation has been proposed for retrieving surface roughness from these texture measures. With the help of backscattering coefficient and surface roughness parameters retrieved from texture measures, clusters can be labeled. The proposed algorithm is applied on SAR image to label land covers namely water, urban and agriculture areas. Land cover labels obtained by proposed method are found to be in good agreement with topographic information.

Unsupervised classification of 'change' and 'no change' pixels and quantitative analysis of changes, i.e., subsidence are taken as next task in chapter VI. For this purpose, various image analysis approaches have been studied and critically analyzed for classifying 'change' and 'no change' pixels, whereas, for quantitative analysis of changes, i.e., subsidence, interferometric approach has been applied. To classify the areas of 'change' and 'no-change', various image analysis approaches like image differencing, minimum ratio detector, Correlation coefficient technique and integrated intensity, texture and orientation difference maps have been applied. Each approach has its own advantages and disadvantages. Therefore, it is difficult to get same area of 'change' and 'no-change' with all these approaches. To get the common area of 'change' and 'no-change', an intersection operator method is proposed. This method is used to obtain more reliable set of 'change' and 'no-change' pixels. By studying the properties of pixels belonging to such change and no-change areas, Weibull probability distribution model is proposed. This model includes location, shape and scale parameter. It is found that this model best suit compared to others like lognormal, exponential or Gaussian distribution for the distribution of pixels on the basis of chi square test (Chamundeeswari et al., 2008a; 2008b). The results obtained by proposed methodology are quite encouraging.

Repeat pass SAR interferometry is potentially a unique tool for precise generation of DEM and large coverage deformation tool. Selection of InSAR image pairs is very crucial and requires analysis of large image sets to identify suitable image pairs. The baseline distance, caused by drift in orbit between passes, provides different viewing angles required for getting interferogram. But if baselines are too large, the accuracy of D-InSAR will decrease since the removal of the topographic phase term can not be performed very accurately. Care should be taken that baselines between image pairs are not too large (<100m). Spatial overlap (>50%) and azimuth spectra overlap

(>90%) of the two images involved in generation of interferogram are also to be considered to get good quality interferogram and hence accurate deformation. In addition, SAR interferometry requires digital elevation models to map deformations occurred. Hence, in this study, D-InSAR using three pass interferometry, that does not require elevation model or any *apriori* information is used for subsidence measurement. The subsidence for major change areas in study site are calculated and found to be in the range of (0-16) mm per year. These results are found to be in agreement with earlier findings (Dixon et al., 2006). Dixon has used permanent scatterers to measure deformation which require DEM, while we have used differential InSAR approach avoiding the need for such additional information like elevation model of the study site.

The quantitative analysis of subsidence with image analysis approach is very difficult. Therefore, an algorithm is proposed in this chapter by which more information about the changes like nature of subsidence (low, medium or high) could be retrieved from image analysis approach. From the Subsidence map obtained by DInSAR, pixels are categorized as low, medium and high subsidence pixels. To avoid cumbersome method of DInSAR, image analysis approach of image ratioing has been attempted to classify the image into low, medium and high subsidence pixels. For identifying low, medium and high subsidence areas, pdf is labeled for each type of subsidence (Chamundeeswari et al., 2008c, Singh et al., 2008a; 2008b). Results are quite in good agreement with the results obtained by DInSAR. Only quantitative analysis cannot be done by this method and it only highlights low, medium and high subsidence region.

The results are validated with the ground truth survey undertaken in and around Haridwar region, India for unsupervised land cover classification. Ground truth survey of agriculture areas reported by Said (2006) is also taken as reference. For classifying 'change' and 'no change' areas from multi temporal SAR images, New Orleans city of USA is considered as study site and comparison of the results is done with the results published by Dixon et al., (2006) using interferometry based subsidence for the years 2002-2005.

Finally in chapter VII, the contributions made in the thesis are summarized and scope of future work is outlined. The obtained analysis and results may give to various users to design monitoring system for land cover classification as well as classification of

'change' and 'no change' areas. This type of study and proposed algorithms will certainly enhance the analytical capability of applications of radar images for end users.

Acknowledgement

First and foremost, I would like to express my deep gratitude to Dr. Dharmendra Singh, my supervisor, for the inspiration, encouragement and expert guidance that have directed me towards my research goals. His insistency in rigor and precise has also benefited me a lot in research styles. He has always been a driving force for the successful completion of this work. Invaluable lengthier discussions in his room have been the building blocks of this thesis.

I would like to thank Dr. Kuldip Singh, my supervisor for the ideas, motivation, and guidance. He has helped me a lot with his valuable suggestions and recommendations during my research work.

I am thankful to the Head of Department, Prof. S. N. Sinha for providing computing and other important facilities for my research work. He has been the Chairman, Department Research Committee during tenure of my research work. I am thankful for the support and encouragement extended to me with his valuable suggestions.

I am obliged to express my sincere thanks to former Head of Department, Dr. D.K.Mehra for providing support and motivation to perform best. He has always been the source of inspiration with his pleasing and positive attitude.

I am indebted to Dr R. Mitra, Chairman, Department Research Committee, for his support and suggestions for the completion of thesis. I would like to thank my research committee members, Dr. R. P. Gupta, and Dr. Ankush Mittal for their constructive suggestions and insightful criticisms, which have helped to refine the quality of the thesis. I am indebted to the Ministry of Human Resource Development (MHRD), Government of India for providing me financial support during my research work.

I am thankful to Canadian Space Agency (CSA) for providing RADARSAT-1 data of New Orleans for my research work.

I'll never forget the time I have spent in the company of my friends, Gunjan, Harish, Rishi, Pant and Abhay Gaikwad for the congenial cheering work environment in the Remote Sensing Lab and rounds of discussions where many naive thoughts have

Contents

List of Tables

List of Figures

Acronyms

ART	Adaptive Resonance Theory
AVHRR	Advanced High Resolution Radiometer
CEOS	Committee on Earth Observation Satellites
cp	'change' pixels
CSA	Canadian Space Agency
DCT	Discrete Cosine Transform
DEM	Digital Elevation Model
DInSAR	Differential Interferometric SAR
DN	Digital Number
EM	Expectation-Maximisation
ENVISAT	Environmental Satellite
ERS	European Remote Sensing Satellite
HMC	Hidden Markov Chain
InSAR	Interferometric SAR
IRS	Indian Remote Sensing Satellite
JERS	Japanese Earth Remote Sensing
LandSat	Land Satellite
LISS	Linear Imaging Self Scanner
MODIS	Moderate Imaging Spectroradiometer
MRD	Minimum Ratio Detector
MRF	Markov Random Field
ncp	'no change' pixels
PALSAR	Phased Array L-Band Synthetic Aperture Radar
PC	Principal Components
PCA	Principal Component Analysis

pdf	Probability Distribution Function
PRI	Precision Image
RADARSAT	Radar Satellite
RMS	Root Mean Square
SAR	Synthetic Aperture Radar
SLC	Single Look Complex

Chapter 1

Introduction

Satellite images for land cover and land use mapping is a key to many diverse applications such as natural resource management, urban planning, farming, soil study, crop monitoring, study of human impacts on environment, and study of damages caused by natural disasters like landslides, hurricanes, erosion or earthquakes and may be applied to many other applications. Satellite images have become popular since they offer cost effective solution for large scale area while offering more choice on the basis of different spatial, spectral and temporal parameters.

Earth observation using satellite imagery is a challenging tool for land cover monitoring. Automated classification of image into various land covers like water, urban and agriculture areas is an imminent necessity for large scale landscape monitoring. Availability of satellite images of earth surface has to be exploited to extract more information from these images to study the environment and human impacts on the environment. When discussing about satellite images, mainly, there are three types of satellite images based on frequency bands used i.e., optical, thermal and microwave bands. There are a lot of reported works for classification of optical and thermal bands. But use of microwave images is still limited whereas it has some advantages over optical and thermal images. To apply the classification technique on microwave / Synthetic Aperture Radar (SAR) images, a lot of complexities are involved in the process. Although various techniques and algorithms are reported for classification of SAR images, but still, uncertainty exists in the classification methods. Therefore, there is a need to explore the possibility of application of SAR images for land cover classification more efficiently and effectively in one hand and in other hand to assess the changes on the land cover observed in qualitative and quantitative way. Image analysis approaches help in classifying 'change' and 'no change' pixels giving a qualitative analysis of changes, whereas SAR Interferometry is a suitable tool to quantify changes like deformation on earth surface.

1.1 Motivation

There are many satellite images available in different operating frequencies. Satellite images that are available can be listed according to their operating domain as optical, thermal and microwave images. Optical and thermal images operate in the visible and IR (Infra Red) regions of the spectrum. Their operational use is weather dependent, since clouds are not transparent at visible/IR wavelengths (0.4-14 μm). Some of the satellite images working on optical and thermal bands can be listed as AVHRR (Advanced High Resolution Radiometer), Landsat (Land Satellite), LISS (Linear Imaging Self Scanner), MODIS (MODerate Imaging Spectroradiometer), IKONOS (derived from greek word 'EIKON' meaning image), IRS (Indian Remote Sensing satellite), SPOT (Satellite Pour L'Observation de la Terra or earth observing satellites) and many others.

On the other hand, radar images, working in microwave region (1 GHz to 30 GHz), are very much atmosphere and weather independent. Radar sensors have specific advantages over optical images due to their operating frequency range. The following advantages can be stated for radar sensors and microwave images.

Its operating mode is independent from external sources like sunlight. Their operating frequency bands drastically reduce the impact of clouds, fog and rain on the images and hence SAR images are less affected by atmospheric and sunlight conditions. This means that they are capable of monitoring geographical areas regularly (even if covered by clouds or if only limited sunlight is available). This makes it possible to plan monitoring of a region with advanced timing defined by the user. These sensors allow all-time, all-weather imaging, an important aspect desirable for continuous and global monitoring of Earth's surface. These images are sensitive to surface characteristics like surface roughness and dielectric property, hence paving way for better understanding of nature of the terrain from the image analysis.

Due to short revisit time provided by SAR based missions like COSMO/SkyMed (COnstellation of Small satellites for Mediterranian basin Observation), TerraSAR-X (X-band SAR), PALSAR (Phased Array L-band Synthetic Aperture Radar), ERS (European Remote Sensing satellite), RADARSAT (Radar Satellite), and ENVISAT (Environmental Satellite), huge amount of multi temporal SAR data is expected to

become systematically available. With the SAR image, it is possible to get 2-dimensional information, whereas for acquiring 3-dimensional information of targets, interferometric approach is commonly used. This interferometry is known as InSAR (Interferometric SAR), whereas to compute changes in height in mm range, researchers are applying Differential Interferometric SAR (DInSAR) approach so that temporal changes can be quantified.

ERS, JERS (Japanese Earth Remote Sensing), ENVISAT, RADARSAT, PALSAR, TerraSAR-X are some of the radar satellite sensors available for various applications. Each pixel in SAR image contains measure of energy backscattered by a small area in the observed environment and provides information about the target characteristics and it is termed as backscattering coefficient. Amplitude of the pixel can also be termed as intensity. The SAR image consists of mainly two information (i) backscattering coefficient and (ii) texture. Target characteristics can be defined by various parameters like shape, structure, roughness, and moisture content. Due to these parameters, SAR images exhibit different backscattering coefficients and different texture information for different targets. The main aim is to extract maximum information of the target and it is quite complex to extract various target information like shape, orientation, moisture or roughness using backscattering coefficient alone. Researchers are using different input observation vectors like multifrequency and multipolarimetric images to solve the ambiguity of various unknowns involved in the targets. Therefore, it is challenging to use single polarized SAR image and extract maximum information of targets or make use of single polarimetric SAR image for various applications like land cover mapping, urban planning, farming, crop monitoring, and damage assessments.

To increase the amount of information that can be extracted from single band SAR, texture information within the image has to be looked at in much greater detail. Texture can be described as spatial property of an image point. In remotely sensed image, texture can be considered as the visual impression of coarseness or smoothness caused by the variability or uniformity of the intensity. In SAR image, it is the variation or uniformity of backscattering coefficient. These texture properties enable different land cover regions like rocks, water, agriculture, urban area etc., appear as different textures. The size at which texture measures are computed is an important parameter. Generally, texture measure is computed using image analysis approach

where a window or filter is applied over neighborhood of each pixel in the image. The size of window applied for computing texture measure is termed as window size. These texture measures are quite dependent on the applied window size. For example, same texture may appear smooth at a lower window size and may appear coarse/rough with a larger window size. This case occurs when window size is not fully encompassing a texture pattern in the first case. These parameters, backscattering coefficient, texture and resolution of analysis, can be effectively put together for the analysis of SAR images.

Ever since the satellite images have become available, considerable effort has been devoted to classification of image data with the aim of producing high quality classified images and establishing accurate inventories of spatial classes. Classification is regarded as fundamental process in satellite image analysis for land cover, land use, monitoring crop characteristic, oil spills and many such applications. It lies at the heart of transformation from available satellite image into useful geographic product. The end product could be land cover classes, agriculture mapping, weather forecasting, terrain nature and many others. Segmentation is a preliminary process of classification. The result of segmentation is a set of regions that collectively cover the entire image such that each of the pixels in a region are similar with respect to some characteristic or computed property, such as color, intensity or texture. Adjacent regions of the image are significantly different with respect to the same characteristics. The intent of classification process is to categorize all pixels in the image into one of several classes (say, land cover). This is done by attaching labels to the clusters obtained by segmentation process reflecting the nature of the group or cluster.

Land cover classification of SAR data can be approached as (i) Clustering the pixels and labeling clusters into various land covers like water, urban and agriculture, and (ii) Classification of 'change' and 'no change' pixels, where land cover has to be classified into two classes, namely, 'change' and 'no change' areas by comparing SAR data that were obtained at different time.

Classification can be performed in two ways: Supervised and Unsupervised. Supervised techniques on SAR images suffer from the need for human interaction to determine classes and training regions (Stathakis and Vasilakos, 2006). In contrast,

unsupervised methods determine classes automatically, but generally show limited ability to accurately divide terrain into natural classes. In the case of supervised classification, prototype pixel samples which are already labeled by virtue of ground truth, existing maps, or inference from experimental data are used for classification. Unsupervised classifier automatically classifies without any need of training using the algorithms which utilize only the information contained in the measured data themselves (Hara et al., 1994). But in practical applications, unsupervised classification is attempted with minimum *apriori* information and fewer user interactions. Unsupervised algorithm selects natural groupings of pixels based on some selective property of image such as intensity or texture. This algorithm still requires user interaction for assigning information classes for the clusters obtained. Still, some algorithms use parameters like thresholding which are to be provided by the user. Hence, to apply unsupervised classification on single polarized SAR images, the algorithm has to be refined such that it requires minimum *apriori* information with lesser user interaction.

Usually for remote sensing applications, K-means and Isodata based clustering is used for unsupervised classification. Both techniques use an input metric like eucledian distance for measuring likeness or similarity of pixels belonging to each cluster. If an accurate model for selecting the metric is unavailable, then the chosen metric may be sub-optimal and the classifier may perform poorly. There are many other unsupervised classification algorithms for satellite images that are based on techniques like K-nearest neighbor clustering, fuzzy models, Markov Random Field (MRF) models, neural networks, genetic algorithms and some others.

Analyzing single polarized SAR data is still a big challenge. For classification of SAR data, backscattering coefficient and texture (i.e., statistical intensity distribution) are the only information available. Based on this, various researchers analyzed SAR data, especially for segmentation purposes (Smits and Dellepiane, 1997; Deng and Clausi, 2004). Some works were based on texture analysis (Acharyya et al., 2003; Rignot and Kwok, 1990; Du, 1990; Jain and Farrokhnia, 1991; Chang and Kuo, 1993). SAR data segmentation is also approached as a problem of identifying homogenous regions and tracing edges within SAR data (Chamundeeswari et al., 2007b).

Maximum researchers are designing single metric using *apriori* knowledge of probability distribution of pixels for classification. They also analyze the image on pixel basis and hence failed to suit the needs of SAR data analysis, lacking the texture or spatial analysis of backscattering coefficient. There are various texture measures like mean, variance, semivariogram, lacunarity, weighted rank fill ratio and wavelet components that could be used for SAR texture analysis. Still there are very few reported works where they have critically analyzed texture measures obtained at various scales for SAR data. The spatial and scale properties of texture present in single polarized SAR data require analysis of textures at various scales to identify land covers like water, urban and agriculture areas. SAR data have both micro and macro textures, which are important features for texture analysis. Therefore, there is a need for multi resolution analysis of SAR data for classification and design of efficient and suitable tool for capturing multi level textures present in it. The main focus in the texture analysis of SAR data is on the construction of suitable texture measures at various scales of resolution with the most discriminative ability. Texture measures to describe the SAR data characteristic for discriminating land cover are to be identified and an effective means of using these measures for further classification process is to be designed.

Classification requires labeling of each clusters identified by SAR data segmentation process. Normally, labeling clusters is performed with the help of ground truth data for single polarized data. There are many research works that either uses multi band data or fully polarimetric data for labeling. For single polarized data, there is a dearth of algorithms for surface discrimination using property of electromagnetic scattering of radar. With the help of analysis of texture measures for varying surface characteristics of different land covers, labeling may be done, so that the complete process of classification may become unsupervised.

Another aspect of classification (that may occur) is classifying 'change' and 'no change' areas where it can be used to detect damages occurring due to natural disasters like earthquake, floods or forest fire with an image pair enclosing the event. Reviews (Lu et al., 2004; Coppin et al., 2004) reveal lack of the use of radar data for thematic application of classifying 'change' and 'no change' pixels. In the general context of classification of 'change' and 'no change' areas, many techniques have been developed: classification of some feature maps, such as image differencing,

image ratioing, selective principal component analysis (PCA) (Mas, 1999) or mutual information (Inglada, 2002) into 'change' and 'no-change' pixels. Fuzzy version of hidden markov chains (Carincotte et al., 2006) are employed for log ratio based unsupervised classification of 'change' and 'no change' pixels. These image analysis approaches give two classes of 'change' and 'no change' areas and no quantitative information about elevation changes or deformation mapping is provided. Interferometric mapping utilizing phase information acquired by SAR sensors is an excellent tool for deformation mapping enabling user to obtain subsidence in terms of millimeter accuracy (Monti-Guarnieri et al., 1993; Ferretti et al., 2007).

Image analysis approaches provide information about presence or absence of changes occurred in the image. For obtaining classification of 'change' and 'no change' pixels, various researchers applied suitable threshold for discriminating them, whereas some others are using the assumption for the distribution of pixels corresponding to 'change' and 'no change' pixels, which is an *apriori* information required about the image. So, improved classification algorithms with minimum *apriori* knowledge about the data and minimum user interaction are the need of the time. For quantitative analysis of change pixels, it is also important to explore the possibility of interferometric techniques, where, nowadays, various researchers are using this technique. Interferometric mapping of earth deformation for analysis of subsidence without using elevation data is also to be explored.

In summary, considering the difficulties in unsupervised classification of single polarized SAR image, considerable amount of research is required to utilize this image for various land cover/ land use classification and monitoring applications. In one hand, classification of land cover is important as well as in another hand, it is also important to identify 'change' and 'no change' areas in SAR image. For this purpose, image analysis approach has to be critically explored. It is also important to know these changes in a quantitative manner. Therefore, it is required to explore the possibility of application of DInSAR with some realistic approach by which quantitative measurement of changes can be obtained for temporal SAR images. Unsupervised classification remains a challenging task till date due to the inherent hurdles like suitable selection of metrics for classification, user interaction for setting parameters involved in the process and requirement of ground truth information for labeling.

Hence study of critical analysis needs to be performed for following tasks:

- Selection of suitable texture measures for single polarized SAR image and developing algorithm to classify on the basis of selected measures.

- Developing an adaptive approach for computing user defined parameters for optimum classification accuracy to design an unsupervised algorithm with minimum user interaction.

- Labeling of clusters so that process of classification becomes completely unsupervised.

- Mapping change pixels both qualitatively and quantitatively by analyzing temporal SAR images in reliable manner.

1.2 Problem Statement

The present dissertation work is an effort to obtain land cover classification in one hand and on the other hand, to classify 'change' and 'no change' pixels in qualitative and quantitative way by considering the limitations and assumptions mentioned (Section 1.1). Furthermore, one of the objectives of the thesis is to extract useful information from a single polarized SAR image by critically analyzing various features describing it and means of utilizing the describing features for land cover classification. The other objective is to study the temporal SAR images and classify the image into 'change' and 'no change' pixels with quantitative assessments. Key challenges and issues inherent in analyzing the SAR images include:

1. Since SAR images contain micro and macro textures, suitable algorithm to analyze these textures for classification purposes.

2. Developing unsupervised classification algorithm with minimum user interaction (For example, user interactions to set the parameters involved in the algorithm which affects classification accuracy has to be minimized).

3. It is very difficult to label the clusters obtained by unsupervised algorithm without the use of ground truth or topographic information. Efforts must be

made in this direction to label various clusters from their surface characteristics.

4. Unsupervised classification of 'change' and 'no change' pixels generally require thresholding for classifying pixels. The choice of thresholds affects the accuracy of the results. Hence, method to find a reliable set of 'change' pixels has to be devised.

5. SAR Interferometry is a precise and valuable tool for mapping deformation on earth surface. With the help of this technique, changes in vertical height of the terrain can be mapped. Three pass interferometry helps in quantitatively mapping these kind of changes with out requiring elevation information. The critical issue with using this method is selection of suitable InSAR image pairs for generating good interferogram and hence accurate mapping. Therefore, applicability of DInSAR for measuring changes is to be explored and means to obtain nature of subsidence by comparing image analysis and interferometric approach. Even though, DInSAR provides accurate measurement of surface changes and is capable of measuring deformation in mm, it is very difficult to obtain suitable InSAR image pairs from which height or deformation can be measured. This is because of the fact that for accurate elevation mapping, a good quality interferogram is required. For generating a good interferogram, image pairs need to pass through some minimum criteria like baseline distance (distance between two sensors), coregistration, and spatial overlap. Hence, these complexities involved in implementing DInSAR call for an alternative approach for quantitative analysis.

Therefore, the various major tasks undertaken in this thesis are as following:

(i) Identifying texture measures that should be most effective for land cover discrimination and devising techniques to compute these measures,

(ii) Defining algorithm to integrate the measures for clustering,

(iii) Labeling of clusters with minimum *apriori* information, and

(iv) Application of image analysis and interferometry for qualitative and quantitative analysis of changes on land surfaces (i.e., subsidence).

1.3 Study area

In this thesis, two study areas have been selected for the application of various tasks undertaken. For land cover classification purposes, Indian region is chosen and for classifying 'change' and 'no change' pixels with quantitative analysis, New Orleans city of USA is considered.
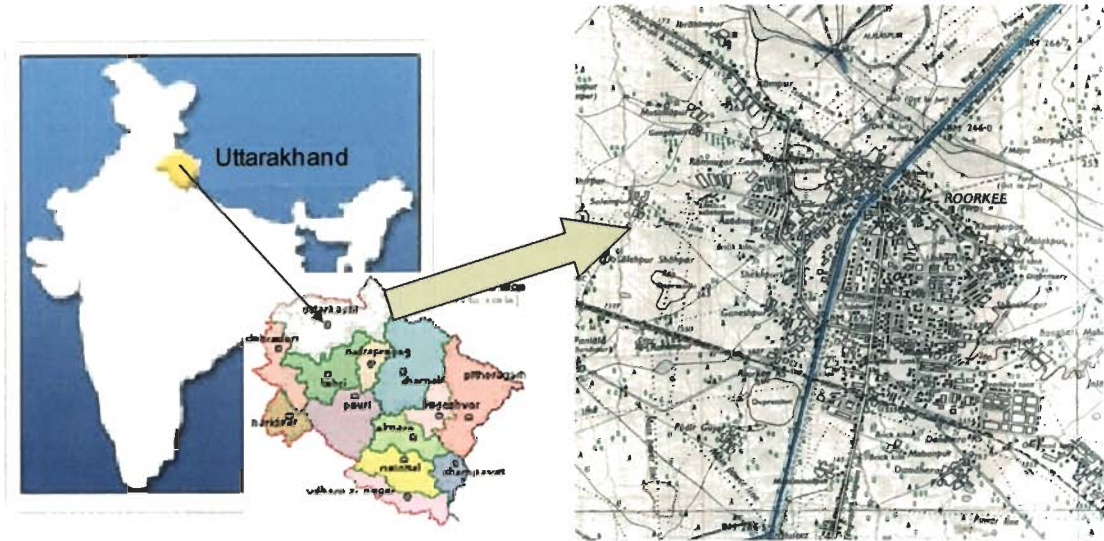
Figure 1.1. Location and topography of Roorkee, India.

1.3.1 Study area for land cover classification

Solani river catchment around Roorkee town in the state of Uttarakhand, India is taken as the study area (Figure 1.1). The area is relatively flat with elevations ranging from 245.5 m to 289.9 m. Its latitude ranges from 29.90° N to 29.83° N, and its longitude ranges from 77.92° E to 77.85° E. The agriculture varieties in this area are mainly wheat, sugarcane, and paddy.

1.3.2 Study area for classifying 'change' and 'no change' pixels and quantitative analysis of changes

For classifying 'change' and 'no change' pixels by comparing two or more SAR images, New Orleans city of USA is taken as the study area. Since the New Orleans is undergoing subsidence for the past few years, it is taken as the study area for qualitatively and quantitatively measuring changes (i.e., subsidence in this context,

even though, image approaches produce 'change' pixels, mapping all changes that may occur due to land cover, land use, surface deformation and such factors). New Orleans is located in Southeastern Louisiana along the Mississippi River of USA. Figure 1.2 shows the aerial view of New Orleans. The city is bordered by Lake Pontchartrain to the north and the Gulf of Mexico to the east and is coextensive with Orleans Parish. New Orleans is among the worst affected area due to land subsidence.

The extent of study area ranges from latitude of 30°3'27″ N to 29°54'43″ N and longitude from 90°15'12″ W to 89°53'36″ W, with elevation varying from -6 ft to +20 ft (Burkett et al., 2003). It has long been recognized that New Orleans is subsiding and is therefore susceptible for catastrophic flooding. Some parts of the New Orleans underwent a rapid subsidence in the three years before Hurricane Katrina struck in August 2005 (Amelung et al., 2006). One such area was next to the Mississippi River-Gulf Outlet (MRGO) canal. Levees have failed here during the peak storm surge. Another area which has undergone higher subsidence is Lake Borgne and its surrounding areas. These are important locations to be studied for their subsidence. Considering these things, study area is chosen such that it encompasses the locations between Lake Pontchartrain and Mississippi river covering MRGO canal areas. A huge amount of datasets of RADARSAT-1 are provided by Canadian Space Agency (CSA) that is also one of the reasons to select this area.
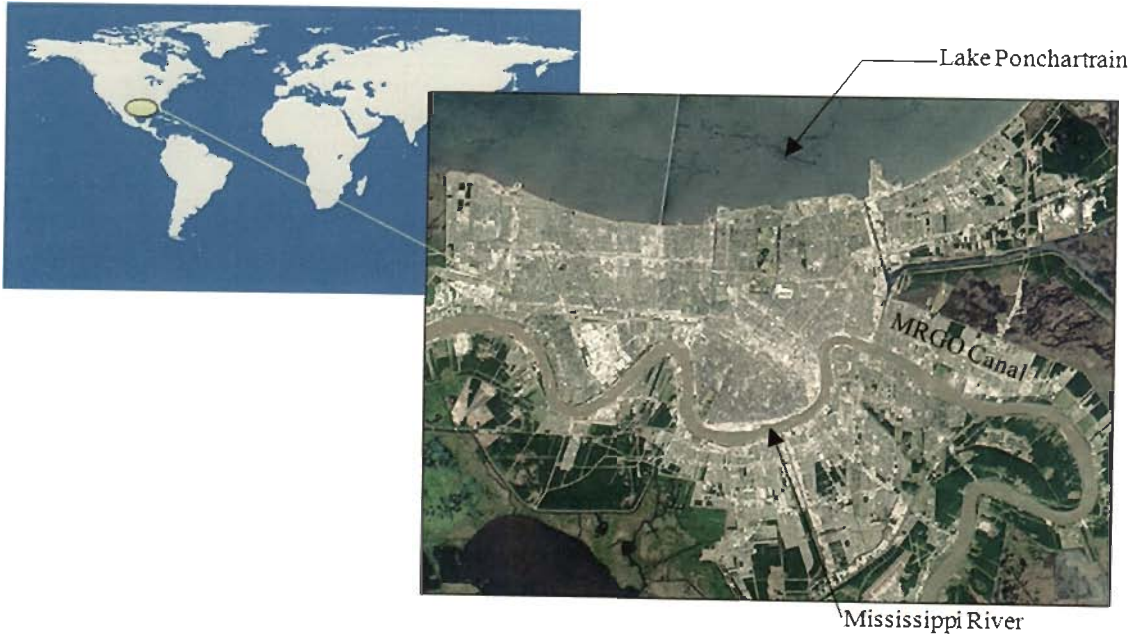
Figure 1.2. Location and aerial view of New Orleans (Google Earth, 2008).

11

1.4 Satellite data used

1.4.1 Satellite data used for land cover classification

Three ERS-2 SAR C-band images with operating frequency of 5.3 GHz and VV polarization at a spatial resolution of ~12.5 m were acquired on three dates:

(i)   July 23, 2001,

(ii)   July 28, 2003, and

(iii)   March 29, 2004.

1.4.2 Satellite data used for classifying 'change' and 'no change' pixels

RADARSAT-1 data in SLC (Single Look Complex) form, acquired from 15 April 2002 to 15 March 2007 (84 data) with 24-day repeat interval was used for developing and checking the algorithm for classifying 'change' and 'no change' pixels and quantitative analysis of changes by interferometry. Standard beam and Fine beam data types were available for analysis and details of these data types are shown in Table 1.1.

Table 1.1. Nominal product characteristics of RADARSAT-1 SLC.

Beam mode	Beam position	Product type	Nominal incidence angle (degrees)	Nominal resolution Range × azimuth (m)	Nominal Image Coverage (km × km)
Standard	S2	SLC	24-32	11.6 × 5.1	100 × 100
Fine	F5	SLC	45-48	4.6 × 5.1	50 × 50

The complete data set of 84 SLC images used for analysis is listed in Appendix A. For implemeting quantitative analysis of changes by interferometry, critical selection of suitable InSAR (Interferometric SAR) image pairs is needed. Hence, by analyzing all the images available, some pairs of images are selected and used for unsupervised classification of 'change' and 'no change' pixels (details are discussed in chapter 6).

1.5 Preprocessing of SAR images

1.5.1 Preprocessing of ERS-2 image

Preprocessing of ERS-2 SAR PRI image consists of three steps (1) Georeferencing, (ii) despeckling and (iii) calculation of backscattering coefficient (Figure 1.3).

(A) Georeferencing

SAR images are acquired in the microwave region of the electromagnetic spectrum. Hence, it is very difficult for the identification of ground control points. These images are georeferenced to geographical coordinates using four corner points and scene centre latitude and longitudinal points (Greku et al., 2006). The coordinates of four corner points and scene centre points are given in the leader file of the data. A first order polynomial transformation function and the nearest neighbor resampling technique have been used to perform georeferencing. These preprocessing steps described here were carried out using software ENVI 4.3.

ERS-2 SAR PRI image

Georeferencing

Despeckling

Calculation of backscattering coefficient

Preprocessed ERS-2 SAR image
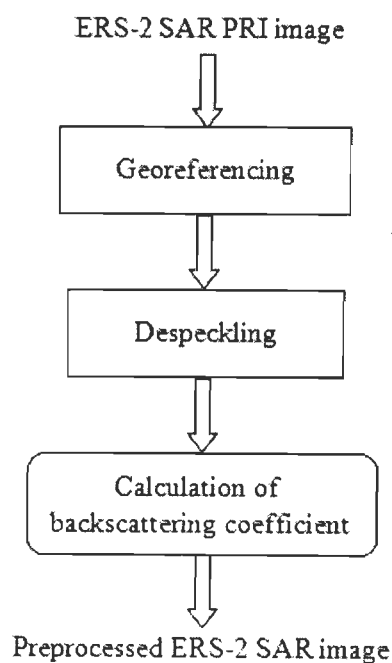
Figure 1.3. Preprocessing of ERS-2 SAR image.

(B) Despeckling

Speckle suppression is carried out on the georeferenced SAR image using the adaptive Lee filter. Lee filter is able to smooth away noise in flat regions but leaves fine details unchanged. Lee filter preserves sharp details, thus preserving boundaries and texture information in SAR image (Lee, 1980).

(C) Calculation of backscattering coefficient

The ERS-2 PRI image has the data in Digital Number (DN) form. The backscattering coefficient (σ^0) can be calculated from the DN using the guidelines provided by European Space Agency (ESA).

The backscattering coefficient can be computed as (Laur et al., 1997).

$$\sigma^0 = \left[\frac{1}{N} \sum_{ij=1}^{ij=N} DN_{ij}^2 \right] \frac{1}{k} \frac{\sin \alpha}{\sin \alpha_{ref}} \qquad (1.1)$$

where N is the number of pixels within the area of interest (i.e. the distributed target), DN_{ij} is the digital number of a pixel at location (i,j), k is given as 889201.00, α and α_{ref} are the local incidence angle and ERS-2 SAR mid range incidence angle respectively.

The local incidence angle α_i can be obtained by

$$\cos \alpha_i = \frac{\left(R_T + H \right)^2 - R_i^2 - R_T^2}{2 R_i R_T} \qquad (1.2)$$

where R_T and H are the Earth radius at the first position of the satellite and ERS-2 SAR altitude. R_i is the slant range to a pixel at location 'i' (these values are provided in leader file).

Thus, preprocessing of ERS-2 SAR PRI image is implemented and the processed SAR image can be used for further analysis.

1.5.2 Preprocessing of RADARSAT-1 image

Flowchart of preprocessing is shown in Figure 1.4.

(A) Georeferencing

Raw RADARSAT data is georeferenced with four corner points and an image centre point given in the leader file. For the SLC (Single Look Complex) data, each pixel in the output data is represented by two digital numbers (DNs) which represents the I and Q component of complex data. Both I and Q component images are georeferenced individually.

(B) Computation of beta nought

The pixel DNs are converted to beta nought or radar brightness values by extraction and application of scaling information. For complex (SLC) single beam products, the radar brightness (β^o_j) for the jth range pixel is given by

$$\beta^o_j = 10*\log_{10}[(DNI_j/A2_j)^2 + (DNQ_j/A2_j)^2] \ dB$$

$$\text{or} \qquad \beta^o_j = 20*\log_{10}(DN_j/A2_j) \ dB \qquad\qquad (1.3)$$

where DNI_j and DNQ_j are the digital values of the I and Q components of the jth pixel from the start of the range line, $A2_j$ is the corresponding range dependent gain (these values are provided in the leader file with data) and $DN_j^2 = DNI_j^2 + DNQ_j^2$. The radar brightness is also termed as beta nought.

Since the computation of backscattering coefficient σ^0 requires the digital elevation model, additional information about the data or study site, we prefer to use radar brightness image itself for the analysis so as to minimize information required for the unsupervised classification. The fact that radar brightness or beta nought is almost always the most appropriate radiometric attribute of radar imagery and sigma nought or backscattering coefficient can be reserved for situations in which local terrain slope and illumination incidence angles are known is endorsed by the CEOS SAR calibration working group (Raney et al., 1994).

Thus the georeferenced radar brigtness image can be used for further analysis.

In the case of interferometric approach, both I and Q components are used to get amplitude and phase values so that phase information can be utilized for the anaysis.

RADARSAT-1 SLC image

Georeferencing

Calculation of beta nought

Preprocessed
RADARSAT-1 image
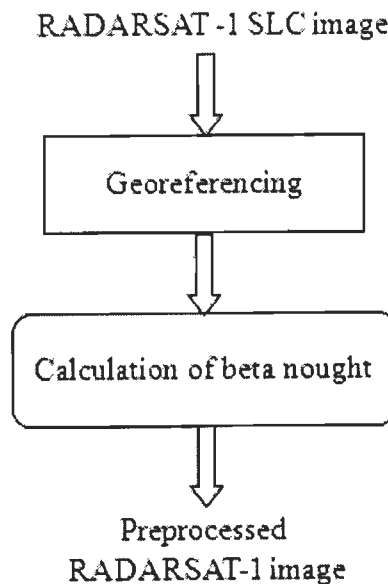
Figure 1.4. Preprocessing of RADARSAT-1 image.

1.6 Framework of the Research

In the proposed research work, an unsupervised approach for land cover classification is critically analyzed for single polarized SAR image. In addition, image analysis and DInSAR approach have been widely explored for getting qualitative and quantitative information about 'change' and 'no change' pixels.

A general strategy was followed for solving the selected tasks as mentioned in section 1.2. The steps are as following:

- Understand the issues related to the problem and identify the limitations of existing classification techniques.

- Preprocessing of the raw images is carried to obtain radar brightness or backscattering coefficient.

- Critically analyze various texture measures for their role in discrimination of various intensity and texture patterns.

16

- Present a suitable algorithm to combine selective texture measures to obtain classified SAR image into various major land cover types.

- Analyze the single polarized SAR image on multi resolution basis using wavelets.

- Propose an approach by which user interaction to select any parameters involved in classification process is minimized and to find optimum parameters.

- Labeling of clusters into major land cover types like water, urban or agriculture areas by analyzing surface characteristics inherent in the image.

- Propose a reliable algorithm for the classification of 'change' and 'no change' pixels by comparing SAR images obtained at different instants, using image analysis approach.

- Use of differential InSAR for measuring quantitative analysis of changes.

- Propose a method by which more information about nature of changes (for example, subsidence) could be obtained by image analysis approach itself because of the complexities involved in implementing DInSAR.

1.7 Organization of the Thesis

The organization of the thesis is as following.

Chapter 2 gives a brief introduction with review on the existing unsupervised classification techniques for single polarized SAR image, role of various texture measures, contribution of wavelet based analysis for SAR image, labeling of clusters and then classification of 'change' and 'no change' pixels using image analysis as well interferometric approach. It is very difficult to get a detailed review covering all above mentioned topics. So, it is tried to present a brief review with relevant works that are carried out in this thesis. In chapter 3, role of various texture measures for classifying SAR image is critically analyzed and PCA based fusion of texture measures is implemented to perform classification. Chapter 4 describes the multiresolution analysis of SAR image using four band wavelets, selection of suitable

wavelet features by adaptive neuro fuzzy algorithm, and classification. In this chapter, an approach to provide user with optimum defined parameters that can be obtained with the algorithm for a specific site is provided so that user interaction can be minimized.

Chapter 5 is concerned with labeling of various clusters into one of major land cover types namely water, urban or agriculture areas. For this purpose, effect of surface roughness parameters on various texture measures is critically analyzed and presented in chapter 5 so that surface roughness can be retrieved for real SAR image. With the knowledge of surface roughness parameter and backscattering coefficient, clusters are labeled. Chapter 6 presents unsupervised classification of 'change' and 'no change' pixels by comparing two SAR images separated by certain time span. Reliable method of obtaining 'change' pixels from image analysis methods is presented. DInSAR is used for obtaining quantitative analysis of changes between image pairs. In addition, a method is proposed by which more information about the nature of subsidence can be retrieved by studying distribution of image ratio pixels belonging to each class of subsidence. Finally, in chapter 7, a summary of the contribution of the thesis is presented and concluding remarks are given.

Chapter 2

Brief Review of Literature

2.1 Introduction

Satellite images are important for the monitoring of earth surface and atmosphere at a global, regional and even local scale. Satellite images provide a repetitive and consistent view of the earth that is invaluable to monitoring the earth system and the effect of human activities on the earth. At any point of time, day or night, multiple satellites are imaging the earth's surface, adding to an ever-expanding database of images that are available to help us for managing and solving the problems involved in human environments. Satellite image analysis techniques have been investigated for providing important coverage, mapping and classification of land cover features such as vegetation, soil, water, forests and urban area.

Land cover and land use classification using satellite image analysis have gained momentum in their role of importance because of its wide range of applications like agriculture, forestry, hydrology, natural resource management, environmental assessment and monitoring (urban growth), damage assessment (effect due to flood, or surface deformation due to natural disasters like landslides and earthquakes), land cover mapping, urban planning and monitoring (Henderson and Xia, 1997; Krieger and Moreira, 2006) and many other applications. Nowadays, various satellite images are available at different frequency spectrums as discussed in chapter 1. Although, each satellite image has its own importance, SAR has some upper hand over other satellite images (Section 1.1). Therefore, it is challenging to interpret SAR images according to our needs and requirements like classification of land cover, crop monitoring, soil moisture estimation, flood extent monitoring, subsidence monitoring and many others. Nowadays, with SAR image, a lot of combinations of observation vectors are available like different polarizations, frequency bands and incidence angles. But challenge is that to use minimum observation vector data (i.e. single frequency and single polarized image) and extract maximum information.

The review of maximum work related to SAR images is quite lengthy. So, we have focused the review mainly on selective topics as following, (which is related to work carried out in this thesis):

- Unsupervised classification of single polarized SAR images based on texture measures.

- Multiresolution based SAR (Single polarized) image analysis for unsupervised classification.

- Labeling of clusters into various major land cover types namely water, urban and agriculture areas.

- Unsupervised classification of 'change' and 'no change' pixels using image analysis and interferometric approach so that qualitative and quantitative analysis of changes can be implemented.

The brief review is concentrated with respect to these above mentioned topics.

2.2 Brief review of works related to unsupervised classification of single polarized SAR image

As discussed in chapter 1 (Section 1.1) SAR image contains information in the form of backscattering coefficient, gray level/ intensity and texture. This information is quite helpful to interpret the SAR images for various applications. Although researchers are applying supervised and unsupervised approaches to the classification of SAR images, unsupervised way of classification is an interesting and challenging way to classify. The aim is to apply classification and extract more information with minimum *apriori* information. In early 1980s, researchers have started segmentation of SAR images on the basis of thresholding gray levels. Various researchers (Weszka 1978; Fu and Mui, 1980, Sahoo et al., 1980) provide good surveys of the existing techniques. Basic method for unsupervised segmentation of images based on gray levels is to select and apply thresholds at the valleys of histogram, if any such valleys exist in the histogram of their intensity levels (Lee and Jurkevich, 1989). To partition an image into meaningful segments by choosing the right threshold is one of the most basic image processing techniques and is not an easy task if no valleys are present in

its histogram or the image is noisy. Several methods like transforming the histogram, deepening the valleys are employed to enable easier selection of thresholds so that classification accuracy is improved (Rosenfield and Kak, 1982). Image thresholding based on Expectation-Maximization (EM) algorithm (Bazi et al., 2007) uses generalized Gaussian distribution for object and background classes to classify images. Selection of threshold is an important parameter to decide classification accuracy. These techniques suffer from the limitation of means to choose appropriate thresholds for segmentation purposes.

Another important parameter in SAR image is its backscattering coefficient. Some researchers have used this parameter for SAR image classification purposes. Eldhuset (1988) has used thresholding on backscattering coefficient for separation of land and water areas in coastal regions. It has also been suggested that radar backscattering coefficient from water is lower and more homogenous than the surrounding areas (Pandey and Hariharan, 1984). It infers that knowledge of backscattering coefficient and texture may increase reliability of various classes in output. In the same way, utility of ERS-1 SAR data for discriminating water bodies from vegetation on the basis of backscattering coefficient is proposed (Dobson et al., 1992; Wu and Linders, 1999) and classification accuracy for measuring the effectiveness of algorithm is carried out using confusion matrix (Congalton, 1983). Techniques like dynamic local thresholding (Haverkamp et al., 1993) and application of second order statistics generated from gray level co-occurrence matrices are used for sea ice classification methods (Nysteun and Garcia, 1992). Statistical texture measures like energy, correlation, inertia, cluster prominence, local homogeneity, entropy, mean and standard deviation for rows and columns of gray level co-occurrence matrices were analyzed to identify statistical measures most useful for discrimination of various classes of sea ice types.

Wavelet based algorithms for extracting texture feature sets were developed (Unser, 1995; Mecocci et al., 1995; Lindsay et al., 1996; Fukuda and Hirosawa, 1999). Gabor filter is proposed to extract texture features for successful segmentation of SAR images (Du, 1990; Clausi and Deng, 2005; Kamarainen et al., 2006) and comparison of co-occurrence matrices and gabor filtering for classification purposes. Scaling is an important parameter for classification of SAR images. The scale at which texture is computed is crucial for encompassing the complete texture (Levy Vehel et al., 1992;

Marceau and Hay, 1999; Bovolo and Bruzzone, 2005). Decision tree classifiers and multi scale texture measures were studied for their use on extracting vegetation cover (Simard et al., 2000). Discrete cosine transform filtering (Ng et al., 1992), Gabor wavelets (Jain and Farrokhnia, 1991; Manjunath and Chellappa, 1991), Fuzzy models for texture characterization (Bellagente et al., 1999), Markov Random Field (MRF) clustering (Smits and Dellepiane, 1997), Particle filter based segmentation (Chen et al., 2005) are some of the other popular methods that have been developed for unsupervised classification techniques (Stathakis and Vasilakos, 2006).

Fuzzy clustering on wavelet transform feature inputs was proposed (Chumsamrong et al., 2000). In this technique, wavelet components are obtained from SAR image and are given as input to modified fuzzy c-means classifier for segmentation. Modified fuzzy algorithm used the neighboring pixels to enhance the noisy image clustering without affecting edges. Unsupervised classification approaches using neural networks are proposed (Azimi-sadjadi et al., 1993; Hara et al., 1994). Some of the unsupervised algorithms suitable for SAR classification are Adaptive Resonance Theory (ART) networks (Rogen et al., 2008), Least Vector Quantization (LVQ) technique and Self Organizing Maps (SOM).

Some researchers have used polarimetric SAR for classification purposes (Yang et al., 2006; Yamaguchi et al., 2005a; Yamaguchi et al., 2006). Use of polarimetric SAR images enhances the classification accuracy (Yamaguchi et al., 1995) but these methods require more observation vectors. MRF is considered as a powerful stochastic tool to model the joint probability distribution of the image pixels in terms of local spatial interactions. MRF models have been used to extract texture features and to model the image segmentation problem. Various researchers have used MRF based image segmentation algorithms (Won and Derin, 1992; Panjwani and Healey, 1995; Melas and Wilson, 2002; Deng and Clausi, 2004, Benyoussef et al., 2008). A common point of all the applications based on MRF models is that the segmentation is highly dependent on the representability of MRF parameters estimated from textures. The MRF based segmentation models may not perform well in which textures cannot be modeled using MRF models and hence the classification process requires nature of probability distribution of texture parameters.

Although researchers are using various techniques for unsupervised classification purposes on SAR images, but all these techniques have their limitations like need of user interaction, need of *apriori* information, and prior knowledge or assumption about the pixel distribution. Therefore, there is a need to carry out some work that can be addressed to these limitations.

2.3 Review of works related to texture measures for unsupervised land cover classification and labeling

2.3.1 Texture measures and fusion of texture measures for classification

Texture provides significant information in the interpretation of SAR images, in addition to using backscatter values alone (Tuceryan and Jain, 1993). Several studies have shown that classification based on texture features can improve the accuracy of the interpretation (Ulaby et al., 1986a; Barber and LeDrew, 1991; Peddle and Franklin, 1991; Barber et al., 1993; Kumar et al., 1999). Four different methods of texture computing namely (i) texture features from gray level cooccurence features (Rignot and Kwok, 1990), (ii) features based on local statistics like power to mean ratio, skewness, kurtosis, contrast and homogeneity measure, (iii) fractal features (Keller et al., 1989), and, (iv) features based on lognormal random field model (Frankot and Chellappa, 1987) have been compared for their discrimination ability for SAR image classification (Solberg and Jain, 1997). He has proposed for investigating neural nets or discriminant analysis for fusion of selective texture features. Similarly, various texture measures like semivariogram (Carr and Miranda, 1988; Dell'Acqua et al., 2006) and lacunarity (Henebry 1995; Chandhuri and Sarkari, 1995) were analyzed for their ability in SAR image classification purposes. Other texture measures like mean, variance, weighted rank fill ratio and wavelet components were also studied for their role on discriminating properties by many researchers (Dobson et al., 1997; Dekker 2003).

Efforts were made to enhance the classification accuracy by fusing the texture measures. K-means algorithm and Isodata algorithm are commonly used for this purpose since these methods are suitable to handle large data sets due to their efficiency and ability to handle numeric variables in real databases (Ohanian and Dubes, 1992; Huang 1998, Adem et al., 2006). This algorithm use equal weight for all

variables while clustering. Hence, various techniques were proposed to enhance K-means algorithm so that automatic weighing of variables is included according to their importance in clustering (Gnanadesikan et al., 1999; Friedman and Meulman, 2002; Modha and Sprangler, 2003).

Other methods using machine learning (Blum and Langley, 1997), feature similarity (Mitra et al., 2002), and cue selection and integration (Dupuis and Vasseur, 2006) are proposed for classification on the basis of texture measures. Since SAR image is having texture as its important property for discrimination of classes, there are many texture measures to compute texture by different approaches. Use of different techniques like gabor filters and co-occurrence probabilities (Clausi and Deng, 2005), Independent component analysis (Gilmore, 2004; Mitianoudis and Stathaki, 2005), fischer discriminant analysis (Yang et al., 2005) were proposed to fuse the texture measures to combine various texture feature. It is observed that these methods are giving some promising results, but unable to explain various role of texture measures and their combined effect. Component analysis approaches the problem of clustering by finding the 'right' features from the data. Principal component analysis (PCA) projects 'd' dimensional data onto a lower dimensional subspace in a way that is optimal in a sum-squared error sense. PCA can be used for fusion of various input variables corresponding to texture measures in SAR images.

2.3.2 Multiresolution analysis of SAR images

In the case of single polarized SAR image, texture is an important property reflecting the nature of the terrain or reflective surface. Texture plays the essential role in assessing the nature of land cover. Wavelet transform is a promising tool for texture analysis because of its ability to examine image at different resolutions (Mallat, 1989; Chang and Kuo, 1993; Laine and Fan, 1993; Greenspan et al., 1994; Yamaguchi et al., 1995b; Lu et al., 1997; Duits et al., 2007). Extraction of wavelet based texture feature set is proposed by Fukuda and Hirosawa (1999) for analyzing SAR images. These proposed feature sets consists of energy of subband images obtained from wavelet decomposition. Energy of subband image can be a texture feature since it represents dominant spatial frequency channels of the original image (Porter and Canagarajah, 1996). Minimum distance classifier calculates the Euclidean distance between the feature vectors of a pixel and template vector representing texture of a class. Then

classifier assigns pixel to the class which has minimum distance. This infers that energy of subbands obtained by wavelet decomposition is a suitable parameter for wavelet based classification algorithms. Till now, researchers are using wavelet decomposition for multi resolution analysis and classification purposes successfully. But for this purpose, they are making various assumptions like size of the local estimator for measuring textures and selection of sub bands. These assumptions make the algorithm highly user dependent. Therefore, this issue has to be undertaken and analyzed properly.

Octave band wavelet decomposition for texture segmentation is studied (Espinal et al., 1988; Niedermeier et al., 2000). Octave band wavelet transform usually provides an efficient representation for frequency in images. But its fixed space frequency tiling does not always match the spectrum of input images. In fact, it has been demonstrated that wavelet coefficients efficiently decorrelates only the images with exponentially decaying power spectra (Davis and Nosratinia, 1998). M-band wavelets provide a solution to overcome this problem. These M-band wavelets provide a mixture of logarithmic and linear frequency resolution and hence these are suitable for characterizing textures of SAR images more efficiently (Steffen et al., 1993; Alkin and Caglar, 1995; Chaux et al., 2006). Although M-band wavelet analysis is suitable for representing textures of SAR images, it results in large number of subbands. For example, if four band wavelet decomposition is used for SAR image, it results in 16 subbands at level 1 and for wavelet decomposition of second level, it results in 256 subbands, 16 subbands from each of subbands at level 1.Thus, a four band wavelet decomposition of a single SAR image results in 272 (i.e.,16 at level 1 +256 at level 2) images and is quite a large number for analysis. Moreover, these subbands may have repetitive information among them.

Many algorithms were proposed to prune the wavelet decomposition tree so that sparse representation is generated (Acharyya and Kundu, 2001; Skretting and Husoy, 2006). Suitable subband selection on the basis of energy computed for subbands (Coifman and Wickerhauser, 1992), neuro fuzzy method for selection (Acharyya and Kundu, 2003), and information-theoretic measure, mutual information (Huang and Selin, 2006), are some of the techniques proposed for sparse representation of textures. Several other systems that provide multiscale and directional image representations include 2D gabor wavelets (Daugman, 1980), the cortex transform

(Watson, 1987), the steerable pyramids (Simoncelli, 1992), brushlets (Meyer and Coifman, 1997) and contourlet transform (Do and Vetterli, 2005). The suitability of M-band wavelet transform for texture based segmentation is emphasized by many works (Liu and Zhou, 2004; Kim and Kang, 2007). It infers that M-band wavelet transform can be used effectively for the analysis of SAR images.

2.3.3 Labeling of various clusters

One of the interesting points in unsupervised classification of SAR image is to label the various classes / clusters (i.e., identification of various clusters). This issue is very challenging. For this purpose, backscattering coefficient has been used and this parameter is dependent on many factors such as radar system parameters like its operating frequency, surface feature parameters like moisture content/ dielectric constant, and surface roughness, and environmental variables. Soil and vegetation properties of the surface is analyzed using SAR images (Dobson et al., 1992, Gohil et al., 1994; Singh, 2006; Dobson et al., 1995, Galletti et al., 2008). The sensitivity of backscattering coefficient to various parameters like soil moisture, canopy and surface roughness is studied (Abdel Messiah and Quegan, 2000; Yamada et al., 2001). Empirical models are developed to retrieve soil moisture from backscattering coefficient (Pandey and Kakar, 1982; Ratha and Venkatraman, 1997). There are many works accomplished in an effort to classify vegetation biomass using multi frequency data (Oh et al., 1992; Pierce et al., 1994; Paloscia et al., 1999; Ferrazzoli et al., 1997; Lucas et al., 2007; Lang et al., 2008). These studies emphasize that backscattering coefficient can play a role to estimate various earth surface properties like moisture, roughness, and vegetation. Generally, researchers are using these parameters to label the clusters. But it is observed that backscattering coefficient alone may not able to clearly label the clusters because it is difficult to set the range of backscattering coefficient for various clusters.

In SAR image, surface roughness is also playing an important role. Surface roughness is an important parameter to study about the surface (Didascaloy et al., 2003). Range of surface roughness parameters namely RMS height and correlation length are associated with each agricultural roughness state is estimated and presented (Davidson et al., 2000; Van der wal et al., 2005). Surface roughness helps in differentiating land covers like water (calm water areas), urban and agriculture areas.

Calm water areas are characterized by smooth surfaces and their backscattering coefficient (Narain et al., 2006). General range of surface roughness for agriculture crops depends on the nature of crops in the study site. Similarly, surface roughness and backscattering coefficient of urban areas are site specific for labeling purposes. This study infers that a detailed analysis is required to analyze the role of surface roughness with backscattering coefficient to label the various clusters.

2.4 Unsupervised classification of 'change' and 'no change' pixels from temporal SAR images and quantitative assessment of changes

In several applications like disaster management and assessment of land erosion, deforestation, environmental monitoring, analysis of forest or vegetation changes, damage assessment, urban growth, agricultural surveys and analysis of urban changes, the contribution of SAR imaging can become valuable, in particular, if classifying 'change' and 'no change' pixels between two observation dates is undertaken in study area. Unsupervised classification of SAR image in to 'change pixels' ('*cp*') and 'no change pixels' ('*ncp*') is characterized by minimum *apriori* knowledge of the ground truth concerning the area to be investigated. The difficulty in collecting ground truth information regularly in time makes it mandatory to develop unsupervised classification techniques to support the analysis of temporal sequences of SAR images (Carlotto, 1997; Coppin et al., 2004).

Image differencing is a simple widely used approach for classifying '*cp*' and '*ncp*' in SAR images. There are many examples of its use for analyzing satellite images to measure soil erosion, deforestation etc., (Singh, 1989; Simoes et al., 2003; Richards, 2005; Wilkinson, 2005). Image ratioing is suitable for SAR classification of changes compared to image differencing since the ratio image obtained by dividing pixel-by-pixel the gray levels at one date by another date cancels common errors (Rignot and Van Zyl, 1993; Villasenor et al., 1993; Oliver and Quegan, 1998; Wu et al., 2007). These two techniques generate a difference image and a ratio image respectively and by applying suitable thresholds on the difference and ratio image yields a classified image of '*cp*' and '*ncp*'. Trial and error procedures are typically adopted for threshold selection (Singh, 1989; Rignot and Van Zyl, 1993; Dierking and Skriver, 2002).

Automatizing threshold selection task is addressed (Moser and Serpico, 2006) and in this proposed method, solution is developed for three different parametric models postulated for 'change' and 'no change' hypothesis i.e. Nakagami ratio, Weibull ratio and Log normal models. Hence, implementation of automatic threshold selection for this proposed method uses assumption of any of the three distribution for '*cp*' and '*ncp*' (Ridd and Liu, 1998; Rogerson, 2002). There are various works reporting preprocessing operations like block averaging, gamma MAP filter, followed by log ratioing and manual thresholding according to a desired probability of false alarms (Dekker 1998; Grover and Quegan, 1999). There are reported works on selection of thresholds for automatic classification of '*cp*' and '*ncp*' (Bazi et al., 2005; Moser and Serpico, 2006). Correlation coefficient can also be used to find change pixels by comparing two images (Rignot and vanZyl, 1993; Radke et al., 2005). Various intensity, texture and orientation saliency maps is used by fusing them for image classification purposes (Itti et al., 1998; Bouzidi et al., 1998a). Multicomponent Hidden Markov Chains (HMC) (Derrode et al., 2003), Fuzzy hidden markov chains (Carincotte et al., 2006), multi scale based approach (Bovolo and Bruzzone, 2005) are some of the other methods used to classify 'change' are used for classifying 'change' and 'no change' pixels,. These techniques give classified image of 'change' and 'no change' pixels but no quantitative information about the changes could be retrieved from the above discussed image analysis approaches.

Interferometric SAR (InSAR) offers a promising solution for quantitative measurement of changes on earth surface covering wide area economically and efficiently (Gabriel et al., 1989; Massonnet et al., 1993; Prats et al., 2008). InSAR derives information by using the interferograms, formed by phase differences between two complex SAR images of the same area but obtained at slightly different positions. Using this concept, interferometry can be used to measure elevation of terrain (Rao et al., 2003; Kumar et al., 2006). Due to the nature of InSAR imaging, the phase in InSAR images is wrapped to the interval $[0, 2\pi]$. Reconstruction of absolute or actual phase is termed as phase unwrapping. This process is the principal stage in constructing digital elevation models from interferometry (Constantini et al., 1999). It has been demonstrated that digital elevation with approximately 2 m relative height accuracy can be achieved suing TerraSAR-X (Moreira et al., 2004; Lenz et al., 2005a; 2005b). There are some papers combining polarimetry and interferometry based on

the analysis of a fully polarimetric radar data acquired in an interferometric mode using a fully polarimetric system (Cloude and Papathanassiou, 1998; Chandra and Keydel, 1999; Alberga and Chandra, 2002; Alberga et al., 2003; Gu et al., 2004).

Another impressive application of radar interferometry is application of Differential Interferometry (DInSAR). This technique enables the mapping of geodynamic phenomena. The principle idea is using two interferometric image pairs of the same area separated in time, and assuming a dynamic deformation occurring in time between the two acquisitions, it is possible to form a differential interferogram where the underlying topography is cancelled and remaining is only the phase information from the deformation itself. It is a technique capable of measuring terrain changes on a wide area (Strozzi et al., 2000; Grey et al., 2003). This fact is emphasized by some successful case studies for application of DInSAR to measure landslide movements (Frunneau et al., 1996; Kimura and Yamaguchi, 2000; Berardino et al., 2002; Colesanti et al., 2003; Hitley et al., 2004; Strozzi et al., 2005; Bovenga et al., 2006).

Generally, surface deformation can be measured by applying stacking interferograms or permanent scatterer techniques,. Stacked interferograms provide an effective means to reduce the atmospheric effects in the deformation map with improvement in accuracy (Yen et al., 2008). Permanent scatterer technique is used to map deformation close to one millimetre (Ferretti et al., 2001; Colesanti et al., 2003). Permanent scatterer technique requires a large number of SAR acquisitions for analysis. Successful mapping of continuous slow landslide movements has been reported by many researchers (Berardino et al., 2002; Prati et al., 2004; Amelung et al., 2006). These techniques require large image stockings available so that critical selection of InSAR image pairs could be performed and accurate deformation be achieved. The main limitation with applying interferometry is the requirement of large image stockings to analyze and find the images with less geometric decorrelation. Due to this fact, analysis of low coherence areas cannot be performed successfully using interferometry. Particularly, in the case of permanent scatterer technique, the technique may be ineffective wherever the density of stable radar targets is relatively low.

All these studies have implied that DInSAR is a successful tool for measuring deformation on earth surface or changes quantitatively. Some critical issues, like

availability and selection of suitable interferometric pairs, and sufficient level of coherence between the selected image pairs for analysis, are involved in the implementation of DInSAR.

Some inferences can be made after doing comprehensive study and critical analysis of the existing methodologies that are as following:

- Selection of texture measures suitable for efficient classification of SAR images is imminent and an effective means of using the chosen texture features has to be critically analyzed.

- There is a need for multiresolution analysis of SAR data. M-band wavelet transform is a suitable approach for capturing micro and macro textures present in SAR image. Due to over complete decomposition by M-bands, suitable technique for optimal choice of subbands is required.

- There is a need to enhance unsupervised classification algorithm that can be used with minimum *apriori* information of the particular site (It means less interaction from the user).

- There is a need to explore some suitable methods to label the various clusters.

- Classification of 'change' and 'no change' pixels on the basis of image analysis approach so that ad-hoc selection of thresholding may be avoided. Various image analysis and statistical measures have to be analyzed for classification of 'change' and 'no change' pixels with temporal SAR imagery. By that, uncertainty in 'change' and 'no change' pixels can be minimized.

- There is a need to explore the possibility of interferometric technique for quantitative measurement of changes like subsidence and efforts should be made to correlate both results that are obtained from image analysis and interferometric approach, so that interferometric complexity can be avoided to produce first hand results of low, medium or high subsidence areas.

Chapter 3

Analysis of Texture Measures for Unsupervised Classification of SAR Images

3.1 Introduction

A digital image can usually be characterized by intensity and textures present in it. The texture of the image represents the intrinsic spatial variability of neighboring pixel values for each pixel within the image, whereas intensity corresponds to pixel value. For SAR images, each pixel value corresponds to mean of backscattering coefficient exists in it and texture corresponds to the spatial pattern of variability of reflectivity. These two properties of image may be quite helpful to carry out classification of SAR images.

Two types of intensity variations within the SAR image are to be considered while applying them for land cover classification:

(i)   Variations in average intensities from one land cover into another (i.e. such as between water and urban, or urban and agriculture areas), and

(ii)   Variations within a land cover related to spatial variance in geometrical attributes of the surface and overlying agriculture or built-up areas, termed as texture variations.

Textural measures of SAR image helps in computing these variations. Therefore, these texture measures are important elements for SAR image interpretation, particularly for single polarized SAR image. It means that texture may play an important role for SAR image classification. Therefore, our focus in this chapter is to choose suitable texture measures for unsupervised classification of single polarized SAR image and to propose an approach to combine the chosen texture measures so that overall classification accuracy can be enhanced.

Statistical characterization of texture requires measurement from a finite sampling window (window is a filter or mask applied with a defined function for each pixel in an image) rather than a single pixel to identify the spatial pattern of the texture.

For measuring textures, usually, moving window is applied to all over the image and for every position of the window on the image, texture measure is computed and centre pixel of the window is replaced by the computed texture measure. Size of the window is a very important parameter for measuring texture. Window size has to be larger than the size of texture pattern to capture the texture (Dell'Acqua et al., 2006). Therefore, care should be taken to find the optimum window size suitable for application.

Researchers are using various texture measures for SAR image classification (Liu, 2008; Song et al., 2007; Gupta et al., 2006). The application of sum and difference histograms is presented for texture based classification (Unser, 1986). A comparative study of various techniques for texture classification like Gabor filters, Wavelet transforms, Discrete cosine transform (DCT) methods, Co-occurrence matrices is presented (Randen and Husoy, 1999). These techniques were compared on the basis of classification errors and computational complexity. It is concluded that wavelets performed better than Gabor filters. Co-occurrence features, Gabor and MRF (Markov Random Field) features were compared and fused for sea SAR imagery classification (Clausi, 2001) and it infers that fusion of various texture features is quite helpful for SAR image classification. Aujol et al., (2003) has demonstrated that wavelet coefficients can be used to identify textures as classes in image. Dekker (2003) has used texture measures like histogram measures, lacunarity, semivariogram, wavelet energy, and fractal dimensions for updating the land cover. Dekker has applied these textural measures individually and in combination using nonparametric distance measures for discrimination of land cover types. He has noted that the classification accuracy improves when adding any of the selected textures or combinations. So, there is a need to critically analyze the role of various texture measures like mean, variance, semivariogram, lacunarity, weighted rank fill ratio and wavelet components for SAR image classification, individually as well as their combined effect on classification accuracy. In addition, there is a need to improvise the algorithm of combining texture measures. Various techniques like K-nearest neighbor classifier, wavelet transforms, PCA approach are used for fusion of texture measures (Solberg and Jain, 1997; Clausi, 2001; Cao et al., 2003). One of the basic principles of PCA is that it fuses information from various input features, gives output as principal components (PCs) in terms of eigen vectors which are orthogonal,

and captures maximum information from the input features (Joliffe, 2002; Bajwa and Hyder, 2005). On the one hand, PCA is used for dimensionality reduction, and on the other hand, it can be used to enhance classification accuracy by fusion of maximum information obtained by single band single polarized SAR image. Therefore, seeing these advantages of PCA, we are focused in this chapter to see the applicability of PCA in enhancing classification accuracy.

For efficient land cover classification, two factors namely (i) choice of texture measures, and (ii) an algorithm to combine the selected texture measures are important. Every texture measure identifies texture patterns by different approaches. In this chapter, texture measures namely, mean, variance, semivariogram, lacunarity, weighted rank fill ratio, and wavelet components are individually critically analyzed for its effect on classifying SAR image for various major land covers like water, urban and agriculture areas. It is also important to know the combined effect of these features on classification accuracy. Therefore, in this chapter, an approach to integrate texture measures using PCA for classification process is proposed. The applicability of PCA for fusing texture measures is analyzed and presented in this chapter.

This chapter is organized as follows. Section 3.2 describes the analysis of contribution of individual texture measures for SAR image classification using synthetic images and real SAR image. This analysis helps in choosing suitable combinations of texture measures for SAR classification. Section 3.3 explains general methodology for unsupervised classification of SAR images using PCA based fusion of texture measures. Results and critical analysis of the proposed algorithm are presented in section 3.4. Conclusion for the chapter is presented in section 3.5.

3.2 Analysis of contribution of individual texture measures

Mean, variance, semivariogram, lacunarity, weighted rank fill ratio, and wavelet components have their own importance in SAR image analysis and its application for land cover classification. Therefore, these texture measures are analyzed for their role in major land cover classification of SAR image into water, urban and agriculture areas.

3.2.1 Texture measures

3.2.1.1 Mean: Mean computes the average intensity over the window and replaces centre pixel by the mean. Therefore, in the process, mean smoothens out noisy pixels. The mean feature image extracted for SAR image captures local fluctuation of amplitude and distributes intensity of impulse noise spikes among surrounding pixels, making noisy pixels less noticeable (Gonzalez and Woods, 2002). For SAR image, mean computes mean backscattering coefficient and thus, helps in discriminating smooth textured areas according to their backscattering coefficient. Mean is given by

$$\mu = \frac{\sum_{i,j} x_{ij}}{n} \tag{3.1}$$

where x_{ij} is the intensity of pixel at location *(i,j)*, *n* is the number of pixels over which mean is computed, and μ is the mean calculated over '*n*' number of pixels.

3.2.1.2 Variance: The best option to capture boundaries and edges is by computing variance. Value of variance corresponds to the level of heterogeneity. It helps in identifying boundary and heterogeneous areas (Gonzalez and Woods, 2002). In case of SAR images, variance may help in locating boundary regions of smooth textured areas and classifying various textured areas on the basis of their heterogeneity. Variance is given by

$$\sigma^2 = \frac{\sum_{i,j} (x_{ij} - \mu)^2}{(n-1)} \tag{3.2}$$

where x_{ij} is the intensity of pixel at location *(i,j)*, *n* is the number of pixels over which variance is computed, and σ^2 is the variance calculated for '*n*' number of pixels.

3.2.1.3 Semivariogram: This is the most common type of variogram. Variogram relates the variance of pixels to its spatial location and describes the scale and pattern of spatial variability. Semivariogram is an effective measure for identifying different texture patterns present in SAR images. It relates the distance or range over which spatial dependence exists. In other words, semivariogram indicates the extent of a texture pattern in an image. Lag distance '*h*' of '*n-1*' is selected for computing

34

semivariogram. For studying the effect of window size on classification accuracy and for finding optimum window size, window size 'n' is varied from 3 to 15 at the interval of 2. When window size is varied from 3 to 15, lag distance 'h' is varied from 2 to 14 (Carr and Miranda, 1988). Hence, effect of varying lag distance is studied by varying the window size for measuring textures.

$$\gamma(h) = \frac{1}{2N} \sum_{i=1}^{n} (x_i - x_{i+h})^2 \qquad (3.3)$$

where x_i stands for intensity at pixel i, and x_{i+h} stands for intensity of pixel at distance h from pixel i, and 'N' is the number of pixel pairs at lag distance 'h' within the chosen window of size '$n \times n$'.

3.2.1.4 Lacunarity: Lacunarity analysis is a multi scaled method for describing patterns of spatial dispersion (Plotnick et al., 1996). The technique of computing lacunarity for scalar data has been defined (Dobson et al., 1997) as

$$\Lambda(r) = \left(\frac{\sigma(r)}{\mu(r)} \right)^2 + 1 \qquad (3.4)$$

where 'r' is the center pixel over '$n \times n$' window, μ is the mean calculated over 'n' number of pixels, and σ is the standard deviation calculated for 'n' number of pixels. Lacunarity features reflect the spatial distribution of gap sizes in texture images. This measure is immensely helpful in the image classification of SAR images that contain rich textures. Lacunarity is computed using the ratio of standard deviation to mean and hence it is dependent on the mean intensity over the window as well as the variation of pixel values from the mean within the window. Therefore lacunarity can be used for discriminating both smooth and coarse textures.

3.2.1.5 Weighted Rank fill ratio: This ratio is an order statistic, which is defined as the ratio of power of 5 % of brightest pixels of the window and the total power of all pixels present in it (Dobson et al., 1997). This factor of texture measure captures brightest pixels present in the window area and fills any data gaps that might have introduced within brighter pixels due to sensor interference or any such factors of noise.

$$\eta = \frac{\text{sum of } \kappa\% \text{ brightest pixels}}{\text{sum of all pixels}} \qquad (3.5)$$

where, κ - is taken as 5 to consider 5% of brightest pixels in the pixel area considered.

3.2.1.6. Wavelet Components: Daubechies wavelets(db4) can be expected to result in high classification accuracy as reported (Bellagente et al., 1999). Daubechies wavelet (db4) function is used for wavelet decomposition. Wavelets from daubechies family are used because of its desirable properties of orthogonality, approximation quality and numerical stability. These properties ensure that no significant information is lost in the decomposition of SAR image in to its wavelet components.
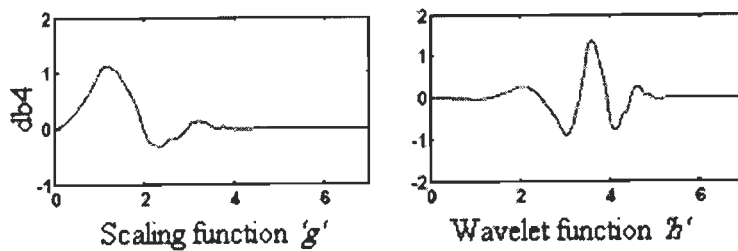
Figure 3.1. Scaling and wavelet function of fourth order daubechies wavelet transform (db4).

Table 3.1. Filter coefficients of db4 wavelet transform.

Scaling function, g*(n)*	Wavelet function, *h(n)*
-0.2304	-0.0106
0.7148	0.0329
-0.6309	0.0308
-0.0280	-0.1870
0.1870	-0.0280
0.0308	0.6309
-0.0329	0.7148
-0.0106	0.2304
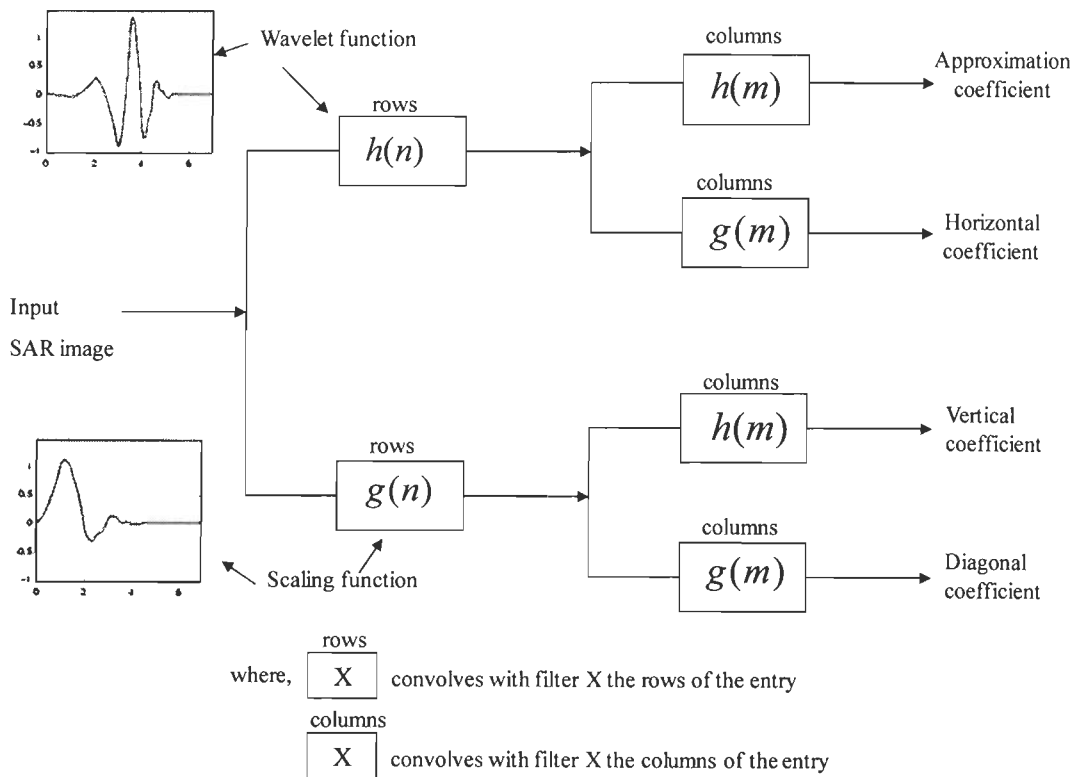
Figure 3.2. Implementation of db4 wavelet transform on SAR input image.

Scaling function 'g' and wavelet function 'h' (Figure 3.1) are used to apply daubechies wavelet transform on SAR image to obtain db4 wavelet components (Strang and Nguyen, 1996). The filter coefficients corresponding to scaling and wavelet functions for fourth order daubechies wavelet db4 are given in Table 3.1 (Ismail and Asfour, 1999). Asymmetric scaling and wavelet functions, 'g' and 'h', are used to decompose SAR image by applying them to rows and columns and convolve them to get four wavelet components as approximation, horizontal, vertical and diagonal coefficients (Figure 3.2).

When wavelet components (i.e., approximation, horizontal, vertical and diagonal coefficient) are computed for SAR image, mean backscattering coefficient is computed by approximation coefficient, whereas, spatial variations of pixel along horizontal, vertical and diagonal directions are computed by horizontal, vertical and diagonal coefficients respectively. Therefore, texture based classification can be performed effectively using all the four wavelet components.

3.2.2 Role of texture measures for image classification

To check the roles of texture measures on classification, two synthetic images based on intensity (S1) and texture (S2) are generated that are shown as Figure 3.3 (a, b). Synthetic image S1 having different intensity levels, is chosen to represent smooth textures and synthetic image S2 is chosen such that it comprises of four different rough textures. These images are acting as test images to analyze how individual texture measure discriminates different texture patterns.
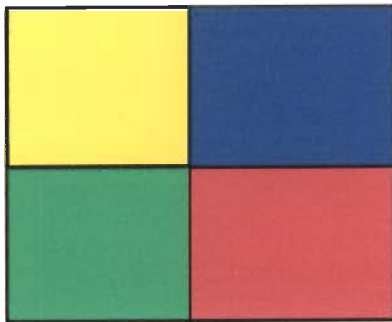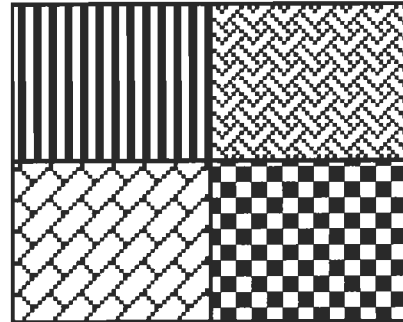
(a) Synthetic image S1   (b) Synthetic image S2

Figure 3.3. Synthetic images.

All texture measures listed in section 3.2.1 are computed individually for both the synthetic images. Here, we are interested only to check the role of individual textures on classification. A sliding window of size '5×5' has been used to compute texture measures. Images of texture measures are obtained with same size as the input images. In synthetic image S1, there are four levels of intensity and hence can be represented as four classes. Similarly, synthetic image S2 has four classes according to four texture patterns. K-means clustering of four classes is performed on the texture measures and classification accuracy is computed as shown in Table 3.2.

Inferences about the role of texture measures can be obtained from Table 3.2. Mean help in differentiating test image with smooth textures because mean computes average intensity over the window smoothing out isolated pixels. Error is introduced in mean image due to the blurred boundaries and edges. The classified image using mean has approximately 10% of error for image S1 and it may be contributed by blurred boundaries. Image S2 has four different textures in it. Since mean computes

38

only average intensity over the window, mean helps in distinguishing only smooth textures efficiently. Therefore, mean produces an accuracy of 35.99% for image S2.

Table 3.2. Classification accuracy for individual texture features computed for synthetic images, S1, S2 and real SAR image.

Sl.No.	Texture measures	Classification Accuracy (%)		
		Synthetic image S1	Synthetic image S2	Real SAR image
1	Mean	90.11	35.99	76.29
2	Variance	49.85	26.56	49.85
3	Semivariogram	50.05	62.04	52.05
4	Lacunarity	81.25	86.87	46.55
5	Weighted rank fill ratio	97.86	43.05	76.10
	Wavelet components			
6	Approximation coefficient	16.09	47.67	48.52
7	Horizontal coefficient	48.24	74.56	37.83
8	Vertical coefficient	48.24	74.55	41.81
9	Diagonal detail coefficient	48.15	75.36	43.35

Variance measure gives zero intensity within the four classes of image S1 and therefore, all the constant intensity level areas corresponding to four classes in S1 are grouped as a single class. This leads to 49.85% accuracy with boundaries of all four classes and only one class, being identified properly. When variance is computed for image S2, all spatial variations of gray level with in texture pattern are identified and hence patterns could not be differentiated by using only variance. Thus, variance helps in identifying boundaries in S1, giving an accuracy of 49.85% but does not help in differentiating patterns in S2, giving lesser accuracy of 26.56%.

Semivariogram results in zero value for equal intensity area within S1. Semivariogram gives the same value for all four classes in image S1 having smooth textures, except for the pixels corresponding to boundary and near boundary region. Therefore, it gives a classification accuracy of only 50.05% with S1. Semivariogram computes spatial pattern of texture in terms of distance and therefore, it can be used for discriminating texture patterns that vary by their spatial dispersion. Hence, it helps in differentiating textures in S2 giving 62.04% of classification accuracy.

Lacunarity measure is dependent on the standard deviation and mean of the pixels within the window (equation 3.4). Lacunarity helps in differentiating both S1 and S2 giving classification accuracies of 81.25% and 86.87% respectively. Mapping of texture and intensity to lacunarity is not unique and same lacunarity values are obtained for more than one combination of texture and intensity pattern. This ambiguity arises when it encounters two regions such that they have same ratio of standard deviation to mean. This may explain the classification error when lacunarity is applied for image S1 and S2.

Weighted rank fill ratio helps in filling up the gaps in brightest pixels present in S1 and thus giving rise to a better accuracy of 97.86% than using mean alone for S1. Since weighted rank fill ratio fills gaps present in the window considered, this measure helps in differentiating smooth textures only. For image S2 having different texture patterns, weighted rank fill ratio produces an accuracy of only 43.05%.

Wavelet components help in differentiating S2 but not S1. Wavelet components provide spatial frequency based descriptors as features for segmenting textures. For smooth images, there are only gradual variations in grey level and components are dominated by low spatial frequencies, whereas, in textured images, grey level varies rapidly and are made up of wide range of frequencies. With the analysis of distribution of frequency components, texture patterns can be distinguished. All the four components of wavelet analysis are to be used together to realize the classification. From Table 3.2, it can be seen that approximation coefficient produces less accuracy of 16.09% with S1. Horizontal, vertical and diagonal coefficients identifies boundaries along the horizontal, vertical and diagonal directions and therefore, they help in obtaining boundary regions in respective directions giving approximately same accuracy of about 48%. These three coefficients give better accuracy of approximately 74 to 75% when they are used for image S2.

With this analysis, it can be inferred that mean (90.11%) and weighted rank fill ratio (97.86%) help in differentiating regions of smooth textures with varying intensity levels. Variance, semivariogram and wavelet components help in identifying boundaries and differentiating various rough texture patterns. Lacunarity measure is dependent on both mean and standard deviation. Therefore, it may be suitable for land cover with varying intensity and texture patterns (81.25% for S1 and 86.87% for S2).

This critical analysis infers that the used texture measures may be quite helpful for classification of SAR images because SAR image includes various land covers like water, urban and agriculture areas, which can be described by various texture patterns.

These texture measures are applied individually on SAR image and corresponding classification accuracy is also listed in Table 3.2. Mean and weighted rank fill ratio have given higher accuracy for image S1 as well as for SAR image, whereas the amount of accuracy is reduced in SAR image in comparison to S1 image. It infers that SAR image has more texture patterns rather than smooth textures. Lacunarity and wavelet components have exhibited good classification accuracy with image S2, whereas, for SAR image, these measures provide accuracy less than 50%. It may be due to the fact that SAR image may have more patterns in comparison to S2 image (In image S2, only four texture patterns are considered). Variance and semivariogram do not provide higher classification accuracy individually because these measures play a role in identifying boundaries of smooth textures or identifying textures on the basis of their spatial extent. This analysis represent that all these measures are playing an important role either in describing intensity or textures to classify SAR image. It has been observed from the Table 3.2 that classification accuracy using individual texture measures for classifying SAR image into major land cover types of water, urban and agriculture areas can reach only up to 76.29%. Each texture measure analyzes SAR image by different approach and helps in identifying different intensity or texture patterns in it. To exploit the advantages of each of these textural measures in classification, these textural measures are to be fused such that maximum information contained in them are used for classification purposes. Its combined effect may include more information that may help to increase classification accuracy. Hence, there is a need of combining texture measures for better classification accuracy.

The texture measures in feature set are combined by PCA and the combined effect of chosen texture measures are evaluated using classification accuracy. A suitable combination of feature set is critically analyzed in checking to improve classification accuracy. For studying the combined effect of texture measures on classification, feature sets shown in Table 3.3 are considered. Texture measures listed against each of the feature set are combined using PCA and classification is performed.

Table 3.3. Feature sets for studying the combined effect of texture measures.

Feature set	Texture measures
I	Mean, Variance
II	Wavelet components
III	Mean, Wavelet components
IV	Mean, Variance, Wavelet components
V	Mean, Variance ,Wavelet components, lacunarity
VI	Mean, Variance, Wavelet components, semivariogram
VII	Mean, Variance Wavelet components, weighted rank fill ratio
VIII	Mean, Variance Wavelet components, semivariogram, lacunarity, weighted rank fill ratio

3.3 Methodology to implement PCA based unsupervised classification on SAR images using texture measures

3.3.1 Data used

Solani river catchment around Roorkee town in the state of Uttarakhand, India is chosen as the study region. ERS-2 SAR C-band image acquired on July 23, 2001 is used for developing and analyzing the proposed approach of unsupervised classification of single polarized SAR image. The complete details of the study area and satellite data can be referred with section 1.3 and 1.4.

3.3.2 Principle of PCA

The central idea of PCA is to reduce the dimensionality of a data set in which there are a large number of interrelated variables while retaining as much as possible of the variation present in the dataset. This reduction is achieved by transforming to a new set of variables, called PCs in terms of eigen vectors, which are uncorrelated, and which are ordered so that the first 'few' retain most of the variations present in 'all of the original variables'.

Although the purpose of PCA is to reduce the number of variables, the ways in which the PCs can actually be used are quite varied. The PCs give an alternative, much simpler description of the data than the original variables. This is evident from the fact that first few PCs (uncorrelated variables) obtained by PCA reproduce most of the variation in all original variables and further, these variables are interpretable. PCA based on correlation matrix is preferred and adopted to combine texture measures since it is desired to treat all variables on an equal footing (Joliffe, 2002).

3.3.3 PCA based fusion approach

Flow chart of the proposed algorithm is given in Figure 3.4. Raw SAR data is available as input for classification of SAR images. Preprocessing of SAR image is performed as discussed in section 1.5. Textural images are extracted from the preprocessed SAR image using the equations (3.1) to (3.5) described in section 3.2. Textural measures are computed without downsampling. Therefore, for a SAR image of size $n \times n$, all the texture measures are also of the size $n \times n$.

For implementing proposed approach, following steps have been adopted.

(i)   Compute texture measures for various window sizes ranging from 3 to 15, in steps of 2, and identify optimal window size for computing texture measures.

(ii)   Normalize texture measures so that each texture measure has zero mean and unity standard deviation.

(iii)   Apply PCA for combining texture measures according to feature sets listed in Table 3.3.

(iv)   Selection of PCs for further classification.

(v)   Clustering by K-means classifier.

(vi)   Labeling of clusters into land covers namely water, urban and agriculture areas using topographic sheet.

All the texture measures are computed for window sizes varying from 3 to 15, in steps of 2, and classification accuracy is calculated. From this analysis, optimum window size for calculating texture measures is chosen. Then, texture measures of SAR image are computed using optimum window size. These texture measures are normalized individually to have zero mean and unity standard deviation. Normalization performs linear scaling of all input features to avoid large dynamic ranges in one or more dimensions. When input features differ by several orders of magnitude, they can undermine smaller but important trends in the data (Aminian et al., 2002; Bishop, 1995). PCA is employed on normalized texture measures to get PCs. Selective PCs are chosen on the basis of cattell's scree test and they are used for further classification by K-means classifier. Then, with the help of ground truth data, clusters in segmented SAR image can be labeled with major land cover types like water, urban and agriculture areas.

ERS-2 PRI Image

⬇

(Preprocessing)

⬇

| Statistical Textural feature extraction | 2-D Wavelet filter |

⬇ ⬇

| Mean Intensity, Variance, Semivariogram, Lacunarity, Weighted rank fill ratio feature images | Wavelet components (Low pass, high pass, horizontal and vertical components) |

⬇ ⬇

Normalization and Feature set combination

⬇

(Fusion using PCA)

⬇

(Multicriteria classification by K-means classifier)

⬇

Classified Image
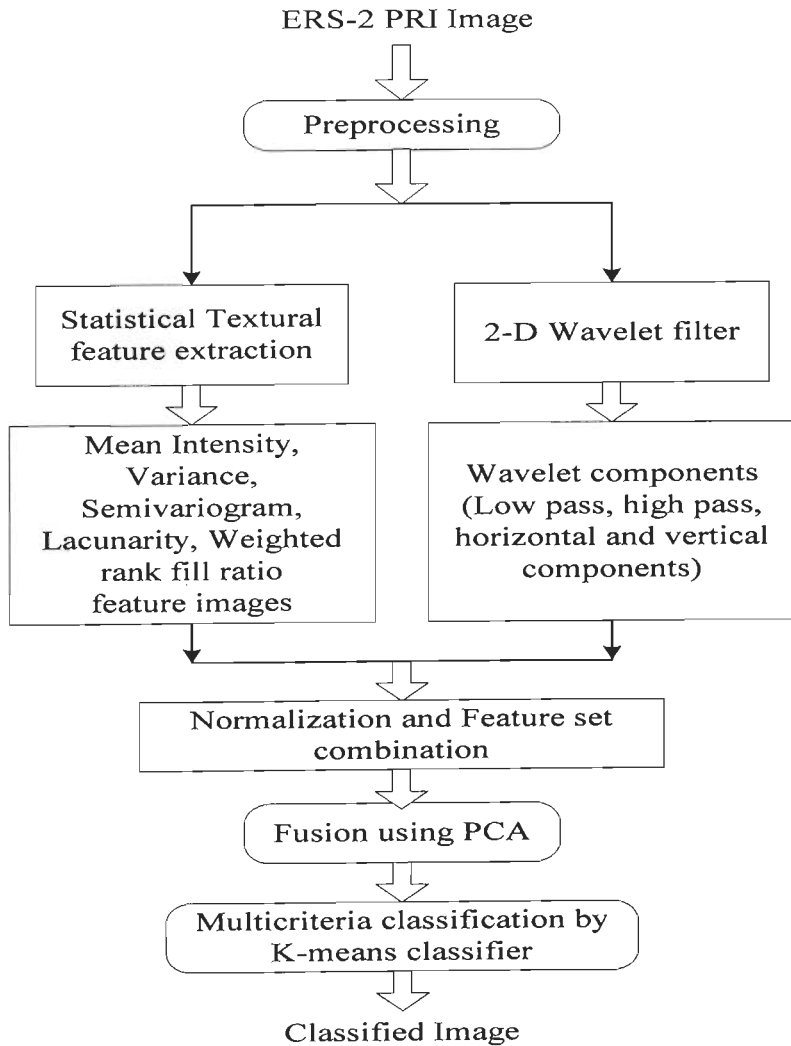
Figure 3.4. PCA based fusion of texture measures for SAR classification.

3.4 Results and critical analysis of proposed algorithm

3.4.1 Selection of optimum window size

In the proposed classification algorithm, texture measures computed for SAR image depend on the window size with which they are computed. Window size depends on the spatial relationships among texture elements. It defines the area around a pixel within which it is assumed that texture patterns are steady. In turn, this number is related to the mean physical size of the textured areas (Dell'Acqua et al., 2006). The texture patterns depend on land cover types. Hence, an optimum window size to measure textures is to be identified.

Feature set VIII comprising of all texture measures is considered for analyzing and identifying optimum window size. Texture measures are computed with window sizes varying from 3 to 15, in steps of 2. Three PCs are chosen using cattell's scree test on PCs obtained by PCA analysis of feature set VIII and are given to K-means classifier. Then, classification accuracy is computed as listed in Table 3.4. It can be observed from Table 3.4 that classification accuracy reaches maximum of 90.39% for window size of '5×5'. Classification accuracy gradually reduces when window size is increased beyond '5×5'. From this analysis, it can be inferred that a window size of '5×5' is optimum for measuring the texture for this SAR image.

Table 3.4. Classification accuracy using feature set VIII for different window sizes.

Window size	Classification accuracy (%)
3	56.31
5	90.39
7	86.31
9	83.86
11	73.34
13	62.97
15	58.34

3.4.2 Analysis of combining texture measures

The different combinations of texture measures are critically analyzed for its effect on classification accuracy. For this purpose, proposed classification approach depicted in Figure 3.4 is implemented for all feature sets listed in Table 3.3. PCA is used for combining texture measures. In this approach, first, PCA is applied on all the texture measures of each feature set of Table 3.3 and PCs are obtained. From these PCs, few of the PCs are chosen using cattell's scree test. Eigen values of the PCs are indicative of the variance contained in them. Most expressive features are identified by their large eigen values. Cattell's scree test is used to identify number of axes required for projection of data so that information is preserved with reduced components. Cattell suggests finding a place where the smooth decrease of eigen values appears to level off to the right of the plot. To the right of this point, presumable, one finds only

'factorial scree'. 'Scree' is the geological term referring to the debris which collects on the lower part of a rocky slope (Cattell, 1966). According to this criterion, eigen values above the scree are chosen for classification process and number of final axes is the number of eigen values considered. For example, selection of PCs from feature set VIII (Table 3.3) is considered. PCA is applied on feature set VIII and eigen values are calculated for the PCs (Table 3.5). Figure 3.5 shows the plot of eigen values versus PCs. Dividing line is drawn such that to the right of dividing point, eigen values level off. Similarly, PCs are chosen for each of the feature sets listed in Table 3.3.

Table 3.5. Eigen values of PCs for feature set VIII.

Principal components	Eigen values
PC1	8.10E+08
PC2	78810
PC3	6252
PC4	327
PC5	324
PC6	118
PC7	108
PC8	49.2
PC9	34.4
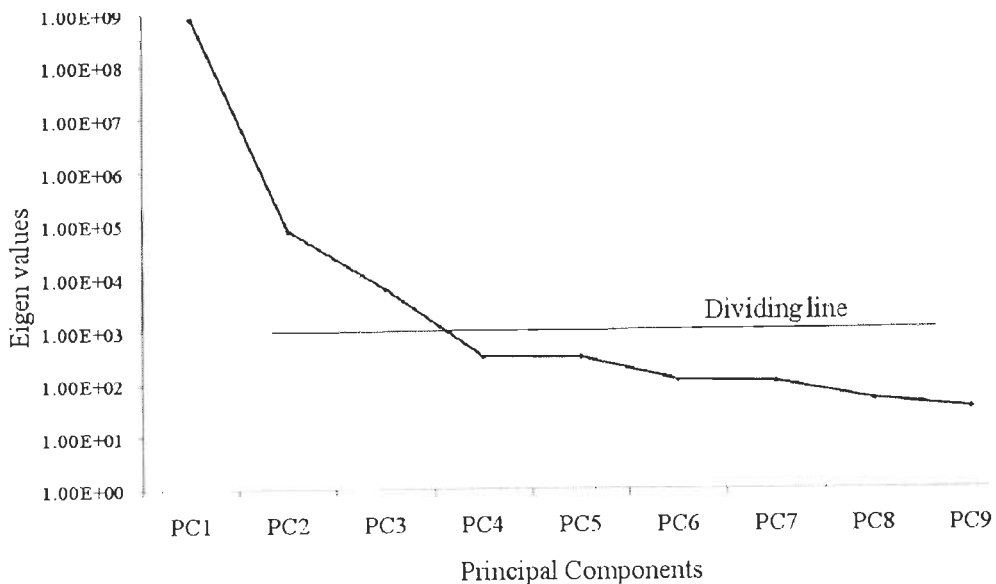
Figure 3.5. Eigen values of PCs for feature set VIII.

Cattell's scree analysis of principal components emphasize the need of selection of only first three components and further experimentally, the role of first three PCs on discriminating ability of major land covers in SAR image is also reconfirmed.

3.4.3 Role of principal components on classification accuracy

For the feature set VIII (Table 3.3), the analysis of how individual principal component (PC) affect in classification is undertaken by computing classification accuracy with first PC alone and then by adding PCs one by one. Results are tabulated in Table 3.6.

Table 3.6. Effect of adding PCs on classification accuracy.

Sl.No.	Principal components	Overall classification accuracy (%)
1	PC1	86.35
2	PC1+PC2	87.40
3	PC1+PC2+PC3	90.39
4	PC1+PC2+PC3+PC4	85.32
5	PC1+PC2+PC3+PC4+PC5	82.21
6	PC1+PC2+PC3+PC4+PC5+PC6	81.13
7	PC1+PC2+PC3+PC4+PC5+PC6+PC7	76.46
8	PC1+PC2+PC3+PC4+PC5+PC6+PC7+PC8	74.35
9	PC1+PC2+PC3+PC4+PC5+PC6+PC7+PC8+PC9	68.87

With principal component one only (PC1), classification accuracy is 86.35%. By adding principal component two (PC2) to the input for K-means classifier, classification accuracy improves to 87.40% (with PC1+PC2) and addition of third component give rise to 90.39% (with PC1+PC2+PC3). Addition of remaining PCs cause drop in classification accuracy which implies that the fourth and successive PCs may introduce noise in the classification hence they are dropped from classification. This analysis also confirms the choice of first three PCs chosen using cattell's scree test.

Scatterplots of first three PCs are shown as 2-dimensional plots (Figure 3.6 a,b,c). Water and agriculture areas can be seen as individual clusters in PC2 vs PC1 (Figure 3.6 a), with few overlapping points. Urban areas can be visualized as a cluster in PC3 vs PC1 (Figure 3.6 b). The input datasets of texture measures is projected onto new dimension space of PCs. Thus by analyzing scatterplots of first three PCs, it can be inferred that the land cover areas become separable in the transformed new feature space. This analysis explains improvement in class separability using PCs.
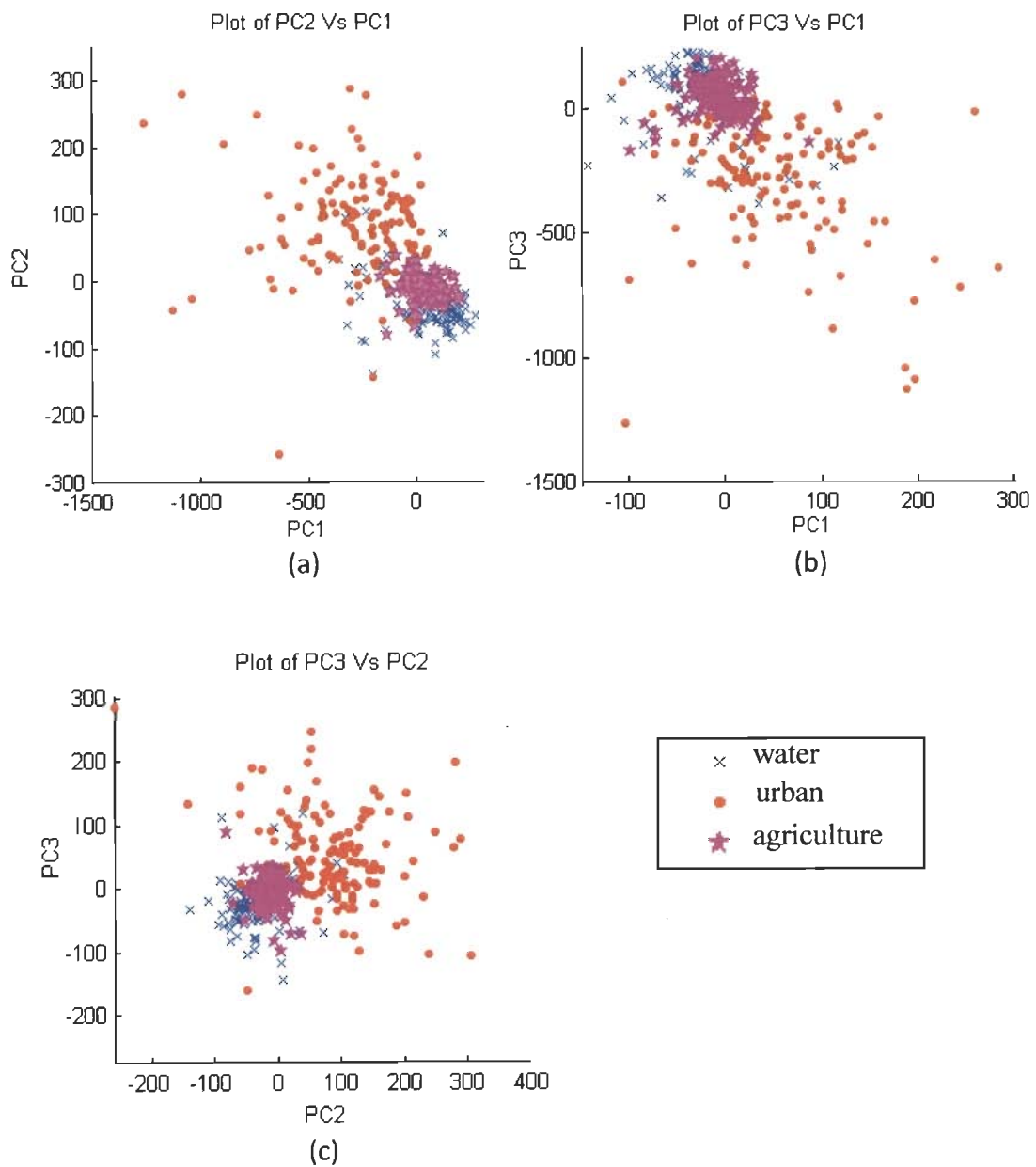
Figure 3.6. Scatterplots (a) PC2 vs PC1, (b) PC3 vs PC1,and (c) PC3 vs PC2.

3.4.4 SAR image classification based on proposed approach

SAR image classification has been carried out for various combinations of texture measures using PCA and non-PCA (K-means clustering). K-means cluster is a simple method where K- is the number of clusters to be grouped by the algorithm. Initial cluster centers termed as mean are chosen randomly. Then, all samples are classified according to nearest mean. Mean for clusters are again computed. This process of classifying samples and computing mean are repeated till there are no changes in means computed for all clusters. Therefore, in non-PCA method, K-means clustering is applied directly on texture measures. In PCA based classification, PCs are obtained by PCA on texture measures. Then, selective components are chosen by cattell's scree test. K-means clustering is applied on selected PCs. Since the cluster centers are chosen randomly in the original K-means algorithm and the obtained results can be different for every run of the algorithm, the overall classification accuracies are obtained by averaging over different runs (50 runs). Overall classification accuracy obtained by K-means and by proposed PCA based classifier is presented in Table 3.7.

Table 3.7. Overall classification accuracy for different feature sets with window size '5×5' for all texture measures by K-means classifier and PCA based classifier.

Sl. No.	Texture measures	Overall classification accuracy (%)	
		non-PCA (K-means)	PCA based classifier (best 3 PCs, except for sl no. 1)
1	Mean, Variance (2 PCs considered for PCA)	59.47	63.03
2	Wavelet components	73.54	84.49
3	Mean, Wavelet components	78.32	87.02
4	Mean, Variance, Wavelet components	74.23	88.16
5	Mean, Variance ,Wavelet components, Lacunarity	72.67	87.21
6	Mean, Variance, Wavelet components, Semivariogram	73.54	88.71
7	Mean, Variance, Wavelet components, Weighted rank fill ratio	68.54	85.99
8	Mean, Variance, Wavelet components, Semivariogram, Lacunarity, Weighted rank fill ratio	67.43	90.39

In the feature set I, mean and variance are considered for classification. For this combination, K-means classifier gives an accuracy of 59.47% whereas, with PCA, it is 63.03%. In this case, only two PCs are obtained by PCA and both these PCs are used for PCA based classifier. Mean corresponds to the average intensity within the window and variance corresponds to the presence of boundaries. For a homogenous area, mean image captures average intensity and variance is zero. When mixed land cover types are encountered within window, degree of heterogeneity increases. Then, variance also increases. By combining these two, homogenous areas identified by mean and boundaries obtained by variance are merged. For this combination, less classification accuracy (approximately 63.03%) has been observed.

It may be due to two reasons:

(i)   Study region has agriculture patches smaller than window size and possibly intermingled with other pixels

(ii) Secondly, it is the property of mean that it smoothen out spiky/isolated pixels and therefore, any particular area like water, urban or agriculture, present as isolated pixel, cannot be correctly classified. (For example, in the study area, small agriculture plots varying from 25 × 25 m to 50 × 50 m are also present (verified by ground truth survey). These plots are present intermingled with urban area and may pose as a spiky pixel in a homogenous area.)

Wavelet components alone are considered for feature set II. Daubechies wavelet analysis computes four wavelet components: approximation, horizontal, vertical and diagonal detail coefficients. Approximation component computes mean and other three components capture variation of pixels in three directions viz., horizontal, vertical and diagonal. Wavelet components capture spatial variation of grey levels and such variation of grey levels is high for texture and less for smooth images (Lindsay et al., 1996). Wavelet components compute pixel variation in three directions and therefore, these components may capture boundary pixels or demarcation points in three directions that may be helpful in classification. When wavelet components are given to K-means classifier, it gives an accuracy of only 73.54%, whereas with PCA based classifier, accuracy increases to 84.49%. This increase in classification accuracy may be explained by the choice of first three PCs capturing maximum information than just using all texture measures. Feature set II using proposed

approach gives better classification accuracy than feature set I (i.e., 84.49%) which represents the importance of wavelet components while obtaining classification.

For the III feature set, mean and wavelet components are considered for analysis. This feature set comprises of five textural measures. When PCA is employed on this feature set, classification accuracy approaches to 87.02%, whereas, without PCA and by K-means classifier, it gives an accuracy of 78.32%. It may be due to the reason that approximation coefficient of wavelet component is merged with mean information because, approximation coefficient also computes mean. The classification accuracy is higher compared to feature set I (which gives an accuracy of 63.03%), where variance is used for identifying boundaries. Since wavelet components computes boundary in all three directions, classification accuracy is improved than that of feature set I. This increase in classification accuracy justifies the increase in complexity by adding additional texture measures.

To analyze the role of variance in classification, variance is added to the feature set III and feature set IV is formed. It is observed that with the application of PCA, classification accuracy approaches 88.16% while with without PCA, it is 74.23%. It is because variance also helps in identifying borders between urban, water and agriculture pixels in addition to the detail coefficients of wavelet components.

Lacunarity, a fractal measure for identifying texture patterns, is added in feature set IV to form next feature set V. This feature set adds the advantage of using ratio of standard deviation to mean as computed by lacunarity in classification process. Classification accuracy of 87.21% is achieved using PCA based classifier as against the K-means classifier giving an accuracy of 72.67%. A decrease in classification accuracy is observed when lacunarity is also considered in the feature set. Lacunarity distinguishes areas with same intensity and different texture patterns also. Lacunarity is different for different textures. Under agriculture areas itself, texture patterns are different for different crops hence use of lacunarity may be effective when applied for more number of classes.

Feature set VI and VII are formed by adding semivariogram and weighted rank fill ratio to the feature set V giving classification accuracy of 88.71 % and 85.99% respectively. With K-means classifier, these feature sets VI and VII give classification accuracy of 73.54% and 68.54% respectively. Semivariogram is also another feature

51

for measuring variance which helps in identifying textures. Weighted rank fill ratio fills out gaps within texture patterns. With a decrease in classification accuracy of ~1 to 3% by PCA based classifier, importance of semivariogram and weighted rank fill ratio, in this case, cannot be assessed.

In feature set VIII, all the textural feature measures extracted are used and PCA is applied and classification is performed with the three PCs of PCA. Classification accuracy is obtained as 90.39%. When all these texture measures are applied to K-means classifier, it gives an accuracy of only 67.43%, which implies the importance of PCA based extraction of PCs from texture measures to improve classification accuracy.

In all the feature sets I to VIII, it can be observed that PCA based classifier performs better than simple K-means classifier giving higher classification accuracy compared to that obtained by K-means classifier alone. It means that it explains the role and importance of each feature on the classification accuracy with PCA.

Figure 3.7 (a) shows the SAR image considered and Figure 3.7 (b) shows the topographic sheet of the same region. Classification results are shown in Figure 3.8. Water, urban and agriculture areas are clustered and labelled in classified image of Figure 3.8. Some areas in the study site are termed as 'unclassified' for which information about the land cover type is not accurately available. 'Unclassifed' areas are the masked areas which are discarded from the evaluation of classification accuracy.

3.4.5 Analysis of classification accuracy

Classification accuracy has been computed on the basis of confusion matrix for various classes like water, urban and agriculture areas. The results are validated with the ground truth survey undertaken in and around Haridwar region, India for unsupervised land cover classification. Ground truth survey of vegetation areas reported by Said (2006) is also taken as reference. The results computed are shown in Table 3.8 (a) and (b). Sample ground truth points of 5000 water pixels, 3500 urban pixels and 1500 agriculture pixels are considered for evaluating classification accuracy.
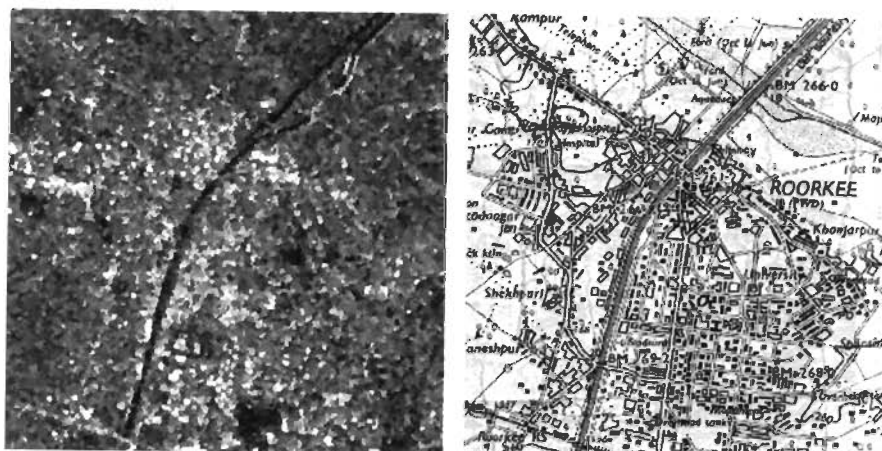
(a)   (b)

Figure 3.7. (a) SAR image and (b) topographic sheet of the study area.
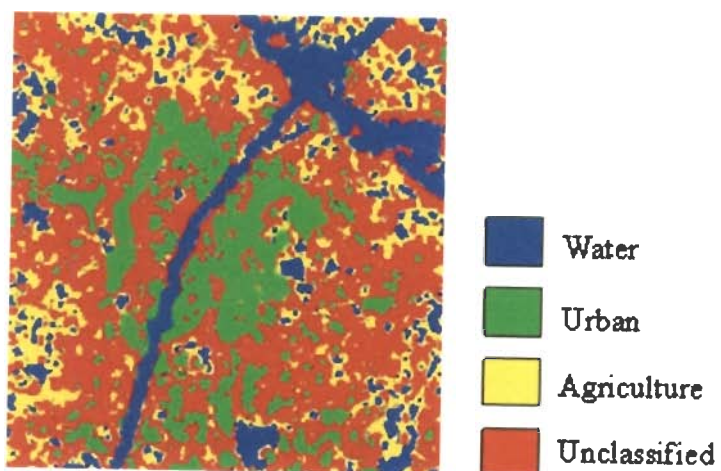
Figure 3.8. Classified image with Feature set (Sl.No. 8) in Table 3.3, showing land cover types, water, urban and agriculture areas.

Table 3.8(a) shows the class by class distribution. Out of 5000 ground truth points representing water, 4850 pixels are identified correctly and 28 pixels are reported as urban and 122 pixels are recognized as agriculture pixels, giving an accuracy of 4850/5000 i.e., 97% in identifying water pixels (Table 3.8 b).

Similarly, 3105 urban pixels out of 3500 pixels are classified as urban pixels and 1084 out of 1500 agriculture pixels are correctly identified. Overall classification accuracy is computed as the ratio of total correctly identified pixels to sum of ground truth points considered giving rise to 9039/10000 = 90.39%.

Table 3.8(b) lists the commission and omission error in pixels as well in percentage. The commission error for water stems from improperly calling other classes water, so that 81 pixels labeled as water are really a composite of other classes. i.e., 25 urban pixels and 56 agriculture pixels are wrongly labeled as water. Hence, it gives rise to commission error of $(25+56)/4931 = 1.64\%$. An error of omission measures between class discrimination and results when one class on the ground is misidentified as other class by the observing classifier. Thus, this classification algorithm fails to recognize and correctly identify all 5000 pixels of water as such, and labels 150 of these water pixels as other classes. Hence, omission error of $(28+122)/5000=150/5000=3\%$ is resulted. Commission and omission error computed in terms of pixels are also represented in percentage. Producer accuracy gives the percentage of correctly identified pixels out of total ground truth pixels considered for a particular land cover. For example, there are 5000 ground truth water pixels considered and 4850 pixels are correctly identified and hence producer accuracy for water is obtained as 4850/5000= 97%. The producer of the map can claim that 97% of the time an area is identified as water was identified as such, 88.71% of the time, an area is identified as such as urban and 72.27% of the time, the area identified as agriculture itself for agriculture areas (Table 3.8 b). User accuracy lists the ratio of correctly identified pixels by the user for a particular land cover type to the total identified pixels. User has identified a total of 4931 water pixels, 3493 urban pixels and 1576 agriculture pixels. Out of 4931 water pixels identified by the user, 4850 pixels are correctly identified whereas remaining 81 pixels are incorrectly labeled as water. Therefore, user of this map will find that 98.37% of the time an area he visits that the map says is water will actually be water.

Table 3.8 (a) Confusion matrix.

Overall classification accuracy = (4850+3105+1084)/10000 = 9039/10000 = 90.39%

	Water	Urban	Agriculture	Total
Water	4850	25	56	4931
Urban	28	3105	360	3493
Agriculture	122	370	1084	1576
Total	5000	3500	1500	10000

Table 3.8 (b) Parameters of classification accuracy for water, urban and agriculture areas.

Parameter	Water		Urban		Agriculture	
	pixels	percent	pixels	percent	pixels	percent
Commission error	81/4931	1.64	388/3493	11.11	492/1576	31.22
Omission error	150/5000	3.00	395/3500	11.29	416/1500	27.73
Producer's accuracy	4850/5000	97.00	3105/3500	88.71	1084/1500	72.27
User's accuracy	4850/4931	98.36	3105/3493	88.89	1084/1576	68.78

3.5 Conclusion

In this chapter, an overview of different texture measures is given and applied to ERS-2 SAR-C band satellite data of Roorkee region, Uttarakhand, India. Contribution of individual textural measures in improving classification accuracy is critically analyzed by varying the combination of textural measures in the feature set. Optimal window size of '5×5' is found to be suitable to capture textures in SAR image considered and is found by computing and analyzing classification accuracy for various window sizes from 3 to 15. It is found that application of PCA transformation on all nine texture measures helps in integrating important information for classification purposes from all these feature measures. Results show that addition of feature measures like lacunarity, semivariogram and weighted rank fill ratio helps in improving classification accuracy up to 90% by properly identifying agriculture areas and this combination of feature set always give higher classification accuracy.

Chapter 4

An Adaptive Algorithm Using Wavelet Features for Unsupervised Classification of SAR Images

4.1 Introduction

In single polarized SAR image classification, information is limited to intensity and texture only and hence, it is difficult to interpret the single polarized SAR image without having any *apriori* information. Therefore, it is important to use these basic features (intensity and texture) to interpret SAR image in order to carry out unsupervised classification. Backscattering coefficient is the intensity / gray level assigned to each pixel due to the reflectance of land cover present in the area corresponding to that pixel. The texture is an important visual cue for describing and assessing various object surfaces. The spatial and scale properties of texture have made it an important attribute in the analysis of remotely sensed images, particularly, SAR images, where different surfaces such as water, urban and agriculture areas can be characterized by distinct texture features. Integrating backscattering coefficient with texture features may also help in distinguishing areas with same texture and different backscattering coefficient levels.

A wide variety of texture analysis methods have been developed for the classification of SAR image. MRF (Manjunath and Chellappa, 1991), Gabor wavelets (Jain and Farrokhnia, 1991), Tree structured wavelets (Chang and Kuo, 1993), Isodata algorithm (Dhodhi et al., 1999), Semivariogram analysis (Atkinson and Lewis, 2000), Support vector machines (Pal and Mather, 2005), Fuzzy probabilistic models (Chanussot et al., 2006) and Contour tracing (Chamundeeswari et al., 2007) are some of the popular methods developed for unsupervised classification of remotely sensed images. Researchers have given emphasis mainly on the construction of texture features with the most discriminative ability. For SAR images, in particular, both micro textures and macro textures are important features in texture analysis for classification purposes. This justifies the use of multi-resolution type analysis and is most effective using wavelets (Acharyya et al., 2003; Wellig et al., 2007).

Even though wavelet transform is established as an efficient and suitable tool for compression and edge detection in SAR images, recent developments of wavelet theory have provided a promising approach to the analysis of SAR images and hence multi-resolution capability of wavelet transform has not yet been explored effectively in capturing different textures of SAR images (Leporini and Pesquet, 1999; Bhattacharya and Mahapatra, 2007). Wavelet packet decomposition is suitable for capturing such micro and macro textures present in SAR images. The octave band wavelet decomposition provides a logarithmic frequency resolution (Steffen et al., 1993). However, it is not suitable for the analysis of high frequency signals with relatively narrow bandwidth. Hence, four-band wavelet decomposition, unlike the standard wavelet analysis, provides a mixture of logarithmic and linear frequency resolution (Alkin and Caglar, 1995) and hence able to characterize textures more efficiently. Most of the unsupervised classification algorithms developed for SAR images include user defined parameters, which have to be set by the user intervention. Users apply either an ad-hoc or trial and error approach to identify the optimal set of parameters, for which maximum achievable classification accuracy can be obtained.

In this chapter, multi-resolution analysis with the help of four-band wavelets is implemented to extract texture features. To restrict the number of sub-bands for further processing, thresholding is applied on the energy computed for each of the sub-bands. Local estimator is used to compute texture features from wavelet coefficients in each sub-band, thus obtaining a texture feature for every sub-band. Texture feature is of same size as the sub-band. Then, backscattering coefficient is integrated with each of the texture features for smooth textured areas. An adaptive neuro-fuzzy algorithm is utilized for ranking the integrated features. Top ranked integrated features are processed by K-means clustering algorithm and land covers are labeled with the help of ground truth data.

To make the algorithm adaptive, variation of classification accuracy with user defined parameters is analyzed and an empirical relationship of the classification accuracy in terms of user defined parameters is developed. The developed relationship can be used to compute the parameters by optimization routine to have maximum classification accuracy that could be achieved by the system. The proposed method speeds up the process of classification and enables the user to obtain an efficient classification of single polarized SAR image where minimum or no *apriori*

information is available, in a single application of the process without any ad-hoc / trial and error approach for identifying parameters involved in classification process.

In this chapter, proposed methodology for implementing classification of SAR image using multi-band wavelets is depicted in section 4.2. An algorithm proposed to obtain optimum user defined parameters involved in classification process is explained in section 4.3. Section 4.4 concludes with features of the proposed unsupervised classification algorithm for single polarized SAR image.

4.2 Classification algorithm using integrated intensity and multi-wavelet features

For the SAR image, preprocessing operations like geo-referencing and despeckling are performed before applying classification process (Section 1.5). Figure 4.1 describes the process implemented for classification process.

The steps involved in classification process using integrated intensity and multi-wavelet features can be stated as:

1. SAR image is georeferenced. Then, despeckling is carried out using adaptive Lee filter. These are preprocessing operations required for SAR image to apply classification process (Section 1.5).

2. Four-band wavelet decomposition is applied on the preprocessed SAR image to get 16 bands at level 1.

3. Energy of each of 16 sub-bands is calculated. By applying energy thresholding, few of the sub-bands at level 1 are selected for further analysis.

4. Selected sub-bands are further decomposed to 16 sub-bands each at level 2.

5. Few of the sub-bands at level 2 are selected by applying energy thresholding on energy of the sub-bands.

6. Texture features of same size as sub-band image are computed for each of the sub-band images.

7. In case of smooth texture regions of each of texture features, backscattering coefficient is incorporated to obtain integrated features, having same dimension as texture feature.

SAR Image

Preprocessing

Four-band wavelet decomposition for two levels

Backscattering coefficient

Checking for energy threshold

Texture measure

Is texture smooth?

Yes

No

Local estimators for texture measure

Integrated feature measure

Texture measure

Adaptive neuro-fuzzy evaluation

K-means clustering

Classified SAR Image
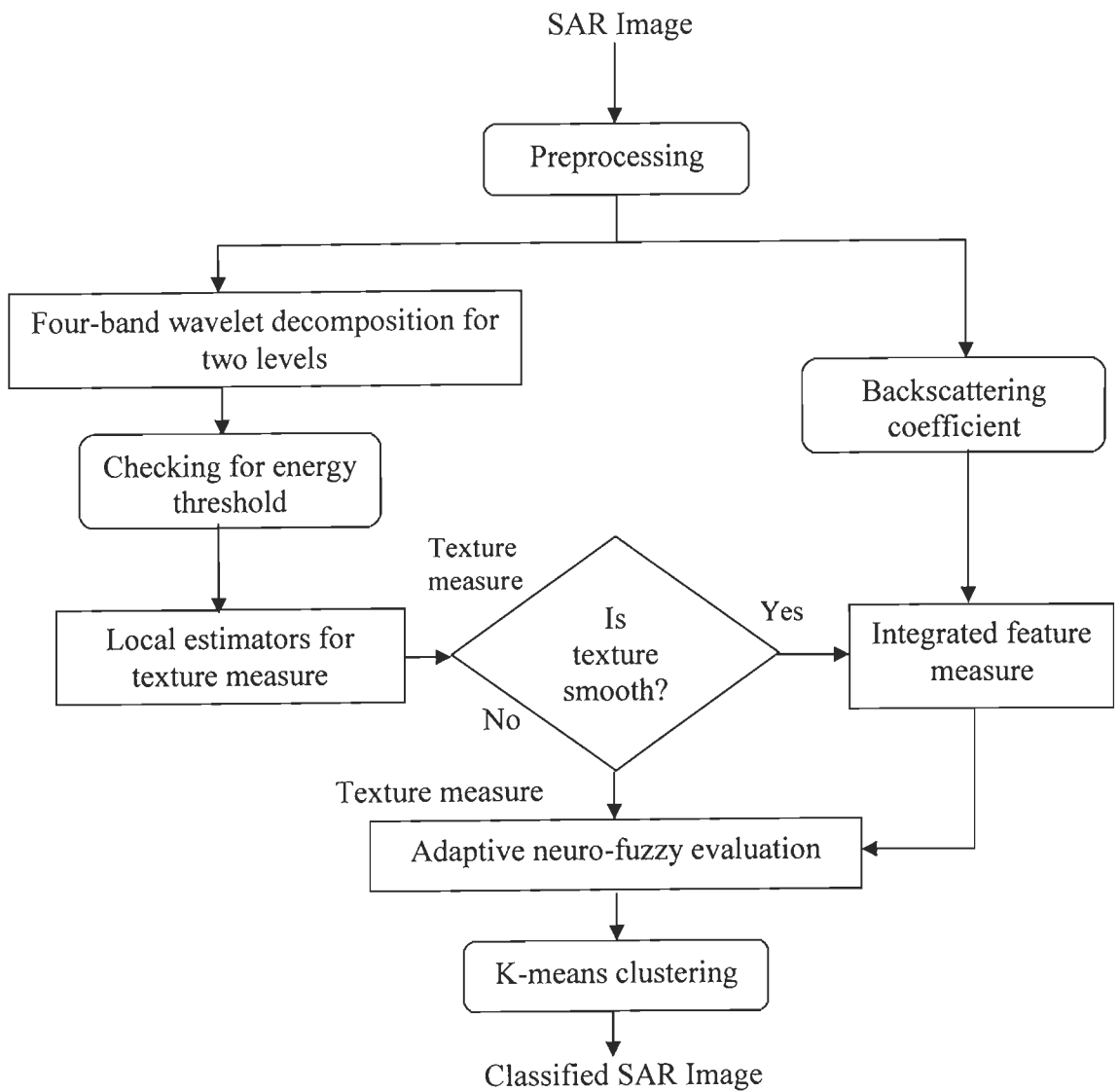
Figure 4.1. Classification of SAR image using integrated intensity and four-band wavelet features.

8. Adaptive neuro fuzzy algorithm is used to rank the integrated features on the basis of their relevancy for classification.

9. Top ranked integrated features are given for K-means classifier.

10. Clusters obtained by K-means classifier are labeled as water and urban areas with the help of ground truth reference to obtain classified image.

4.2.1 Data used

Solani river catchment around Roorkee town in the state of Uttarakhand, India is taken as the study region. Three ERS-2 SAR C-band images acquired on 23 July 2001, 28 July 2003 and 29 March 2004 are used for analysis in the present study. Section 1.3 and 1.4 give the details about the study region and satellite data used in this chapter. SAR image acquired on 23 July 2001 is used for developing the proposed classification algorithm to obtain user defined parameters. Then the proposed algorithm is validated for the images acquired on 28 July 2003 and 29 March 2004.

4.2.2 Four-band wavelet decomposition

The M-band wavelets are able to zoom onto narrow high frequency components of the signal (Zou and Tewfik, 1992). The wavelet packet decomposition process helps in tiling the images at different resolutions so that the texture patterns at all scales are integrated and compiled when reconstructing the classified image (Unser, 1995). Hence, classification algorithm for SAR images is proposed using four-band wavelet filters. These filters are chosen such that it has perfect reconstruction ability (Alkin and Caglar, 1995). When four-band wavelet decomposition is applied on SAR image, it is decomposed into 16 images. Here, SAR image which is decomposed is termed as 'parent band' and each of 16 images obtained as a result of decomposition is called as 'sub-band'. When applying wavelet decomposition, no down-sampling of images is performed so that size of sub-band images remain the same as their parent band and by this way, invariance to translation is achieved. Four-band wavelet decomposition of the image gives rise to 16 sub-band images of the same size as that of the original image. These 16 sub-bands are said to be sub-bands at level 1. If all these sub-bands at level 1 are considered for further decomposition, the 16 sub-bands at level 1 give rise to 16 sub-bands at level 2 each, leading to a total of 256 sub-bands at level 2.

4.2.3 Selection of sub-bands by energy thresholding

If all these sub-bands obtained by four-band wavelet decomposition are to be considered for further computation, this will lead to processing of large volume of data. Processing with lesser energy bands may also provide the same solution since the information is redundant when taking all sub-bands for analysis. Hence, choosing fewer sub-bands at each level is imperative to make the process computationally efficient. It is quite evident that the process of extracting the features from all these sub-bands will be an exhaustive search. SAR image is first decomposed into 16 sub-bands at level 1, and these sub-bands are decomposed further only if energy calculated for each of the sub-bands satisfies thresholding criteria.

Energy of each of the sub-bands is calculated using equation (4.1). Most significant sub-bands are to be identified on the basis of their energy, to decide whether further decomposition of the particular channel would generate more information or not. This search enables one to zoom into any desired frequency channel for further decomposition. SAR image is divided into 16 sub-bands at level 1. Among these sub-bands, those for which energy values exceed ε_1 % of the energy of parent band are considered and decomposed further. A sub-band is further decomposed if it's energy value is more than ε_2 % of the total energy of all sub-bands at the current scale.

For each decomposed sub-band image $S_b(m,n)$, energy is calculated as

$$e = \frac{1}{MN} \sum_{m=1}^{M} \sum_{n=1}^{N} |S_b(m,n)|, \qquad 1 \leq m \leq M, 1 \leq n \leq N, \qquad (4.1)$$

where $M \times N$ is the size of image, and (m, n) represent row and column of a pixel in the image.

A particular sub-band is chosen only if it contains more than 3% (ε_1) of its parent band energy and has more than 2% (ε_2) of the total energy of all the sub-bands at the current level. Empirically, these values are found to be suitable for SAR images to choose significant bands. Energy thresholding is applied to reduce the number of sub-bands chosen for further processing by choosing sub-bands with significant

information. ε_1 and ε_2 are chosen such that, more than one sub-band but not all sub-bands, are chosen for further decomposition.

4.2.4 Computation of texture features

Raw wavelet coefficients present in individual sub-bands are not sufficient for texture information. Since texture is to be characterized by some statistical property linked with it, a local estimator is used to compute texture features from these wavelet coefficients. Local estimator constitutes a nonlinear operator followed by a smoothing filter applied to each sub-band. Thus, local estimator computes texture feature and size (row/column) of the square window applied to compute this texture feature is termed as 'size of the local estimator'. Sub-bands obtained at level 1 and level 2 capture textures at different resolutions present in SAR image. To suitably capture the texture pattern obtained at different levels, size of local estimator has to be different at each of this level. Hence, two different local estimators are applied for sub-bands at level 1 and 2 and they are termed as 'local estimator 1' and 'local estimator 2' respectively. The texture feature, $feat_{tex}$ is given by

$$feat_{tex} = \frac{1}{R}\sum_{m=1}^{M}\sum_{n=1}^{N} abs\left(S_b\left(m,n\right)-\overline{S}(x,y)\right) \qquad (4.2)$$

where $R = w^2$, w is the row/column size of the square window around the central pixel (x,y), over which the texture feature is calculated, $S_b(m,n)$ is the sub-band image at pixel (m,n) within the mask, $\overline{S}(x,y)$ is the sub-band image averaged over a mask of $w \times w$ centered around (x,y), $abs\left(S_b\left(m,n\right)-\overline{S}(x,y)\right)$ is the magnitude of difference between sub-band image at location (m,n) and average sub-band image within the mask.

Thus, texture feature computes texture using local estimator for each of the sub-bands chosen at level 1 and level 2. These computed texture features are of the same size as sub-bands. When four-band wavelet decomposition is applied on SAR image, sub-bands are obtained without down-sampling. Therefore, sub-bands obtained are of the same size as SAR image. The local estimator is applied as a moving window to all over the image and replaces every centre pixel of the window by computed texture

feature using equation (4.2). This leads to computed texture features to have same size as sub-bands.

4.2.5 Integration of backscattering coefficient with texture features

The backscattering coefficient plays an important role in describing the object surface. For example, water can be detected by low backscattering coefficient whereas urban areas are characterized by high backscattering coefficient (Ulaby et al., 1986b). Integrating backscattering coefficient with texture features helps in distinguishing two areas with same smooth texture pattern and different backscattering coefficients. If the texture pattern is found to be perfectly smooth in any location (x,y) for a particular resolution, then $feat_{tex}(x,y)$ computed for that band is zero. When a texture feature is zero or negligible at any pixel location (x,y), the backscattering coefficient at that location is incorporated to get integrated feature, $feat_{int}$. The threshold for $feat_{tex}$ is set very low i.e., 0.001 by setting the working precision of 3 digits. To capture backscattering coefficient for smooth texture patterns, the following equation is used.

If $feat_{tex}(x,y) = 0$ or negligible/ less than threshold (0.001),

$$feat_{int}(x,y) = c * S_b(x,y) + offset$$

$$\text{else } feat_{int}(x,y) = feat_{tex}(x,y) \tag{4.3}$$

where $feat_{int}$ is the integrated feature measure having both backscattering coefficient and texture information contained in a corresponding sub-band. The c factor and $offset$ are introduced only to differentiate the backscattering coefficient from the texture features captured by the integrated feature measure. Thus, the integrated feature measure is obtained as output. This integrated feature measure comprises of texture feature and backscattering coefficient component in the place of smooth texture. For every texture feature, integrated feature is obtained in this manner. Gaussian filter is applied on integrated features to obtain smoothed integrated features with less sparse distributions.

This is followed by a smoothing stage using the Gaussian low pass filter $h_G(x, y)$ to get the feature of individual sub-band images.

$$feat_b(x, y) = \sum_{(a,b) \in G_{x,y}} \Gamma \left(feat_{int}(a,b) h_G(x-a, y-b) \right) \qquad (4.4)$$

The Gaussian window helps in smoothing the results. The size of the smoothing filter is based on the measure of spectral content of the image. Spectral Flatness Measure (SFM) gives overall image activity (Jayant and Noll, 1984). If the SFM is low, an image has low spectral content and this type of image requires a larger window size of smoothing filter. Empirically, a gamma value of 40 for Gaussian smoothing filter is found to be suitable for application to SAR images. Integrated features are ranked according to their relevancy for classification purposes so that fewer and optimum number of features is chosen for further analysis. Choosing only the features which are relevant for classification will increase the similarity between the same pair of patterns giving rise to higher classification accuracy.

4.2.6 Ranking of integrated features by adaptive neuro-fuzzy algorithm

The integrated features are ranked according to the information contained in them using the neuro-fuzzy feature evaluation index (Pal et al., 2000). The principle lies in comparing every feature with all other features for checking similarity. Then, weights/ranks are allotted such that chosen features have similarity in patterns within the classes.

Back propagation network used for ranking integrated features is shown in Figure 4.2. The neural network is designed with three layers, an input layer with 'n' nodes, a hidden layer with 'n' nodes and an output layer with 2 nodes, where 'n' is the dimension of features in the complete feature space to be ranked.

All the integrated features (equation 4.3, section 4.2.5) are presented to this network with 'n' nodes and each feature is compared with all other features for its closeness and similarity.

The weights are updated using the formula

$$\Delta w_j = -\eta \frac{\partial E}{\partial w_j}, \qquad (4.5)$$

where,

$$E = \frac{2}{s(s-1)} \sum_p \sum_c \frac{1}{2} \left[\mu_{pc}^T \left(1 - \mu_{pc}^o \right) + \mu_{pc}^o \left(1 - \mu_{pc}^T \right) \right] \quad (4.6)$$

where E is the training error, w_j is the weight connecting the jth hidden layer and node T in the output layer, η is the learning rate of the back propagation network, μ_{pc}^T and μ_{pc}^o are the membership functions of transformed and original feature space, and s is the number of samples in the feature space. The neural network is trained until the Δw_j is less than 0.001.

Error 'E' attains a minimum after convergence. Then the weights of the links connecting hidden nodes and the output node indicate the order of importance of features. The ranking of the integrated features is given by the value of the weighting coefficients connecting 'n' nodes in the hidden layer and μ_{pc}^r. Any 'r' number of integrated features can be chosen according to their rank of importance. Then, for the top ranked features, the K-means algorithm (Tou and Gonzalez, 1974) is employed to cluster the feature space to obtain a segmented image. This is the general procedure for the classification of SAR images based on integrating backscattering coefficient and multi-wavelet based texture features.
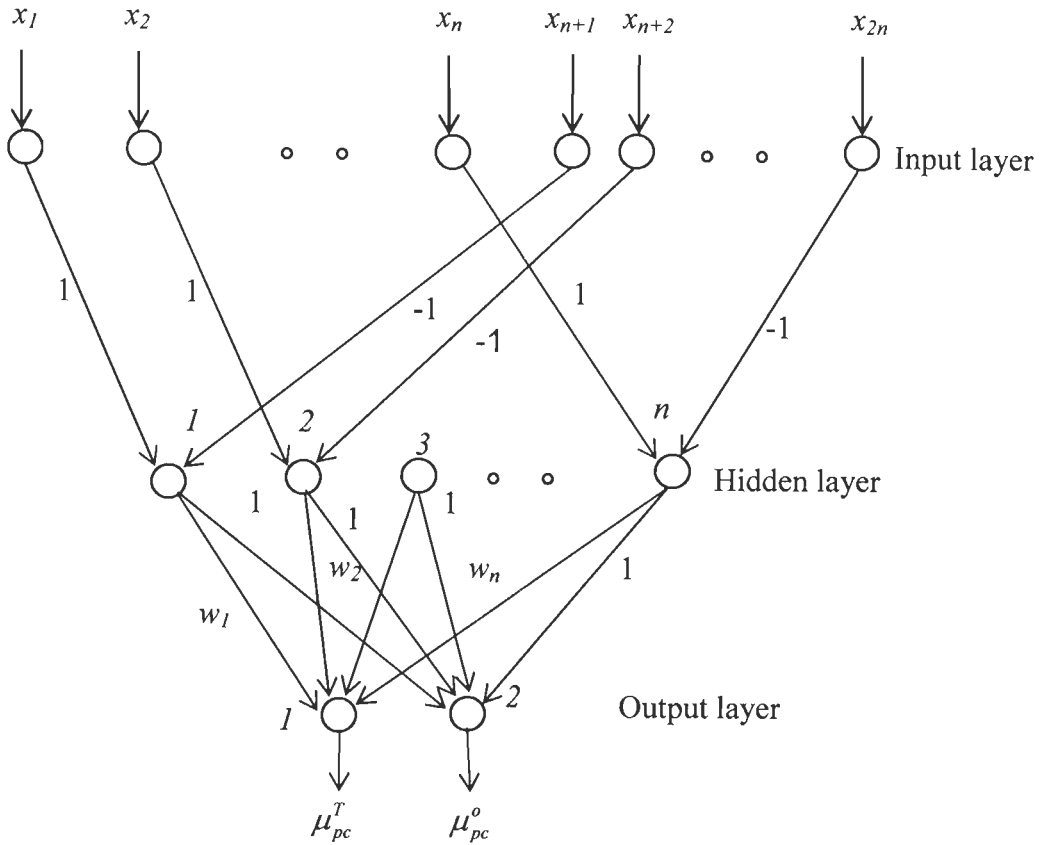
Figure 4.2. Back propagation network for ranking integrated features.

4.3 Proposed adaptive approach for user independent algorithm

4.3.1 User defined parameters

In this proposed classification algorithm for SAR image using wavelets, the parameters to be defined by the user are (i) size of the local estimator 1, (ii) size of the local estimator 2, and (iii) number of integrated features chosen for K-means algorithm. Whenever classification is to be done for the SAR images by this method, it requires that the user has to vary these parameters arbitrarily till satisfied results are obtained. Because of the large size of the image involved, application of the classification process is time consuming. If the user has to try with all the parameters in ad-hoc manner, time required for successful classification is very high. The user may or may not hit at the proper combination to get the maximum classification accuracy, which can be obtained by this process. Hence, an adaptive algorithm is proposed in this chapter to determine user defined parameters involved in the classification algorithm. Initially, the effect of varying individual user defined

parameters on classification accuracy is studied and then, an empirical relation is developed for classification accuracy in terms of these parameters. The developed relation should enable the user to specify classification accuracy and obtain optimal user defined parameters so that the parameters can be applied in one step to achieve SAR image classification.

4.3.2 Effect of number of integrated features on classification accuracy

As depicted in Figure 4.1, top ranked integrated features from adaptive neuro-fuzzy algorithm are given to K-means classifier for classification. The number of integrated features to be chosen represents parameter 3 as listed in section 4.3.1. To study the effect of integrated features on classification accuracy, the number of features is varied keeping other parameters, local estimator 1 and 2 fixed at 13 and 15 respectively. Here, the aim is just to check the dependency of number of integrated features on classification accuracy. Table 4.1 lists the classification accuracy for various numbers of integrated features. Figure 4.3 shows the variation of classification accuracy by varying the number of integrated features. Similar study has also been done for fixing local estimator 1 and 2 as 11 and 17, and similar types of variations have been observed.

Table 4.1. Effect of number of integrated features on classification accuracy with fixed local estimator 1 and local estimator 2 as 13 and 15 respectively.

Number of integrated features	Classification accuracy (%)
2	75.66
4	73.64
6	77.46
8	83.21
10	69.71
11	89.13
12	70.49
14	71.25
16	70.90
18	90.16
21	90.20
27	84.59

In Figure 4.3, it can be observed that classification accuracy varies as number of integrated features increases from 2 to 11. From the graph, it can be inferred that there is an optimal number of integrated features at which classification accuracy reaches a maximum value and then for other numbers of integrated features, accuracy is reduced. The relationship between classification accuracy and the number of integrated features is obtained by curve fitting method with $R^2 = 0.70665$ as

$$y = b_0^f + b_1^f x_1 + b_2^f x_1^2 + b_3^f x_1^3 \tag{4.7}$$

where 'x_1' is the number of integrated features and 'y' is the classification accuracy in percentage. The values of the coefficients b_0^f, b_1^f, b_2^f and b_4^f are obtained as 20.439688, 14.24912, −0.988513 and 0.0197516 respectively. This equation describes the dependency of classification accuracy on number of integrated features, when other two parameters are constant.
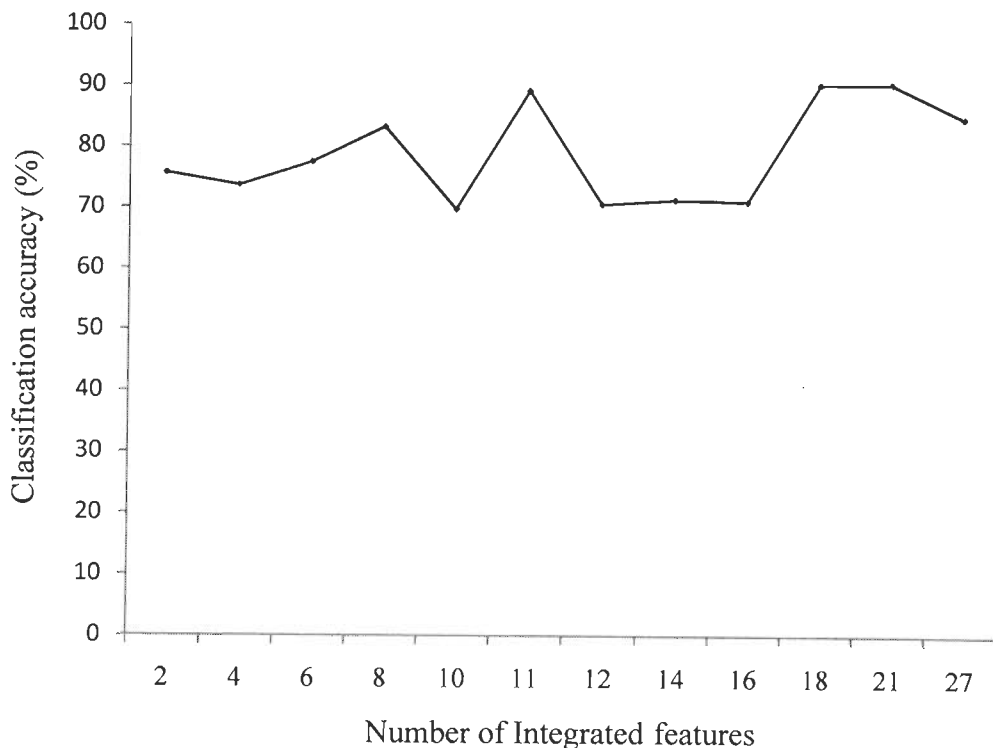
Figure 4.3. Effect of number of integrated features on classification accuracy.

68

The problem of obtaining optimum x_l can be stated as

Maximizing $$\min_{x_1}\left(b_0^f + b_1^f\, x_1 + b_2^f x_1^2 + b_3^f\, x_1^3\right)$$

subjected to $$2 \le x_1 \le 27$$

$$b_0^f + b_1^f x_1 + b_2^f x_1^2 + b_3^f x_1^3 \le 95 \tag{4.8}$$

This optimization problem is solved using *'fmincon'* routine in optimization toolbox of PC-MATLAB and number of integrated features is obtained as 11 for which estimated accuracy is 83.86%.

4.3.3 Variation of classification accuracy with local estimators

To study the effect of window size of local estimator 1 on the classification accuracy, keeping local estimator 2 fixed at 15 and number of integrated features as 11 (optimal value obtained from previous step in section 4.3.2), window size of local estimator 1 is varied from 3 to 17 in steps of 2 and classification algorithm is applied. Similar analysis has been carried out by keeping local estimator 2 fixed at 11 and number of integrated features as 11. Similar variations in classification accuracy are observed.

Table 4.2. Effect of window size of local estimator 1 on classification accuracy with fixed values of window size of local estimator 2 = 15, and number of features = 11.

Window size of local estimator 1	Classification accuracy (%)
3	69.23
5	85.96
7	83.61
9	83.25
11	83.01
13	82.13
15	81.74
17	81.53
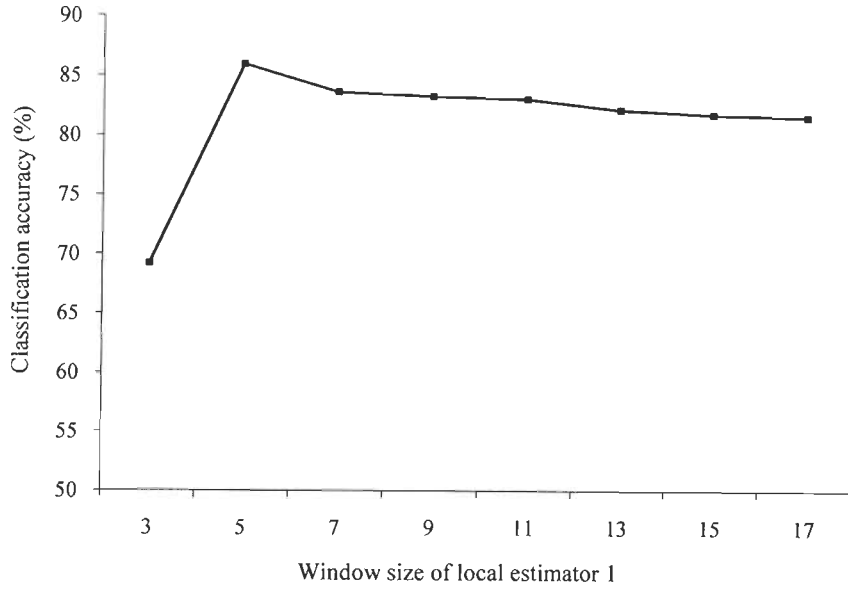
Figure 4.4. Variation of classification accuracy with local estimator 1.

The classification accuracy in terms of window size of local estimator 1 is obtained by the curve fitting method with $R^2 = 0.9736$.

$$y = b_0^{l1} + b_1^{l1} x_2 + b_2^{l1} x_2^2 + b_3^{l1} x_2^3 \qquad (4.9)$$

where x_2 is the window size of local estimator 1. The values of the coefficients b_0^{l1}, b_1^{l1}, b_2^{l1} and b_3^{l1} are obtained as 2.88535, 27.7645, −2.7966 and 0.08516 respectively.

Optimum value for window size of local estimator 1 is found to be 7 giving an accuracy of 89.41% theoretically by the similar optimization routine as problem formulation in equation (4.8) with constraints describing lower and upper bound on variable x_2. When window size of local estimator 1 is varied beyond 17, the classification accuracy is approximately constant.

Hence, variable 'x_2' can be bounded as

$$3 \leq x_2 \leq 21 \qquad (4.10)$$

From the previous two steps, the optimum value for integrated features is obtained as 11 and window size of local estimator 1 is 7 when the effect of them on classification accuracy is considered individually. In the third step, the optimum values of window

size of local estimator 1 and number of integrated features are considered as constant and the window size of local estimator 2 is varied from 3 to 19 in steps of 2 and classification algorithm is applied on the SAR image.

Table 4.3. Effect of window size of local estimator 2 on classification accuracy with fixed window size of local estimator 1 = 7, number of integrated features = 11.

Window size of local estimator 2	Classification accuracy (%)
3	81.75
5	76.60
7	79.62
9	82.55
11	84.15
13	84.00
15	83.61
17	89.13
19	83.48
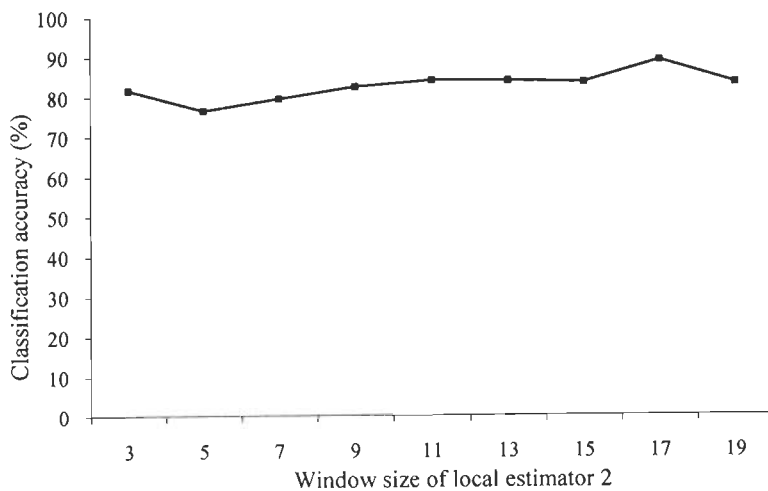
Figure 4.5. Variation of classification accuracy with local estimator 2.

Figure 4.5 shows how classification accuracy (Table 4.3) varies with window size of local estimator 2. Similar processing as in the previous two steps is done and the relation of local estimator 2 with classification accuracy is expressed as

$$y = b_0^{\prime 2} + b_1^{\prime 2} x_3 + b_2^{\prime 2} x_3^2 + b_3^{\prime 2} x_3^3 \qquad (4.11)$$

where 'x_3' is the window size of local estimator 2. The values of the coefficients $b_0^{\prime 2}$, $b_1^{\prime 2}$, $b_2^{\prime 2}$ and $b_3^{\prime 2}$ are obtained as 8.26188, 23.453162, -2.14704 and 0.059995 respectively. This expression is depicting the observed data with an R^2 of 0.87936 and corresponding results are shown in Table 4.3. The optimum value for local estimator 2 is found as 9 with classification accuracy of 89.17% applying similar process as before in computing optimized x_2 from equation (4.9). These optimum values are obtained considering the individual effects of user defined parameters on classification accuracy. The coefficient of determination, R^2 (>0.7) for the above relations suggests that all the three parameters viz., window size of local estimator 1, window size of local estimator 2 and number of features play important role in optimizing classification accuracy.

4.3.4 Classification accuracy in terms of user defined parameters

To develop the algorithm to compute classification accuracy in terms of all these three parameters, classification algorithm is applied with local estimator 1 varying from 3 to 17, local estimator 2 from 3 to 19 and number of features from 2 to 27 and the classification accuracy is computed. Figure 4.6 and 4.7 show the variation of classification accuracy for corresponding combinations and computed results are shown in Table 4.4. Figure 4.6 (a) to (i) show the variation of classification accuracy with window size of local estimator 1 for fixed values of local estimator 2.

From the figure 4.6 (a) to (i), it can be inferred that increase in window size of local estimator 1 beyond 17 does not make significant improvement in classification accuracy. It is obvious that maximum classification accuracy occur in the range of 7 to 15 for window size of local estimator 1. Figure 4.7 (a) to (h) shows classification accuracy vs. window size of local estimator 2 with fixed values of local estimator 1. For varying window size of local estimator 2 from 3 to 15, classification accuracy varies from 70% to 90%. Increasing window size of local estimator 2 beyond 17

makes the accuracy drops down to 70% or lesser values. It represents that classification accuracy is highly dependent on x_1, x_2, and x_3.

Table 4.4. Effect of variation of window size of local estimator 1 and local estimator 2 on classification accuracy.

Window size of local estimator 1	Classification accuracy (%)								
	Window size of local estimator 2								
	3	5	7	9	11	13	15	17	19
3	72.5	79.35	84.57	83.01	73.79	92.37	69.23	98.27	94.10
5	77.68	78.83	81.77	82.71	68.41	85.03	85.96	60.63	64.89
7	81.75	76.60	79.62	82.55	84.15	83.99	83.61	89.13	83.48
9	72.10	82.51	80.66	82.79	84.05	83.90	83.25	82.75	82.47
11	84.62	83.57	81.60	82.63	84.11	83.54	83.01	71.35	70.62
13	81.38	83.87	81.54	82.65	83.86	83.21	82.13	71.06	70.44
15	82.34	83.62	81.10	82.86	83.52	82.82	81.74	81.24	70.14
17	80.92	83.65	81.34	82.97	83.61	82.67	81.53	81.19	82.11
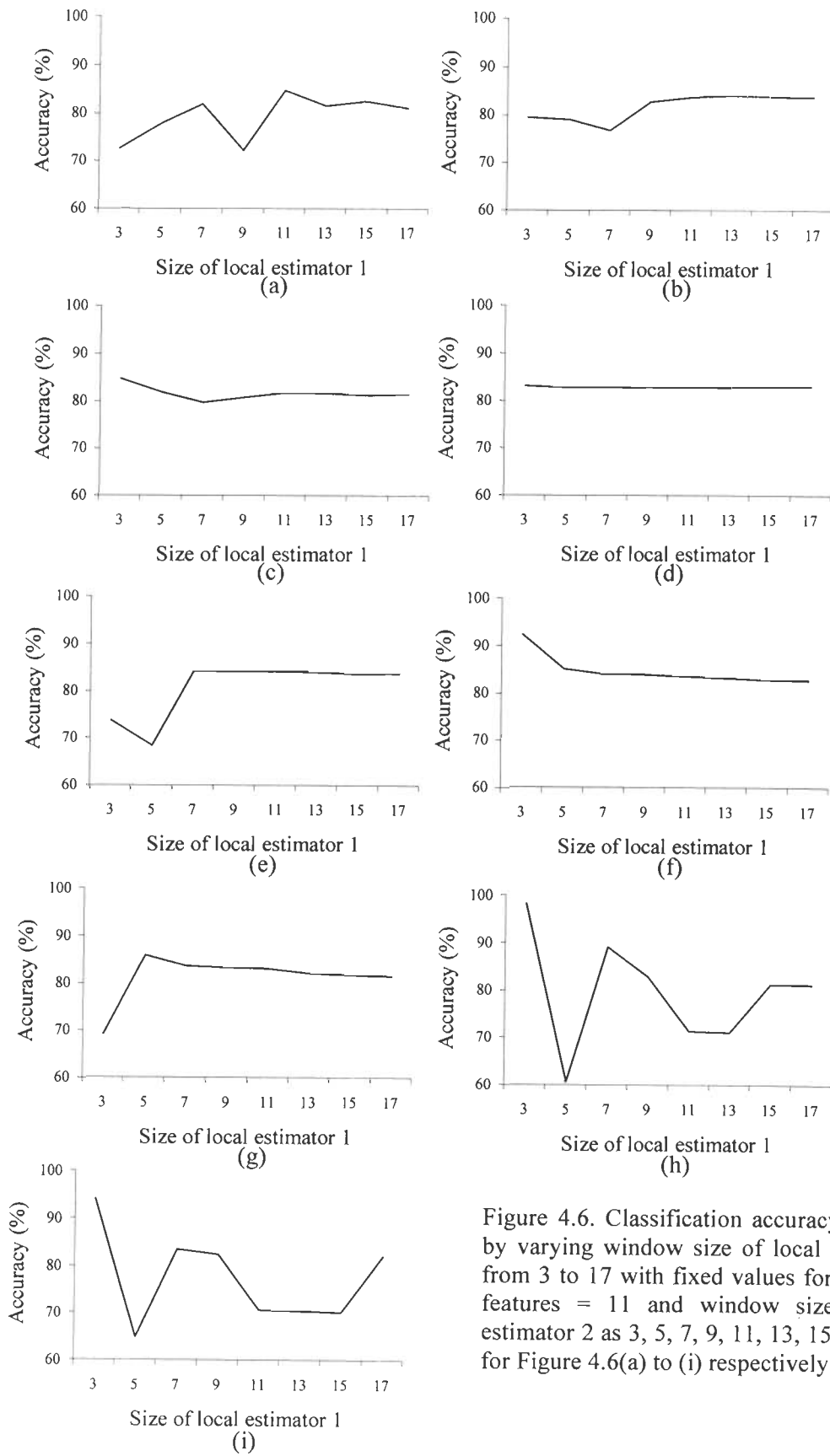
Figure 4.6. Classification accuracy is plotted by varying window size of local estimator 1 from 3 to 17 with fixed values for number of features = 11 and window sizes of local estimator 2 as 3, 5, 7, 9, 11, 13, 15, 17 and 19 for Figure 4.6(a) to (i) respectively.

74
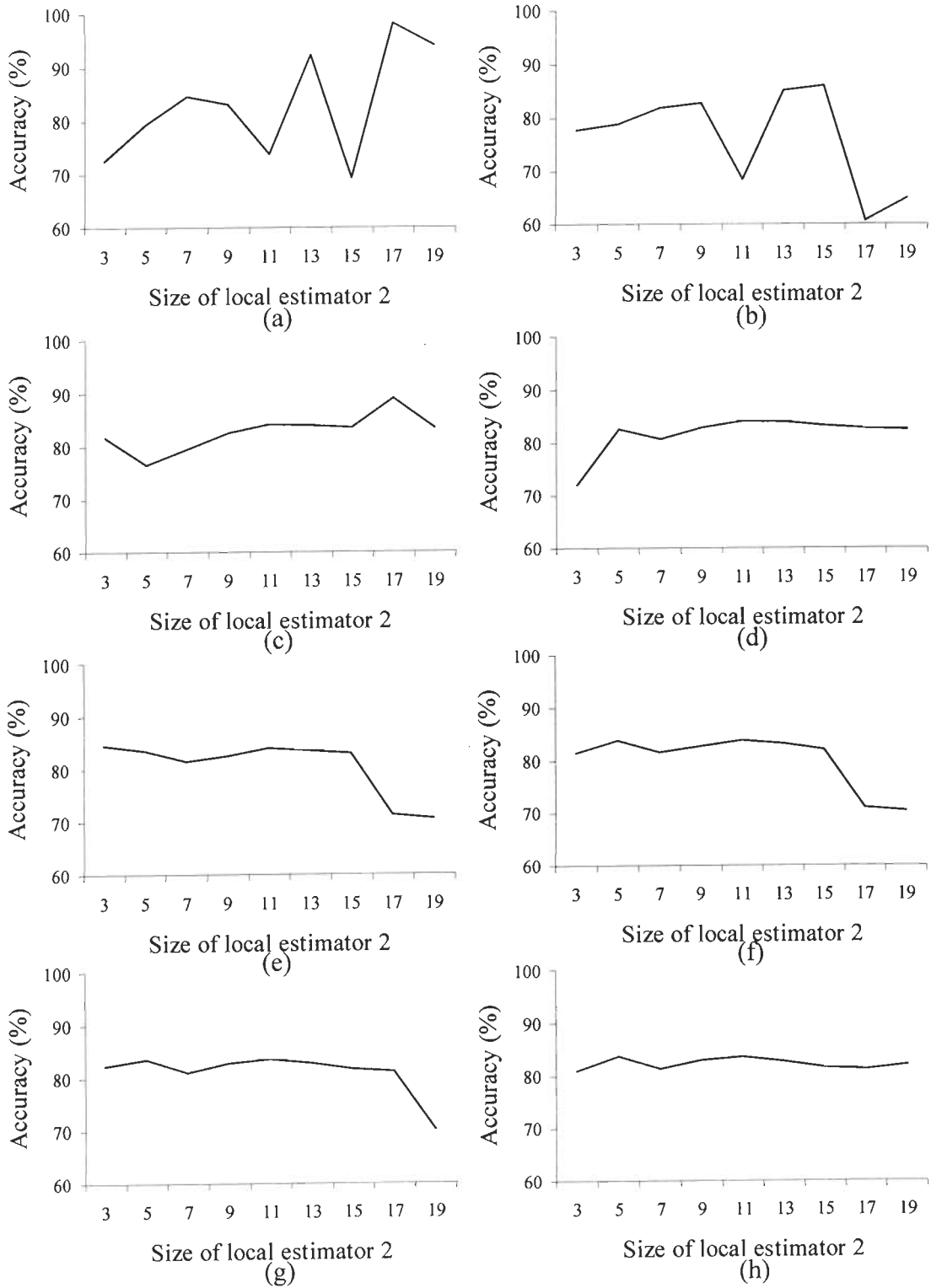
Figure 4.7. Classification accuracy is plotted by varying window size of local estimator 2 from 3 to 19 with fixed values for number of features = 11 and window sizes of local estimator 2 as 3,5,7,9,11,13,15 and 17 for Figure 4.7 (a) to (h) respectively

A multiple regression has been carried out to understand the relationship among y, x_1, x_2, and x_3.

$$y = b_0 + b_1 x_1 + b_2 x_2 + b_3 x_3 \qquad (4.12)$$

where x_1 is the number of features, x_2 is the window size of local estimator 1 and x_3 is the window size of local estimator 2. Multiple regression is applied on the observed data to get the above relation with R^2 of 0.7117. The values of the coefficients b_0, b_1, b_2 and b_3 are obtained as -1.9×10^{-14}, 7.0489812, 0.054974 and -0.101554 respectively. The relationship obtained for classification accuracy in terms of coefficients b_0, b_1, b_2 and b_3 are very much site dependent and may be used in future years. For the same site and similar land conditions for succeeding years, the same user defined parameter set can be used. Equation (4.12) is solved by maximizing y using function,

$$\min_{x_1, x_2, x_3} \left(b_0 + b_1 x_1 + b_2 x_2 + b_3 x_3 \right) \qquad (4.13)$$

subjected to

$$
\begin{aligned}
&2 \le x_1 \le 27 \\
&3 \le x_2 \le 21 \\
&3 \le x_3 \le 21 \\
&b_0 + b_1 x_1 + b_2 x_2 + b_3 x_3 \le 100
\end{aligned}
\qquad (4.14)
$$

Optimum values of the parameters are found to be window size of local estimator 1 is 7, window size of local estimator 2 is 11 and number of features is 14. Another combination that gives optimal result is [14, 7, 15]. For this optimization process, the lower and upper boundary values for all three parameters are set as [2, 3, 3] and [27, 21, 21] respectively, since increasing the parameters beyond the upper boundary does not improve the performance as were checked in earlier steps (section 4.3.3). The upper boundary constraint for classification accuracy is set as 100%. This is the final expression for classification accuracy in terms of user defined parameters (equation 4.13), number of integrated features, window size of local estimator 1 and window size of local estimator 2.

4.3.4 Optimum user defined parameters and their validation

Using the optimization routine, user can set the desired classification accuracy with specific lower and upper boundary values for parameters and initial guess value lying anywhere within the boundary range and one can get the user defined parameters directly using Equation (4.13). By applying those values directly in the classification algorithm, successful classification of SAR images can be implemented in one step without consuming a lot of time. For the optimum combinations of user defined parameters [number of features, window size of local estimator 1, window size of local estimator 2] as : set 1 [14,7,11] and set 2 [14,7,15], classification algorithm is applied for SAR image of July 23, 2001, with which optimal parameters are developed. To show the validation of algorithm over extended data, the same combinations of user defined parameters are applied on the SAR images of the same area obtained on July 28, 2003, and March 29, 2004 and results are computed and shown in Table 4.5. The overall accuracy is computed and tabulated considering only the water and urban pixels in both the ground truth data and classified image (Table 4.5).

Table 4.5. Classification results obtained with user defined parameters.

Sl. No	Date of SAR image	User defined parameters	Overall accuracy	Water		Urban	
				Producer's accuracy	User's accuracy	Producer's accuracy	User's accuracy
1	July 23, 2001	[14,7,11]	86.56	91.60	88.19	77.17	83.16
2	July 23, 2001	[14,7,15]	85.92	94.41	85.04	71.19	88.01
3	July 28, 2003	[14,7,11]	89.08	92.54	89.21	84.21	88.89
4	July 28, 2003	[14,7,15]	93.70	99.62	91.23	83.52	99.22
5	March 29,2004	[14,7,11]	80.80	99.84	88.14	82.45	98.74
6	March 29,2004	[14,7,15]	87.26	98.62	83.39	84.62	97.43

It can be seen from the table that the optimum combinations of parameters obtained from the above algorithm gives good results for images obtained on July 28, 2003 and March 29, 2004. Overall accuracy can be used as a good measure for analyzing classification accuracy. When the user defined parameters [14,7,15] obtained by

77

proposed classification methodology is applied for SAR image of July 28, 2003, confusion matrix of classified image is presented (Table 4.6). Overall accuracy is the ratio of correctly identified urban and water pixels to the total urban and water pixels present in the image and is computed as 93.70 %.

Table 4.6. Confusion matrix for user defined parameters [14,7,15] for SAR image acquired on July 28, 2003.

Overall classification accuracy = (380 + 780)/1238 = 1160/1238 = 93.70%

Class	Water	Urban	Total
Ground truth (pixels)			
Water	380	3	383
Urban	75	780	855
	455	783	1238
Ground truth (percentage)			
Water	83.52	0.38	30.94
Urban	16.48	99.62	69.06
	100.00	100.00	100.00

Table 4.7. Accuracy parameters for user defined parameters [14,7,15] for SAR image acquired on July 28, 2003.

Accuracy parameters	Water		Urban	
	Pixels	Percentage	Pixels	Percentage
Commission error	3/383	0.78	75/855	8.77
Omission error	75/455	16.48	3/783	0.38
Producer's accuracy	380/455	83.52	780/783	99.62
User's accuracy	380/383	99.22	780/855	91.23

Statistical analysis of accuracy assessment (Table 4.6) gives the confusion matrix, accuracy parameters i.e., commission and omission errors, producer's accuracy and user's accuracy for each land cover type in both percent and pixels (Table 4.7). For the confusion matrix, only the water and urban area pixels present in ground truth data and the classified images are considered. Confusion matrix is a square array set out in rows and columns which expresses the number of cells assigned to a particular land-cover type relative to the actual land cover type. The columns represent the reference data while rows indicate land cover type assigned by classification process.

The results are validated with the ground truth survey undertaken in and around Haridwar region, India for unsupervised land cover classification. Ground truth

survey of vegetation areas reported by Said (2006) is also taken as reference. As can be seen in Table 4.6, there are 455 water pixels and 783 urban pixels in reference data and 383 water pixels and 855 urban pixels in the classified data. All correct classifications (on pixel basis) are indicated on the major diagonal of the error matrix. For example, in this case, 380 pixels were correctly classified as water and 780 pixels as urban area. The off diagonal elements indicate misclassification which is a combination of commission and omission error. Overall accuracy is computed by dividing the total correctly identified pixels by the total number of pixels in the reference data for corresponding classes.

An error of commission is a measure of the ability to discriminate within a class and occurs when the classifier incorrectly commits pixels of the class being sought to other classes. In this example, the commission error for water stems from improperly calling other classes water, so that three pixels labeled as water are really a composite of other classes. An error of omission measures between class discrimination and results when one class on the ground is misidentified as other class by the observing classifier. Thus, this classification algorithm fails to recognize and correctly identify all 455 pixels of water as such, and labels 75 of these pixels as other classes. Commission and omission error computed in terms of pixels are also represented in percentage in Table 4.7.

Accuracies of individual category can also be computed in similar manner. The total number of correct pixels in a category is divided by the total number of pixels of that category as derived from the reference data (i.e. column total) is termed as "Producer's accuracy" because the producer of the classification is interested in how well a certain area is classified. On the other hand, if the total number of correct pixels in a category is divided by the total number of pixels that were classified in that category, this measure is called "User's accuracy". The producer of the map can claim that 83.52% of the time an area identified as water is identified as such. User of the map finds that 99.22% of the time an area that the map says water is actually water.Figure 4.8 (a) corresponds to the original SAR image, 4.8 (b) shows classified SAR image with color attributes changed to highlight water and urban areas identified. In the classified SAR image, blue corresponds to the water area and green corresponds to the urban area of the region.
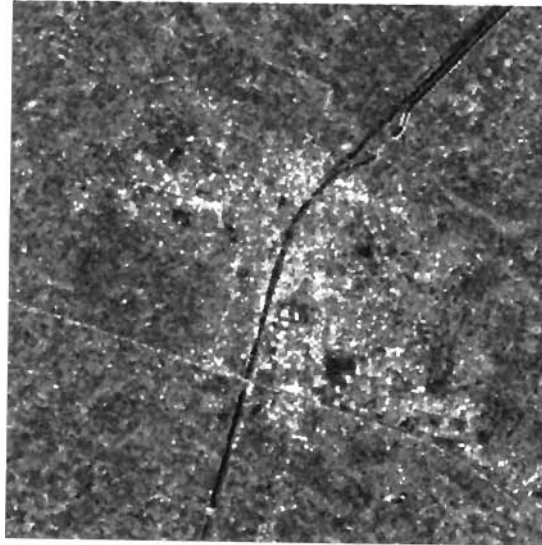
(a)
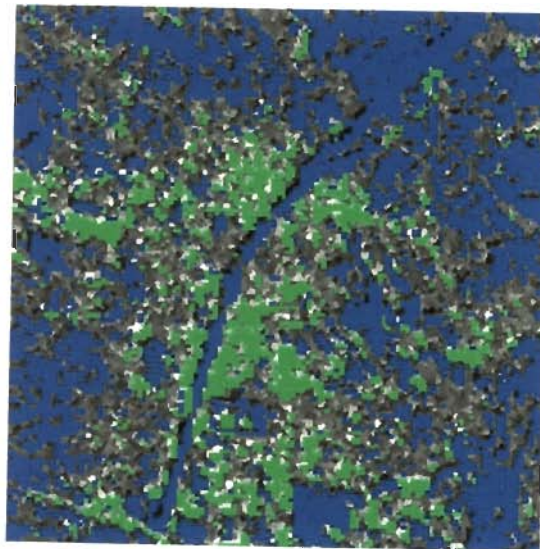
■ Water   ■ Urban

(b)

Figure 4.8. (a) SAR image and (b) classified SAR image with blue representing water area and green representing urban areas, overlapped on SAR image.

4.4 Conclusion

The goal of this chapter was to implement multi- resolution analysis of SAR image so that micro and macro textures present in SAR image along with backscattering coefficient can be effectively utilized for classification purposes and to obtain optimum user defined parameters involved in the classification algorithm. Usually, unsupervised classification processes involve ad-hoc approach for parameters involved in the implementation of algorithm. To get maximum achievable classification accuracy obtainable by the system, user has to rely on ad-hoc process of choosing parameters involved in the process which will be time-consuming. Hence, an adaptive algorithm was proposed in this chapter so that user defined parameters are obtained for maximum achievable accuracy that could be achieved, in a single application of algorithm with out any ad-hoc approach. By analyzing the effect of classification accuracy by varying each of the user defined parameters, an empirical relation is developed for classification accuracy in terms of these user- defined parameters. In the developed relation, user can specify the required classification accuracy ($\leq 100\%$) and obtain user defined parameters by optimization routine with constraints on the range of these parameters as applied in equation (4.14).

From the developed relation specific to the site considered, the number of features is identified as 14 and the corresponding sizes for local estimators 1 and 2 are 7 and 11 respectively for optimum classification as shown in this chapter. By experimental results and analysis, it is shown that, with an optimal parameter set, classification accuracy for identifying water and urban areas could be achieved up to 93.7%. These optimum parameters provide satisfactory results when applied for the SAR image of the same area taken at different time instants, viz. 28 July 2003 and 29 March 2004. Once the user defined parameters are identified specific for a site, then, classification of the SAR image can be achieved using the same parameters for the SAR image obtained in successive years. Thus proposed algorithm helps in achieving unsupervised classification of SAR image into major land covers like water and urban areas using multi-resolution analysis with the help of wavelets thus exploiting both backscattering coefficient and multi-wavelet based texture features.

Chapter 5

Critical Analysis of Texture Measures Based on Roughness Parameters for Labeling the Clusters in SAR Images

It is well known that unsupervised classification of a single polarized SAR image is accomplished mainly by two steps

(i) Clustering the SAR image into groups or clusters on the basis of backscattering coefficient and textures present in SAR image.

(ii) Labeling the various clusters (For example, land cover types such as water, urban, agriculture or any other areas).

In this context, labeling is termed as naming the various clusters or groups of pixels according to nature of the terrain as a certain land cover type it belongs to. Labeling of various clusters is a crucial and important aspect to identify various clusters in their original class (here, land cover class is assumed as class, whereas, in general, class may refer to any group of targets). Generally, researchers are carrying out labeling using topographic information of the same area or using backscattering coefficient obtained from the SAR image. Use of topographic sheet for labeling reflects the need for *apriori* information. It is very difficult to get a clear cut picture of various clusters using backscattering coefficient because the range of backscattering coefficients are generally intermingled for different clusters (Wang and Rao, 1993; Martinez and Toan, 2007). Therefore, it is needed to analyze or propose some approach by which dependency of labeling of various clusters on these factors (i.e., ground truth points, backscattering coefficient) may be minimized.

Backscattering coefficient is a quite important parameter in SAR image analysis for various applications, of which, labeling of clusters is one of them. SAR image is widely recognized for its potential in investigating soil and vegetation properties (Dobson et al., 1992; Bouzidi et al., 1998b; Madhavan et al., 1999; Anitha et al., 2006; Prakash and Singh, 2008). Land cover classification has been attempted by Dobson (Dobson et al., 1995) by estimating terrain attributes by analyzing the

sensitivity of backscatter coefficient to various parameters ranging from surface roughness, canopy architecture, soil moisture content, and aboveground biomass of vegetation with its moisture status. Many researchers have worked on retrieving physical parameters of the surface, namely, its soil moisture content and surface roughness by investigating radar backscattering response of surfaces (Singh et al., 1986; Mohan et al., 1990; Singh and Sharma, 1992; Singh 1995; Das et al., 2006; Pant et al., 2008). Although electromagnetic scattering from surfaces have been extensively studied for a long time, retrieval of surface parameters could be done for specific conditions like that of bare soil, or agriculture areas (Pampaloni and Paloscia, 1986, Ferrazzoli et al., 1997; Qiang et al., 2007). These retrieved parameters may help to label the clusters for various classes. But a lot of uncertainty exists because of existence of various land cover types on monitored earth surface. For example, a study area may not be purely of bare soil or agriculture but consists of various land cover types like water, urban structures, agriculture plots and many such areas.

Empirical models for backscattering coefficient for Horizontal-Horizontal (HH), Vertical-Vertical (VV) and Horizontal-Vertical (HV) polarizations in terms of surface roughness and relative dielectric constant of the soil surface have also been developed (Oh et al., 1992; Dubois et al., 1995; Oh, 2004). The results of these research works are applicable only for bare soil surfaces and may not hold good for urban regions with built-up areas and streets. Many works have been published on discriminating among various species and retrieving biomass from radar vegetation studies (Pierce et al., 1994, Paloscia et al., 1999, Ferrazzoli et al., 1997, Lucas et al., 2007). Most of these use multifrequency and multipolarization SAR images for crop classification. Since the focus is to use single C-band SAR image for classification purposes, these methodologies have limitations that they require images obtained at different polarization and operating frequencies. Multi-temporal C-band SAR data (C-HH, C-VV) collected by ERS-2 and ENVISAT were analyzed for their ability in mapping forested wetland and separating wetland from upland (Lang et al., 2008). All these works emphasize the ability of SAR images to discriminate agriculture areas from other land cover types.

For studying the separability of urban regions in SAR image, radar response from various urban features is to be studied. It has been shown that some typical urban features like pavement, grass, and buildings can be separated on the basis of their

average vertical dimensions (Xia and Henderson, 1997). In this work, they have listed the predicted appearance (on the basis of roughness) on radar imagery for various urban features. For small scale features whose vertical heights are measured in centimeters such as water, paved roads and grass areas, the predicted value of vertical height is in reasonable agreement with the observed values (Jensen et al., 1983). However, the extrapolation to residential and commercial environments with heights measured in meters is not straight forward. It is unknown at what height a particular surface object will act as corner reflectors to radar signals and to what degree building walls at certain orientations will cause multiple reflections (Fujito and Miho, 2006; Ainsworth et al., 2008). But still, the analysis of urban features on the basis of roughness parameters help in clustering them into wide groups like bare soil, bushes or buildings. Even though there are many reported works for retrieval of soil moisture content from backscattering coefficient, this may not be helpful for labeling the various land covers of water, urban and vegetation areas since the range of backscattering coefficients for these types of land covers are overlapping (Ferrazzoli et al., 1997; Bindlish and Barros, 2001).

Therefore there is a need to include some more measures from SAR image to label the clusters. Roughness is one of the important parameter to describe the nature of the terrain or surface and it is defined as vertical deviations of a surface from a reference level and it may be helpful to label the various clusters into land cover types. Therefore, labeling the clusters can be attempted using the surface roughness parameters. The contribution of the roughness element depends on the surface characteristics. Each pixel of a SAR image represents an estimate of the radar backscatter for that area on the ground. Darker areas in the image represent low backscatter whereas brighter areas represent high backscatter. The SAR backscattered intensity generally increase with the roughness (Ulaby et al., 1986). Roughness is a relative quantity that represents deviation in surface height related to a reference surface. For SAR images, the reference length scale for surface roughness is the wavelength of the microwave. If the surface fluctuation is less than the microwave wavelength, then the surface is considered smooth. For example, in the case of ERS-1 SAR image with a wavelength of 5.6 cm, if the surface has a fluctuation of the order of 2 cm, the surface is smooth and it appears dark. If the surface fluctuation is much more than 5.6 cm, say 20 cm, then surface appear bright. Flat surface such as calm

water, paved roads, runways normally appear as dark in SAR image since most of the incident radar pulses are reflected away. However, rough water surfaces may appear bright especially when the incidence angle is small (Makynen et al., 2002). In the case of urban areas where city streets or buildings are lined up in such a way that the incoming radar pulses are able to bounce off the streets and bounce again off the buildings (called a double bounce), then directly back towards the radar, they appear very bright in SAR images. Agriculture areas have intermediate backscattering coefficient. The surface fluctuation of agriculture areas is also intermediate to flat surfaces and urban areas. Hence, use of backscattering coefficient along with surface roughness may help in labeling various clusters.

This study reflects that surface roughness parameter may be a suitable parameter to help in labeling of clusters. Therefore, the focus in this chapter is to induct surface roughness with backscattering coefficient to label various clusters (i.e. major land cover types). For this purpose, a detailed analysis of surface roughness with various texture measures (mean, variance, semivariogram, lacunarity, weighted rank fill ratio and wavelet components) has been carried out. This detailed analysis may help to identify some texture measures for describing roughness. This analysis is not directly possible with real SAR images because it needs a lot of input parameters like actual values of roughness parameters from the land cover. Therefore, many synthetic images are generated for varying roughness. We have proposed an empirical relation to estimate roughness parameters. Although moisture is playing an important role in SAR image analysis, it may not give a major impact while calculating texture measures. Variation of moisture content results in variation in the level of backscattering coefficient but not the signature or nature of variation (Ulaby et al., 1986). When texture is measured over a small window size (as mentioned in section 3.4.1), moisture content can be assumed to be approximately constant over the window since texture measures calculate deviation from the mean or average backscatter coefficient and hence moisture content is assumed to have less impact on measuring texture measures (Rahman et al., 2008).

This chapter is organized as following: Section 5.1 describes the methodology of generating synthetic images with varying surface roughness parameters. Effect of varying surface roughness on texture measures is analyzed critically in section 5.2. Section 5.3 shows methodology to obtain surface roughness from the suitable texture

measures. Section 5.4 explains the computation of surface roughness for real SAR data and labeling of clusters using roughness and backscattering coefficient. Section 5.5 concludes the chapter 5 stating the applicability and advantages of the proposed approach for labeling clusters in SAR image.

5.1 Generation of synthetic images with varying roughness measures

The main aspect of characterizing the roughness of a surface is the choice of suitable parameters to represent roughness. For SAR images, vertical size of the scatterers and the distribution of these scatterers in the horizontal plane are important for studying the surface roughness. There are two statistical parameters known as the standard deviation of surface height variation, termed as root mean square (RMS) height and abbreviated as 's' and the correlation length, denoted by 'l'. RMS height, standard deviation of surface height, represented by 's' is a measure of vertical roughness whereas correlation length, representing correlation on horizontal plane , denoted by 'l', is a measure of horizontal roughness. 's' and 'l' are taken in units of cm.

To obtain the effect of 's' and 'l' on image texture that may be helpful for labeling different clusters, a detailed analysis is required. It is very difficult to carry out this detailed analysis in the SAR images. Therefore, there is a need to generate various synthetic images for different 's' and 'l' and critically analyze the texture measure variations on these roughness parameters.

5.1.1 Surface roughness parameters

The RMS height of a surface indicates the degree of variation of the height measurement of a surface above an arbitrary plane. The greater the spread of height measurements, the greater is the value of RMS height.
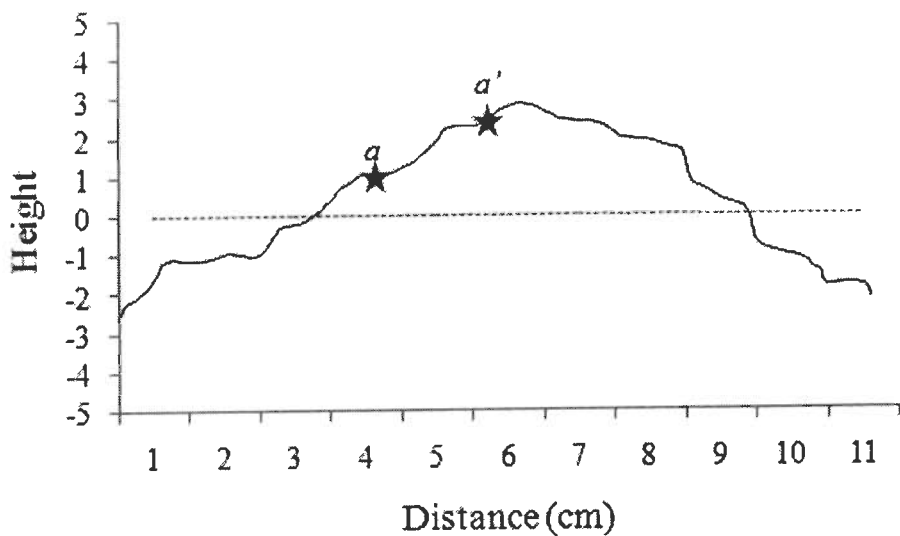
Figure 5.1. Surface profile.
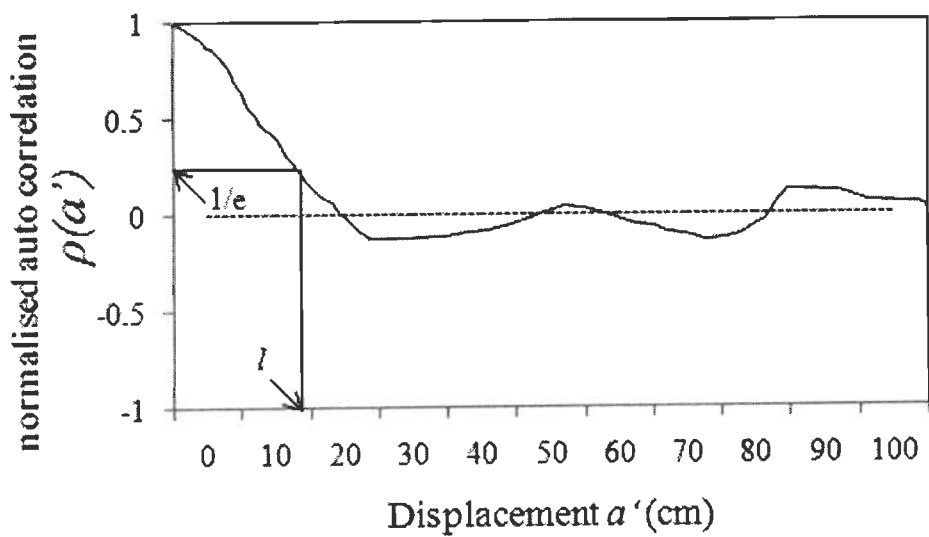
Figure 5.2. Autocorrelation function.

For the series $Z_i = 1, 2, ...N$, the RMS height for the discrete one dimensional case is given by

$$s = \left[\frac{1}{(N-1)} \left(\sum_{i=1}^{N} \left(Z_i^2 \right) - N \left(\overline{Z} \right)^2 \right) \right]^{\frac{1}{2}}$$ (5.1)

where,

$$\overline{z} = \frac{1}{N} \sum_{i=1}^{N} Z_i$$ (5.2)

and N is the number of samples.

The relationship between the height above an arbitrary plane of one point located at point 'a' and the height of another point 'a''' distant from 'a' (Figure 5.1) can be statistically expresses in the form of an autocorrelation coefficient. The variation in the value of the autocorrelation coefficient as the distance between the two points increases is referred to as the autocorrelation function. The correlation length ('l') is the displacement from the original point 'a' when there exists no statistical relationship between the two points. The normalized autocorrelation function, $\rho(a')$ in the discrete case (Figure 5.2) is given by

$$\rho(a') = \frac{\sum_{i=1}^{N+1-j} Z_i Z_{j+i-1}}{\sum_{i=1}^{N} Z_i^2}$$ (5.3)

for a spatial displacement $a' = (j-1)\Delta x$, where j is an integer ≥ 1. The spacing interval Δx between measurements is such that

$$\Delta x < 0.1\lambda$$ (5.4)

where 'λ' is the wavelength of the radar (= 5.6cm for ERS-1 SAR image).

The surface correlation length 'l' is defined as the displacement a' for which $\rho(a')$ in the discrete case is equal to $(1/e)$ (Figure 5.2).

$$\rho(a') = \frac{1}{e}$$ (5.5)

where, $e = 2.7183$.

5.1.2 Synthetic images with varying roughness measures

RMS height, (i.e., standard deviation of surface height), represented as 's' is a measure of vertical roughness and correlation length, 'l', representing the correlation on the horizontal plane is a measure of horizontal roughness are the parameters chosen to describe the roughness of the surface. To study and analyze the effect of variation of surface roughness on texture measures, synthetic images with different combinations of 's' and 'l' are generated.

The classical surface roughness parameters, i.e., RMS height (s) and correlation length (l) are taken as input. The surface profile generation algorithm by Fung and Chen (1985) is modified for 2D surface profile.

The surface profile height Z is described by

$$Z(k) = \sum_{j=-M}^{M} W(j)X(j+k) \qquad (5.6)$$

where $Z(k)$ is the surface height distribution, $X(i)$ is a Gaussian random deviate with zero mean and unit variance, and $W(j)$ is the weight function. The surface is characterized by Gaussian correlation function for which the weight function is defined as

$$W(j) = s\left(\frac{2\Delta x}{l\sqrt{\pi}}\right)^{1/2} \exp\left[-2\left(\frac{j\Delta x}{l}\right)^2\right] \qquad (5.7)$$

Δx is the sampling distance, and it is considered as unity since discrete profiles and consequently discrete image is considered.

The following steps are executed to generate 2D images with varying surface roughness parameters 's' and 'l':

- Consider 2D surface image of size (m, n) is to be generated for a specific value of 's' and 'l'.

- For the specified 's' and 'l', surface profile height Z is generated for $k=1,..n$ using equations (5.6) and (5.7).

- In the equation 5.6, $X(i)$ is a Gaussian random deviate with zero mean and unit variance. Random numbers are generated such that they follow the Gaussian distribution with zero mean and unit standard deviation (/variance).

- Using the same value of 's' and 'l', 'm' 1D profiles using steps 2, 3 are generated.

- Since the random numbers generated are not unique, the procedure gives rise to different 1D surface profiles.

- Each 1D profile is arranged in a row and 'm' such rows are formed using 'm' 1D profiles generated from step 4.

- Surface heights are obtained as pixel vertical roughness i.e., $Z(i,j)$.

- As 's' and 'l' are used for generating 1D surface profiles and such 1D profiles are extended to form 2D surface images, the average values of 's' and 'l' are the same for generated 2D synthetic images.

By using the above steps, various synthetic images have been generated by varying RMS height,'s' from 0.1 to 5.0 in steps of 0.1 and correlation length 'l' from 0.5 to 15 in steps of 0.5. This gives rise to 50 values of 's' and 30 values of 'l'. For each value of 's', 30 values of 'l' are used to generate 30 synthetic images. Hence for 50 different values of 's', (30×50) i.e., 1500 synthetic images are generated from all combinations of 's' and 'l'. These generated synthetic images are used for further analysis.
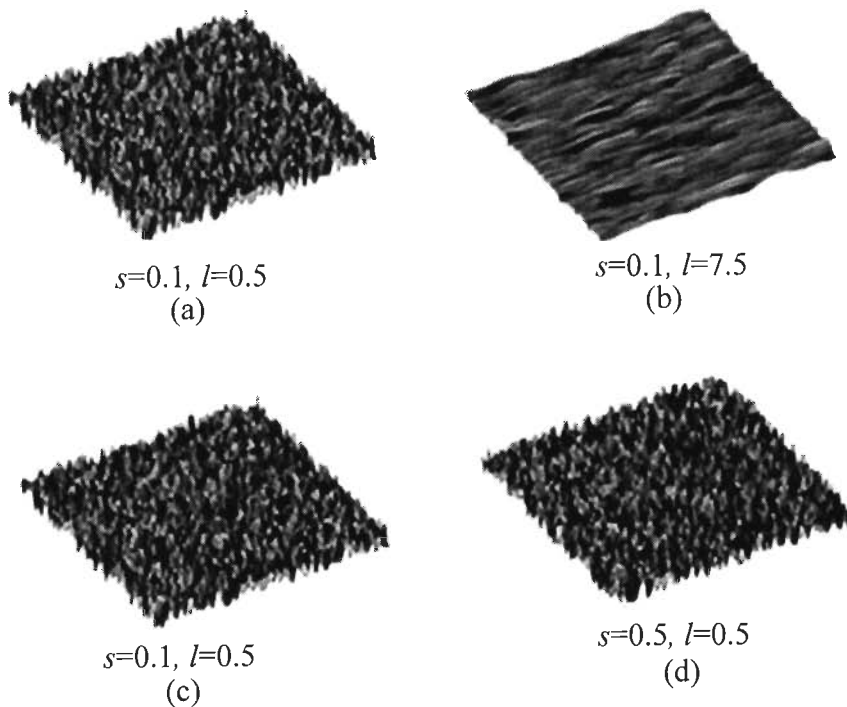
Figure 5.3. Synthetic images with varying 's' and 'l'. For example, (a) and (b) corresponds to synthetic images with constant $s = 0.1$, and varying 'l' of 0.5 and 7.5 respectively, (c) and (d) synthetic images with constant 'l' of 0.5 and varying 's' of 0.1 and 0.5 respectively.

For example, in Figure 5.3 (a) to (d), first two images (a) and (b) represents synthetic images of varying 'l' values of 0.5 and 7.5 with fixed value of 's'= 0.1. Then, the next two images (c) and (d) corresponds to synthetic images of fixed value of 'l'= 0.5 and varying 's'= 0.1 and 0.5 respectively. Figure 5.3 (a) and (b) depicts how the surface is represented when correlation length is increased from a lower value of 0.5 to 7.5. As the correlation length increases, surface becomes smooth. Similarly, as the RMS height increases, surface becomes rough (Figure 5.3 c,d). Thus, synthetic images to represent surfaces with varying roughness parameters, 's' and 'l' are generated for further study.

5.2 Analysis of texture measures for surfaces with varying roughness parameters

Texture measures namely mean, variance, semivariogram, lacunarity, weighted rank fill ratio and wavelet components are computed for various generated synthetic images (approximately 1500 images) for different 's' and 'l'.

As it is well known that window size is also playing an important role for doing texture analysis, all the six texture measures are computed by varying window size from 3 to 19 in steps of 2 to understand about the effect of window size on particular texture measure and surface roughness. For example, samples of various texture measures for different 's', 'l', and window size, 'w'. Here only few cases are shown in Table 5.1. But in actual, texture measures were computed for all 1500 synthetic images. Sample values are chosen such that effect of each parameter, i.e., RMS height, correlation length and window size on texture measures can be studied. For fixed value of 'l'= 0.5 and two different fixed values of 's'= 0.1 and 0.5, window size is varied from 3 to 19 in steps of 2, texture measures are computed. Then, for a higher value of 'l'=7.5 as fixed, and 's'= 0.5, window size is varied from 3 to 19 insteps of 2. From this, effect of window size on various values of 's' and 'l' can be studied. Next, by keeping window size fixed at 5 (i.e., 5×5 window) and 's' fixed at three different values of 0.1, 0.5, and 1.5, correlation length is varied from 0.5 to 2.5 in steps of 0.5 so that effect of correlation length on texture measures can be observed. From the same set of readings, window size is fixed at 5, three fixed values of 'l' as 0.5, 1.5 and 2.5, effect of varying RMS height 's' as 0.1, 0.5 and 1.5 can be noted.

Table 5.1. Texture measures for sample combinations of '*s*' and '*l*'.

RMS height 's'	Correlation length 'l'	Window size 'w'	Mean	variance	Semivariogram	lacunarity	Weighted rank fill ratio	Approximation coefficient of wavelet components
0.1	0.5	3	0.027	0.0019	0.0252	4.5737	0.0748	0.1506
0.1	0.5	5	0.075	0.0019	0.0253	4.0667	0.0746	0.1502
0.1	0.5	7	0.147	0.0018	0.0248	3.9847	0.0746	0.1504
0.1	0.5	9	0.243	0.0018	0.0250	3.9540	0.0748	0.1501
0.1	0.5	11	0.364	0.0017	0.0252	3.9386	0.0748	0.1510
0.1	0.5	13	0.508	0.0016	0.0253	3.9294	0.0749	0.1502
0.1	0.5	15	0.676	0.0016	0.0250	3.9235	0.0748	0.1502
0.1	0.5	17	0.869	0.0015	0.0243	3.9203	0.0748	0.1506
0.1	0.5	19	1.087	0.0015	0.0257	3.9182	0.0748	0.1507
0.5	0.5	3	0.135	0.0469	0.1232	4.6945	0.3746	0.7539
0.5	0.5	5	0.375	0.0457	0.1229	4.1425	0.3741	0.7540
0.5	0.5	7	0.735	0.0446	0.1240	4.0446	0.3742	0.7532
0.5	0.5	9	1.216	0.0435	0.1246	4.0082	0.3748	0.7538
0.5	0.5	11	1.818	0.042	0.1240	3.9898	0.3747	0.7542
0.5	0.5	13	2.541	0.0405	0.1263	3.9797	0.3743	0.7486
0.5	0.5	15	3.386	0.0393	0.1227	3.9728	0.3743	0.7493
0.5	0.5	17	4.352	0.0378	0.1226	3.9678	0.3741	0.7562
0.5	0.5	19	5.437	0.0364	0.1219	3.9637	0.3738	0.7532
0.1	7.5	3	0.056	0.0007	0.0032	106.7986	0.1555	0.3112
0.1	7.5	5	0.156	0.0007	0.0077	49.9896	0.1554	0.3117
0.1	7.5	7	0.306	0.0007	0.0112	39.8251	0.1552	0.3114
0.1	7.5	9	0.506	0.0007	0.0136	35.7196	0.1552	0.3114
0.1	7.5	11	0.756	0.0007	0.0149	33.7185	0.1552	0.3112
0.1	7.5	13	1.055	0.0007	0.0153	32.5612	0.1551	0.3117
0.1	7.5	15	1.405	0.0007	0.0153	31.816	0.1551	0.3115
0.1	7.5	17	1.805	0.0007	0.0153	31.3219	0.1551	0.3116
0.1	7.5	19	2.255	0.0007	0.0154	30.9341	0.1551	0.3117
0.1	0.5	5	0.075	0.0019	0.0253	4.0667	0.0746	0.1506
0.1	1	5	0.068	0.0009	0.0182	5.9400	0.0681	0.1356

RMS height 's'	Correlation length 'l'	Window size 'w'	Mean	variance	Semivariogram	lacunarity	Weighted rank fill ratio	Approximation coefficient of wavelet components
0.1	1.5	5	0.081	0.0007	0.0162	10.256	0.0812	0.1626
0.1	2	5	0.093	0.0007	0.0150	14.5228	0.093	0.1859
0.1	2.5	5	0.107	0.0007	0.0161	20.1254	0.1071	0.2134
0.5	0.5	5	0.375	0.0457	0.1229	4.1425	0.3741	0.7539
0.5	1	5	0.341	0.0227	0.0903	6.1951	0.3412	0.6806
0.5	1.5	5	0.411	0.0181	0.0820	10.7176	0.4115	0.8213
0.5	2	5	0.475	0.0167	0.0744	15.8317	0.4779	0.9496
0.5	2.5	5	0.531	0.0163	0.0691	20.0358	0.5319	1.0622
1.5	0.5	5	1.126	0.4027	0.3642	4.2528	1.1279	2.2515
1.5	1	5	1.013	0.2095	0.2722	6.0038	1.0133	2.026
1.5	1.5	5	1.215	0.1719	0.2411	10.1246	1.2149	2.4297
1.5	2	5	1.402	0.163	0.2295	14.8863	1.4022	2.7981
1.5	2.5	5	1.598	0.1511	0.2090	19.4649	1.5941	3.1903
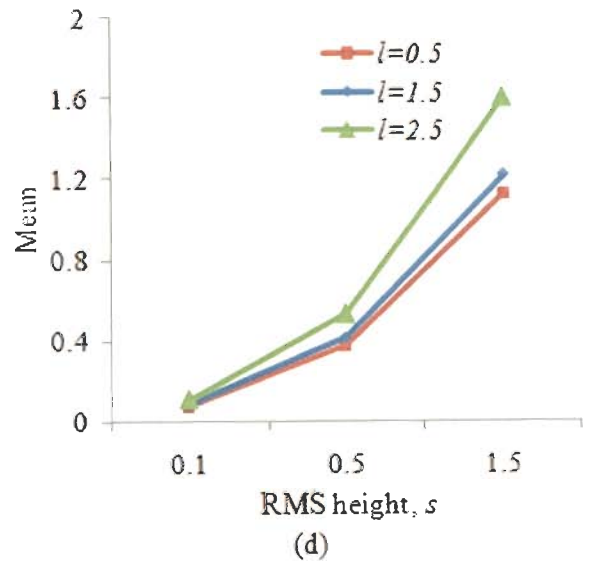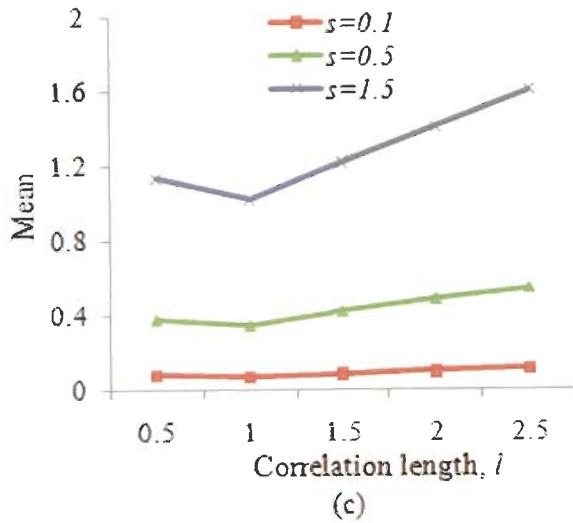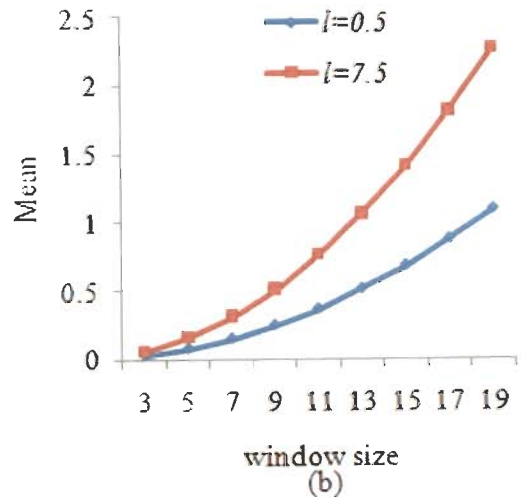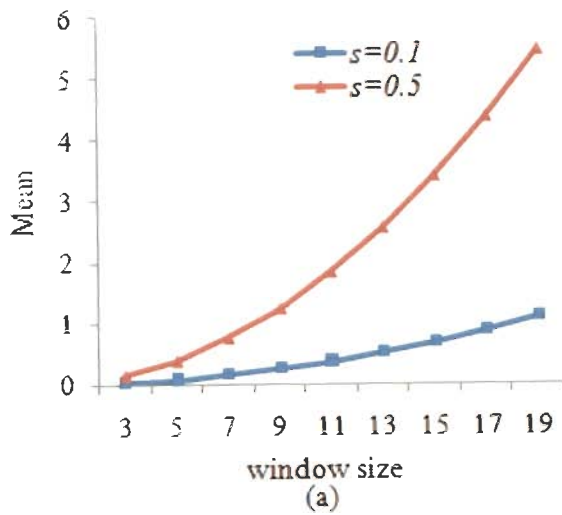
Figure 5.4. (a) variation of 'mean' with respect to window size for fixed l = 0.5 and s = 0.1,0.5, (b) variation of 'mean' with respect to window size for fixed s = 0.1 and l = 0.5,7.5, (c) variation of 'mean' with respect to correlation length is plotted for window size = 5 and s = 0.1,0.5,1.5, and (d) variation of 'mean' with respect to RMS height, s is plotted for window size = 5 and l = 0.5,1.5, 2.5.
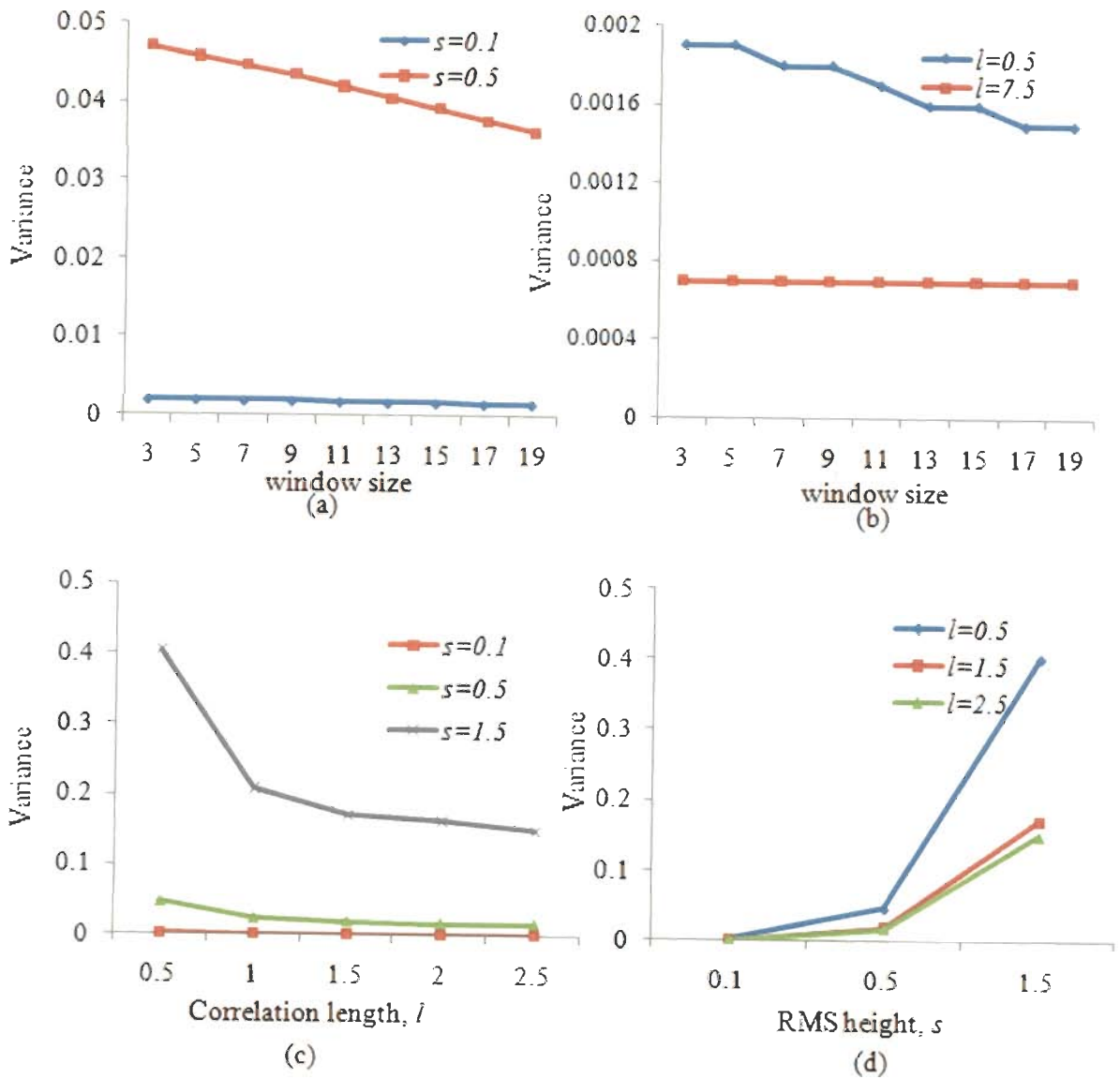
Figure 5.5. (a) variation of 'variance' with respect to window size for fixed l = 0.5 and s = 0.1,0.5, (b) variation of 'variance' with respect to window size for fixed s = 0.1 and l = 0.5,7.5, (c) variation of 'variance' with respect to correlation length is plotted for window size = 5 and s = 0.1,0.5,1.5, and (d) variation of 'variance' with respect to RMS height, s is plotted for window size = 5 and l = 0.5,1.5, 2.5.
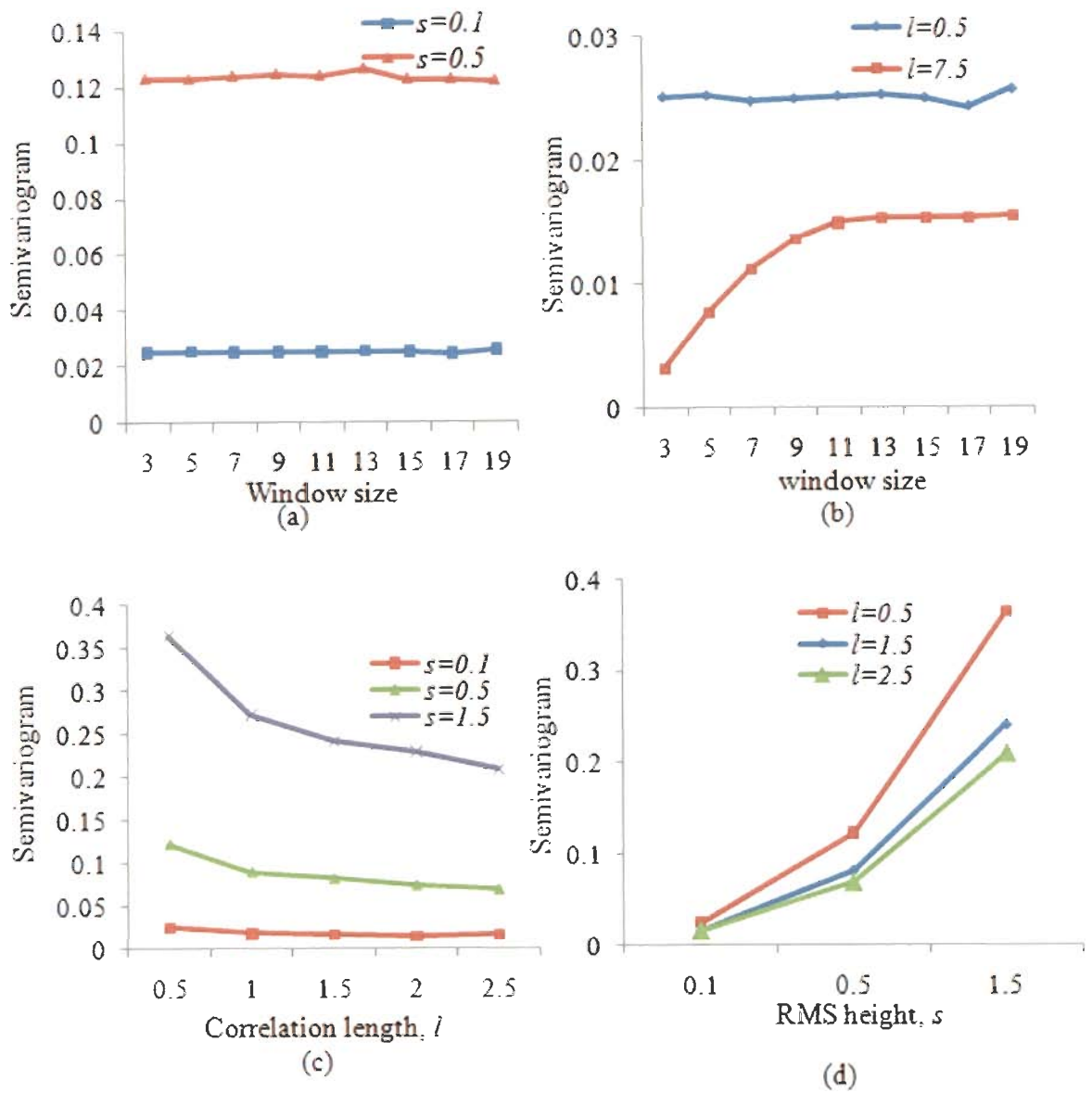
Figure 5.6. (a) variation of 'semivariogram' with respect to window size for fixed $l = 0.5$ and $s = 0.1, 0.5$, (b) variation of 'semivariogram' with respect to window size for fixed $s = 0.1$ and $l = 0.5, 7.5$, (c) variation of 'semivariogram' with respect to correlation length is plotted for window size = 5 and $s = 0.1, 0.5, 1.5$, and (d) variation of 'semivariogram' with respect to RMS height, s is plotted for window size = 5 and $l = 0.5, 1.5, 2.5$.
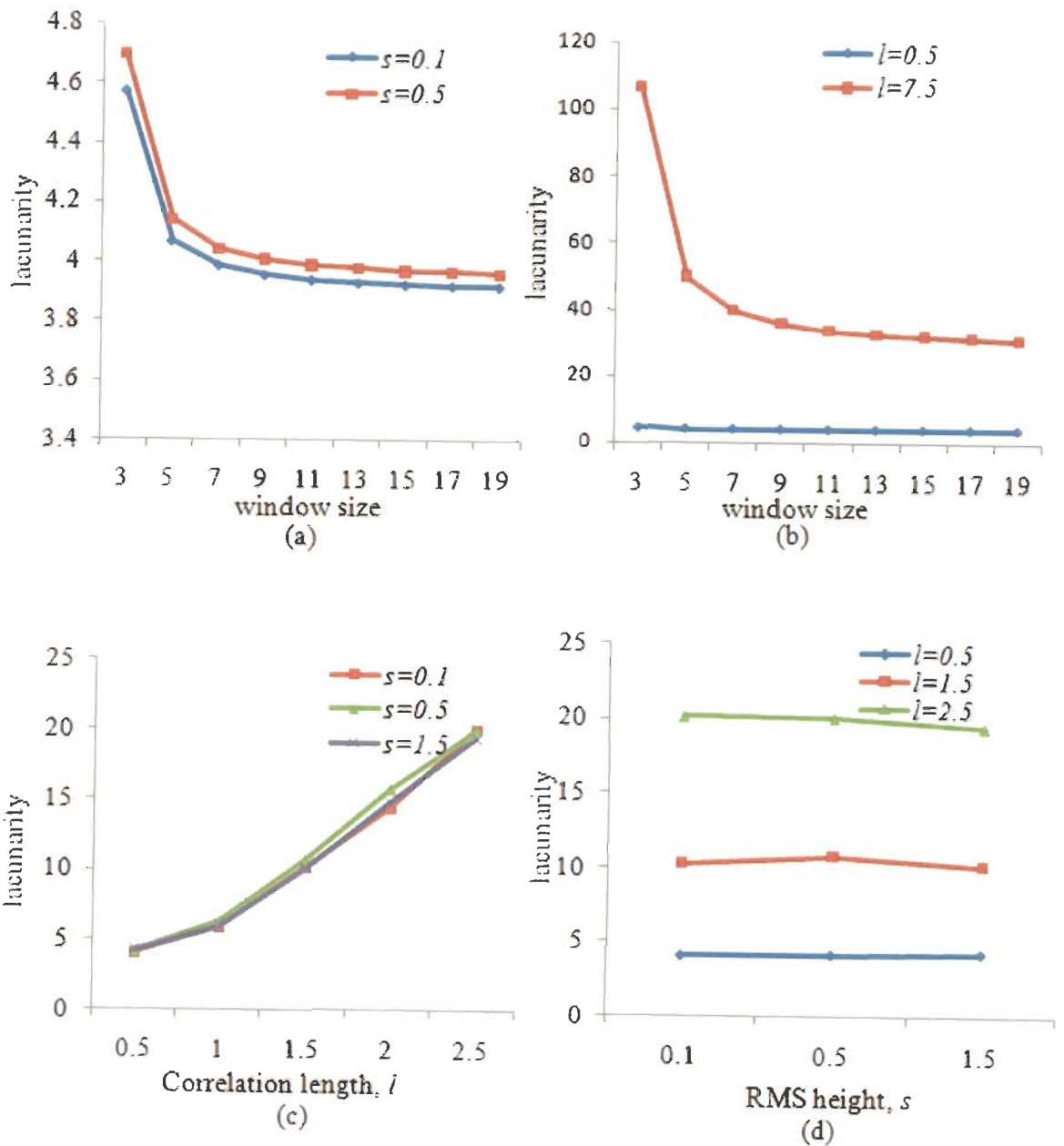
Figure 5.7. (a) variation of 'lacunarity' with respect to window size for fixed l = 0.5 and s = 0.1,0.5, (b) variation of 'lacunarity' with respect to window size for fixed s = 0.1 and l = 0.5,7.5, (c) variation of 'lacunarity' with respect to correlation length is plotted for window size = 5 and s = 0.1,0.5,1.5, and (d) variation of 'lacunarity' with respect to RMS height, s is plotted for window size = 5 and l = 0.5,1.5, 2.5.
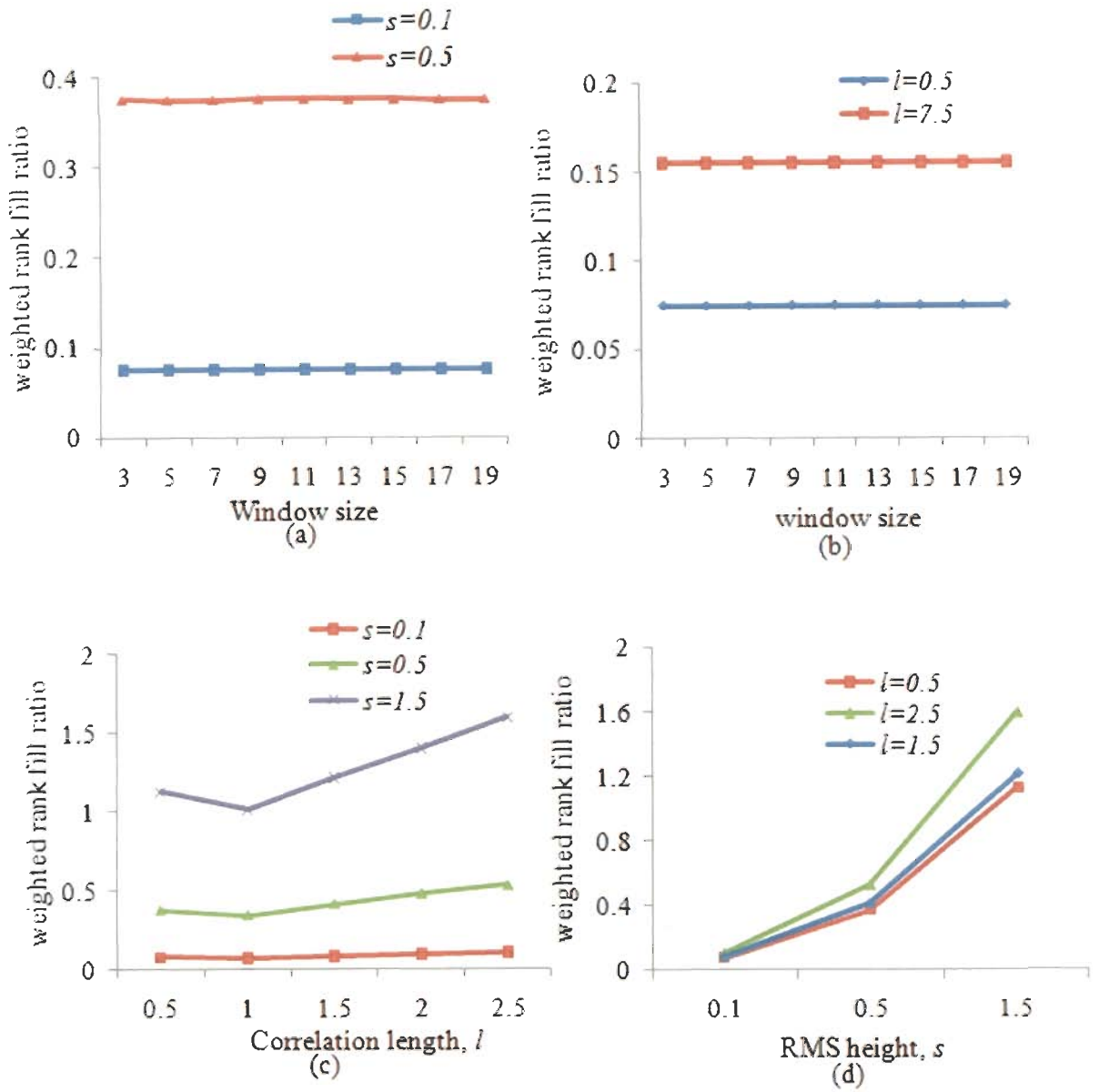
Figure 5.8. (a) variation of 'weighted rank fill ratio' with respect to window size for fixed $l = 0.5$ and $s = 0.1, 0.5$, (b) variation of 'weighted rank fill ratio' with respect to window size for fixed $s = 0.1$ and $l = 0.5, 7.5$ (c) variation of 'weighted rank fill ratio' with respect to correlation length is plotted for window size $= 5$ and $s = 0.1, 0.5, 1.5$, and (d) variation of 'weighted rank fill ratio' with respect to RMS height, s is plotted for window size $= 5$ and $l = 0.5, 1.5, 2.5$
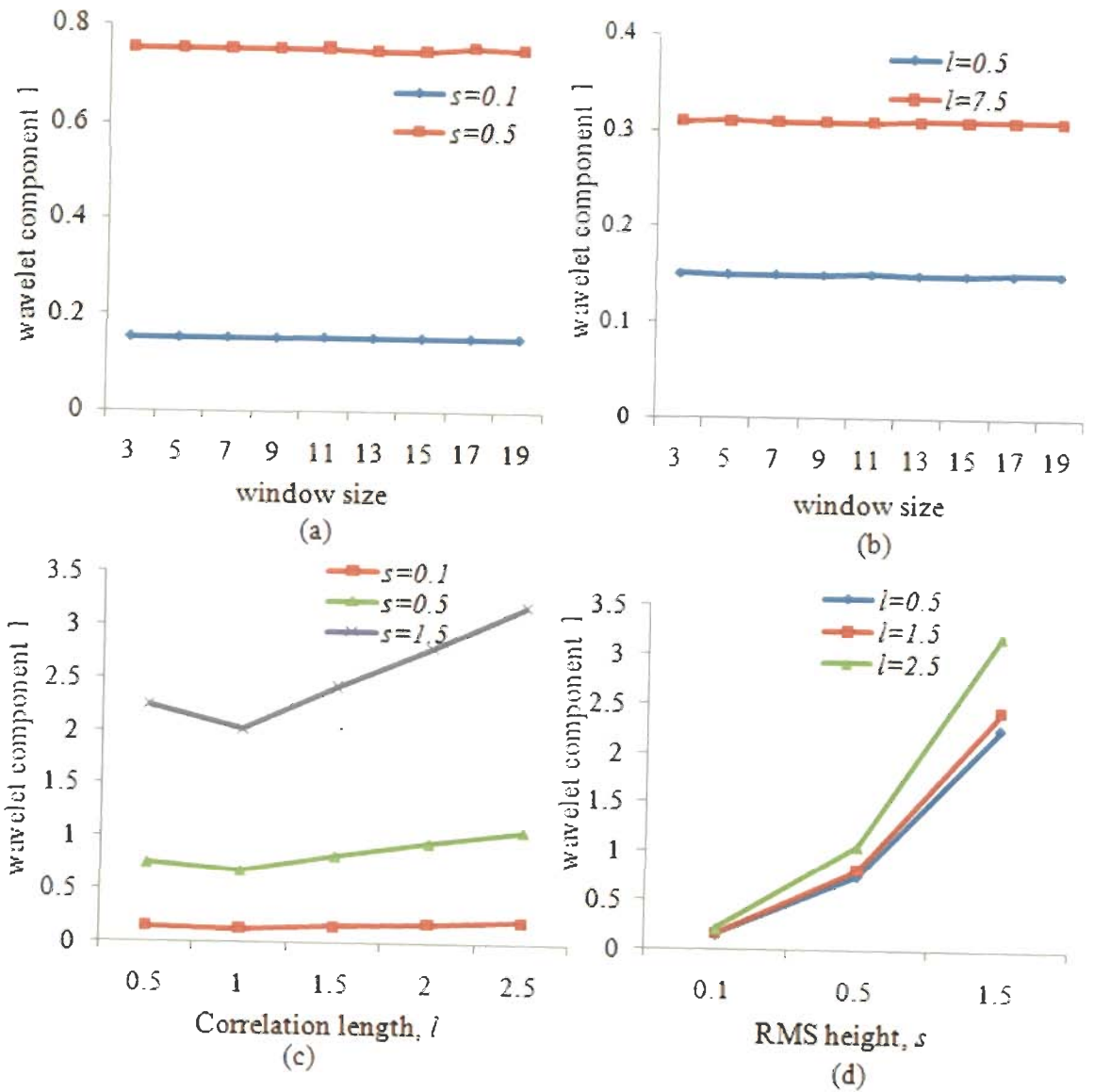
Figure 5.9. (a) variation of 'wavelet component 1' with respect to window size for fixed $l = 0.5$ and $s = 0.1, 0.5$, (b) variation of 'wavelet component 1' with respect to window size for fixed $s = 0.1$ and $l = 0.5, 7.5$ (c) variation of 'wavelet component 1' with respect to correlation length is plotted for window size = 5 and $s = 0.1, 0.5, 1.5$, and (d) variation of 'wavelet component 1' with respect to RMS height, s is plotted for window size = 5 and $l = 0.5, 1.5, 2.5$.

Effect of three parameters, namely two roughness measures, '*s*' and '*l*', and window size on 'mean' is studied. Figure 5.4 (a) and (b) shows the variation of 'mean' with window sizes. This is plotted for fixed values of '*s*' and '*l*'. As the window size increases, 'mean' also increases. Hence, it is quite dependent on window size. Figure 5.4 (c) shows the variation of 'mean' with correlation lengths for different '*s*' and fixed window size of '5×5'. It shows that for low values of '*s*', effect of correlation length is negligible. As '*s*' increases, variation in 'mean' is more while increasing correlation length. From figure 5.4 (d), it can be inferred that 'mean' is varying according to RMS height and little variation for varying correlation lengths.

Next, variations of texture measure, 'variance' for varying window size, '*s*' and '*l*' are studied. Figure 5.5 (b) shows that for higher values of '*s*', 'variance' is dependent on window size. 'variance' reduces as the window size increases. Figure 5.5 (c) shows how 'variance' changes for increasing correlation lengths for fixed for different '*s*' with fixed window size '5×5'. For lower value of '*s*', effect of correlation length on 'variance' is negligible (Figure 5.5 c). As the '*s*' increases, 'variance' also increases (Figure 5.5 d). This refers that effects of both roughness measures are interdependent.

'Semivariogram' is considered as the next texture measure for analysis. From Figure 5.6 (a) and (b), it can be inferred that window size has less impact on 'semivariogram' and is dependent only on '*s*' and '*l*'. Figure 5.6 (c) shows that as the correlation length increases for fixed window size '5×5', there is less variation in 'semivariogram' for lower values of '*s*' and more variations as '*s*' increases. Figure 5.6 (d) shows that 'semivariogram' increases for increasing '*s*'. Hence, 'semivariogram' is more dependent on RMS height, '*s*' than '*l*'.

When effect of window size is studied on 'lacunarity' for fixed values of '*s*' and '*l*', less variation in 'lacunarity' with window size has been observed (Figure 5.7 a and b). From Figure 5.7 (c), it can be observed that '*s*' has negligible impact on 'lacunarity'. As correlation length increases, 'lacunarity' also increases (Figure 5.7 c and d). Therefore, it can be inferred that 'lacunarity' may mainly depend on correlation length.

'Weighted rank fill ratio' hardly varies with increasing window size (Figure 5.8 a and b). Effect of correlation length is also negligible for lower values of '*s*' (Figure 5.8 c).

As RMS height increases, 'weighted rank fill ratio' increases (Figure 5.8 d). It can be concluded that 'weighted rank fill ratio' is highly dependent on 's'.

For analyzing the effect of surface roughness measures, wavelet components (db4) are computed. When analyzing, it is found that horizontal, vertical and diagonal detail components vary in negligible amount. Hence, only 'wavelet component 1', i.e., approximation coefficient, is taken for analyzing the effect. Window size has very less impact on 'wavelet component 1' (Figure 5.9 a and b). Figure 5.9 (c) and (d) shows that 'wavelet component 1' is dependent on RMS height, 's' and vary less with correlation lengths for low values of 's', that reflects that 'wavelet component 1' is quite dependent on RMS height, 's'.

This detailed analysis infers behavior of texture measures for roughness parameters and window size. It is clearly observed that some of these texture measures are highly influenced by RMS height 's' and some are highly influenced by correlation length 'l'. It means that 's' and 'l' may be estimated by these texture measures and these estimated values may then be helpful for labeling. Therefore, in the next step, an empirical analysis has been carried out to compute roughness with these measures.

5.3 Computing surface roughness from texture measures

For various values of 's', 'l', and window sizes, texture measures are calculated from the synthetic images as generated in section 5.1.2. Polynomial regression is employed on this observation to express each of the texture measures in terms of window size and roughness measures, 's' and 'l'. Defining equations and its coefficients with R^2 values is given in Table 5.2.

It is observed from Table 5.2 that 'semivariogram', 'weighted rank fill ratio' and 'wavelet component 1' have higher impact on 's', 'l' and 'w' because R^2 value is higher than 0.9, whereas other texture measures like 'mean', 'variance' and 'lacunarity' have R^2 values less than 0.7. Hence, only the three texture measures, semivariogram, weighted rank fill ratio and wavelet component1 are considered for further analysis.

Table 5.2. Texture measures in terms of roughness parameters and window size.

Sl.No	Textural measures	Defining equation	Parameters				R^2
			a_0^{1-6}	a_1^{1-6}	a_2^{1-6}	a_3^{1-6}	
1	Mean , y_1	$y_1 = a_0^1 + a_1^1 s + a_2^1 l + a_3^1 w$	−4.7766	5.2276	0.1980	0.3989	0.6942
2	Variance, y_2	$y_2 = a_0^2 + a_1^2 s + a_2^2 l + a_3^2 w$	−0.0152	0.1413	−0.0017	−0.0004	0.6775
3	Semivariogram, y_3	$y_3 = a_0^3 + a_1^3 s + a_2^3 l + a_3^3 w$	−0.0004	0.1694	−0.0042	0.0014	0.9145
4	Lacunarity, y_4	$y_4 = a_0^4 + a_1^4 s + a_2^4 l + a_3^4 w$	15.6121	−0.5422	7.2148	−1.3732	0.6521
5	Weighted rank fill ratio, y_5	$y_5 = a_0^5 + a_1^5 s + a_2^5 l + a_3^5 w$	−0.0616	0.882	0.032	−0.0001	0.9368
6	Wavelet component 1, y_6	$y_6 = a_0^6 + a_1^6 s + a_2^6 l + a_3^6 w$	−0.1258	1.7652	0.0659	0.0014	0.9365

a_0^{1-6}, a_1^{1-6}, a_2^{1-6} and a_3^{1-6} are the coefficients of defining equations for texture measures (sl.no. 1 to 6) and y_{1-6} represents six texture measures, 'mean', 'variance', 'semivariogram', 'lacunarity', 'weighted rank fill ratio' and 'wavelet component 1' respectively. 's', 'l' and 'w' represents RMS height, correlation length and window size respectively.

The coefficients of defining equations for texture measures, a_1^{1-6}, a_2^{1-6} and a_3^{1-6} represents the slope, indicating sensitivity of 's' , 'l', and window size, 'w' on respective texture measures, whereas a_0^{1-6} measures the noise. It is clearly observed from the Table 5.2 that a_2 values are very less for 'semivariogram', 'weighted rank fill ratio' and wavelet component1 that represents that the correlation length is less sensitive with texture measures whereas a_1 values are quite significant. It represents that these three texture measures are quite sensitive to RMS height, 's'. While observing coefficient a_0 that represents sensitivity of these texture measures with window size, its value is quite low. It means a fixed window size can be used for measuring these texture measures. This analysis infers that the texture measures, 'semivariogram', 'weighted rank fill ratio' and 'wavelet component 1' play major role for measuring the roughness parameter, RMS height. Taking care of all these analysis, a relationship among RMS height 's' , semivariogram, 'weighted rank fill ratio' and

wavelet component1 has been developed using regression analysis, that can be expressed as

$$s = a_0 + a_1 \text{ (semivariogram)} + a_2 \text{ (weighted rank fill ratio)} + a_3 \text{ (wavelet component 1)}$$

$$(5.8)$$

By polynomial regression fit to the observed data (same set of data of approximately 1500 images used for computing texture measures in section 5.2), the coefficients a_0, a_1, a_2, a_3 are obtained as 0.0110, 2.3915, 5.4634 and -2.4103 respectively and R^2 is 0.9739. Similarly, polynomial regression fit is tried to obtain relationship for correlation length in terms of these measures, but R^2 is 0.4768 that confirms our earlier findings that the three texture measures namely 'semivariogram', 'weighted rank fill ratio' and 'wavelet component 1' are less sensitive on correlation length, 'l'.
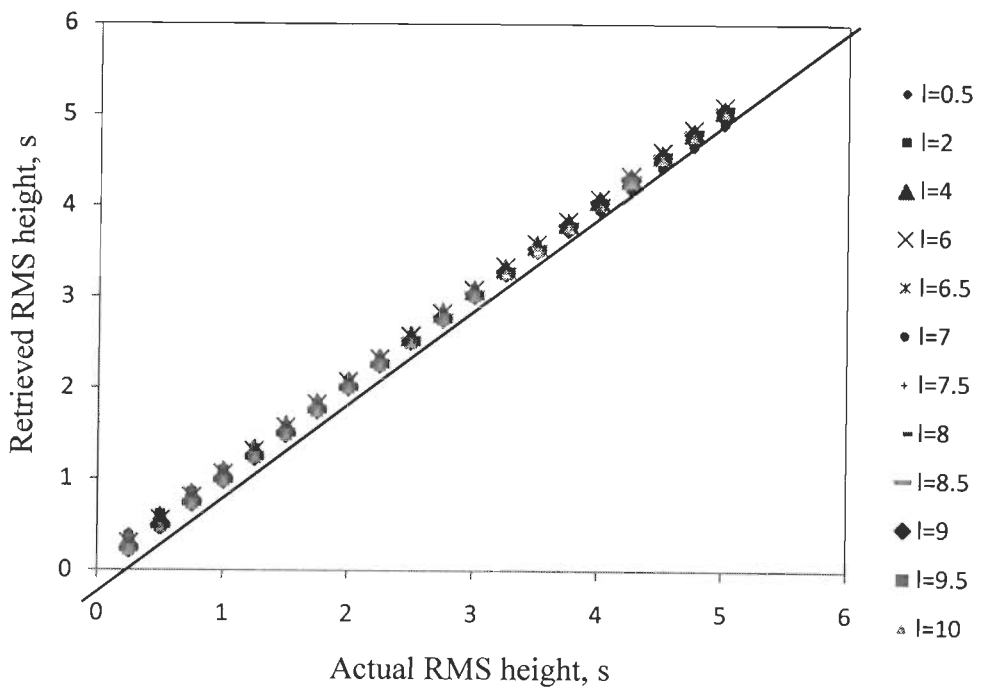
Figure 5.10. Scatter plot of retrieved RMS height vs actual RMS height,'s'.

The empirical relationship developed (equation 5.8) is tested with about 200 synthetic images to retrieve RMS height 's'. Synthetic images with RMS height varying from 0.25 to 5 in steps of 0.25 (hence 20 different 's') and ten correlation length, l = 0.5, 2, 4, 6, 6.5, 7, 7.5, 8, 8.5, 9, 9.5 and 10 (random values of l) are chosen . Three texture measures, 'semivariogram', 'weighted rank fill ratio' and 'wavelet component 1' are computed and RMS height 's' is retrieved from these computed texture measures using equation (5.8). Figure 5.10 shows the scatterplot of retrieved RMS height with actual RMS height and it can be inferred that retrieved RMS height closely follows actual RMS height. This shows that surface roughness parameter, RMS height can be retrieved effectively using the mentioned three texture measures with the help of equation 5.8.

5.4 Computation of roughness parameter, RMS height for real SAR image

5.4.1 Data used

ERS-2 SAR C-band image acquired on July 23, 2001 is used for developing and analyzing the proposed approach of unsupervised classification of single polarized SAR image. ERS-2 SAR C-band image of July 28, 2003 is used for validating the results for labeling. The complete details of the study area with latitude / longitude co-ordinates and satellite data can be referred with section 1.3 and 1.4.

5.4.2 Proposed methodology to compute RMS height, 's' for SAR image

Clusters obatined by any of the proposed methods of SAR segmentation (Chapter 3 or chapter 4) can be taken as input for labeling. These clusters are to be labeled with major land cover types of water, urban and vegetation areas.

5.4.2.1 Steps involved in computing RMS height can be stated as listed

- SAR image segmentation is implemented using any one of the proposed methods in chapter 3 and 4 and clusters identified by the proposed algorithm is taken as input.

- In each of the cluster, image is divided in to groups of pixels of size 5×5. For each of these pixel groups, three texture measures viz., 'semivariogram', 'weighted rank fill ratio' and 'wavelet component 1' are calculated.

- Using the equation (5.8), rms height, 's' is computed from these three texture measures.

- Similarly, RMS height is calculated for all groups of pixels of size 5×5 in each of the clusters.

5.4.2.2 Critical analysis to label the various clusters

- Segmented image obtained by PCA based fusion approach (Chapter 3) is labeled with the help of topographic sheet and hence label of clusters are known.

- RMS height 's' is calculated for all groups of pixels within every cluster belonging to various land cover types like water, urban and agriculture areas (Section 5.4.2.1). In Table 5.3, three texture measures, semivariogram, weighted rank fill ratio and wavelet component 1 and RMS height 's' calculated from these measures for 10 samples of each land cover types, i.e., water, urban and vegetation areas are listed.

- From the calculated RMS height 's' for all groups of pixels with in each land cover type, range of 's' can be specified for that land cover. Similarly, range of 's' is computed for urban and vegetation areas and are shown in Figure 5.11.

Various values of texture measures with computed RMS height (from equation 5.8) is shown in Table 5.3. The points w^{1-10}, u^{1-10} and a^{1-10} are shown in figure 5.11. Typical ranges of each of texture measures (Figure 5.11) is identified by analyzing more than 30 clusters having about 100 groups of pixels belonging to each type of land cover. Typical ranges are presented in Table 5.4.

Table 5.3. RMS height calculated in real SAR image for water, urban and agriculture areas.

Land cover type	Texture Measures			RMS height
	Semivariogram	Weighted rank fill ratio	Wavelet component 1	
Water [w_1-w_{10}]	[0.045,0.045, 0.034,0.023, 0.014,0.036, 0.033,0.018, 0.042,0.044]	[0.4,0.4, 0.34,0.37, 0.24,0.22, 0.16,0.07, 0.34,0.32]	[0.8,0.07, 0.4,0.53, 0.56,0.24, 0.45,0.7, 0.65,0.45]	[0.472,0.443, 0.398,0.347, 0.298,0.399, 0.390,0.32, 0.449,0.45]
Urban [u_1-u_{10}]	[30,28, 26,24, 22,21.8, 20,28, 24,27]	[0.6,0.57, 0.54,0.45, 0.38,0.33, 0.5,0.22, 0.14,0.05]	[10,8.7, 9.3,5.7, 6.3,6.3, 9.7,7.9, 3.8,4.2]	[156.37,145.94, 135.58,125.05, 114.68,113.64, 104.44,145.89, 124.96,140.55]
Agriculture [a_1-a_{10}]	[0.8,2.1, 2.7,3.2, 0.28,0.19, 0.43,0.38, 0.46,0.22]	[0.5,0.43, 0.36,0.48, 0.53,0.27, 0.63,0.17, 0.34,0.28]	[10,4, 5.1,6.3, 8.3,9.1, 8.2,7.6, 4.8,9.6]	[4.76, 11.27, 14.42,17.07, 1.99,1.55, 2.77,2.47, 2.78,1.72]

w_1-w_{10} represent 10 samples of water areas and corresponding texture measures with RMS height's' are listed. Similarly u_1-u_{10} represent 10 samples of urban areas and a_1-a_{10} represent 10 samples of agriculture areas.
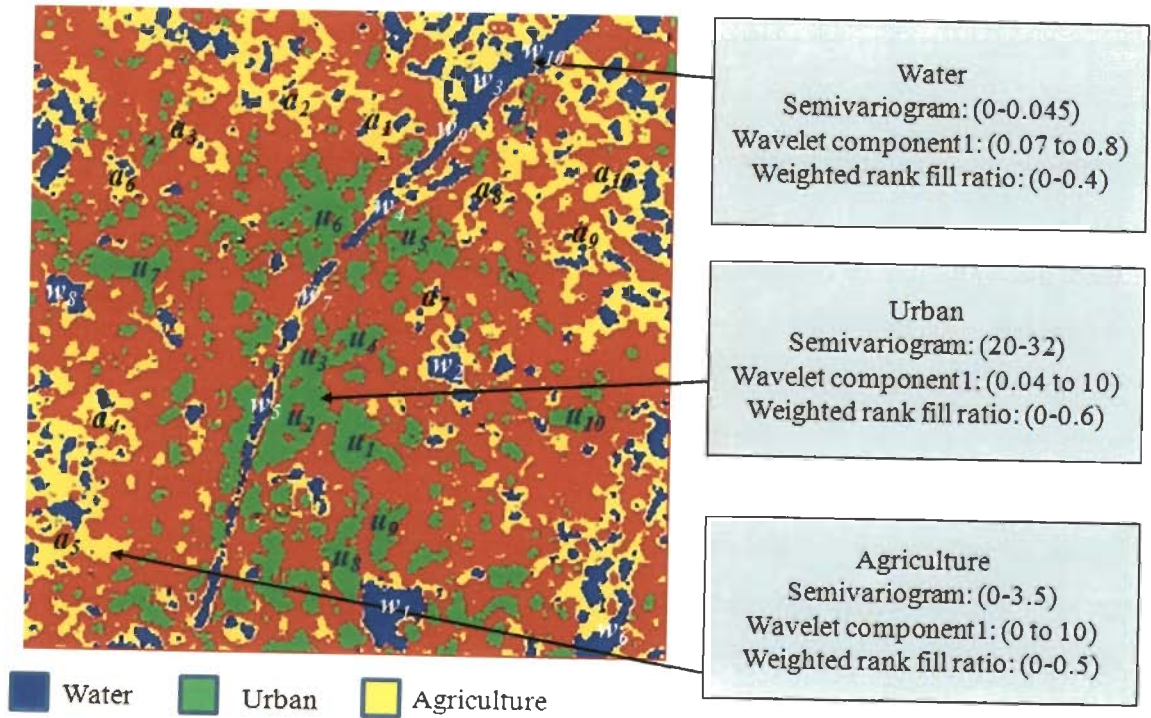
Figure 5.11. Clustered SAR image- texture measures for each cluster.

Table 5.4. Typical range of RMS height for major land covers.

Land cover type	Water	Urban	Agriculture
Typical values of RMS height 's' (cm)	<0.5	(100 and higher)	(0.7-20)

From the analysis, it is observed that RMS height 's' may be used to differentiate land cover on the basis of roughness (Table 5.4). If the RMS height is less than 0.5 cm, then the variation is insignificant when compared with wavelength (C-band SAR image has wavelength of 5.6 cm). The water area in this region is calm and hence surface is smooth. These ranges may not be applicable for rough water surface. In such case, backscattering coefficient can also be used to decide the nature of land cover (Evans et al., 1992). We have analyzed approximately more than 1000 water pixels for this image and the approximate range of backscattering coefficient is (-24 to -28) dB, which is approximately the same range as reported in other works (Dobson et al., 1992; Mäkynen and Hallikainen, 2005). Although it is very difficult to get clear cut demarcation of backscattering coefficient for different clusters, range of surface roughness measure is different for various land cover types namely water, urban and agriculture areas (Karvonen et al., 2005). In this study region, agriculture regions are mostly wheat, sugarcane and paddy. For these agriculture regions, RMS height 's' is obtained to be in the range of (0.7-75) cm. Then, for urban areas, values of 's' are higher. These values may vary according to the nature of the constructed area. For this SAR image, range of 's' corresponding to urban areas is 100 cm or higher (Xia and Henderson, 1997).

Table 5.5. Decision rules for labeling of clusters into water, urban and agriculture areas.

Land cover type	Water	Urban	Agriculture
Range of '*s*' (cm)	<0.5	(100 and higher)	(0.7-75)
Range of 'backscattering coefficient'	(-24 to -28)dB	(-8 to -15)dB	(-5 to -12)dB

Table 5.5 clearly shows that with the help of RMS height 's' and backscattering coefficient, clusters can be labeled. If the RMS height 's' is <0.5 cm and backscattering coefficient is in the range of (-24 to -28)dB, then the cluster is labeled as water. Similarly, the conditions stated in Table 5.5 are applied for labeling urban and agriculture areas. Range of backscattering coefficient of urban is in the range of (-8 to -15) dB and for agriculture areas is (-5 to -12) dB (Paloscia et al., 1999; Ferrazzoli et al., 1997).

The decision rules for labeling the clusters are tested with SAR data of July 28, 2003. SAR segmentation process is carried out to segment the images into various clusters. Now, the clusters are to labeled with our proposed approach. For this purpose, pixels within each cluster are grouped into sets of 5×5 pixels. Then, each of the groups of pixels, texture measures namely 'semivariogram', 'weighted rank fill ratio' and 'wavelet component 1' are computed. Using equation 5.8, RMS height 's' is computed from these texture measures. On the basis of RMS height and the mean backscattering coefficient within each window, the groups of pixels are labeled as one of the major land cover types i.e., water, urban and agriculture areas. Figure 5.12 shows the labeled SAR image of July 28, 2003 with major land cover types of water, urban and agriculture areas, which represent that roughness is playing a fruitful role with the backscattering coefficient to label the various clusters.

110
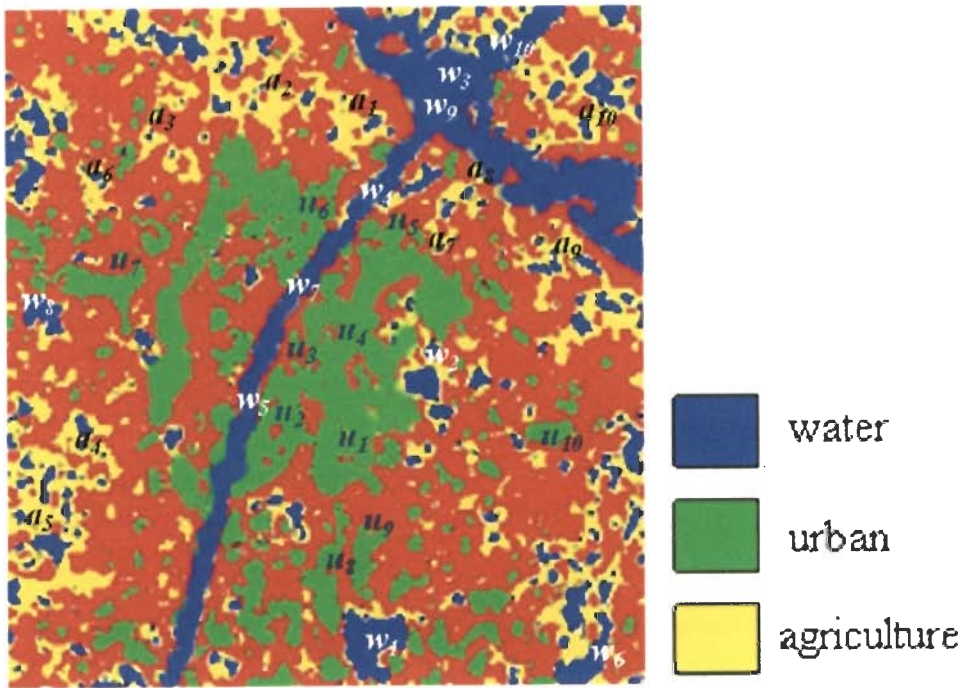
Figure 5.12. Labeled image of July 28, 2003.

5.5 Conclusion

Texture measures like mean, variance, semivariogram, lacunarity, 'weighted rank fill ratio', wavelet components are analyzed critically for their variation when surface roughness measures, RMS height 's' and correlation length 'l' are varied. This is accomplished by developing synthetic images with varying 's' and 'l'. When computing texture measures, window size is varied to observe and incorporate the effect of window size, if required. From the analysis, it is found that three texture measures, semivariogram, 'weighted rank fill ratio' and 'wavelet component 1' are suitable for measuring 's'. It is found that 'l' and window size are less sensitive for these three texture measures, which helps to propose an empirical relation among 's' and these three texture measures. The empirical relation developed with the synthetic images has been validated with real SAR images and results are quite encouraging. It means various major clusters like water, urban or agriculture areas can be easily labeled by considering roughness and backscattering coefficient. This infers that use of roughness with backscattering coefficient may resolve the problem of labeling of various clusters.

Chapter 6

Unsupervised Classification of 'Change' and 'No Change' Pixels with Quantitative Analysis of Changes by Image Analysis and Interferometric Approach

6.1. Introduction

One of the major applications of SAR image is for developing the monitoring system for various applications like land cover and land use dynamics, hazards monitoring and damage assessments by discerning areas of change on digital images between two or more dates of a scene.

For designing any monitoring system, first important issue is to identify the changes occurred in both microscopic and macroscopic level, for example, in the case of SAR, from pixel level to a group of pixels. For this purpose, it is important to classify the temporal SAR image in to 'change pixels' ('cp') and 'no change pixels' ('ncp') on the basis of analysis of individual pixel and spatial analysis of pixels. The main aim of detecting changes (i.e., mapping 'cp' and 'ncp') is to obtain both qualitative and quantitative analysis of changes on earth surface.

By comparing SAR images obtained at different dates (two or more), change pixels and no change pixels (denoted as 'cp' and 'ncp' in this chapter) can be mapped on the image. When classifying 'cp' and 'ncp', we aim at: (a) detecting the geographic location of changes and (b) quantifying the amount of change. Therefore, in this chapter, the task of mapping 'cp' and 'ncp' is divided in to two sub tasks.

(i) Firstly, qualitative analysis of 'cp' and 'ncp' is implemented using image analysis approach so that locations of changes may be detected, and

(ii) Secondly, quantitative analysis of changes is computed using differential interferometry so that changes are measured in units.

For this purpose, four image analysis techniques namely (i) image differencing (ii) minimum ratio detector (iii) correlation coefficient and (iv) integrated intensity, texture and orientation difference have been used. These image analysis techniques give a mapping of 'cp' and 'ncp' of the SAR image. To get reliable set of 'cp' and 'ncp', it is required to take intersection of all the results obtained by these four individual methods. It is difficult to check the authenticity of the results of 'cp' and 'ncp'. A probability distribution function (pdf) based approach is proposed to check the reliability of mapping change pixels in the region. 'cp' and 'ncp' can be defined by suitable probability distribution so that for succeeding years of the same data, pixels are classified into 'change' and 'no change' areas on the basis of pdf parameters itself.

The next aim is to obtain quantitative analysis of changes occurred on earth surface. This is carried out using DInSAR and a subsidence map is obtained as output. The quantitative analysis of subsidence with image analysis approach is very difficult. Therefore, an algorithm is proposed in this chapter by which more information about the changes like nature of subsidence (low, medium or high) could be retrieved from results of image analysis approach.

Researchers are using various methods to obtain 'cp' and 'ncp' (Berroir et al., 1996; Bouzidi et al., 2003; Boucher et al., 2006; Chatterjee et al., 2006; Gamba et al., 2006; Bovolo and Bruzzone, 2007; Chaabane et al., 2007). For this purpose, they are using image analysis tools. Popular image analysis techniques for classifying 'change' and 'no change' pixels as applied to SAR images are (i) image differencing and (ii) image ratioing. Rignot and Van Zyl (1993) have discussed about these two techniques and complementing characters of these techniques for mapping 'cp' and 'ncp' using the structural and dielectric properties of remotely sensed surfaces. Image ratioing is found to be better adapted to statistical characteristics of SAR data taking care of common errors. Unsupervised classification of 'cp' and 'ncp' based on image differencing has also been used (Mas, 1999; Bruzzone and Prieto, 2000; Melgani and Moser, 2002). Bruzzone and Prieto (2000) have discussed the problem of identifying suitable threshold for discriminating 'cp' and 'ncp'. He has used statistical parameters of 'change' and 'no change' classes computed using expectation maximization (EM) algorithm, formulated under the assumption that the conditional density functions of classes can be modeled using gaussian distribution. Higher order statistics were

analyzed for mapping 'change' and 'no change' pixels in SAR images (Bujor et al., 2004). Bujor et al., (2004) have shown that ratio of means was useful to identify step changes and that the second and third order log cumulants were useful for progressive changes that appear in succeeding images in multi temporal analysis. Multi scale change analysis for SAR images is also proposed by Inglada and Mercier (2007). Correlation coefficient approach is attempted to map the changes occurred in the image. Gray scale and contrast difference caused by different receiving conditions and receiving times are possible to be eliminated because correlation coefficient does not change with linear change of gray scale (Zhang et al., 2003). Most of the techniques, researchers developed in this context, have used thresholding or prior assumption of distribution of pixels (Rogerson, 2002). Hence, mapping of 'change' and 'no change' pixels depends on these assumptions. Therefore, it is needed to design such an approach by which end user can confidentially say about 'change' and 'no change' pixels. By studying the properties of pixels belonging to 'change' and 'no change' areas, suitable distribution model is proposed.

All these algorithms provide a distance measure which indicates the relative magnitude of change, but they do not provide quantitative measurement of changes. The advance of DInSAR technology has offered a viable solution for large scale mapping deformations quantitatively.

SAR interferometry (InSAR) is an established technique to measure terrain topography. The application of this technique is based on the generation of an interferogram using two complex SAR images of the same area acquired from two slightly different angles.

SAR interferometry requires digital elevation models to map deformation occurred (Zebker and Goldstein, 1986; Rao et al., 2003; Schiavon et al., 2003). The permanent scatterer technique of measuring subsidence or deformation may prove to be ineffective wherever the density of stable radar targets is relatively low (Ferretti et al., 2001; Noferini et al., 2005). InSAR techniques based on interferogram stacks have been proposed (Ferretti et al., 2000, 2007, Strozzi et al., 2001, Berardino et al., 2002, Mora et al., 2003). These techniques are expensive due to large image stacks employed. These large image stacks are employed either to remove atmospheric artifacts or to identify permanent scatterers. The deformation analysis using

permanent scatterer can be very scarce and may not cover complete site area even though it utilizes large stacks of InSAR image pairs. Many successful cases indicate the potential of DInSAR for detecting changes in land surface (Nagler et al., 2002; Strozzi et al., 2005; Bovenga et al., 2006).

DInSAR is potentially a unique tool for precise generation of DEM (Digital Elevation Model) and it enables the mapping of subsidence on a large scale. The principle idea behind DInSAR can be stated as: using two interferometric image pairs (requiring three acquisitions of the image, out of which, one is termed as master and other two are slave images, hence, it is also termed as three pass interferometry) of the same area separated in time such that a dynamic deformation has occurred between master and one of the slave acquisitions, it is possible to form a differential interferogram where the underlying topography is cancelled and remaining is only the phase information corresponding to deformation itself.

Therefore, in this chapter, DInSAR technique using three pass interferometry, that does not require elevation model, has been employed to measure subsidence or to map quantitative changes on earth surface. The quantitative analysis of subsidence with image analysis approach is difficult in one hand, whereas with DInSAR, it is very complex. To avoid the complexity and measure the range of subsidence in low, medium and high subsidences, an approach using pdf for labeling level of subsidence from simple image analysis technique of minimum ratio detector is proposed in this chapter.

This chapter is organized as follows. Section 6.2 describes the proposed method of obtaining reliable set of 'change' pixels using image analysis approach. Section 6.3 explains the application and validity of suitable pdf model for distribution of 'change' and 'no change' pixels. Section 6.4 explains interferometric based approach of obtaining quantitative subsidence. Section 6.5 describes the proposed approach by which nature of subsidence (like low, medium or high subsidence areas) can be labeled from results of image analysis approach. Conclusion for this chapter is given in section 6.6.

6.2. Classifying 'change' and 'no change' pixels using image analysis approach

6.2.1 Data used

New Orleans city of USA has been taken as the study area (details of study region are discussed in section 1.4 and 1.5). RADARSAT-1 data set in SLC (Single Look Complex) form, acquired from 15 April 2002 to 15 March 2007 (Appendix A) are obtained and analysed. Since the results obtained by image analysis and interferometric approach, image pairs passing the critical selection of InSAR image pairs are chosen for classifying 'change' and 'no change' pixels using image analysis approach. Image pairs with approximately one year of interval from 2002 to 2007 (Table 6.1) of New Orleans city of USA are chosen. For the year 2005-2006, two sets of image pairs are considered to quantify changes. This is because of the criteria to be satisfied by InSAR image pairs.

Table 6.1. List of image pairs with acquisitions approximately one year apart.

Sl.No	Year span	InSAR image pair				Beam mode/ product type
		Master image		Slave image		
		Data ID	Acquisition date (yyyy-mm-dd)	Data ID	Acquisition date (yyyy-mm-dd)	
1	2002-2003	6	2002-08-13	20	2003-11-12	S2/SLC
2	2003-2004	20	2003-11-12	26	2004-04-04	S2/SLC
3	2004-2005	26	2004-04-04	37	2005-03-06	S2/SLC
4	2005-2005	36	2005-03-01	53	2005-11-20	F5/SLC
5	2005-2006	52	2005-11-01	59	2006-02-05	S2/SLC
6	2006-2007	68	2006-09-04	84	2007-03-15	F5/SLC

116

6.2.2. Image analysis approach

Four image analysis techniques for classifying 'change' and 'no change' areas are employed using (i) image differencing, (ii) minimum ratio detector, (iii) correlation coefficient analysis, and (iv) integrated intensity, texture and orientation difference. All these algorithms provide a distance map. By applying suitable thresholds on distance maps, classification of 'change' and 'no change' areas are obtained.

6.2.2.1 Image differencing

Image differencing is a very simple method in which absolute values of difference between corresponding pixels in two images is calculated and larger values in the difference map, then indicates locations of change. If images I_1 and I_2 are two images obtained at different time instants t_1 and t_2, then difference map D (Ridd and Liu, 1998) can be obtained as

$$D(i,j) = abs\left(I_1(i,j) - I_2(i,j)\right) \tag{6.1}$$

where i,j represents row and column index of the images, I_1 and I_2 represent images compared for classifying 'change' and 'no change' pixels, and D represents difference map. Difference map is also of the same size as input images I_1 and I_2. The selection of exact thresholding value depends on the application and also depends on the nature and magnitude of change desired to be detected. Threshold used for change detection in SAR images in this application is given by

$$\text{Threshold} = \text{mean} + (n * \text{standard deviation}) \tag{6.2}$$

where 'n' is taken as 1. This will enable threshold selection independent of the original intensity values of the image. 'n' values can be chosen in the range (0.7-1.4) for optimal change detection (Ridd and Liu, 1998).

6.2.2.2 Minimum ratio detector (MRD)

Minimum ratio detector computes ratios of the means computed for both images $\left(\dfrac{\mu_1}{\mu_2}, \dfrac{\mu_2}{\mu_1}\right)$ and uses the minimum ratio of the two. In this technique, changes are measured by dividing the intensity values, pixel per pixel, and are expressed in decibels (that is, taking ten times the logarithm in base ten of the ratio of the

117

intensities). This ratio method is preferred over image differencing because image ratioing is robust to radiometric errors (Van Zyl et al.,1993). When computing intensity ratio, these effects cancel out each other because these errors are reproduced in repeat pass imagery.

Distance map by minimum ratio detector is obtained as

$$r_{MRD}(i, j) = 1 - \min\left(\frac{\mu_1}{\mu_2}, \frac{\mu_2}{\mu_1}\right)$$

(6.3)

where i,j represents row and column index of pixel, μ_1 and μ_2 are mean intensities calculated for images, I_1 and I_2 over a local neighborhood of pixel (i,j), and r_{MRD} represents distance map produced by MRD algorithm.

In this equation (6.3), window size of 5×5 is chosen for calculating mean intensity. Both images are normalized and scaled to range [0, 1] using equation (6.4).

$$I(i, j) = \frac{I(i, j) - \min(I)}{max(I) - \min(I)}$$

(6.4)

where *min(I)* represents minimum value of pixel in image I and *max(I)* represents maximum value of pixel in image I If images are not normalized, negative mean in either image I_1 or I_2 will result in MRD distance greater than one. This ensures that MRD distance map also has the range [0, 1]. Threshold of 0.7 (Van Zyl et al., 1993) is used to obtain change detection map. The pixels having MRD greater than or equal to 0.7 is labeled as 'change' and other pixels are 'no change' pixels.

6.2.2.3 Modified correlation coefficient

Correlation between two images can be interpreted as the closeness between two images in its features, textural patterns and distribution of spatial patterns (Zhang et al., 2003).

Correlation coefficient is usually given by

$$\gamma = \frac{\sum\limits_{m,n=1}^{w} \left(x_{mn} - \overline{x}\right)\left(y_{mn} - \overline{y}\right)}{\sqrt{\sum\limits_{m,n=1}^{w} \left(x_{mn} - \overline{x}\right)^2} \sqrt{\sum\limits_{m,n=1}^{w} \left(y_{mn} - \overline{y}\right)^2}} \qquad (6.5)$$

where w- window size, x_{mn} and y_{mn} represents pixel at position row, column as *(m,n)* within the window, $\overline{x}$ and $\overline{y}$ represents the mean values of both the compared images within the window.

In the distance map obtained by this method, value '0' represents no correlation and hence more change and value '1' represents complete correlation and no change. Intensity of changes can also be mapped with the values of correlation. There are some limitations in applying correlation coefficient. If one of the test images has constant or uniform intensity, denominator factor $\left(x_{mn} - \overline{x}\right)$ or $\left(y_{mn} - \overline{y}\right)$ becomes zero. γ is undefined due to division by zero.

To avoid this undefined condition, equation (6.5) is modified as

If $\left(x_{mn} - \overline{x}\right)$ or $\left(y_{mn} - \overline{y}\right) = 0$, Correlation coefficient, $\gamma = 1 - abs\left(\dfrac{\overline{x} - \overline{y}}{scalefactor}\right)$,

$$(6.6)$$

else, correlation coefficient is given by equation (6.5).

where, $scalefactor = \max(\max(I_1, I_2))$. According to equation (6.6), if one of the images has constant intensity making denominator zero, then, ratio of absolute value of the difference in means of two images within local neighborhood to maximum intensity of two images is considered. When mean of both images are equal, then, $(\overline{x} - \overline{y})$ becomes zero and correlation coefficient is one implying that both images are completely correlated. If mean of one image is zero and other image is non-zero, then ratio of difference in intensity to maximum intensity of both images is taken as deviation from correlation. If both means are non-zero, then definition for correlation coefficient is used.

Threshold of (0.3-0.8) is applied on correlation coefficient to classify 'change' and 'no change' pixels (Zhang et al., 2003). The pixels with γ values from 0.3 to 0.8 are considered as 'change' pixels and remaining pixels are termed as 'no change' pixels. Due to the presence of speckle, low γ values may be misleading and hence the pixels of γ less than 0.3 are not taken as 'change' pixels.

6.2.2.4 Integrated Intensity, texture and Orientation difference map

Figure 6.1 shows the process of obtaining distance map using intensity, texture and orientation features. Gabor wavelet filter is used to obtain orientation features for both images. Textural features are obtained using discrete moment transform and Intensity features are extracted by using simple intensity difference maps.

Intensity difference maps are obtained similar to image differencing. Each pixel in intensity difference map is obtained as absolute difference between corresponding pixels in images, I_1 and I_2.

Discrete moment transform is used to extract the texture features of the image and is given by

$$
\begin{aligned}
dmt1^{p,q}(x,y) &= \sum_{r=-1}^{+1}\sum_{s=-1}^{+1} I_1(x-r,y-s)r^p s^q \\
dmt2^{p,q}(x,y) &= \sum_{r=-1}^{+1}\sum_{s=-1}^{+1} I_2(x-r,y-s)r^p s^q
\end{aligned}
\tag{6.7}
$$

For $(p,q)=(0,1)$, $(1,0)$ and $(1,1)$, $dmt1$ and $dmt2$ are computed, thereby, three texture feature images are obtained for each input image, I_1 and I_2. Three texture difference images are produced as absolute difference of corresponding pixels in texture images

$$
texturediff^{p,q} = \left| dmt1^{p,q} - dmt2^{p,q} \right|
\tag{6.8}
$$

Similarly, texture difference images are obtained from all three texture images computed for images, I_1 and I_2 (Itti et al., 1998).
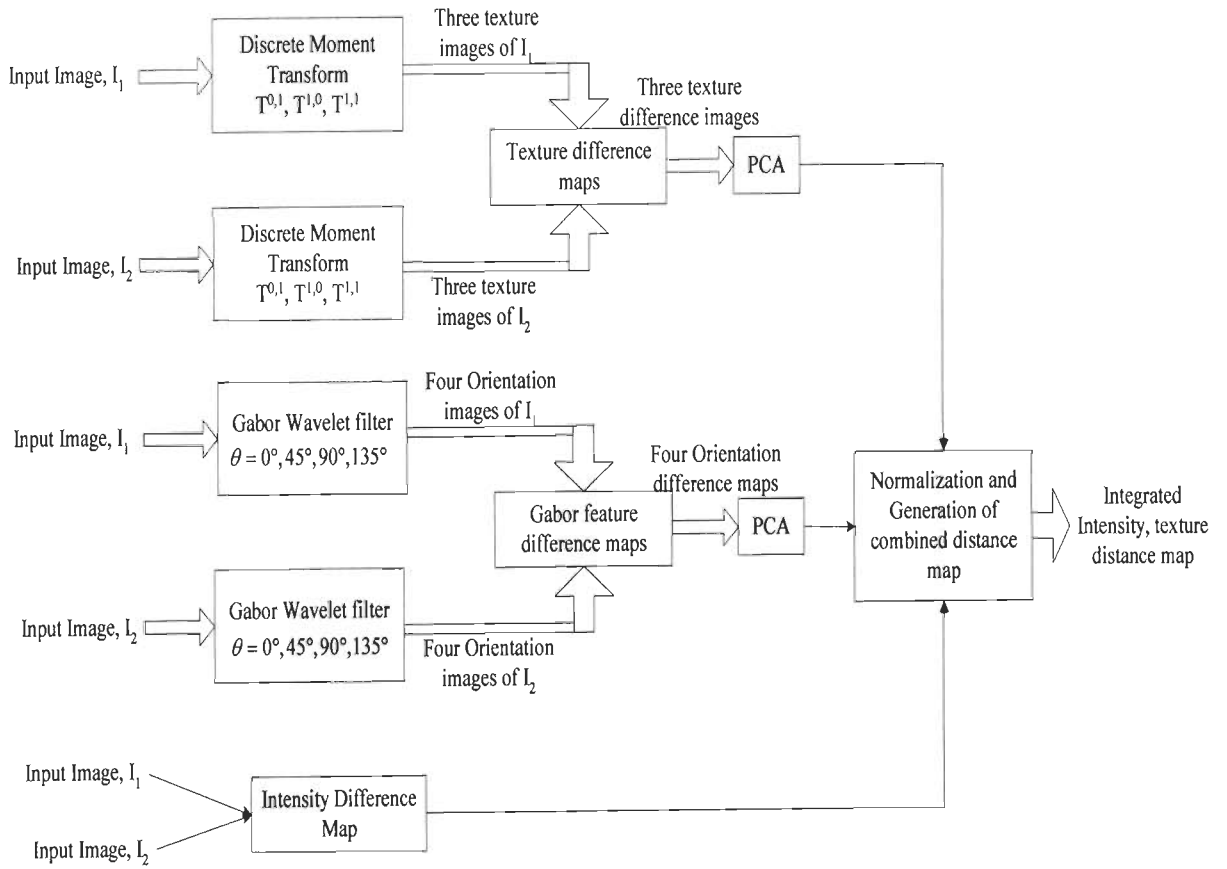
Figure 6.1. Computation of distance map using intensity, texture and orientation features.

Gabor wavelet filter is applied on input images I_1 and I_2 to generate four feature images corresponding to four orientations, $\theta = 0°, 45°, 90°, 135°$. Gabor filter coefficients $g(x, y, \theta)$ are designed for four varying orientations (Kyrki et al., 2004). Input image is convolved with gabor filter corresponding to four orientations to obtain four orientation maps.

Orientation map is given by

$$orient1(x, y, \theta) = \left\| I_1(x, y) \otimes g(x, y, \theta) \right\|$$
$$orient2(x, y, \theta) = \left\| I_2(x, y) \otimes g(x, y, \theta) \right\|$$

(6.9)

where *orient1(x,y, θ)* is the orientation map obtained for image I_1 and orientation, *θ,* *orient2(x,y, θ)* is the orientation map obtained for image I_2 and orientation, *θ,* and $I_1(x,y)$ and $I_2(x,y)$ are the input images with *(x,y)* as row and column of a pixel, *g(x,y, θ)* is the gabor filter coefficient and *θ* is the orientation angle

Thus, four orientation maps for each input image are obtained. Four Orientation difference maps are obtained as absolute difference of corresponding pixels in orientation images.

$$Orientdiff(\theta_1) = \left| orient1(\theta_1) - orient2(\theta_1) \right| \qquad (6.10)$$

Similarly, orientation difference images for all four orientations are obtained.

Four orientation difference images, three texture difference images and an intensity difference image are obtained from input images, I_1 and I_2. PCA is employed to capture maximum information from the input features (discussed in section 3.3.2). PCA is applied on four orientation images and principal components with cumulative variance of greater than 80% is chosen to represent orientation difference. Similarly, PCA applied on three texture difference maps to obtain first principal components, required to represent more than 80% of variance in the input dataset to represent texture difference. Now, three difference images representing intensity difference, texture difference and orientation difference are obtained. Difficulty in combining these three difference images into a single distance map is that they represent non-comparable modalities with different dynamic ranges and extraction mechanisms. Initially, all the difference images are scaled to [0-1] range. After scaling, Normalization is applied and it includes the following steps: (1) Compute maximum of the difference image, 'g' (2) Find local maxima and average all local maxima, m_{ave} (3) Multiply the difference image by $(g-m_{ave})$. This normalization operator promotes map having lesser number of strong peaks. At the same time, it suppresses maps having large number of comparable peak responses (Itti et al., 1998).

After normalization, combined distance map is obtained as linear combination of all three difference images.

$$Dist(i,j) = orientdiff(i,j) + texturediff(i,j) + intensitydiff(i,j) \qquad (6.11)$$

Distance map by integrating intensity, texture and orientation difference features is obtained. Threshold of (mean $+n*$ standard deviation) as applied for image

differencing is used for obtaining change detection map. Since the input features are normalized to have zero mean and unity standard deviation, 'n' is taken as 0.7.

6.2.2.5 Comparison of four image analysis approaches

Image differencing is a very simple method of change detection. The difference image depends on both relative change between the intensity (back scattering coefficient) values in two images and also reference intensity. This leads to higher change detection error for changes occurred in high intensity regions of the image than in low intensity regions. This behavior is an undesired effect that renders difference operator not suitable to identify changes irrespective of average backscattering coefficient.

The minimum ratio detector shows two main advantages over difference image. The first one is that the ratio-image distribution depends only on relative change in the average intensity between two dates and not on reference intensity level. Thus changes are detected in the same manner in both low and high intensity regions. The second advantage is that ratioing allows reduction in common multiplicative error components (which are due to both multiplicative sensor calibration errors and the multiplicative effects of the interaction of the coherent signal with the terrain geometry) as far as these components are same for images acquired with same geometry.

Correlation coefficient is used as a distance measure for change detection. This technique helps in identifying de-correlation between two images that could be caused either by movement of scatterers within resolution cell due to external disturbances or by the change of scatterers in their nature and distribution between the two dates. Hence, temporal de-correlation provides information about the structural and dielectric properties of the surface.

Ratio analysis alone is not sufficient for change detection, and higher order statistics or multi-scale analysis may be helpful to map changes (Bujor et al., 2004; Inglada and Mercier, 2007) and this is fulfilled by fourth technique using intensity, texture and orientation difference maps. This technique computes change detection map by integrating changes obtained at pixel level, texture level and changes occurring along different orientations.

Comparison of the four techniques reveals that they complement each other in obtaining 'change' and 'no change' pixels. Image differencing helps in identification of all changes occurring in high intensity regions even though, it misses out in low intensity areas. Image ratioing removes multiplicative noise components and changes are detected irrespective of their average intensity level. Correlation coefficient helps in identifying decorrelation due to surface properties. Fourth method of integrating intensity, texture and orientation difference measures integrates intensity changes, texture changes at multi-scales and changes along orientations at $\theta = 0°, 45°, 90°, 135°$. So, all these four methods of image analysis techniques are employed to classify 'change' and 'no change' pixels.

6.2.3. Proposed approach to obtain reliable set of 'change' pixels
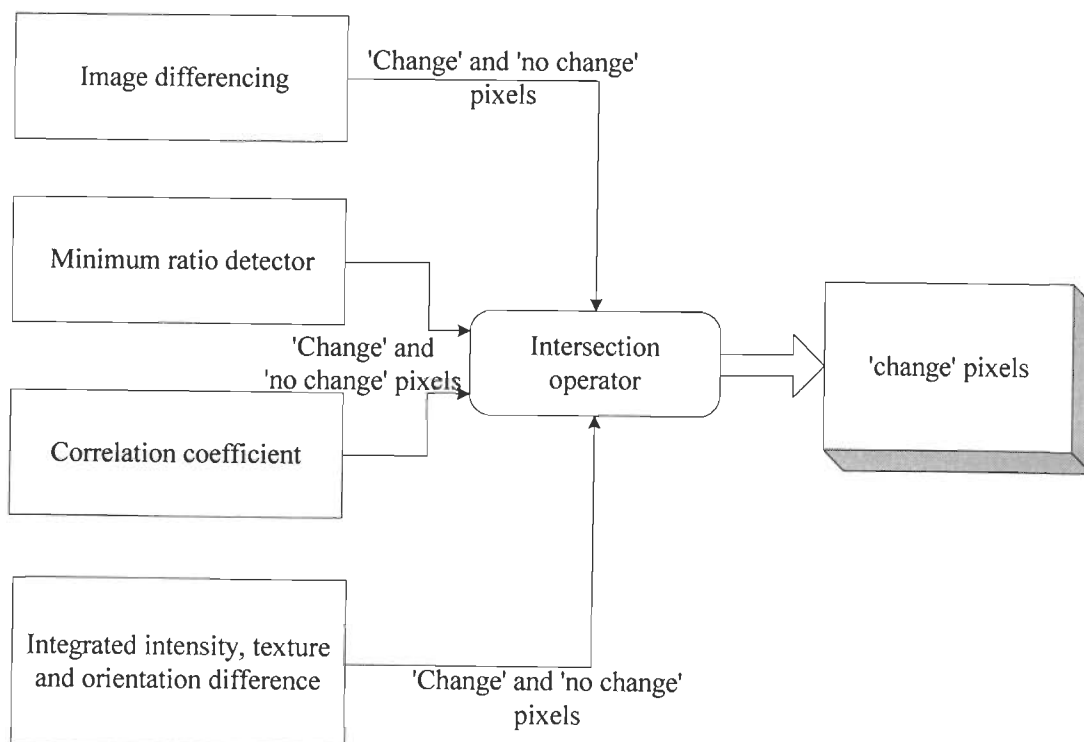
Figure 6.2. Proposed approach to obtain reliable set of 'change' pixels.

Each of the four image analysis approach of classifying 'change' and 'no change' pixels is different. Therefore, it is difficult to get the same set of 'change' and 'no change' pixels.

Image differencing computes difference of the two images pixel by pixel and hence this operator gives larger distance in higher intensity areas and less distance for lower intensity areas. A single threshold for both types of varying intensity levels may not be suitable to identify all 'change' and 'no change' pixels. Image ratioing removes common multiplicative noises introduced in the images. Correlation coefficient computes distance measured on the basis of decorrelation between the scatterers in the study region. Changes in the pixel level, texture variations and changes along different orientations are used for computing distance map using fourth method of integrated intensity, texture and orientation difference.

By analysis of each of the four methods on classifying 'change' and 'no change' pixels, it can be inferred that each technique generates change detection map by different approaches. To combine the results obtained by all the four methods and obtain reliable 'change' and 'no change' pixels, an intersection operator is used. Intersection operator uses a logical AND operator to identify common 'change' pixels as classified by four image analysis techniques used. This intersection operator confirms the reliability of 'change' pixels obtained by the proposed approach.

6.2.4. Implementation of proposed classifier for 'change' and 'no change' pixels on SAR image

For evaluating the proposed classifier, RADARSAT-1 data of New Orleans city, USA has been chosen. The list of RADARSAT-1 data chosen for analysis is listed in section 6.2.1. Two co-registered SAR images acquired at two different dates with approximately one year span (Sl.no.1 of Table 6.1), are chosen. The objective is to obtain a map representing the changes occurred in the region considered between the two dates of acquisitions.

Four image analysis techniques explained in section 6.2.2.1 to section 6.2.2.4, are implemented for the chosen image pair. Final set of 'change' pixels is obtained by intersection of all the 'change' pixels obtained by each of the image analysis technique. Change pixels obtained by each of the four methods are shown in Figure 6.3(a) to 6.3(d). Reliable set of 'change' and 'no change' areas identified by proposed approach is shown in Figure 6.4.
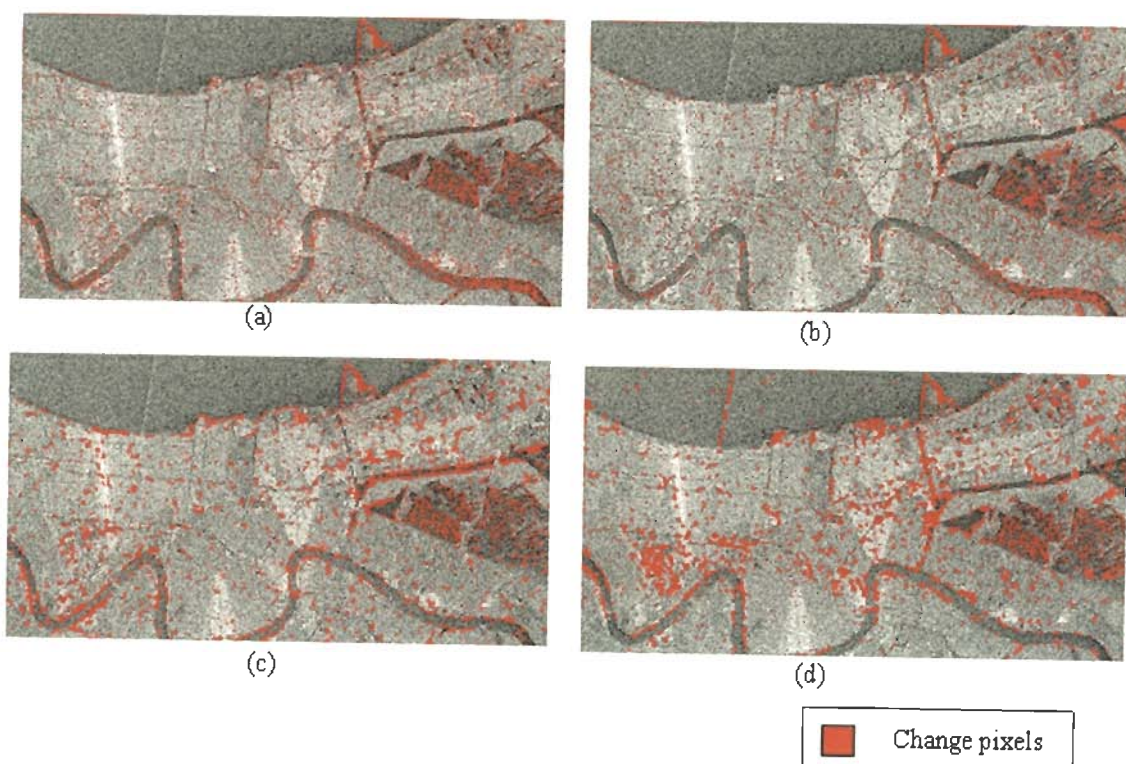
Figure 6.3. Change pixels obtained by four methods (a) Image differencing (b) Minimum ratio detector (c) Correlation coefficient, and (d) Integrated intensity, texture and orientation difference for the image pair sl.no.1 of Table 6.1.
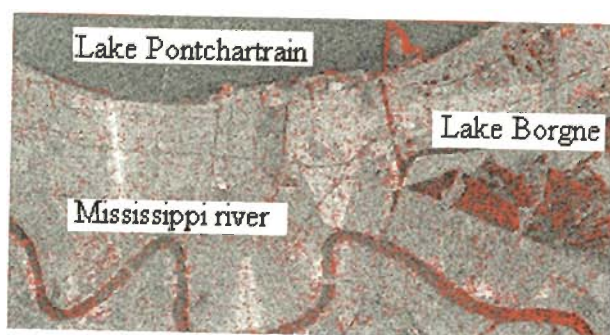
Figure 6.4. Classified 'change' pixels by proposed approach.
*'change' pixels are marked by 'red'.

In figure 6.4, Change pixels are marked by 'red'. The classification of 'change' and 'no change' pixels is obtained by intersection of all common 'change' pixels obtained by four image analysis approaches. From the change detection map obtained in Figure

6.4, it can be observed that changes have taken place in Lake Borgne area, banks of Mississippi river and borders of Lake Pontchartrain. Lake Borgne area is one of the areas identified to have undergone severe subsidence. Statistics of 'change' pixels obtained by each of the methods for image pair (Sl.no.1 of Table 6.1) is listed in Table 6.2.

Table 6.2. Statistics of 'change' pixels mapped for the year (2002-2003) by image analysis techniques.

Total number of pixels in the image = 1027 ×540 = 554580.

Sl.No.	Image analysis technique	Number of change pixels	Change pixels (%)
1	Image differencing	67840	12.23
2	Minimum ratio detector	72352	13.05
3	Correlation coefficient	108510	19.57
4	Integrated intensity, texture and orientation difference maps	126013	22.72
5	Proposed approach of applying intersection operator on classified change pixel map from all four methods	62450	11.26

Number of change pixels classified by each of the four image analysis technique and percentage of change pixels with respect to total number of pixels in the image considered are listed in Table 6.2. Image differencing detects less number of change pixels whereas integrated intensity, texture and orientation difference map has produced about 22.72% of change pixels. Since the fourth method (sl.no.4) is taking texture and orientation differences in addition to single pixel image differencing, this method detects more number of change pixels. Change pixels found by both image differencing and minimum ratio detector are almost similar (Table 6.3). This can be inferred by comparing change pixel map (Figure 6.3 a and b). Correlation coefficient has more common pixels obtained from integrated intensity, texture and orientation difference maps. Our observations confirm that these regions have undergone changes in the observed period (September 2002- November 2003).

Table 6.3. Comparison of 'change' pixels obtained by four methods.

Sl.No	Methods that are compared	D Equation.common 'change'+ 'no change' pixels)/Total number of pixels (%)
1	Image differencing and Minimum ratio detector	84.26
2	Image differencing and Correlation coefficient	73.32
3	Image differencing and Integrated intensity, texture and orientation difference maps	74.24
4	Minimum ratio detector and Correlation coefficient	85.64
5	Minimum ratio detector and Integrated intensity, texture and orientation difference maps	83.62
6	Correlation coefficient and Integrated intensity, texture and orientation difference maps	75.12

6.2.5 Classification of 'change' and 'no change' pixels for the study region from 2002-2005

Subsidence map for the New Orleans is obtained quantitatively using permanent scatterers with the help of interferometry and published (Dixon et al., 2006). The subset of the same study region taken for analysis in this chapter is shown in Figure 6.5. Change pixels identified for each image pair of table 6.1 by proposed approach are cumulatively shown in Figure 6.6.

Comparison of these two images show that maximum changes identified by yellow or orange in Figure 6.5 are identified as change pixels (marked by red) by proposed approach. More changes are detected near banks of River Missississippi and in Lake Borgne areas. These areas are identified as change areas by proposed method also.
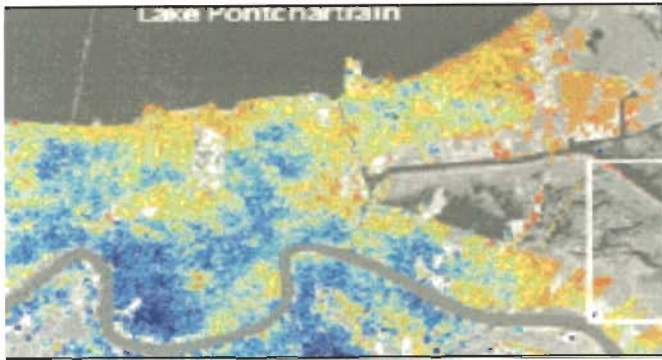
Figure 6.5. Subsidence map as published by Dixon et al., (2006) using permanent scatterer based interferometry (Blue shows low or no subsidence areas and red corresponds to high subsidence areas with colors blue, green, yellow, orange and red in increasing orders of subsidence).
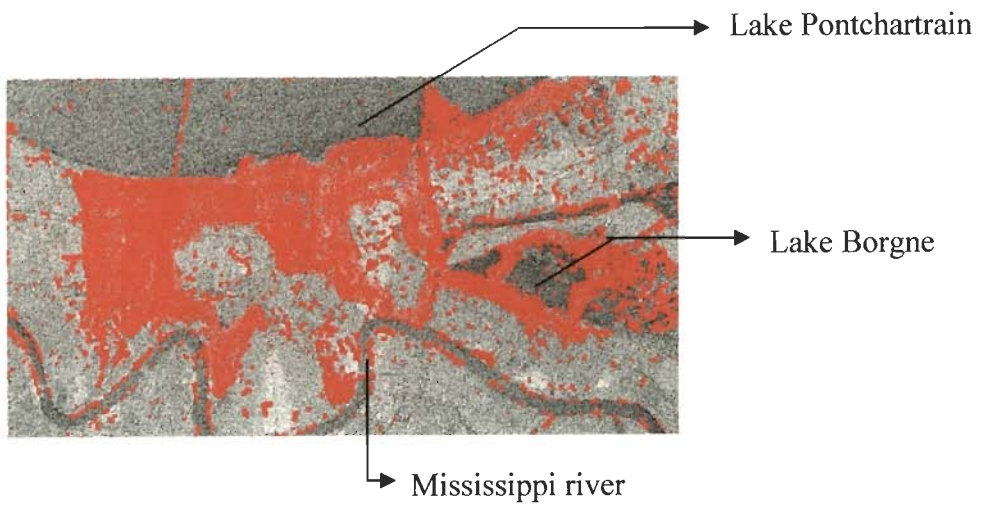
Figure 6.6. Cumulative change map obtained for the years 2002-2005 (image pairs listed in Table 6.1).

Change pixels are marked by red.

6.2.6. PDF model for 'change' and 'no change' pixels

Reliable set of 'change' and 'no change' pixels are obtained from four image analysis techniques using an intersection operator as depicted in Figure 6.2. This set of pixels is used for analysing distribution of pixels corresponding to each class. A suitable probability density function is selected on the basis of R^2 to fit the data corresponding to 'change' and 'no change' pixels. Probability distributions like gaussian, log-lognormal, logistic, normal and weibull distributions are tested with group of pixels representing 'change' and 'no change' pixels. Goodness of fit test is conducted using Chi-squared test. The chi squared statistic is given by

$$\chi^2 = \sum_{i=1}^{k} \frac{\left(O_i - E_i\right)^2}{E_i} \qquad (6.12)$$

where O_i is the observed frequency for bin i, E_i is the expected frequency for bin i as calculated by $E_i = F(x_2 - x_1)$, F is the cumulative probability distribution of the pdf being tested and x_1, x_2 are the limits for bin i. k is the total number of bins chosen in data.

The chi square test is used to determine if a sample comes from a population with specific distribution. This test is applied to binned data, so the value of test statistic depends on how the data is binned. The optimal choice of number of bins is chosen such that data is grouped into intervals of equal probability (Evans et al., 2001). Chi squared statistics is compared for data representing group of 'change' and 'no change' pixels for every image pair with all the above four mentioned distributions. Then, distribution which has lesser chi square error and matching both 'change' and 'no change' pixels in the image pairs (2002-2003 and 2003-2004) are chosen. Weibull distribution fits the distance measure corresponding to integrated intensity, texture and orientation distance with lower chi square statistic of 4.322 (Table 6.4).

From table 6.4, it is obvious that weibull 3P fits the data distribution of integrated intensity, texture and orientation difference, which is confirmed by chi square test giving lesser chi square. For other statistics like DN, intensity, intensity difference, correlation coefficient or minimum ratio does not fit any statistic discriminating 'change' and 'no change' pixels and their chi square statistic were well above 60.

Table 6.4. Chi squared test statistic for various distributions of change pixels of year (2002-2003) corresponding to distance measures of four image analysis approach.

Sl.No	Distribution	Chi squared test statistics			
		Image difference operator	Minimum ratio	Correlation coefficient	Integrated intensity, texture and orientation distance
1	Weibull- 3P	60.42	45.37	36.08	6.342
2	Weibull	68.76	36.12	42.24	35.632
3	Gaussian	38.27	48.76	60.46	28.34
4	Normal	26.42	20.93	72.38	18.93

The probability density function for weibull-3P distribution is given by

$$f(x) = \frac{\alpha}{\beta}\left(\frac{x-\gamma}{\beta}\right)^{\alpha-1} \exp\left(-\left(\frac{x-\gamma}{\beta}\right)^{\alpha}\right) \qquad (6.13)$$

where α - shape parameter, β - scale parameter and γ - location parameter of the distribution.

As the name implies, γ, location parameter determines the offset/ location at which distribution starts. α, shape parameter is also known as weibull slope. Value of α is equal to slope of the line in probability plot. When $\alpha =1$, then it becomes two parameter weibull plot. β, the scale parameter has the same effect on distribution as change in abscissa scale. Figure 6.7(a)- (c) shows the frequency counts of integrated intensity, texture and orientation distance for image pairs 2002-03, 2003-04 and 2004-05. Consider figure 6.7(a), α shape parameter is with narrow difference for change and no change pixels with values 2.902 and 2.426.

If β, scale parameter is increased when α and γ are constant, its height reduces and plot is stretched to the right. Hence, plot corresponding to change pixel is in the right to that of no change pixels (Xiao et al., 2006). In figure 6.7(b), even though β has

increased from 'no change' to 'change' pixels, peak value has decreased. The plot has stretched more to the right along with the constraint that area under the pdf curve has to be constant at one. On the x-axis, it can be seen that in fig 6.7(b) alone, plot is stretched to distance measure >35, whereas in figure 6.7(a) and 6.7(c), plot is limited to 35 and 25 respectively. This explains why peak of change pixels distribution has reduced compared to no change pixels in fig 6.7(b) alone. The parameters obtained for 2002-2003 in Table 6.5 shows the mean of parameters obtained for pixels of size varying from 5×5 to 10×10 and approximately 40 groups of pixels were used. For γ <4.5 and β <8.5, the distribution represents the set of 'no change' pixels and otherwise, they represent the set of 'no change' pixels. γ, location parameter plays an important role in discriminating change pixels. γ decides the offset/ location at which distribution starts. For 'no change' pixels, distribution is towards the origin and <4.5. For change pixels, γ is away from the origin (>4.5).

From the analysis of probability distribution of distance map obtained by integrated intensity, texture and orientation difference map belonging to 'change' and 'no change' pixels, the range of parameters of weibull-3P distribution is set by analyzing more than 40 groups of pixels belonging to 'change' and 'no change' areas. Then, for the next year, say for example, 2003-2004, Data ID 20 and 26 are chosen for validation. For the image pair, integrated intensity, texture and orientation difference measure is computed. The whole difference image is divided into groups of pixels of size 5 × 5. For each of the group of pixels, weibull distribution parameters are computed. From the range of weibull parameters, the group of pixels is labeled as 'change' or 'no change' areas. Similarly, this analysis is validated by checking with succeeding years of 2004-05 as shown in table 6.6.

Table 6.5. Parameters for weibull 3P distribution fitting 'change' and 'no change' pixel statistics.

Temporal span	Change pixels			No change pixels		
	α	β	γ	α	β	γ
2002-'03	2.902	15.563	4.562	2.426	8.371	3.911
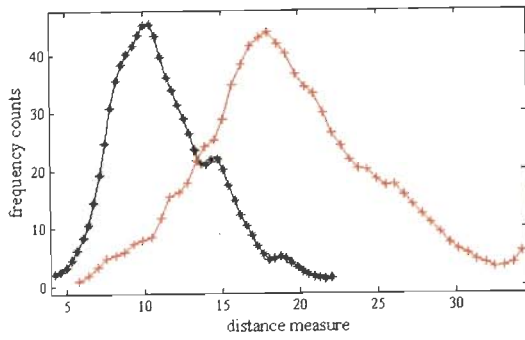
Figure 6.7(a)
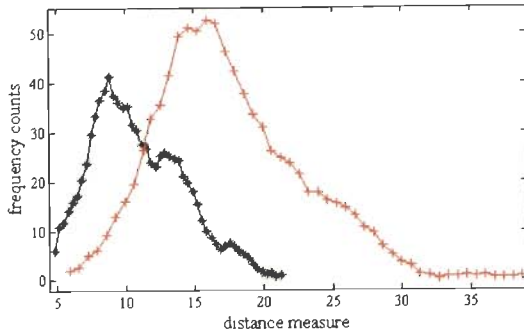
Figure 6.7(b)
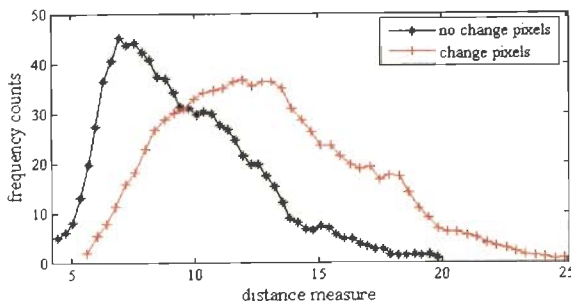
Figure 6.7(c)

Figure 6.7. Probability distribution curve for 'change' and 'no change' pixels for the periods.

(a) 2002-2003 (b) 2003-2004 and (c) 2004-2005.

Legends mentioned in 6.5(c) is applicable for both figures 6.5(a) and 6.5(b).

Table 6.6. Validation of 'change' and 'no change' pixel distribution.

Temporal span	Change pixels			No change pixels		
	α	β	γ	α	β	γ
2003-'04	2.460	13.864	5.237	2.054	7.356	4.351
2004-'05	2.155	8.644	5.314	1.921	5.977	4.247

133

It is observed from the Table 6.6 that the proposed pdf approach for 'change' and 'no change' pixels are giving quite satisfactory results for succeeding years. It can be inferred that 'change' and 'no change' pixels can be distinguished from pdf analysis of distance measure corresponding to integrated intensity, texture and orientation difference method calculated for group of pixels (of size '5×5'). With the help of weibull- 3P parameters for distance measures belonging to 'change' and 'no change' pixels, these pixels can be labeled.

6.3. Interferometric approach for quantitative analysis of changes

New Orleans city of USA has long been recognized by the scientists that it is undergoing subsidence and is therefore susceptible for catastrophic flooding (Dixon et al., 2006). New Orleans has undergone rapid subsidence before Hurricane Katrina has struck this city in August 2005 (Amelung et al., 2006). In this section of the chapter, quantitative analysis of changes in New Orleans city, has been carried out by differential interferometry is presented. From this analysis, pixels are grouped according to their nature of subsidence like low, medium and high levels of subsidence. By studying and critically analyzing the properties of pixels belonging to various areas like low, medium or high subsidence areas, an approach to label pixels according to their levels of subsidence by simple image analysis approach of minimum ratio detector is proposed.

6.3.1 Principle of measuring subsidence by DInSAR

The principle of SAR interferometry is that the phase of received backscattered signal is used to measure path length differences with accuracy of mm range. The path length differences can be related to terrain height and deformations of the earth's surface. SAR interferometry uses two complex images to derive required information by exploiting phase of the signals. One imaging parameter has to be different for second image compared to first one. The imaging parameter by which acquisition of second image varies determines type of interferometry. When two images are acquired by the same antenna in repeated passes over the same area at different times, repeat pass interferometry is implemented. This is an ideal situation for measurement of deformation on earth's surface between the two acquisition times. It is extremely

sensitive to small changes in elevation occurring in the time interval between passes, hence, allowing precise and rapid determination of relative displacement (Bamler and Hartl, 1998).
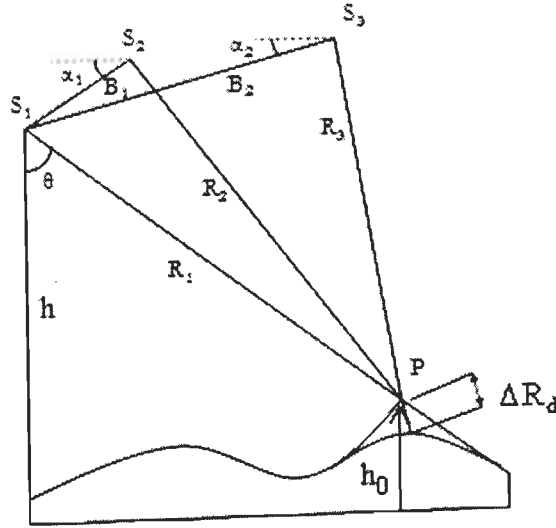
Figure 6.8. Principle of differential interferometry.

In Figure 6.8, S_1, S_2, and S_3 are position of antennas. Position of point P before and after displacement of ΔR_d is considered for analysis. First image acquisition of P is captured by antennas, S_1 and S_2, which are separated by baseline B_1. Second image acquisition, after P has assumed to undergone a displacement of ΔR_d is acquired using S_1 and S_3 separated by baseline B_2. θ is the look angle and R_1, R_2 and R_3 are range distances of antenna S_1, S_2, and S_3. The height of antenna S_1 is denoted as 'h' and height of the point 'P' is denoted as 'h_0'. In the first image acquired before displacement has occurred, the received signal forming a point P_1 in the scene is given by

$$s_1(R_1) = |s_1(R_1)| \exp\left(\frac{4\pi}{\lambda} R_1\right) \tag{6.14}$$

In the second image, acquired after the change or displacement of scatterer has occurred, the corresponding received signal forming the point P (Bamler and Hartl, 1998) is

$$s_2(R_2) = |s_2(R_2)| \exp\left(\frac{4\pi}{\lambda}(R_2 + \Delta R_d)\right) \tag{6.15}$$

135

Due to time delay between acquisitions, interferometric phase of interferogram, formed using two images, contains the following terms:

$$\phi = \phi_{topo} + \Delta\phi_{\Delta R_d} \qquad (6.16)$$

ϕ_{topo} is the topography induced phase, and $\Delta\phi_{\Delta R_d}$ accounts for possible displacement of scatterer between observations. It is assumed that there is negligible effect due to atmosphere as well as scattering behavior of scatterrer (Fruneau and Sarti, 2000).

Any movement of a scatterer between the observations with a component of ΔR_d (change in range) into the line-of-sight direction gives rise to an interferometric phase of

$$\Delta\phi_{\Delta R_d} = \frac{4\pi}{\lambda}\Delta R_d \qquad (6.17)$$

Since the wavelength is in the order of centimeters, D-InSAR can measure displacements down to millimetre accuracy. All the phase terms in equation (6.16) correspond to D-InSAR measurements. To measure the displacement using interferometric phase of equation (6.16), the topography induced phase term is to be removed. One method is to use purely interferometric approach to remove topography using third SAR image of the scene.

This third image is to be acquired such that it is assumed that minimum or no change has occurred in scatterers with respect to the first acquired image. Hence, third image has to be acquired very closely in time with first image. Third image acquired is used for identifying and removing phase induced by topography.

In the third image acquired, the received signal from point P is

$$s_3(R_3) = |s_3(R_3)| \exp\left(\frac{4\pi}{\lambda}R_3\right) \qquad (6.18)$$

The interferometric phase of the interferogram, formed between first and third image, contain only the original topography (Bamler and Hartl, 1998).

$$\phi_2 \approx \frac{4\pi}{\lambda} B_{2\parallel} = \frac{4\pi}{\lambda} B_2 \sin\left(\theta_2 - \alpha_2\right) \tag{6.19}$$

Using the cosine law, ΔR (=(R_3-R_2)) may be expressed in terms of imaging parameters as

$$R_3 = (R_1 + \Delta R) = R_1^2 + B_2^2 - 2R_1 B_2 \cos\left(\pi/2 - \theta_0 + \alpha\right)$$
$$\sin(\theta_0 - \alpha) = \frac{(R_1 + \Delta R)^2 - R_1^2 - B_2^2}{2R_1 B_2} \tag{6.20}$$

The height 'h' of the point 'P' is given by

$$h = h_0 - R_1 \cos\theta_0 \tag{6.21}$$

The differential interferogram and hence displacement of scatterer can be obtained by following steps:

1. Phase of the interferogram (I) obtained using first and second image contains phase due to topography and phase due to displacement of scatterers.

2. Then, phase of the interferogram (II) obtained by first and third image contains phase due to topography alone.

3. Differential interferogram is obtained by subtracting phase of interferogram II from phase of interferogram I (Figure 6.10)

4. Now, differential interferogram contain phase term caused only by the line of sight component of displacement ΔR_d.

6.3.2 Selection of InSAR image pairs

Selection of suitable InSAR image pairs is very crucial for obtaining interferogram. Special considerations are to be taken while choosing the image pairs. Considering the orbital geometry, a satellite orbit may exhibit a small degree of drift such that satellite does not return to exact same location on subsequent orbit repeats. The separating distance is called baseline. This baseline between passes provides the different viewing angles required for getting interferogram. But if baselines are too large, the accuracy of DInSAR will decrease since the removal of the topographic phase term cannot be performed very accurately.

```
┌──────────────────────┐
│  InSAR image pair    │
└──────────┬───────────┘
           │
┌──────────▼───────────┐
│ Compute baseline from│
│     Orbital data     │
└──────────┬───────────┘
           │
       ◇ BL <200m ◇
           │
┌──────────▼───────────┐
│  Compute  overall    │
│   image coherence    │
└──────────┬───────────┘
           │
     ◇  Over all       ◇
       coherence>0.65
           │
┌──────────▼───────────┐
│ Compute Interferogram│
└──────────────────────┘
```
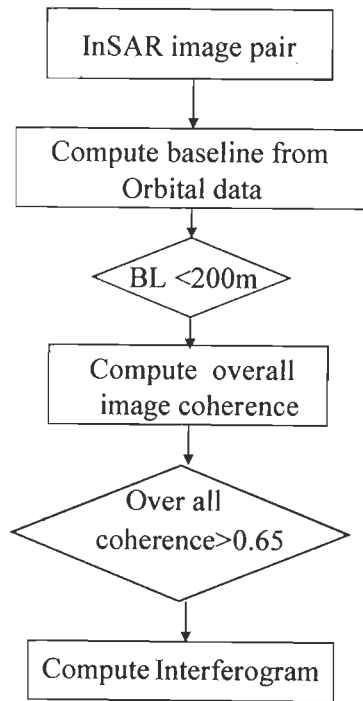
Figure 6.9. Selection of suitable InSAR image pairs.

Care should be taken that baselines between image pairs (< 1km for RADARSAT fine beam data, and in this work, image pairs with baseline distance less than 200m are chosen) are not too large. Spatial overlap (>50%) and azimuth spectra overlap (>90%) also have to be considered. Coherence is computed for the complete image involved in InSAR image pair and if the overall coherence is greater than 0.65, the image pair is suitable for generating interferogram. These conditions stated are to be satisfied to generate a reliable interferogram. This is depicted in Figure.6.9.

6.3.3. Quantitative analysis of change using DInSAR

Image pairs with approximately one year of temporal span are chosen so that any deformation occurred on the surface within this period can be mapped. As given in equation (6.16), the interferometric phase between this image pair includes phase due to topography and phase due to surface change. Phase due to topography is derived using another interferometric pair with minimum time interval (in RADARSAT-1, 24 day interval) between them assuming no changes in surface has taken place in this

138

interval. Interferometric phase with 24 day interval represents due to elevation alone is subtracted from interferometric phase with 1 year interval to get phase due to surface change alone (Figure 6.10).
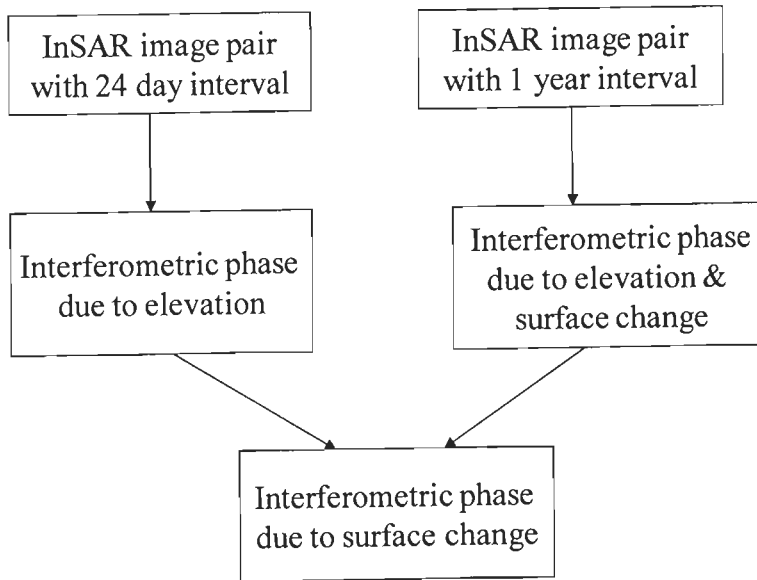
Figure 6.10. Quantitative analysis of changes using DInSAR.

For example, to measure changes on earth's surface from 2002 to 2003, images of Data ID: 6,7, and 20 are chosen (Appendix A). Here, image of Data ID: 6 is taken as master image. Interferogram obtained by image pair of Data ID: 6 and 20 contains interferometric phase of topography and phase due to displacement. Topographic phase can be determined from interferogram obtained with 24 day interval using images of data id: 6 and 7 are used and is subtracted to get phase due to displacement.

Using equation (6.17), displacement can be obtained as

$$\Delta R_d = \phi_d \frac{\lambda}{4\pi} \tag{6.22}$$

Thus, actual displacement in range of *mm* can be obtained by differential interferometry.

6.3.4. Implementation and results obtained by DInSAR

6.3.4.1 Data used

Details of the study area and satellite data used for the analysis by DInSAR is discussed in section 1.4 and 1.5. Eighty four SLC datasets (Appendix A) acquired from Canadian Space Agency (CSA) are analyzed to find some suitable InSAR (Interferometric SAR) image pairs and that is used for the quantitative analysis of changes (i.e., subsidence) occurred in the study region.

InSAR image pairs should be chosen such that they have a common master image and two slave image such that one slave image has 24 day interval and other slave image has approximately one year are chosen. Slave images with more than one year temporal gap are not considered for measuring subsidence since temporal decorrelation may become high affecting the accuracy of measurement. Criteria for selection of InSAR image pairs, explained in section 6.3.2 should be satisfied by both InSAR image pairs considered for analysis. By rigorous analysis of all possible image pairs from available dataset (Appendix A), some image pairs are chosen. Table 6.1 (Section 6.2) gives the details of the DInSAR image pairs chosen for measuring surface change and topography (same set of image pairs as was used for the classification of 'change' and 'no change' pixels by image analysis approach, so that results can be compared). Table 6.7 lists the InSAR image pairs chosen with minimum interval of 24 day for measuring phase due to topography.

Table 6.7 InSAR image pairs for generating DEM. (for every year DinSAR image pair of Table 6.1).

| Sl.No | Year | InSAR image pair (for measuring elevation) | | | | Beam mode/product type |
| | | Master image | | Slave image | | |
		Data ID	Acquisition date (yyyy-mm-dd)	Data ID	Acquisition date (yyyy-mm-dd)	
1	2002	6	2002-08-13	7	2002-09-06	S2/SLC
2	2003	20	2003-11-12	19	2003-10-19	S2/SLC
3	2004	26	2004-04-04	25	2004-03-11	S2/SLC
4	2005	36	2005-03-01	38	2005-03-25	F5/SLC
5	2005	52	2005-11-01	54	2005-11-25	S2/SLC
6	2006	68	2006-09-04	70	2006-09-28	F5/SLC

6.3.4.2 Computing height from InSAR image pairs

First, InSAR image pair with 24-day interval is considered for measuring topography. For example, image pairs with master image of Data ID 6 and slave image of Data ID 7 are taken. These following steps of analysis are carried out using Sarscape 3.0.

1. Geocoded master and slave image are taken as input and by analyzing geographical co-ordinates of both images, subset of both master and slave images with overlapping regions are chosen.

2. Coregistration of both subset master and slave images is carried out to validate the InSAR image pair for spatial and spectral overlap. Spatial overlap in the ground range projected coordinates of slave on master image should have a minimum of 30%. Range spectral overlap is to be checked and it should not be less than 50% to have acceptable baseline decorrelation.

3. Interferogram is generated from the master image, and the conjugate of the slave image.

4. Enhancing interferogram has two main functions:

   (i)   Calculation of phase coherence map

   (ii)   Enhancement of interferometric phase in preparation for phase unwrapping

   Interferometric coherence is defined as the absolute value of the normalized complex cross-correlation between the images I_1 and I_2 and is measured by

$$\gamma = \frac{\left| \langle I_1 I_2^* \rangle \right|}{\sqrt{\langle I_1 I_1^* \rangle \langle I_2 I_2^* \rangle}} \tag{6.23}$$

   where I_1 and I_2 are image pairs used for generating interferogram

Phase slope estimation (from interferogram) can be done only in areas with good coherence. If temporal decorrelation has occurred between the two passes in an InSAR pair, then the slope estimates may become quite noisy. Hence, coherence is calculated for window of 100 pixels and if coherence is greater than 0.3, only then, those areas are selected for computing phase, and

141

thereby, for determining height. Otherwise, areas with low coherence are masked and height is not estimated in these areas.

5. The observed phase of each SAR antenna is restricted to the interval $[-\pi, \pi)$ and hence interferometric phase is also wrapped to the interval $[-\pi, \pi)$ (Eineder and Adam, 2005). Phase unwrapping is performed on the phase of the interferogram. For computing height from phase, actual phase has to be computed. This process is called phase unwrapping. Fast weighted least squares approach is adopted for phase unwrapping (Lovergine et al., 1999).

6. From the obtained phase, elevation/ height of the terrain can be computed using equation (6.21).

This procedure is depicted in Figure 6.11.

6.3.4.3 For obtaining height due to surface change and topography.

Steps 1 to 5 is carried out for an image pair of approximately one year apart (For ex, Sl.no.1 of Table 6.1) and phase due to surface change and topography is obtained. By subtracting phase due to topography obtained by first InSAR run, phase due to surface change alone can be obtained and hence height due to surface change can be computed.

Images of Data ID 6 and 7 are chosen for measuring topography. Master and slave images are shown in Figure 6.12 and Figure 6.13. Subsets of the master and slave images with overlapping regions are chosen. Condition for spatial overlapping that common overlapping region of master and slave regions should be a minimum of 50% of master image. For this chosen image pair, overlapping regions are more than 90%. Slave image is co-registered with master image and interferogram is generated (Figure 6.14). Interferogram shows noisy regions in lake areas due to wavy nature of water bodies. Enhanced interferogram is determined after computing interferometric coherence. Coherence map is given by Figure 6.15. Phase unwrapping is performed to obtain absolute phase corresponding to height (Figure 6.16). The regions with less coherence (less than 0.3) are masked and these regions are not considered for computing height.

```
           Master image        Slave image
                │                    │
                ▼                    ▼
        ┌────────────────────────────────┐
        │   Subset of master and slave   │
        │   images with overlapping      │
        │            regions             │
        └────────────────────────────────┘
                        │
                        ▼
        ┌────────────────────────────────┐
        │         Co-registration        │
        └────────────────────────────────┘
                        │
                        ▼
        ┌────────────────────────────────┐
        │         Generation of          │
        │         Interferogram          │
        └────────────────────────────────┘
                        │
                        ▼
        ┌────────────────────────────────┐
        │          Enhancing             │
        │         Interferogram          │
        └────────────────────────────────┘
                        │
                        ▼
        ┌────────────────────────────────┐
        │       Phase unwrapping         │
        └────────────────────────────────┘
                        │
                        ▼
        ┌────────────────────────────────┐
        │    Phase to height conversion  │
        └────────────────────────────────┘
                        │
                        ▼
                  Elevation map
```
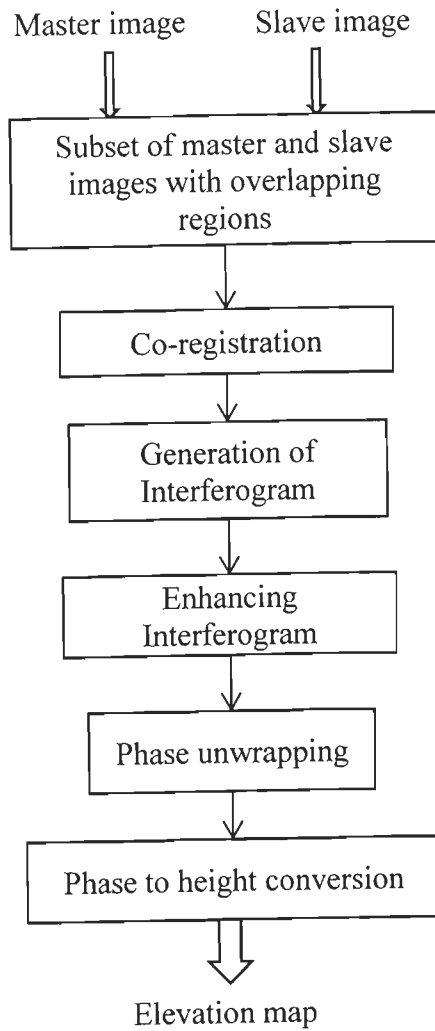
Figure 6.11. Procedure to obtain elevation map of the study region using interferometry.
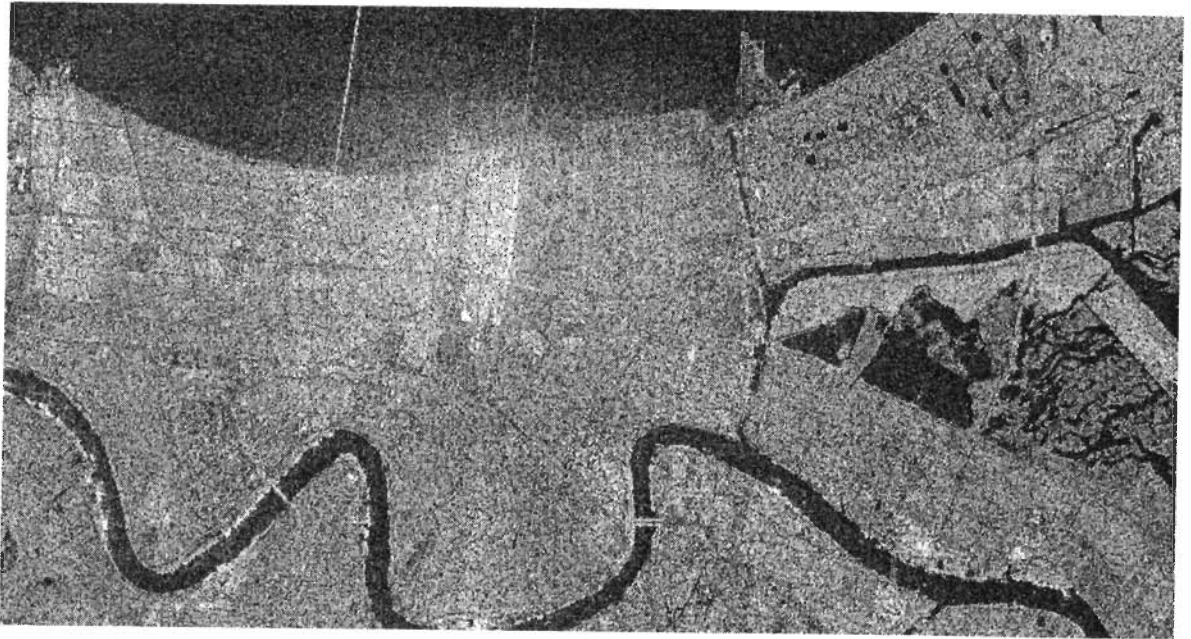
Figure 6.12. Georeferenced master image of Data ID: 6 (Sl.no.1,Table 6.7).
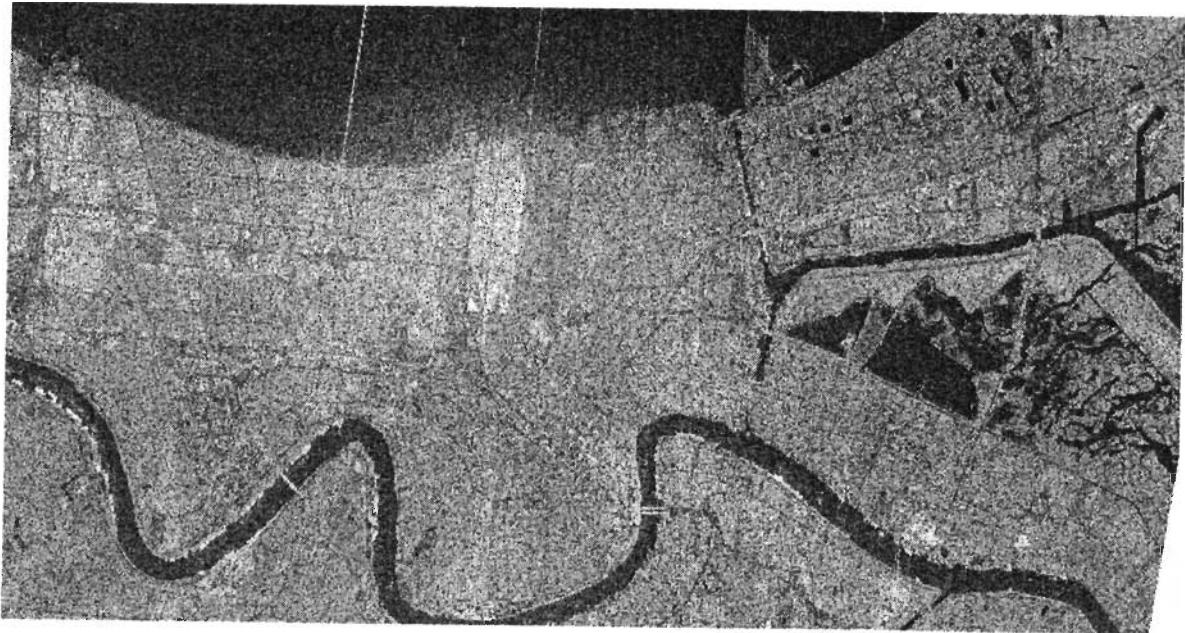
Figure 6.13. Georeferenced Slave image of Data ID:7(Sl.no.1, Table 6.7).
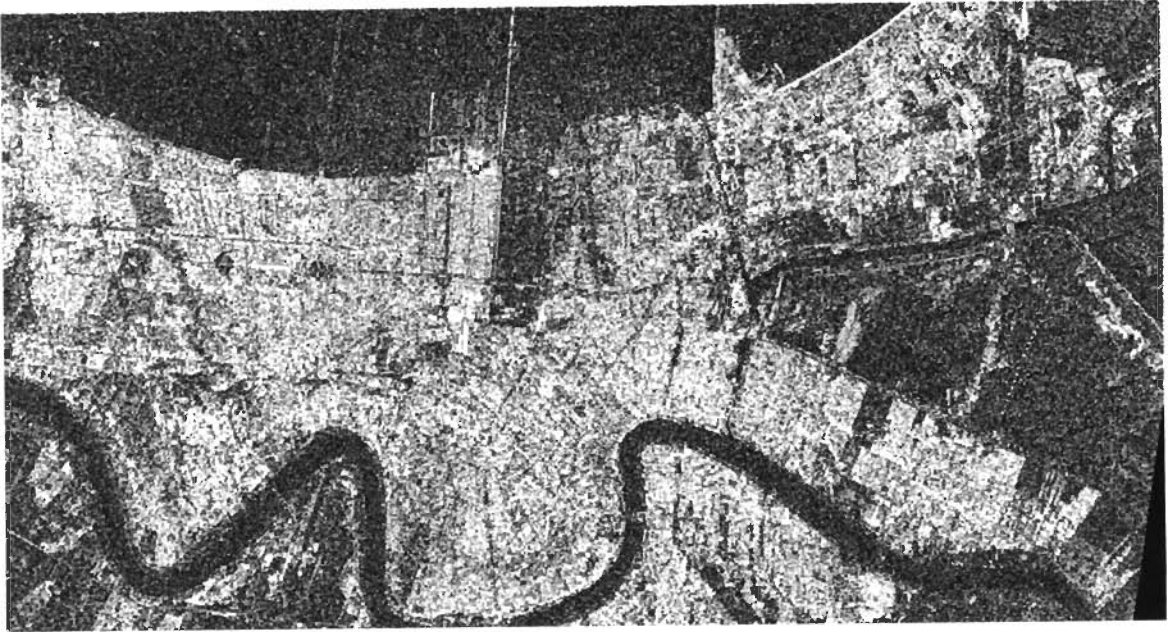
Figure 6.14. Coherence map.
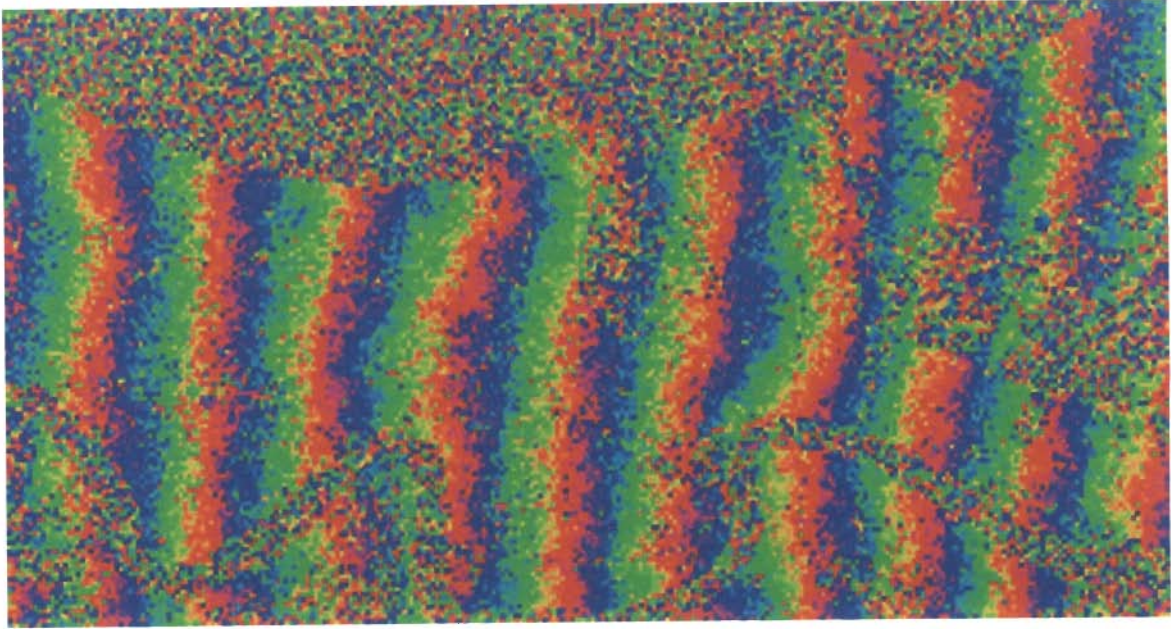
Figure 6.15. Interferogram using master image (Figure 6.12) and slave image (Figure 6.13).
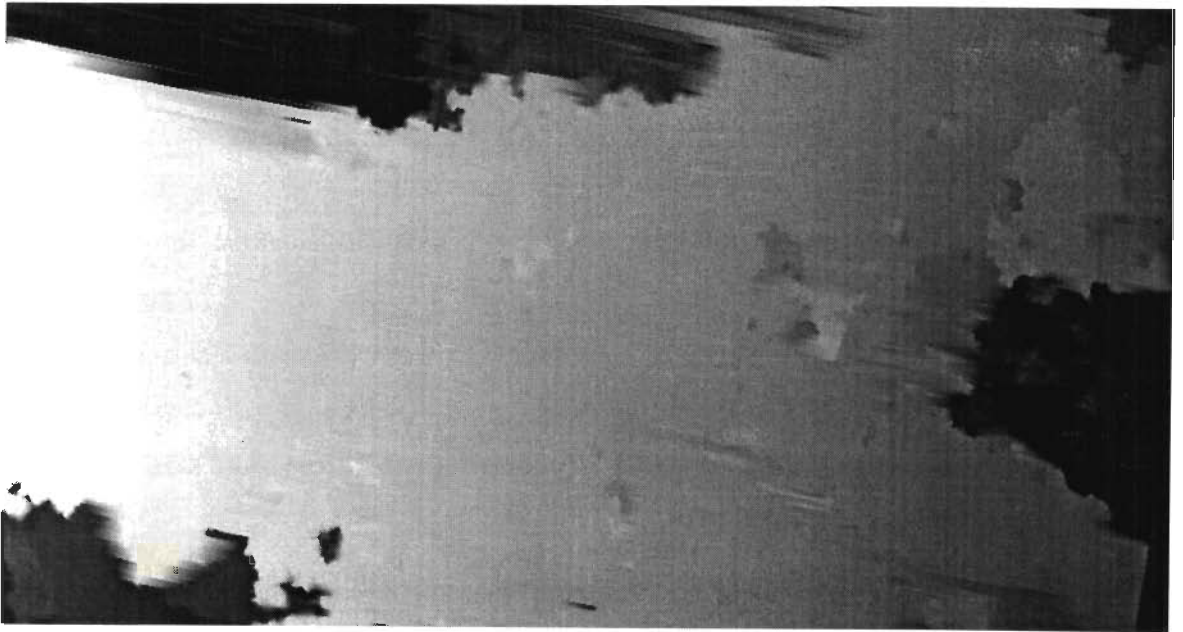
Figure 6.16. Unwrapped phase (Phase due to elevation).

Similar steps of obtaining phase are followed for image pairs with approximately one year temporal span. Then, phase due to elevation obtained by first InSAR image analysis is subtracted from the phase obtained by second InSAR image pair. Then, surface change in terms of height is computed from the subtracted phase. This process is carried out for all image pairs listed in Table 6.1. Results are shown in Figure 6.17 and Figure 6.18.

Figure 6.17 (a) and (b) shows subsidence on study site from (i) 2002 to 2003 and (ii) 2003 to 2004, respectively. Subsidence measured from 2003 to 2004 observes a dispersed subsidence and is more compared to year 2002 to 2003. It can also be seen that areas near Lake Borgne has suffered more subsidence in the order of -16 mm. Subsidence is also observed near banks of Mississippi river. Figure 6.18 (a) shows the subsidence as measured between 2003 and 2004. Subsidence is spread over large areas during the period when Hurricane Katrina has attacked in august 2005. In the figure 6.18 (b), subsidence measured for the period March 01, 2005 & Nov. 20, 2005 and subsidence measured from Nov. 11, 2005 and Feb. 5, 2006 are summed and the displacements shown are sum of changes observed by individual differential interferograms. Then, displacements computed by both the interferograms are added and is shown as superimposed on SAR image. From the Figure 6.18 (b), it is obvious that changes have been observed in many places. The deformation mapped here

corresponds to the range change distance and negative sign indicates "away from the sensor". Time period between the two acquisitions is nine months and a maximum of -14 mm displacement, marked by red, is observed. Subsidence map (2002-2005) was published (Dixon et al., 2006) for the same region of New Orleans city (Figure 6.19). This map presents cumulative change due to surface displacement for three years from 2002-2005. In this map, blue corresponds to low or no subsidence levels. Variation of color from blue to red corresponds to higher levels of subsidence. Our results confirms with that of the earlier published subsidence map. Some difference is there in change pixels from our results because Dixon et al (2006) has considered cumulative change of 3 years span.
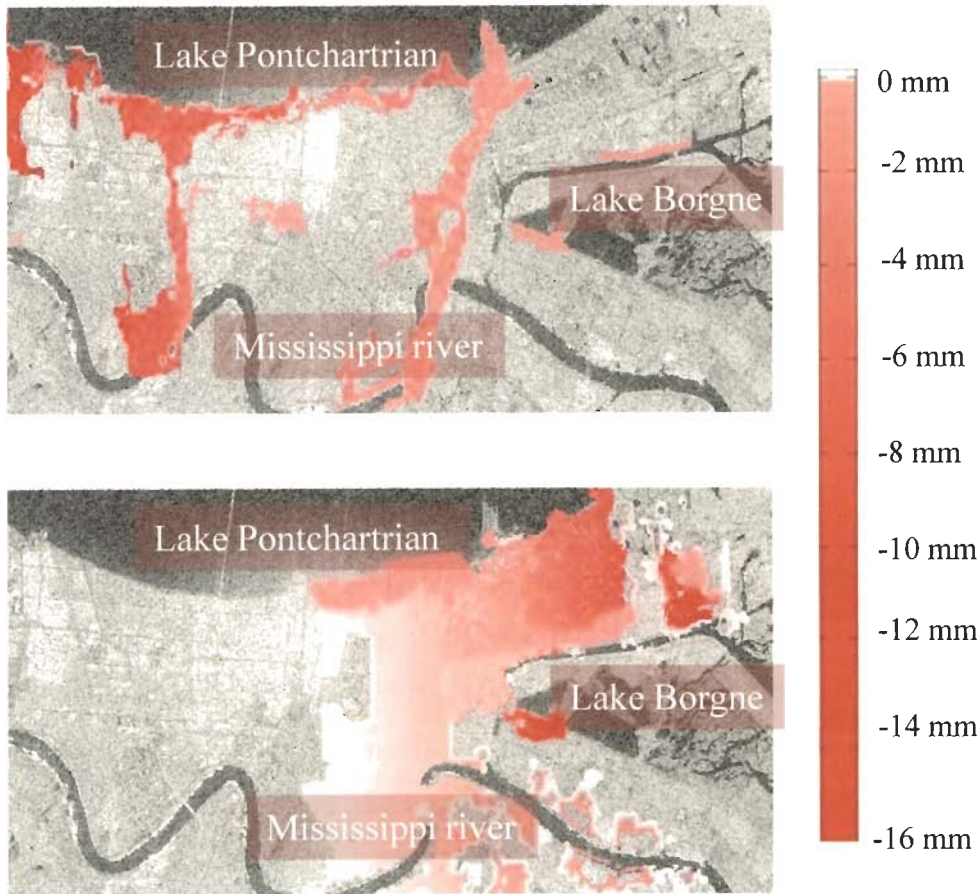
Figure 6.17. (a) and (b) correspond to subsidence obtained for (a) 2002 to 2003 and (ii) 2003 to 2004 using image pairs of :(i) Data ID: 6 and 20 (ii) Data ID: 20 and 26.

Figure 6.18 (a)

Figure 6.18 (b)

Figure 6.18 (c)

■ (-14 to -12)mm	■ (-12 to -10)mm	■ (-10 to -8)mm
■ (-8 to -6)mm	■ (-6 to -4)mm	■ (-4 to -2)mm	■ (-2 to 0)mm
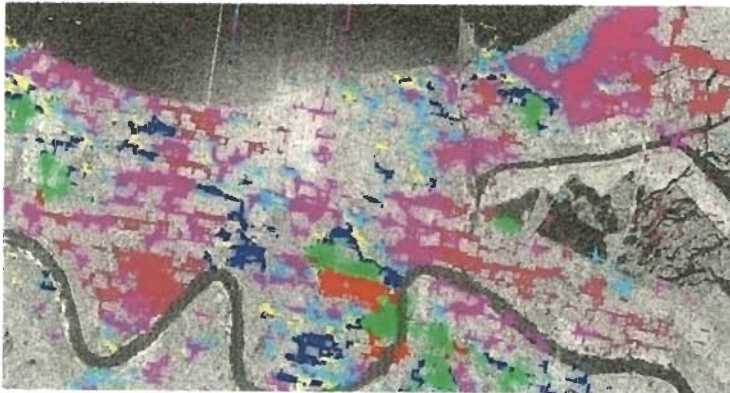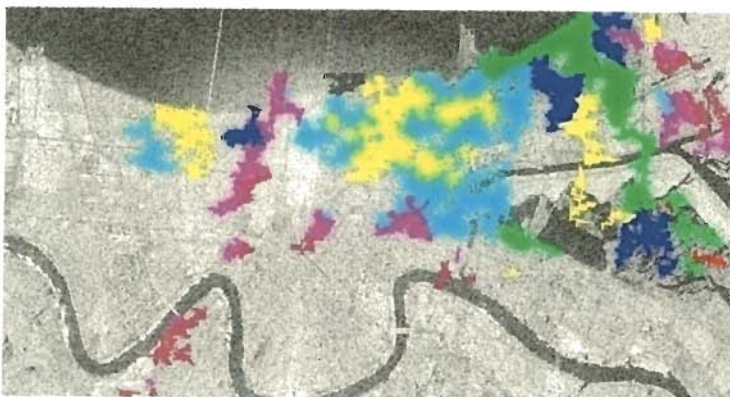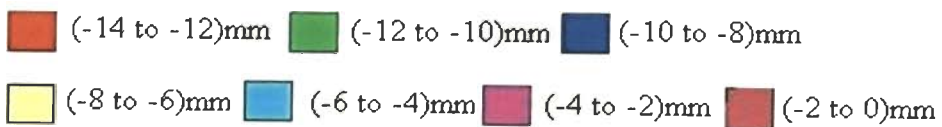
Figure 6.18 (a), (b) and (c) corresponds to subsidence obtained from 2004 to 2007.

(a) Data ID 26 and 37 (2004-2005),

(b) Cumulative changes measured by image pairs of: Data ID: 36 & 53 and Data ID: 52,59, (2005-2006) and

(c) Data ID 68 and 84 (2006-2007).
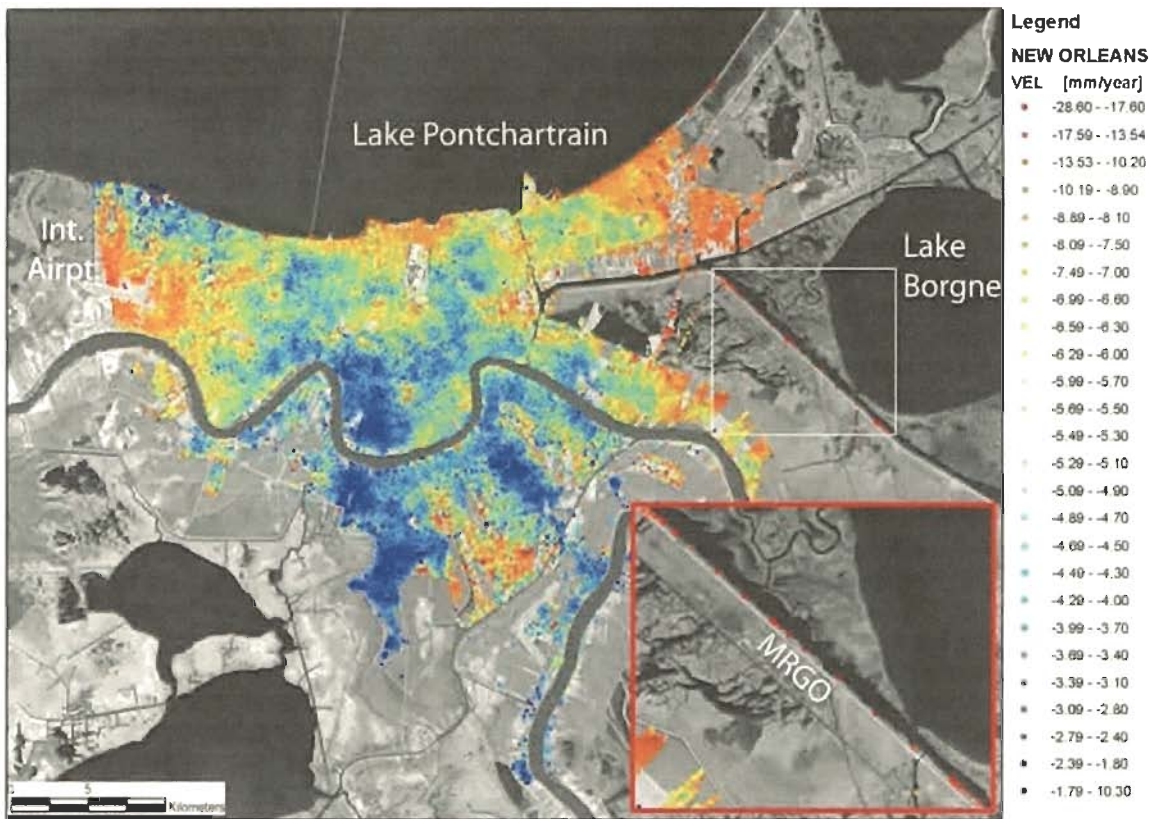
Figure 6.19. Subsidence map (2002-2005) obtained using permanent scatterers (Dixon et al., 2006)

Blue to Red corresponds to increasing levels of subsidence.

6.3.5. PDF analysis for categorizing subsidence levels

For performing probability distribution analysis, areas identified to undergo subsidence in the study site is grouped to three types of subsidence as low, medium and high subsidence areas according to quantitative values of subsidence obtained by DInSAR. Low subsidence areas correspond to areas with subsidence (-4 to 0) mm. Medium and high subsidence label corresponds to areas with subsidence ranges as (-10 to -4) and (-4mm or higher to -10mm). For subsidence areas labeled like this, pdf of image ratios of corresponding image pairs are plotted in Figure 6.20 (similar to the analysis carried out in section 6.2.6). The probability distribution curve of all three types of subsidence shown in Figure 6.20 follows the same pattern with pdf curve corresponding to low subsidence to right and medium subsidence to left and high subsidence curve hovers around the centre between the other two curves. As is

observed from the graph (Figure 6.20), low subsidence pdf centers around 1. This can be explained by the fact that low subsidence corresponds to areas with very less changes in back scattering coefficient and hence image ratio is around 1. For high subsidence areas, one of the values in image ratio is very high and if this higher value is in denominator for ratioing, then image ratio corresponds to values nearer zero, hence pdf corresponding to high subsidence areas are centered on zero. Then, medium subsidence areas may occur either to the extreme left or right but they are away from ratio value of 0 or 1. Image ratios of corresponding pixels that belong to low, medium and high subsidence areas are computed. Then, obtained pdf is fitted with common frequency distributions like exponential, gaussian, log normal, inverse gamma and weibull distributions and suitable frequency distribution is chosen with the help of R^2 values. This R^2 values measures how successful the fit is in explaining the variation of the data. Put another way, R-square is the square of the correlation between the response values and the predicted response values. It is also called the square of the multiple correlation coefficient and the coefficient of multiple determination. R-square can take on any value between 0 and 1, with a value closer to 1 indicating a better fit. For example, an R^2 value of 0.94 means that the fit explains 94% of the total variation in the data about the average. It is observed from analysis of distribution of image ratio pixels, gaussian distribution fits the probability distribution of image ratio of varying subsidence areas.

Probability distribution of image ratios correspond to gaussian distribution of equation (6.24) because it has maximum R^2 value than other pdf and the parameters are listed in table 6.5.

$$f(x) = a_1 \exp\left(-\left(\left(x - b_1\right)/c_1\right)^2\right) \qquad (6.24)$$
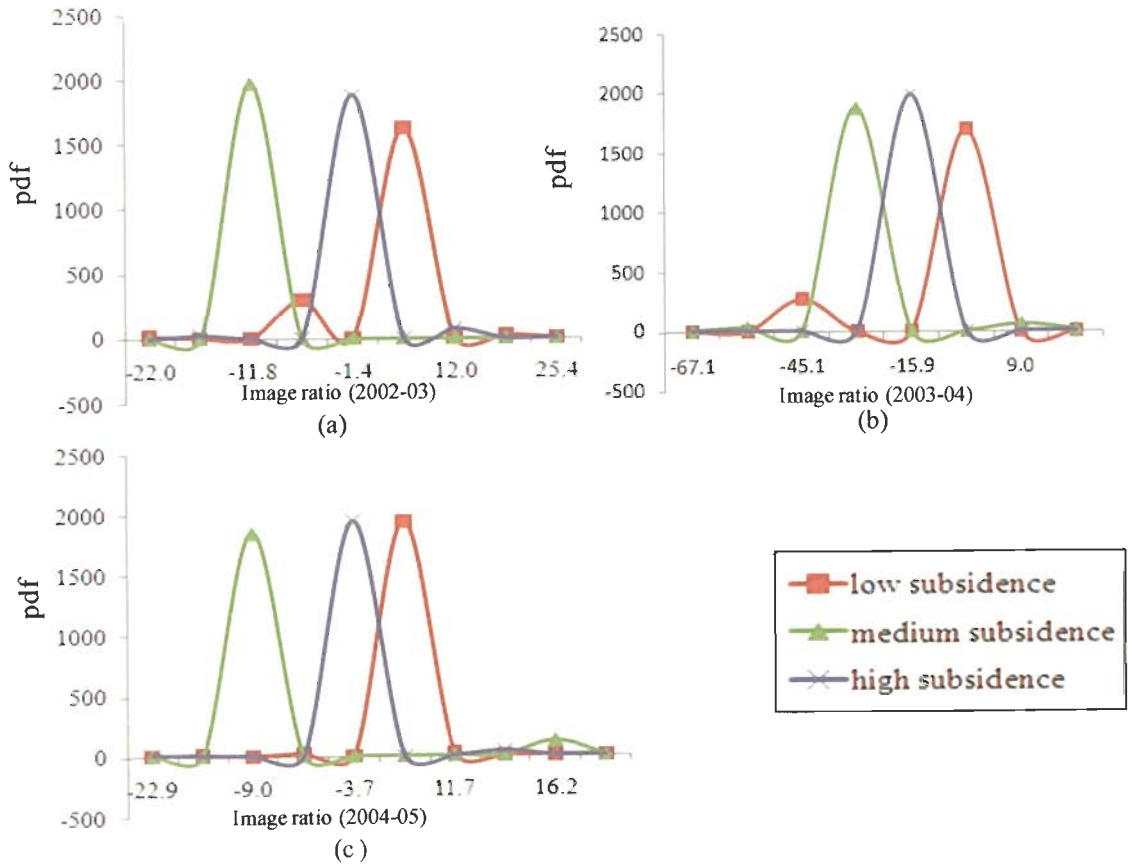
Figure 6.20 pdf curve for three types of subsidence areas (a) image ratio of 2002 and 2003 (b) image ratio of 2003-2004 and (c) image ratio 2004 to 2005.

In the gaussian distribution, parameter a_1 corresponds to peak of the curve, b_1 corresponds to position of the centre of the peak and c_1 corresponds to width of the bell shaped curve. Consider Figure 6.20(a) and Table 6.8 corresponding to subsidence in 2002-'03. From actual subsidence computed by D-InSAR, subsidence areas are grouped such that low, medium and high subsidence areas are obtained. InSAR image pair used to obtain this subsidence is Sept 06, 2002 & Nov 12, 2003.

Table 6.8. Gaussian probability distribution parameters for image ratios of low, medium and high subsidence areas.

Subsidence area	Year	Gaussian probability distribution parameters		
		a_1	b_1	c_1
Low	2002-'03	1929	6.358	1.799
	2003-'04	1787	-1.919	3.414
	2004-'05	2106	2.286	1.704
Medium	2002-'03	1997	-11.736	1.823
	2003-'04	2557	-24.480	2.467
	2004-'05	2874	-9.233	0.336
High	2002-'03	1998	-0.920	1.955
	2003-'04	2288	0.2298	0.067
	2004-'05	2006	-3.477	1.330

The gaussian distribution is chosen because the data analysis of low, medium and high subsidence pixels gives R^2 value of 0.97 and greater. As is observed from the figure 6.18, low, medium and high subsidence areas can be demarcated using position of the centre of the peak and hence parameter b_1 plays an important role in differentiating nature of subsidence. From the analysis of probability distribution of image ratio obtained by minimum ratio detector belonging to 'low', 'medium' and 'high' subsidence levels, the gaussian parameters are set by analyzing 50 groups of pixels belonging to each of the subsidence areas. Then, for the next year, 2003-2004 DInSAR image pair, minimum image ratio by MRD is computed. The whole

'minimum image ratio' image is divided in to groups of pixels of size 5 × 5. For each of the group of pixels, gaussian parameters are computed. From the range of gaussian parameters, the group of pixels is labeled as one of the subsidence area as 'low', 'medium' or 'high' subsidence areas. Similarly, this analysis is validated by checking with succeeding years of 2004-05 as shown in Table 6.8.

6.4. Conclusion

A method for obtaining reliable set of 'change' and 'no change' pixels from image analysis techniques is presented. Distance measure obtained by integrated intensity, texture and orientation difference map corresponding to two set of classified pixels, 'change' and 'no change' pixels, is found to follow weibull-3P distribution. Validation by weibull distribution model is also implemented for succeeding years of analysis. Scale parameter β plays a vital role in discriminating 'change' and 'no change' pixels as discussed.

The subsidence obtained by DInSAR shows that areas of larger changes are identified near Lake Borgne, and in the boundaries of Mississippi river. Lake Borgne is reported to be identified as an area of major land subsidence as found by other studies also. Our subsidence results also confirm the earlier findings by Dixon et al., 2006. Dixon has used permanent scatterers technique which requires elevation data for application of interferometry to measure subsidence. It can be concluded that surface deformation can be monitored quantitatively in the scale of mm with the help of temporal analysis of D-InSAR. Statistical analysis of image ratios of pixels identified by interferometry is accomplished by grouping them to different levels of subsidence. This analysis helps us to guide in identifying presence and level of subsidence from analysis of image ratios itself before applying DInSAR.

Chapter 7

Conclusions and Future Work

7.1 Contributions of the Thesis

This section aims to provide a summary of structure, central ideas, results and key contributions of this thesis.

The present work deals with exploring the possibility of analyzing single polarized SAR image for land cover classification in unsupervised way and determine the 'change' and 'no change' pixels on SAR image with quantitative assessment of changes. The motivation behind this research work was to critically analyze unsupervised land cover classification for SAR images and develop algorithm specifically to meet the needs of single polarized SAR image analysis on one hand, and on the other, it should use minimum *apriori* information and requires less interaction for its implementation. In addition, focus is also to use unsupervised algorithm for obtaining qualitative and quantitative analysis of 'change' and 'no change' pixels from two SAR images obtained at different times.

ERS-2 SAR images for Roorkee, India are used for developing and testing the unsupervised classification algorithm for land cover classification. The acquired images are of ERS-SAR PRI for three different dates (Section 1.4). These images are georeferenced using the corner co-ordinates and center coordinate provided in the leader file. Image despeckling is carried out to reduce speckle noise in SAR images. Adaptive Lee filter is used to implement despeckling. Sharp details present in the image are preserved while applying this filter, thus preserving boundaries and textural information in SAR images. Then, backscattering coefficient is calculated from the DN values. This process is known as preprocessing and after that these images are ready for further study and analysis.

Unsupervised classification of 'change' and 'no change' pixels is applied on RADARSAT-1 images acquired for New Orleans city of USA (Section 1.3). 84 SLC datasets were obtained from Apr. 15, 2002 to Mar. 15, 2007 (Appendix A). Classification of 'change' and 'no change' pixels, with the quantitative assessment of

154

changes, is carried out for the New Orleans area of USA. These images are georeferenced and radar brightness is calculated from the DN values. From the complete dataset available, suitable InSAR image pairs (Section 6.2) satisfying various criteria like baseline distance, spatial overlap and coherence, are chosen for DInSAR analysis.

The contributions of this thesis on land cover classification are as following:

- In the first part of the research, the role of various texture measures like mean, variance, semivariogram, lacunarity, weighted rank fill ratio and wavelet components for classifying images is critically analyzed using synthetic images and real ERS-1 SAR image. After analysis, it is found that these texture measures may play a very crucial role for land cover classification, if they are properly used. For this purpose, a detailed study with combination of texture measures has been carried out. For combining the individual effect of each texture, it is found that PCA can also play an important role because PCA has the advantage of projecting the input textures into a new feature space with improved class separability. So, PCA has been applied to combine the texture measures and it is observed that the classification accuracy increases in comparison to that without PCA. Therefore, it can be inferred that this type of analysis and approach is quite helpful in near future for land cover classification of single polarized SAR image using various texture measures.

- The multiresolution analysis of SAR images is taken as the next task. M-band wavelets provide a mixture of logarithmic and linear frequency resolution and hence suitable to analyze micro and macro textures present in the single polarized SAR image. To represent the texture features present in ERS-2 SAR image, local estimator is applied on wavelet coefficients of M-band wavelets. In an effort to reduce user interactions for carrying out unsupervised classification, an approach is proposed to obtain user defined parameters directly by defining an empirical relation for classification accuracy. Thus, an approach by which user can directly find the optimum parameters that could give maximum classification accuracy in SAR image for particular region/site.

- Labeling of clusters in ERS-2 SAR image into major land cover types like water, urban and agriculture is the next task. Generally, researchers are using

thresholding approach on backscattering coefficient for separating land cover types, for example, water and land. This approach suffers from the limitation that selection of thresholding becomes difficult when histogram of backscattering coefficient does not have valley. It is difficult to label the clusters only on the basis of backscattering coefficient since the range of backscatter is overlapping for major land cover types. Some researchers are using topographic sheet or ground truth for labeling, that means it also needs a minimum *apriori* information to label the clusters. So, to minimize these difficulties on labeling, surface roughness is proposed as a modulating factor with backscattering coefficient for classification. In this work, we have presented a relation by which surface roughness parameter, RMS height, '*s*' can be calculated from texture measures. On the basis of surface roughness and backscattering coefficient, land cover types can be labeled and very satisfactory results have been obtained on ERS-2 SAR images.

- The next task of this thesis is unsupervised classification of 'change' and 'no change' areas and quantitative assessment of changes. New Orleans of USA has been taken as the study area and RADARSAT-1 data of this area is used for analyzing unsupervised classification of changes with their quantitative assessments. This problem of unsupervised classification of SAR images in to 'change' and 'no change' areas is analyzed using image analysis and interferometric approach. To get a reliable set of 'change' and 'no change' pixels, four methods of image differencing, minimum ratio detector, correlation coefficient, and integrated intensity, texture, and orientation difference maps are used. An intersection operator is proposed to apply on the results of these four image analysis methods. This gives rise to reliable 'change' and 'no change' pixels from image analysis approach. To strengthen the results, probability distribution of pixels of each of the four methods in image analysis approach is studied. It has been found that weibull distribution-3P parameters are quite helpful in distinguishing 'change' and 'no change' areas using integrated intensity, texture and orientation difference map. Therefore, with the help of this analysis, 'change' and 'no change' pixels can be classified by comparing SAR images obtained at different instants using image analysis.

- DInSAR is a precise measurement tool. Therefore, the next task is to explore the possibility of using DInSAR for quantitative assessment of changes. It helps in discerning small changes on the earth surface. This helps in quantifying changes (in our case, subsidence) that has occurred on earth surface. DInSAR requires no elevation model for its implementation. Inspite of its advantages, DInSAR is a complex process involving suitable selection of InSAR image pairs, complex process of interferogram generation and phase unwrapping. Hence an alternate approach by which a group of pixels can be labeled as low, medium or high subsidence areas is proposed. Image ratio belonging to each of these groups is analyzed for their probability distribution. Gaussian pdf fits the data and it is observed that gaussian parameters can help in distinguishing various levels of subsidence like low, medium or high subsidence areas.

The softwares used for this work are mainly ENVI 4.3, IDL 6.0, Erdas Imagine 9.2, EV-InSAR 3.1, Sar Scape 3.0, and various codes are developed in MATLAB R2006a. The results obtained by this study show that single polarized SAR image has significant capabilities in land cover classification for describing different surfaces like that of water, urban or agriculture areas. In the case of classifying 'change' and 'no change' pixels, image analysis give a comprehensive view of locations of changes that have occurred. To obtain a complete and detailed analysis of changes on earth surface like subsidence, DInSAR can be effectively used. By the proposed approach developed by comparing image analysis and interferometric techniques, more information about the nature of subsidence could be obtained from simple image analysis techniques like image ratioing.

7.2 Future Scope

Present thesis work has the scope and capabilities to extend it further. A few major ones are listed as following.

Based on the algorithms and approaches proposed in this thesis, an automated land cover monitoring system for SAR image can be developed for a specific site, so that continuous monitoring could be carried out for succeeding years. This

monitoring system will be quite helpful in extending the automated monitoring of various land cover over a large scale.

- In this thesis, quantitative analysis of changes or subsidence measurement is carried out using differential interferometry. Interferometry using permanaent scatterers can also be developed so that analysis of individual pixel deformation could be studied in detail.

- The present research work explores new paths in the direction of developing user independent algorithms. The proposed approach presents the user with optimum parameters to be applied for enhancing classification accuracy.

Appendix A

Specifications of RADARSAT data of New Orleans city of USA used for classifying 'change' and 'no change' pixels and subsidence analysis.

Data ID	Acquisition Date (yyyy-mm-dd)	Beam mode	Product type
1	2002-04-15	S2	SLC
2	2002-05-09	S2	SLC
3	2002-06-02	S2	SLC
4	2002-06-26	S2	SLC
5	2002-07-20	S2	SLC
6	2002-08-13	S2	SLC
7	2002-09-06	S2	SLC
8	2003-01-04	S2	SLC
9	2003-01-28	S2	SLC
10	2003-02-21	S2	SLC
11	2003-03-17	S2	SLC
12	2003-04-10	S2	SLC
13	2003-05-04	S2	SLC
14	2003-05-28	S2	SLC
15	2003-06-21	S2	SLC
16	2003-07-15	S2	SLC
17	2003-09-01	S2	SLC
18	2003-09-25	S2	SLC
19	2003-10-19	S2	SLC
20	2003-11-12	S2	SLC
21	2003-12-06	S2	SLC

Data ID	Acquisition Date (yyyy-mm-dd)	Beam mode	Product type
22	2003-12-30	S2	SLC
23	2004-01-23	S2	SLC
24	2004-02-16	S2	SLC
25	2004-03-11	S2	SLC
26	2004-04-04	S2	SLC
27	2004-04-28	S2	SLC
28	2004-05-22	S2	SLC
29	2004-07-09	S2	SLC
30	2004-08-26	S2	SLC
31	2004-10-13	S2	SLC
32	2004-11-30	S2	SLC
33	2004-12-19	F5	SLC
34	2005-01-17	S2	SLC
35	2005-02-05	F5	SLC
36	2005-03-01	F5	SLC
37	2005-03-06	S2	SLC
38	2005-03-25	F5	SLC
39	2005-04-18	F5	SLC
40	2005-04-23	S2	SLC
41	2005-05-12	F5	SLC
42	2005-06-05	F5	SLC
43	2005-06-10	S2	SLC
44	2005-06-29	F5	SLC
45	2005-07-23	F5	SLC

Data ID	Acquisition Date (yyyy-mm-dd)	Beam mode	Product type
46	2005-07-28	S2	SLC
47	2005-08-16	F5	SLC
48	2005-09-09	F5	SLC
49	2005-09-14	S2	SLC
50	2005-10-03	F5	SLC
51	2005-10-27	F5	SLC
52	2005-11-01	S2	SLC
53	2005-11-20	F5	SLC
54	2005-11-25	S2	SLC
55	2005-12-14	F5	SLC
56	2005-12-19	S2	SLC
57	2006-01-07	F5	SLC
58	2006-01-31	F5	SLC
59	2006-02-05	S2	SLC
60	2006-02-24	F5	SLC
61	2006-03-01	S2	SLC
62	2006-03-20	F5	SLC
63	2006-03-25	S2	SLC
64	2006-04-13	F5	SLC
65	2006-04-18	S2	SLC
66	2006-05-12	S2	SLC
67	2006-07-23	S2	SLC
68	2006-09-04	F5	SLC

Data ID	Acquisition Date (yyyy-mm-dd)	Beam mode	Product type
69	2006-09-09	S2	SLC
70	2006-09-28	F5	SLC
71	2006-10-03	S2	SLC
72	2006-10-22	F5	SLC
73	2006-10-27	S2	SLC
74	2006-11-15	F5	SLC
75	2006-11-20	S2	SLC
76	2006-12-09	F5	SLC
77	2006-12-14	S2	SLC
78	2007-01-02	F5	SLC
79	2007-01-07	S2	SLC
80	2007-01-26	F5	SLC
81	2007-01-31	S2	SLC
82	2007-02-19	F5	SLC
83	2007-02-24	S2	SLC
84	2007-03-15	F5	SLC

Bibliography

1. Abdel M. M., and Quegan S., "Variability in ERS scatterometer measurements over land," IEEE Transactions on Geoscience and Remote Sensing, vol. 38, no. 4, 2000, pp. 1767-1776.

2. Acharyya M., and Kundu M. K., "An adaptive approach to unsupervised texture segmentation using M-Band wavelet transform," Signal Processing, vol. 81, no. 7, 2001, pp. 1337-1356.

3. Acharyya M., De R. K., and Kundu M. K., "Segmentation of remotely sensed images using wavelet features and their evaluation in soft computing framework," IEEE Transactions on Geoscience and Remote Sensing, vol. 41(1), no. 12, 2003, pp. 2900-2905.

4. Adem S., Vitse I., Johannsen C., and Monbaliu J., "Sediment type unsupervised classification of the Molenplaat, Westerschelde estuary, The Netherlands," EARSeL Proceedings, vol. 5, no. 2, 2006, pp. 146-160.

5. Ainsworth T. L., Schuler D. L., and Lee J. S., "Polarimetric SAR characterization of man-made structures in urban areas using normalized circular-pol correlation coefficients," Remote Sensing of Environment, vol. 112, no. 3, 2008, pp. 2876-2885.

6. Alberga V., and Chandra M., "Combined application of target decomposition methods and polarimetric SAR interferometry: some preliminary results," Proceedings of SPIE, vol. 4543, 2002, pp. 140.

7. Alberga V., Chandra M., and Pipia L., "Supervised classification of coherent and incoherent polarimetric SAR observables," Proceedings of SPIE, vol. 4883, 2003, 181p.

8. Alkin O., and Caglar H., "Design of efficient M-band coders with linear phase and perfect reconstruction properties," IEEE Transactions on Signal Processing, vol. 43, no.7, 1995, pp. 1579-1590.

9. Amelung F., Dixon T. H., Ferretti A., and Novali F., "Subsidence in New Orleans measured with permanent scatterer interferometry," Geological

Society of America Abstracts with Programs, vol. 38, no. 7, 2006, pp. 290-291.

10. Aminian F., Aminian M., and Colliyns H. W., "Analog fault diagnosis of actual circuits using neural networks," IEEE Transactions on Instrumentation and Measurement, vol. 51, 2002, pp. 544-550.

11. Anitha D., Mohan S, and Patel A. B., "Multi-frequency SAR signatures of forest class covering parts of Rajpipla, Gujarat," Proceedings of SPIE, the International Society for Optical Engineering, vol. 6410, 2006, pp. 641005.1-641005.11.

12. Atkinson P. M., and Lewis P., "Geostatistical classification for remote sensing: an introduction," Computers and Geosciences, vol. 26, no. 4, 2000, pp. 361-371.

13. Aujol J. F., Aubert G., and Blanc-Feraud L., "Wavelet based level set evolution for classification of textured images," IEEE Transactions on Image Processing, vol. 12, no. 12, 2003, pp. 1634-1641.

14. Azimi-Sadjadi M. R., Ghaloum S., and Zoughi R., "Terrain Classification in SAR Images using Principle Components Analysis and Neural Networks", IEEE Transactions on Geoscience and Remote Sensing, 1993, pp.511-514.

15. Bajwa I. S., and Hyder S. I., "PCA based image classification of single layered cloud types," Proceedings of IEEE Symposium on Emerging Technologies, 2005, pp. 365-369.

16. Bamler R., and Hartl P., "Synthetic Aperture radar Interferometry," Inverse Problems, vol. 14, no. 4, 1998, pp. R1-R54.

17. Barber D. G., and LeDrew E. F., "SAR sea ice discrimination using texture statistics: A multivariate approach," Photogrammetric Engineering and Remote Sensing, vol. 57, no. 4, 1991, pp. 385-395.

18. Barber D. G., Shockr M. E., Fernandes R. A., Soulis E. D., Flett D. G., and LeDrew E.F., "A comparison of second order classifiers for SAR sea ice discrimination," Photogrammetric Engineering and Remote Sensing, vol. 59, no. 9, 1993, pp. 1397-1408.

19. Bazi Y., Bruzzone L., and Melgani F., "An unsupervised approach based on the generalized Gaussian model to automatic change detection in multitemporal SAR images," IEEE Transations on Geoscience and Remote Sensing, vol. 43, no. 4, 2005. pp. 874-887.

20. Bazi Y., Bruzzone L., and Melgani F., "Image thresholding based on the EM algorithm and the generalized Gaussian distribution," Pattern Recognition, vol. 40, no 2, 2007, pp. 619-634.

21. Bellagente M., Gamba P., and Savazzi P., "Fuzzy texture characterization of urban environments by SAR data," Proceedings of International Geoscience and Remote Sensing Symposium, IGARSS '99, 1999, vol. 2, pp. 1232-1234.

22. Benyoussef L., Carincotte C., and Derrode S., "Extension of higher-order HMC modeling with application to image segmentation," Digital Signal Processing, vol. 18, no. 5, 2008, pp. 849-860.

23. Berardino P., Fornaro G., Lanari R., and Sansosti E., "A new algorithm for surface deformation monitoring based on small baseline differential SAR interferograms," IEEE Transactions on Geoscience and Remote sensing, vol. 40, no. 11, 2002, pp. 2375-2383.

24. Berroir J. P., Merlin I., and Cohen I., "A numerical model for large deformation," International Conference on Pattern Recognition, '96, vol. 1, 1996, pp. 471-475.

25. Bhattacharya C., and Mahapatra P. R., "A discrete wavelet transform approach to multiresolution complex SAR image generation," IEEE Letters on Geoscience and Remote Sensing, vol. 4, no. 3, 2007, pp. 416-420.

26. Bindlish R., and Barros A. P., "Parameterization of vegetation backscatter in radar-based soil moisture estimation," Remote Sensing of Environment, vol. 76, 2001, pp. 130-137.

27. Bishop C. M., "Neural networks for pattern recognition," New York: Oxford University press, 1995.

28. Blum A., and Langley P., Selection of relevant features and examples in machine learning," Artificial Intelligence, vol. 97, no.1/2, 1997, pp. 245-251.

29. Boucher A., Seto K. C., and Journel A. G., "A novel method for mapping land cover changes: Incorporating time and space with Geostatistics," IEEE Transactions on Geoscience and Remote Sensing, vol. 44, no. 11, 2006, pp. 3427-3435.

30. Bouzidi S., Belhaj S., Herlin I., and Berroir J., "An approach for land cover change detection using low spatial resolution data," IEEE International Geoscience and Remote Sensing Symposium, IGARSS '03, vol. 3, 2003, pp. 1585-1587.

31. Bouzidi S., Berroir J-P., and Herlin I., "A remote sensing data fusion approach to monitor agricultural areas," Pattern Recognition, 1998, Proceedings of Fourteenth International Conference, vol. 2, 1998a, pp. 1387-1389.

32. Bouzidi S., Berroir J-P., and Herlin I., "An operational approach to monitor vegetation using remote sensing," IEEE International Conference on Acoustics, Speech and Signal Processing, 1998b, vol. 5, 1998, pp. 2697-2700.

33. Bovenga F., Nutricato R., Refice A., and Wasowski J., "Application of multi-temporal differential interferometry to slope instability detection in urban/peri-urban areas," Engineering Geology, vol. 88, no. 3-4, 2006, pp. 218-239.

34. Bovolo F., and Bruzzone L., "A detail-preserving scale-driven approach to change detection in multitemporal SAR images,", IEEE Transactions on Geoscience and Remote Sensing, vol. 43, no. 12, 2005, pp. 2963-2972.

35. Bovolo F., and Bruzzone L., "A split based approach to unsupervised change detection in large size multitemporal images: Application to Tsunami damage assessment," IEEE Transactions on Geoscience and Remote Sensing, vol. 45, no. 6, 2007, pp. 1658-1670.

36. Bruzzone L., and Prieto F., "Automatic analysis of the difference image for unsupervised changedetection," IEEE Transactions on Geoscience and Remote Sensing, vol. 38, no. 3, 2000, pp. 1171-1182.

37. Bujor F., Trouve E., Valet E., Nicolas J. M., and Rudant J. P., "Application of log-cumulants to the detection of spatiotemporal discontinuities in multitemporal SAR images," IEEE Transactions on Geoscience and Remote Sensing, vol. 42, no.10, 2004, pp. 2073-2084.

38. Bujor F., Trouve E., Valet E., Nicolas J. M., Rudant J-P., "Application of log-cumulants to the detection of spatiotemporal discontinuities in multitemporal SAR images," IEEE Transactions on Geoscience and Remote Sensing, vol. 42, no. 10, 2004, pp. 2073-2084.

39. Burkett V. R., Zilkoski D. B., Hart D. A., "Sea-level rise and subsidence: implications for flooding in New Orleans, Louisiana," In: Prince, K.R., Galloway, D.L. (Eds.), Subsidence Interest Group Conference, Proceedings of the Technical Meeting. Galveston, 2001.

40. Cao W., Bicheng L., and Yong Z., "A remote sensing image fusion method based on PCA transform and wavelet packet transform," International

Conference on Neural Networks and Signal Processing 2003, vol. 2, 2003, pp. 976-981.

41. Carincotte C., Derrode S., Bourennane S., "Unsupervised change detection on SAR images using fuzzy hidden Markov chains," IEEE Transactions on Geoscience and Remote Sensing, vol. 44, no. 2, 2006, pp. 432-441.

42. Carlotto M. J., "Detection and analysis of change in remotely sensed imagery with application to wide area surveillance," IEEE Transactions on Image Processing, vol. 6, no. 1, 1997, pp. 189-202.

43. Carr J. R., and De Miranda F. P., "The semivariogram in comparison to the co-occurrence matrix for classification of image texture," IEEE Transactions on Geoscience and Remote Sensing, vol. 36, no. 6, 1988, pp. 1945-1952.

44. Cattell R. B., "The scree test for the number of factors," Multivariate Behaviour Research, vol. 1, no. 2, 1966, pp. 245-276.

45. Chaabane F., Avallone A., Tupin F., Briole P., and Maitre H., "A multi-temporal method for correction of tropospheric effects in differential SAR interferometry: Application to the gulf of Corinth earthquake," IEEE Transactions on Geoscience and Remote Sensing, vol. 45, no. 6, 2007, pp. 1605-1615.

46. Chamundeeswari V. V., and Singh D., "Computationally efficient extraction and integration of multi-wavelet based features for segmentation of SAR images," International Symposium on Geospatial Databases for Sustainable Development, vol. 36, no. 4, 2006, pp. 69-74.

47. Chamundeeswari V. V., Singh D., and Singh K., "An adaptive method with integration of multi-wavelet based features for unsupervised classification of SAR images," Journal of Geophysics and Engineering, vol. 4, 2007a, pp. 384-393.

48. Chamundeeswari V. V., Singh D., and Singh K., "An analysis of texture measures in PCA-based unsupervised classification of SAR images," IEEE Geoscience and Remote Sensing Letters, Accepted (in Press), 2009.

49. Chamundeeswari V. V., Singh D., and Singh K., "Unsupervised land cover classification of SAR images using greedy kernel PCA," III International Conference on Microwaves, Antennas, Propagation and Remote Sensing, ICMARS 2006, 2006a, pp. 141-142.

50. Chamundeeswari V. V., Singh D., and Singh K., "Unsupervised land cover classification via feature selection and integration using PCA," 13th Symposium in Earthquake Engineering Department, 2006b, vol. 2, pp. 163-167.

51. Chamundeeswari V. V., Singh D., and Singh K., "Unsupervised land cover classification of SAR images by contour tracing," IEEE International Geoscience and Remote Sensing Symposium, IGARSS 2007, 2007b, pp. 547-550.

52. Chamundeeswari V. V., Singh D., Singh K., and Wiesbeck W., "A critical analysis to generate change detection map using SAR interferometry for land subsidence monitoring of New Orleans city of USA," IEEE International Geoscience and Remote Sensing Symposium, IGARSS 2008, 2008a.

53. Chamundeeswari V. V., Singh D., Singh K., and Wiesbeck W., "A novel approach to land subsidence with analysis and validation using probability distribution function," National Symposium on Advances in Remote Sensing Technology and Applications with Special Emphasis on Microwave Remote Sensing, 2008b.

54. Chamundeeswari V. V., Singh D., Singh K., and Wiesbeck W., "Change detection module for New Orleans city of USA using differential SAR interferometry," 37th COSPAR Scientific Assembly, 2008c.

55. Chandhuri B. B., and Sarkar N., "Texture segmentation using fractal dimension," IEEE Transactions on Pattern Analysis and Machine Intelligence, vol. 17, no.1, 1995, pp. 72-77.

56. Chandra M., and Keydel W., "Influence of propagation phase-shifts in polarimetric SAR interferometry," IEEE International Geoscience and Remote Sensing Symposium, IGARSS '99, Proceedings, vol. 4, 1999, pp. 2218-2220.

57. Chang T., and Kuo C. C. J, "Texture analysis and classification with tree structured wavelet transform," IEEE Transactions on Image Processing, vol. 2, no. 4, 1993, pp. 429-441.

58. Chanussot J., Benediktsson J. A., and Fauvel M., "Classification of remote sensing images from urban areas using a fuzzy probabilistic model," IEEE Letters on Geoscience and Remote Sensing, vol. 3, no. 1, 2006, pp. 40-44.

59. Chatterjee R. S., Fruneau B., Rudant J. P., Frison P. L., Lakhera R. C., Dadhwal V. K., and Saha R., "Subsidence of kolkata (Calcutta) city, India

during the 1990s as observed from space by differential synthetic aperture radar interferometry (D-InSAR) technique," Remote Sensing of Environment, vol. 102, no. 1-2, 2006, pp. 176-185.

60. Chaux C., Duval L., and Pesquet J.-C., "Image analysis using a dual-tree M-band wavelet transform," IEEE Transactions on Image Processing, vol. 15, no. 8, 2006, pp. 2397-2412.

61. Chen Y., Gu Y., Gu J., and Yang J., "Particle filter based road detection in SAR image," IEEE International Symposium on Microwave, Antenna, Propagation and EMC Technologies for Wireless Communications, MAPE 2005, vol. 1, 2005, pp. 301-305.

62. Chumsamrong W., Thitimajshima P., and Rangsanseri Y., "Synthetic aperture radar (SAR) image segmentation using a new modified fuzzy c-means algorithm," IEEE International Geoscience and Remote Sensing Symposium, IGARSS 2000, vol. 2, 2000, pp. 624-626.

63. Clausi D. A., "Comparison and fusion of co-occurrence, Gabor and MRF texture features for classification of SAR sea ice imagery," Atmosphere-Ocean, vol. 39, no. 3, 2001, pp. 183-194.

64. Clausi D. A., and Deng H., "Design-based texture feature fusion using Gabor filters and co-occurrence probabilities," IEEE Transactions on Image Processing, vol. 14, no. 7, 2005, pp. 925-936.

65. Cloude S. R., and Papathanassiou K. P., "Polarimetric SAR interferometry," IEEE Transactions on Geoscience and Remote Sensing, vol. 36, no. 5, 1998, pp. 1551-1565.

66. Coifman R. R., and Wickerhauser M. V., "Entropy-based algorithms for best basis selection," IEEE Transactions on Information Theory, vol. 38, no. 2, 1992, pp.713-718.

67. Colesanti C., Ferretti A., Prati C., and Rocca F., "Monitoring landslides and tectonic motion with the permanent scatterers technique," Engineering Geology, vol. 68, no. 1/2, 2003, pp. 3-14.

68. Congalton B. G., "A quantitative method to test for consistency and correctness in photointerpretaion," Photogrammetric Engineering and Remote Sensing, vol. 49, 1983, pp. 69–74.

69. Constantini M., Farina A., and Zirilli F., "A fast phase unwrapping algorithm for SAR interferometry," IEEE Transactions on Geoscience and Remote Sensing, vol. 37, no. 1, 1999, pp. 452-460.

70. Coppin P., Jonckheere I., Nachaerts K., and Muys B., "Digital change detection in ecosystem monitoring: A review," International Journal of Remote Sensing, vol. 25, no. 9, 2004, pp. 1565-1596.

71. Das A. K., Singh C. P., Mohan S, and Ajai, "Polarization signatures of land cover classes using L-band polarimetric SAR data," Proceedings of SPIE, the International Society for Optical Engineering, vol. 6410, 2006, pp. 641003.1-641003.12.

72. Daugman J., "Two-dimensional spectral analysis of cortical receptive field profile," Vision Research, vol. 20, pp. 847–856, 1980.

73. Davidson M. W. J., Toan T. L., Mattia F., Satalino G., Manninen T., "On the characterization of agricultural soil roughness for radar remote sensing studies," IEEE Transactions on Geoscience and Remote Sensing, vol. 38, no. 2, 2000, pp. 630-640.

74. Davis G., and Nosratinia A., "Wavelet-Based Image Coding: An Overview," Applied and Computational Control, Signals, and Circuits, vol. 1, no. 1, 1998.

75. Dekker R. J., "Speckle filtering in satellite SAR change detection imagery," International Journal of Remote Sensing, vol. 19, 1998, pp. 1133-1146.

76. Dekker R. J., "Texture analysis and classification of ERS SAR images for map updating of urban areas in the Netherlands," IEEE Transactions on Geoscience and Remote Sensing, vol. 41, no. 9, 2003, pp. 1950–1958.

77. Dell'Acqua F., Gamba P., and Trianni G., "Semi-automatic choice of scale dependent features for satellite SAR image classification," Pattern Recognition Letters, vol. 27, no. 4, 2006, pp. 244-251.

78. Deng H., and Clausi D. A., "Unsupervised image segmentation using a simple MRF model with a new implementation scheme," Pattern Recognition, vol. 37, 2004, pp. 2323-2335.

79. Derrode S., Mercier G., and Pieczynski W., "Unsupervised change detection in SAR images using a multicomponent HMC model," in Proceedings of 2nd International Workshop Analysis of Multitemporal Remote Sensing Images Ispra, Italy, 2003, pp. 16-18.

80. Dhodhi M. K., Saghri J. A., Ahmad I., and Ul-Mustafa R., "D-Isodata : A distributed algorithm for unsupervised classification of remotely sensed data on network of workstations," Journal of Parallel and Distributed Computing, vol. 59, no. 2, 1999, pp. 280-301.

81. Didascalou D., Dottling M., Geng N., and Wiesbeck W., "An approach to include stochastic rough surface scattering into deterministic ray-optical wave propagation modeling," IEEE Transactions on Antennas and Propagation, vol. 51, no.7, 2003, pp. 1508-1515.

82. Dierking W., and Skriver H., "Change detection for thematic mapping by means of airborne multitemporal polarimetric SAR imagery," IEEE Transactions on Geoscience and Remote Sensing, vol. 40, no. 3, 2002, pp. 618-636.

83. Dixon T. H., Amelung F., Ferretti A., Novali F., Rocca F., Dokka R., Sella G., Kim S-W., Wdowinski S., and Whitman D., "Subsidence and Flooding in New Orleans," Nature, vol. 441, 2006, pp. 587-588.

84. Do M. N., and Vetterli M., "The contourlet transform: an efficient directional multiresolution image representation," IEEE Transactions on Image Processing, vol. 14, no. 12, 2005, pp. 2091-2106.

85. Dobson M. C., Pierce L., Kellndorfer J., and Ulaby F., "Use of SAR image texture in terrain classification," Proceedings of International Geoscience and Remote Sensing Symposium, IGARSS '97, vol. 3, 1997, pp. 1180-1183.

86. Dobson M. C., Pierce L., Sarabandi K., Ulaby F. T., and Sharik T., "Preliminary analysis of ERS-1 SAR for forest ecosystem studies," IEEE Transactions on Geoscience and Remote Sensing, vol. 30, no. 2, 1992, pp. 203-211.

87. Dobson M. C., Ulaby F. T., and Pierce L. E., "Land-cover classification and estimation of terrain attributes using synthetic aperture radar," Remote Sensing of Environment, vol. 51, no. 1, 1995, pp. 199-214.

88. Du L. J., "Texture segmentation of SAR images using localized spatial filtering," Proceedings of International Geoscience and Remote Sensing Symposium, IGARSS '90, 1990, pp. 1983-1986.

89. Dubois P. C., Van Zyl J. J., and Engman E. T., "Measuring soil moisture with imaging radar," IEEE Transactions on Geoscience and Remote Sensing, vol. 33, no. 4, 1995, pp. 915-926.

90. Duits R., Felsberg M., Granlund G., and Romeny B. H., "Image analysis and reconstruction using a wavelet transform constructed from a reducible representation of the Eucledian motion group," International Journal of Computer Vision, vol. 72, no. 1, 2007, pp. 79-102.

91. Dupuis A., and Vasseur P., "Image segmentation by cue selection and integration," Image and Vision Computing, vol. 24, 2006, pp. 1053-1064.

92. Eineder M., Adam N., "A maximum-likelihood estimator to simultaneously unwrap, geocode, and fuse SAR interferograms from different viewing geometries into one digital elevation model," IEEE Transactions on Geoscience and Remote Sensing, vol. 43, no. 1, 2005, pp. 24-36.

93. Eldhuset K., "Automatic ship and ship wake detection in spaceborne SAR images from coastal regions," International Geoscience and Remote Sensing Symposium, IGARSS '88, vol. 3, 1988, pp. 1529-1533.

94. Espinal F., Jaweth B.D., and Kubota T., "Wavelet based fractal signature analysis for automatic target recognition," Optical Engineering, vol. 37, no. 1, 1988, pp. 166-174.

95. Evans D. L., Farr T. G., and Van Zyl J. J., "Estimates of surface roughness derived from synthetic aperture radar (SAR) data," IEEE Transactions on Geoscience and Remote Sensing, vol. 30, no. 2, 1992, pp. 382-389.

96. Evans M., Hastings N., and Peacock B., "Statistical Distributions," Third edition, New York: John Wiley, 2001.

97. Ferrazzoli P., Paloscia S., Pampaloni P., Schiavon G., Sigismondi S., and Solimini D., "The potential of multifrequency polarimetric SAR in assessing agricultural and arboreous biomass," IEEE Transactions on Geoscience and Remote Sensing, vol. 35, no. 1, 1997, pp. 5-17.

98. Ferretti A., Prati C., and Rocca F., "Nonlinear subsidence rate estimation using permanent scatterers in differential SAR interferometry," IEEE Transactions on Geoscience and Remote Sensing, vol. 38, no. 5, 2000, pp. 2202-2212.

99. Ferretti A., Prati C., and Rocca F., "Permanent scatterers in SAR interferometry," IEEE Transactions on Geoscience and Remote Sensing, vol. 39, no. 1, 2001, pp. 8-20.

100. Ferretti A., Savio G., Barzaghi R., Borghi A., Musazzi S., Novali F., Prati C., and Rocca F., "Submillimeter accuracy of InSAR time series: experimental

validation," IEEE Transactions on Geoscience and Remote Sensing, vol. 45, no. 5, 2007, pp. 1142-1153.

101. Frankot R. T., and Chellappa R., "Lognormal random field models and their applicatiosn to radar image analysis," IEEE Transactions on Geoscience and Remote Sensing, vol. 25, 1987, pp. 195-206.

102. Friedman J. H., and Meulman J. J., "Clustering objects on subsets of attributes," Journal of Royal Statistical Soceity: Series B, vol. 6, no. 4, 2004, pp. 815-849.

103. Fruneau B., and Sarti F., "Detection of ground subsidence in the city of Paris using radar interferometry: Isolation from atmospheric artifacts using correlation," Geophysical Research Letters, vol. 27, no. 24, 2000, pp. 3981-3984.

104. Fu K.S., and Mui J. K., "A survey of image segmentation," Pattern Recognition, vol. 13, 1980, pp. 3-16.

105. Fujita M., and Miho Y., "Analysis of a microwave backscattering mechanism from a small urban area images with SIR-C," IEEE Geoscience and Remote Sensing Letters, vol. 3, no. 1, 2006, pp. 10-14.

106. Fukuda S., and Hirosawa H., "A wavelet-based texture feature set applied to classification of multifrequency polarimetric SAR images," IEEE Transactions on Geoscience and Remote Sensing, vol. 37, no. 5, 1999, pp. 2282-2286.

107. Fung A. K., and Chen M. F., "Numerical simulation of scattering from simple and composite random surfaces," Journal of Optical Society of America, A-2, vol. 2, no. 12, 1985, pp. 2274-2284.

108. Gabriel A. K., Goldstein R. M., and Zebker H. A., "Mapping small elevation changes over large areas: differential radar interferometry, "Journal of Geophysical Research, vol. 94, no. B7, 1989, pp. 9183- 9191.

109. Galletti M, Bebbington D. H. O., Chandra M, and Boerner T., "Fully polarimetric analysis of weather radar signatures," IEEE Radar Conference, RADAR '08, 2008, pp. 1-6.

110. Gamba P., Acqua F. D., and Lisini G., "Change detection of multi temporal SAR data in urban areas combining feature based and pixel based techniques," IEEE Transactions on Geoscience and Remote sensing, vol. 44, no. 10, 2006, pp. 2820-2827.

111. Gilmore E. T., Frazier P. D., and Chouikha M. F., "An independent component analysis based image classification scheme," IEEE International Conference on Acoustics, Speech, and Signal Processing 2004 (ICASSP '04), vol. 3, 2004, pp. 577-580.

112. Gnanadesikan R., Kettenring J., and Tsao S., "Weighting and selection of variables for cluster analysis," Journal of Classification, vol. 6, 1999, pp. 3-26.

113. Gohil B. S., Mathur A. K., and Pandey P. C., "An algorithm for sea surface temperature estimation from ERS-1 ATSR using moisture dependent coefficients: a simulation study," International Journal of Remote Sensing, vol. 15, no. 5, 1994, pp. 1161-1167.

114. Gonzalez R. C., and Woods R. E., "Digital Image Processing," Englewood Cliffs, NJ: Prentice Hall, 2002.

115. Google Earth. Available at http://earth.google.com/earth.html, 2008.

116. Greenspan H., Goodman R., Chellappa R., and Anderson C. H., "Learning texture discrimination rules in a multiresolution system," IEEE Transactions on Pattern Analysis and Machine Intelligence, vol. 16, no. 9, 1994, pp. 894-901.

117. Greku R., Milinevsky G., Ladanovsky Y., Bakhmach P., and Greku T., "Topographic and geodetic research by GPS, echosounding and ERS altimetric, and SAR interferometric surveys during ukrainian antarctic expeditions in the west antarctic," In: F"utterer D. K, Damaske D, Kleinschmidt G, Miller H, Tessensohn F (eds) Antarctica, Contributions to Global Earth Sciences. Springer, Berlin, Heidelberg, 2006, pp 383–390.

118. Grey W. M. F., Luckman A. J., and Holland D., "Mapping urban change in the UK using satellite radar interferometry," Remote Sensing of Environment, vol. 87, no. 1, 2003, pp. 16-22.

119. Grover K., and Quegan S., "Quantitaive estimation of tropical forest cover by SAR," IEEE Transactions on Geoscience and Remote Sensing, vol. 37, no. 1, 1999, pp. 479-490.

120. Gu J., Yang J., Zhang H., Peng Y., Wang C., and Zhang H., "Speckle filtering in polarimetric SAR data based on the subspace decomposition," IEEE Transactions on Geoscience and Remote Sensing, vol. 42, no. 8, 2004, pp. 1635-1641.

121. Gupta L., Lekshmi S., Majumdar J., and Das S., "Study of the performance of different texture features for classification of SAR images," IET International Conference on Visual Information Engineering 2006, 2006, pp. 315-320.

122. Hara Y., Atkins R. J., and Yueh S. H., "Application of neural networks to radar image classification," IEEE Transactions on Geoscience and Remote Sensing, vol. 32, no. 1, 1994, pp. 100-109.

123. Haverkamp D., Soh, L. K., Tsatsoulis C., "A dynamic local thresholding technique for sea ice classification," International Geoscience and Remote Sensing Symposium, IGARSS '93, Better Understanding of Earth Environment, vol, 2, 1993, pp. 638-640.

124. Henderson F. M., and Xia Z-G., "SAR applications in human settlement detection, population estimation and urban land use pattern analysis: A status report," IEEE Transactions on Geoscience and Remote Sensing, vol. 35, no. 1, 1997, pp. 79-85.

125. Henebry G. M., "Lacunarity as a texture measure for SAR imagery," International Journal of Remote Sensing, vol. 16, no. 3, 1995, pp. 565-571.

126. Hitley G. E., Burgmann R., Ferretti A., Novali F., and Rocca F., "Dynamics of slow-moving landslides from permanent scatterer analysis," Science, vol. 304, 2004, pp. 1952-1955.

127. Huang K., and Selin A., "Information-theoretic wavelet packet sub-band selection for texture classification," Signal Processing, vol. 86, no. 7, 2006, pp. 1410–1420.

128. Huang Z., "Extensions to the K-means algorithms for clustering large datasets with categorical values," Data Mining and Knowledge Discovery, vol. 2, no. 3, 1998, pp. 283-304.

129. Inglada J. "Similarity measures for multisensor remote sensing images," IEEE International Symposium on Geoscience and Remote Sensing, 2002. IGARSS '02. 2002, vol. 1, 2002, pp. 104-106.

130. Inglada J., and Mercier G., "A new statistical similarity measure for change detection in multitemporal SAR images and its extension to multiscale change analysis", IEEE Transactions on Geoscience and Remote sensing, vol. 45, no. 5, 2007, pp. 1432-1445.

131. Ismail A. R., and Asfour S. S., "Discrete wavelet transform: a tool in smoothing kinematic data," Journal of Biomechanics, vol. 32, 1999, pp. 317-321.

132. Itti L., Koch C., and Neibur E., "A model of saliency-based visual attention for rapid scene analysis," IEEE Transactions on Pattern Analysis and Machine Intelligence, vol. 20, no. 11, 1998, pp. 1254-1259.

133. Jain A. K., and Farrokhnia F. "Unsupervised texture segmentation using Gabor filters," Pattern Recognition, vol. 24, 1991, pp. 1167-1186.

134. Jayant N. S., and Noll P., "Digital coding of waveforms: Principles and applications to speech and video," Englewood Cliffs, New Jersey: Prentice Hall, 1984.

135. Jensen J. R., Bryan M. L., Friedman S. Z., Henderson F. M., Holz R. K., Lindgren D., Toll D. L., Welch R. A., and Wray J. R., "Urban/Suburban land use analysis," Manual of Remote Sensing, J. E. Estes and G. A. Thorley, Eds., 2nd edition, American Soceity of Photogrammetry and Remote Sensing vol. 2, ch.30, 1983, pp. 1571-1666.

136. Jolliffe I. T., "Principal component analysis," in Springer series in Statistics, 2nd edition, Berlin, germany: Springer-Verlag, 2002.

137. Kamarainen J. K., Kyrki V., and Kälviäinen H., "Invariance properties of gabor filter based features- Overview and applications," IEEE Transactions on Image Processing, vol. 15, no. 5, 2006, pp.1088-1099.

138. Karvonen J., Simila M., and Makynen M., "Open water detection from Baltic sea ice Radarsat-1 SAR imagery," IEEE Geoscience and Remote Sensing Letters, vol. 2, no. 3, 2005, pp. 275-279.

139. Keller J. M., Chen S., and Crownover R. M., "Texture description and segmentation through fractal geometry," Computer Vision, Graphics, and Image Processing, vol. 45, 1989, pp. 150-166.

140. Kim S. C., and Kang T. J., "Texture classification and segmentation using wavelet packet frame and Gaussian mixture model," Pattern Recognition, vol. 40, no. 4, 2007, pp. 1207-1221.

141. Kimura H., and Yamaguchi Y., "Detection of landslide areas using satellite radar interferometry," Photogrammetric Engineering and Remote Sensing, vol. 66, no. 3, 2000, pp. 337-344.

142. Krieger G., and Moreira A., "Spaceborne bi- and multistatic SAR: potential and challenges," IEEE Proceedings on Radar, Sonar and Navigation, vol. 153, no. 3, 2006, pp. 184-198.

143. Kumar P., Krishna A. P., Nathawat M. S., Singh C. P., Kandya A. K., Mohan S, and Ajai, "Tree height estimation in Tundi reserved forest using SAR interferometry," Microwave Remote Sensing of the Atmosphere and Environment V, Proceedings of SPIE, vol. 6410, 2006, pp. 641004.1-641004.7.

144. Kumar R., Sarkar A., and Pandey P.C., "Estimation of ocean depths off Goa coast using ERS-1 Synthetic aperture radar," Continental Shelf Research, vol. 19, no. 2, 1999, pp. 171-181.

145. Kyrki V., Kamarainen J. K., and Kälviäinen H., "Simple gabor feature space for invariant object recognition," Pattern Recognition Letters, vol. 25, no. 3, 2004, pp. 311-318.

146. Laine A., and Fan J., "Texture classification by wavelet packet signatures," IEEE Transactions on Pattern Analysis and Machine Intelligence, vol. 15, 1993, pp. 1186-1191.

147. Lang M. W., Kasischke E. S., Prince S. D., and Pittman K. W., "Assessment of C-band synthetic aperture radar data for mapping and monitoring coastal plain forested wetlands in the mid-atlantic region, U.S.A.," Remote Sensing of Environment, vol. 112, no.11, 2008, pp. 4120-4130.

148. Laur H., Bally P., Meadows P., Sanchez J., Schaettler B., and Lopinto E., "Derivation of the backscattering coefficient σ^0 in ESA ERS SAR PRI products," ESA Doc.:ES-TN-RS-PM-HL09, no. 2, 1997.

149. Lee J. S., "Digital Image Enhancement and noise filtering by use of local statistics," IEEE Transactions on Pattern Analysis and Machine Intelligence, vol. 2, no. 2, 1980, pp. 165-168.

150. Lee J. S., and Jurkevich I., "Segmentation of SAR images," IEEE Transactions on Geoscience and Remote Sensing, vol. 27, no. 6, 1989, pp. 674-680.

151. Lenz R., Pontes J., and Wiesbeck W., "A high accuracy calibration and receive instrument for TerraSAR-X ground calibration," European Microwave Conference, 2005, vol. 3, 2005, pp. 4-6.

152. Lenz R., Pontes J., and Wiesbeck W., "The TerraSAR-X ground calibration system and pattern estimation software," IEEE International Geoscience and Remote Sensing Symposium, IGARSS '05, vol. 7, 2005, pp. 4894-4897.

153. Leporini D., and Pesquet J-C., "High order wavelet packets and cumulant field analysis," IEEE Transactions on Information Theory, vol. 45, no. 3, 1999, pp. 863-877.

154. Levy V. J., Mignot P., Berroir J.-P., "Multifractals, texture, and image analysis," IEEE Computer Society Conference on Computer Vision and Pattern Recognition, 1992. CVPR '92, 1992, pp. 661-664.

155. Lindsay R. W, Percival D. B., and Rothrock D. A., "The discrete wavelet transform and the scale analysis of the surface properties of sea ice," IEEE Transactions on Geoscience and Remote Sensing, vol. 34, no. 3, 1996, pp. 771-787.

156. Lindsay R. W., Percival D. B., and Rothrock D. A., "The discrete wavelet transform and the scale analysis of the surface properties of sea ice," IEEE Transactions on Geoscience and Remote Sensing, vol. 34, no. 3, 1996, pp. 771-787.

157. Liu Y., and Zhou X., "Automatic texture segmentation for texture-based image retrieval," International Multimedia Modelling Conference, 2004, pp. 285-290.

158. Liu Z., "Minimum distance texture classification of SAR images in contourlet domain," International Conference on Computer Science and Software Engineering, 2008, vol. 1, 2008, pp. 834-837.

159. Lovergine F. P., Stramaglia S., Nico G., Veneziani N., "Fast weighted least squares for solving the phase unwrapping problem," IEEE International Geoscience and Remote Sensing Symposium, IGARSS '99, vol.2, 1999, pp. 1348-1350.

160. Lu C. S., Chung P. C., and Chen C. F., "Unsupervised texture segmentation via wavelet transform," Pattern Recognition, vol. 30, no. 5, 1997, pp. 729-742.

161. Lu D., Mausel P., Brondizio E., and Moran E., "Change detection techniques," International Journal of Remote Sensing, vol. 25, no. 12, 2004, pp. 2365-2407.

162. Lucas R., Rowlands A., Brown A., Keyworth S., and Bunting P., "Rule-based classification of multi-temporal satellite imagery for habitat and agricultural

land cover mapping," ISPRS Journal of Photogrammetry and Remote Sensing, vol. 62, no. 3, 2007, pp. 165-185.

163. Madhavan B. B., Venkataraman G., Mohan B. K., and Shah S. D., "Airborne SAR and IRS-1A LISS II Data Interpretation of Coastal Geomorphology in Godavari Delta, India," Geocarto International, vol. 14, no. 2, 1999, pp. 52-61.

164. Makynen M. P., Manninen A. T., Simila M. H., Karvonen J. A., and Hallikainen M. T., "Incidence angle dependence of the statistical properties of C-band HH-polarization backscattering signatures of the Baltic sea ice," IEEE Transactions on Geoscience and Remote Sensing, vol. 40, no. 2, 2002, pp. 2593-2605.

165. Mäkynen M., and Hallikainen M., "Passive microwave signature observations of the Baltic Sea ice," International Journal of Remote Sensing, vol. 26, no. 10, 2005, pp. 2081-2106.

166. Mallat S. G., "A theory for multi-resolution signal decomposition: the wavelet representation," IEEE Transactions on Pattern Analysis and Machine Intelligence, vol. 11, no. 7, 1989, pp.674–693.

167. Manjunath B. S., and Chellappa R., "A note on unsupervised texture segmentation," IEEE Transactions on Pattern Analysis and Machine Intelligence, vol. 13, no. 5, 1991, pp. 478–483.

168. Marceau D., and Hay G., "Remote sensing contributions to the scale issue," Canadian Journal of Remote Sensing, vol. 25, no. 4, 1999, pp. 357-366.

169. Martinez J. M., and Toan T. L., "Mapping of flood dynamics and spatial distribution of vegetation in the Amazon floodplain using multitemporal SAR data," Remote Sensing of Environment, vol. 108, no. 3, 2007, pp. 209-223.

170. Mas J. F., "Monitoring land-cover changes: a comparison of change detection techniques," International Journal of Remote Sensing, vol. 20, no. 1, 1999, pp. 139-152.

171. Massonnet D., and Feigl K. L., "Radar interferometry and its applications to changes in the earth's surface," Reviews of Geophysics, vol. 36, no. 4, 1998, pp. 441-500.

172. Mecocci A., Gamba P., Marazzi A., and Barni M., "Texture segmentation in remote sensing images by means of packet wavelets and fuzzy clustering," Proceedings of SPIE European Symposium on Satellite and Remote Sensing II, vol. 2584, 1995, pp. 142-151.

173. Melas D., and Wilson S. P., "Double markov random fields and Bayesian image segmentation," IEEE Transactions on Signal Processing, vol. 50, no. 2, 2002, pp. 357-365.

174. Melgani F., and Moser, G., Serpico S. B., "Unsupervised change-detection methods for remote sensing images," Optical Engineering, vol. 41, no. 12, 2002, pp. 3288-3297.

175. Meyer F. G., and Coifman R. R, "Brushlets: A tool for directional image analysis and image compression," Journal of Applied and Computational Harmonic Analysis, vol. 5, 1997, pp. 147–187.

176. Mitianoudis N., and Stathaki T., "Pixel-based and region-based image fusion schemes using ICA bases, Information Fusion," Special Issue on Image Fusion: Advances in the State of the Art, vol. 8, no. 2, 2007, pp. 131-142.

177. Mitra P., Murthy C. A., and Pal S. K., "Unsupervised feature selection using feature similarity," IEEE Transactions on Pattern Analysis and Machine Intelligence, vol. 24, no. 3, 2002, pp. 301-312.

178. Modha D. S., and Sprangler W. S., "Feature weighting in K-means clustering," Machine Learning, vol. 52, no. 3, 2003, pp. 217-237.

179. Mohan S, Mehta N. S., Mehta R. L., Parul P., Bora V. H., Sule K. K., Purohit S. S., Rai S. S. Singh A. P., and Ramakrishna Y., "Multi-frequency microwave measurements for soil moisture," Proceedings of National symposium on Remote Sensing for Agricultural Applications, 1990, pp. 357-363.

180. Monti-Guarnieri A., Parizzi F., Pasquali P., Prati C., and Rocca F., "SAR interferometry experiments with ERS-1," Geoscience and Remote Sensing Symposium, 1993 IGARSS '93. Better Understanding of Earth Environment, vol. 3, 1993, pp. 991-993.

181. Mora O., Mallorqui J. J., and Broquetas A., "Linear and nonlinear terrain deformation maps from a reduced set of interferometric SAR images," IEEE Transactions on Geoscience and Remote Sensing, vol. 41, no. 10, 2003, pp. 2243-2253.

182. Moreira A., Krieger G., Hajnsek I., Hounam D., Werner M., Riegger S., and Settelmeyer E, "TanDEM-X: a TerraSAR-X add-on satellite for single-pass SAR interferometry," Geoscience and Remote Sensing Symposium, IGARSS '04, vol.2, 2004, pp. 1000-1003.

183. Moser G., and Serpico S. B., "Generalized minimum-error thresholding for unsupervised change detection from SAR amplitude imagery," IEEE Transactions on Geoscience and Remote Sensing, vol. 44, no. 10, 2006, pp. 2972-2982.

184. Moser G., and Serpico S.B., "Generalized minimum-error thresholding for unsupervised change detection from SAR amplitude imagery," IEEE Transactions on Geoscience and Remote Sensing, vol. 44, no. 2, 2006, pp. 2972-2982.

185. Nagler T., Rott H., Kamelger A., "Analysis of landslides in Alpine areas by means of SAR interferometry," IEEE International Geoscience and Remote Sensing Symposium, IGARSS '02, vol. 1, 2002, pp. 198-200.

186. Narain A., Mohan S., and Bhanderi R. J., "Evaluation of air-borne C- and X-band SAR data covering parts of Darbhanga for flood signatures," Proceedings of the SPIE, the International Society for Optical Engineering, vol. 6412, 2006, pp.64120U1-64120U7.

187. Ng I., Tan T., and Kittler J., "On local linear transform and Gabor filter representation of texture," International Conference on Pattern Recognition, 1992, pp. 627-632.

188. Niedermeier A., Romaneesen E., and Lehner S., "Detection of coastline SAR images using wavelet methods," IEEE Transactions on Geoscience and Remote Sensing, vol. 38, 2000, pp. 2270-2281.

189. Noferini L., Pieraccini M., Mecatti D., Luzi G., Atzeni C., Tamburini A., and Broccolato M., "Permanent scatterers analysis for atmospheric correction in ground based SAR interferometry," IEEE Transactions on Geoscience and Remote Sensing, vol. 43, no. 7, 2005, pp. 1459-1471.

190. Nystuen J. A., Garcia F. W. Jr., "Sea ice classification using SAR backscatter statistics," IEEE Transactions on Geoscience and Remote Sensing, vol. 30, no. 3, 1992, pp. 502-509.

191. Oh Y., "Quantitative retrieval of soil moisture content and surface roughness from multipolarized radar observations of bare soil surfaces," IEEE Transactions on Geoscience and Remote Sensing, vol. 42, no. 3, 2004, pp. 596-601.

192. Oh Y., Sarabandi K., and Ulaby F. T., "An empirical model and an inversion technique for radar scattering from bare soil surfaces," IEEE Transactions on Geoscience and Remote Sensing, vol. 30, no. 2, 1992, pp. 370-381.

193. Ohanian P. P., and Dubes R. C., "Performance evaluation for four classes of textural features," Pattern Recognition, vol. 25, 1992, pp. 819-833.

194. Oliver C., and Quegan S., "Understanding synthetic aperture radar images," Norwood, MA: Artech House, 1998.

195. Pal M., and Mather P. M., "Support vector machines for classification in remote sensing," International Journal of Remote Sensing, vol. 26, no. 5, 2005, pp.1007-1011.

196. Pal S. K., De R. K., and Basak J., "Unsupervised feature evaluation: a neuro-fuzzy approach," IEEE Transactions on Neural Networks, vol. 11, no. 2, 2000, pp. 366-376.

197. Paloscia S., Macelloni G., Pampaloni P., and Sigismondi S., "The potential of C-band and L-band SAR in estimating vegetation biomass: The ERS-1 and JERS-1 Experiments," IEEE Transactions on Geoscience and Remote Sensing, vol. 37, no. 4, 1999, pp. 2107-2110.

198. Pampaloni P., and Paloscia S., "Microwave emission and plant water content: A comparison between field measurements and theory," IEEE Transactions on Geoscience and Remote Sensing, vol. GE-24, no. 6, 1986, pp. 900-905.

199. Pandey P. C., and Hariharan T. A., "Advances in microwave remote sensing of the ocean and atmosphere," Journal of Earth System Science, vol. 93, no. 3, 1984, pp. 257-282.

200. Pandey P. C., and Kakar R. K., "An empirical microwave emissivity model for a foam-covered sea," IEEE Journal of Oceanic Engineering, vol. 7, no. 3, 1982, pp. 135-140.

201. Panjwani D. K., and Healey G., "Markov random field models for unsupervised segmentation of textured coloured images," IEEE Transactions on Pattern Analysis and Machine Intelligence, vol. 17, no. 10, 1995, pp. 939-954.

202. Pant T., Singh D., Srivastava T, "Multifractal analysis of SAR images for unsupervised classification," International Conference on Recent Advances in Microwave Theory and Applications, MICROWAVE 2008, pp.427-430.

203. Peddle D. R., and Franklin S. E., "Image texture processing and data integration for surface pattern discrimination," Photogrammetric Engineering and Remote Sensing, vol. 57, no. 4, 1991, pp. 413-420.

204. Pierce L. E., Ulaby F. T., Sarabandi K., and Dobson M. C., "Knowledge based classification of polarimetric SAR images," IEEE Transactions on Geoscience and Remote Sensing, vol. 32, no. 4, 1994, pp. 1081-1086.

205. Plotnick R. E., Gardner R. H., Hargrove W. W., Prestegaard K., and Perlmutter M., "Lacunarity analysis: A general technique for the analysis of spatial patterns," Physical review E, Statistical Physics, Plasmas, Fluids, and Related Interdisciplinary Topics, vol. 53, no. 5, 1996, pp. 5461-5468.

206. Porter R., and Canagarajah N., "A robust automatic clustering scheme for image segmentation using wavelets, "IEEE Transactions on Image Processing, vol. 5, no. 4, 1996, pp. 662-665.

207. Prakash R., Singh D., "Microwave sensitivity analysis of soil texture at C-band with bistatic scatterometer for remote sensing," International Conference on Recent Advances in Microwave Theory and Applications, MICROWAVE 2008, pp.211-213.

208. Prati C., Rocca F., Ferretti A., "Requirements for a space mission for DInSAR and PS analysis based on past and present missions," IEEE International Geoscience and Remote Sensing Symposium, IGARSS '04. vol. 3, 2004, pp.1695-1698.

209. Prats P., Mallorqui J. J., Reigber A., Scheiber R., Moreira A., "Estimation of the temporal evolution of the deformation using airborne differential SAR interferometry," IEEE Transactions on Geoscience and Remote Sensing, vol. 46, no. 4, 2008, pp. 1065-1078.

210. Qiang Y., Fang C., and Wen H., "A validation method for bare soil surface parameters inverted by Oh empirical model using integral equation method," 1st Asian and Pacific Conference on Synthetic Aperture Radar 2007, pp. 211-214.

211. Radke R. J., Andra S., Al-kofahi O., and Roysam B., "Image change detection algorithms: a systematic survey," IEEE Transactions on Image Processing, vol. 14, no. 3, 2005, pp. 294-307.

212. Rahman M. M., Moran M. S., Thoma D. P., Bryant R., Collins C. D. H., Jackson T., Orr B. K., and Tischler M., "Mapping surface roughness and soil

moisture using multi-angle radar imagery without ancillary data," Remote Sensing of Environment, vol. 112, no. 2, 2008, pp. 391-402.

213. Randen T., and Husoy J. H., "Filtering for texture classification: a comparative study," IEEE Transactions on Pattern Analysis and Machine Intelligence, vol. 21, no. 4, 1999, pp. 291-310.

214. Raney R. K., Freeman T., Hawkins R. W., and Bamler R., "A plea for radar brightness," International Geoscience and Remote Sensing Symposium, 1994. IGARSS '94. Surface and Atmospheric Remote Sensing: Technologies, Data Analysis and Interpretation, vol. 2, 1994, pp.1090-1092.

215. Rao Y. S., Rao K. S., Venkataraman G., Khare M., and Reddy C. D., "Comparison and Fusion of DEMs derived from InSAR and optical stereo techniques," Third ESA International Workshop on ERS SAR Interferometry, 2003.

216. Ratha D. S. and Venkataraman G., "Application of Statistical methods to study seasonal variation in the mine contaminants in soil and groundwater of Goa, India," Environmental Geology, vol. 29 (3/4), 1997, pp 253-262.

217. Richards J. A., "Analysis of remotely sensed data: The formative decades and future," IEEE Transactions on Geoscience and Remote Sensing, vol. 43, no. 3, 2005, pp. 422-432.

218. Ridd M. K., and Liu J., "A Comparison of four algorithms for change detection in an urban environment," Remote Sensing of Environment, vol. 63, no. 2, 1998, pp. 95-100.

219. Rignot E. J. M., and Van Zyl J. J., "Change detection techniques for ERS-1 SAR data," IEEE Transactions on Geoscience and Remote Sensing, vol. 31, no. 4, 1993, pp. 896-906.

220. Rignot E., and Kwok R., "Extraction of textural features in SAR images: Statistical model and Sensitivity," IEEE International Geoscience and Remote Sensing Symposium, 1990. IGARSS '90, vol. 1, 1990, pp. 1979-1982.

221. Rogan J., Franklin J., Stow D., Miller J., Woodcock C., and Roberts D., "Mapping land-cover modifications over large areas: A comparison of machine learning algorithms, Remote Sensing of Environment," Earth Observations for Terrestrial Biodiversity and Ecosystems Special Issue, vol. 112, no. 5, 2008, pp. 2272-2283.

222. Rogerson P. A., "Change detection thresholds for remotely sensed images," Journal of Geographical Systems, vol. 4, 2002, pp. 85-97.

223. Rosenfield A., and Kak A. C., "Digital Picture processing," vol. II, New York: Academic, 1982.

224. Sahoo P. K., Soltani S., Wong A. K. C., and Chen Y., "A survey of image thresholding techniques," Computer Vision, Graphics and Image Processing, vol. 41, no. 2, 1980, pp. 233-260.

225. Said S., "Soil moisture retrieval using microwave remote sensing data," Department of Civil Engineering, IITR, Roorkee, 2006, pp. 248.

226. Schiavon G., Del Frate F., D'Ottavio D., and Stramondo S., "Landslide identification by SAR interferometry: the Sarno case," IEEE International Geoscience and Remote Sensing Symposium, 2003. IGARSS '03. vol. 4, 2003, pp. 2428-2429.

227. Siegert F., and Hoffmann A., "The 1998 forest fires in east Kalimantan (Indonesia): A quantitative evaluation using high resolution ERS-2 SAR images and NOAA-AVHRR hotspot data," Remote Sensing of Environment, vol. 72, no. 1, 2000, pp. 64-77.

228. Simard M., Saatchi S. S., and De Grandi G., "The use of decision tree and multiscale texture for classification of JERS-1 SAR data over tropical forest," IEEE Transactions on Geoscience and Remote Sensing, vol. 38, no. 5, 2000, pp. 2310-2321.

229. Simoes M., Gilson A. P., Singh D. C., Singh K. P., Heitor L. C. C., Fraga E., Berroir J. P., Herlin I., Vieira H. V., and Santos U. P., "Remote sensing and spatial decision support system for environmental degradation monitoring," IEEE International Geoscience and Remote Sensing Symposium, IGARSS '03, vol. 3, 2003, pp. 2088-2090.

230. Simoncelli E. P., Freeman W. T., Adelson E. H., and Heeger D. J., "Shiftable multiscale transforms," IEEE Transaction on Information Theory, vol. 38, no. 2, 1992, pp. 587–607.

231. Singh A., "Digital change detection techniques using remotely sensed data," International Journal of Remote Sensing, vol. 10, 1989, pp. 989-1003.

232. Singh D., "Scatterometer performance with polarization discrimination ratio approach to retrieve crop soybean parameter at X-band," International Journal of Remote Sensing, vol. 27, no. 19, 2006, pp. 4101, 4115.

233. Singh D., Chamundeeswari V. V., Sharma S., and Sharma H., "An importance of satellite based radar images to monitor change detection on earth surface," International Conference on Radio Sciences, ICRS 2008, 2008a.

234. Singh D., Chamundeeswari V. V., Singh K., and Wiesbeck W., "Monitoring and change detection of natural disaster (like subsidence) using synthetic aperture radar (SAR) data," International Conference on Recent Advances in Microwave Theory and Applications, MICROWAVE 2008, 2008b, pp. 419-421.

235. Singh K. P., "Monitoring of oil spills using airborne and spaceborne sensors," Advances in Space Research, vol. 15, no.11, 1995, pp.101-110.

236. Singh K. P., Gray A. L., Hawkins R. K., and O'Neil R. A., "The Influence of Surface Oil on C-and Ku-Band Ocean Backscatter," IEEE Transactions on Geoscience and Remote Sensing, vol. GE-24, no. 5, 1986, pp.738-744.

237. Singh K. P., Sharma S. K., "Evaluation of soil moisture by bistatic microwave remote sensing," Adavances in Space Research, vol. 12, no. 7, 1992, pp. 69-72.

238. Skretting K., and Husay J. H., "Texture classification using sparse frame based representations," EURASIP Journal on Applied Signal Processing, no. 1, 2006, pp. 102.

239. Smits P. C., and Dellepiane S. G., "Synthetic aperture radar image segmentation by a detail preserving Markov random field approach," IEEE Transactions on Geoscience and Remote Sensing, vol. 35, no. 4, 1997, pp. 844-857.

240. Solberg A. H. S., and Jain A. K., "Texture fusion and feature selection applied to SAR imagery," IEEE Transactions on Geoscience and Remote Sensing, vol. 35, no. 2, 1997, pp. 475-479.

241. Song Y. S., Sohn H. G., and Park C. H., "Efficient water area classification using radarsat-1 SAR imagery in a high relief mountainous environment," Photogrammetric Engineering and Remote Sensing, vol. 73, no. 3, 2007, pp. 285-296.

242. Stathakis D., and Vasilakos A., "Comparison of computationally intelligence based classification techniques for remotely sensed optical image classification," IEEE Transactions on Geoscience and Remote Sensing, vol. 44, no. 8, 2006, pp.2 305-2318.

243. Steffen P., Heller P. N., Gopinath R. A., and Burrus C. S., "Theory of regular M-band wavelet bases," IEEE Transactions on Signal Processing, vol. 41, no. 12, 1993, pp. 3497-3510.

244. Strang G., and Nguyen T., "Wavelets and Filter Banks". Wellesley, Cambridge, MA, 1996.

245. Strozzi T., Dammert P. B. G., Wegmuller U., Martinez J. M., Askne J. I. H., Beaudoin A., and Hallikainen M. T., "Landuse mapping with ERS SAR Interferometry," IEEE Transactions on Geoscience and Remote Sensing, vol. 38, no. 2, 2000, pp. 766-775.

246. Strozzi T., Farina P., Corsini A., Ambrosi C., Thüring M., Zilger J., Wiesmann A., Wegmüiller U., and Werner C., "Survey and monitoring of landslide displacements by means of L-band satellite SAR interferometry," Landslides, vol. 2, no. 3, 2005, pp. 193-201.

247. Strozzi T., Wegmüller U., Tosi L., Bitelli G. and Spreckels V., "Land subsidence monitoring with differential SAR interferometry," Photogrammetric Engineering and Remote Sensing, vol. 67, no. 11, 2001, pp. 1261–1270.

248. Tou J. T., and Gonzalez R. C., "Pattern recognition principles," Reading, MA: Addison Wesley, 1974.

249. Tuceryan M., and Jain A. K., "Texture analysis," Handbook of Pattern Recognition and Computer vision, Singapore: world specific, 1993, pp. 235-276.

250. Ulaby F. T., Kouyate F., Brisco B., and Lee Williams T. H., "Textural information in SAR images," IEEE Transactions on Geoscience and Remote Sensing, vol. 24, 1986, pp. 235-245.

251. Ulaby F. T., Moore R. K., and Fung A. K., "Microwave remote sensing, Active and passive," vol. II, Norwood, M. A: Artech House, 1986.

252. Unser M., "Sum and difference histograms for texture classification," IEEE Transactions on Pattern Analysis and Machine Intelligence, vol. 8, no. 1, 1986, pp. 118-125.

253. Unser M., "Texture classification and segmentation using wavelet frames," IEEE Transactions on Image Processing, vol. 4, no. 11, 1995, pp. 1549-1560.

254. Van der Wal D., Herman P. M. J., and Van Den Dool A. W., "Characterization of surface roughness and sediment texture of intertidal flats

using ERS SAR imagery," Remote Sensing of Environment, vol. 98, 2005, pp. 96-109.

255. Van-Zyl J. J., Chapman B. D., Dubois P., and Shi J., "The effect of topography on SAR calibration," IEEE Transactions on Geoscience and Remote Sensing, vol. 31, no. 5, 1993, pp.1036-1043.

256. Villasenor J., Fatland D., and Hinzman L., "Change detection on Alaska's north slope using repeat pass ERS-1 SAR images," IEEE Transactions on Geoscience and Remote Sensing, vol. 31, no. 1, 1993, pp. 227-236.

257. Wang J. R., and Rao K. S., "The effect of topography on the SAR measurements of surface soil moisture," IEEE International Geoscience and Remote Sensing Symposium, IGARSS '93, vol. 2, 1993, pp. 598-600.

258. Watson A. B, "The cortex transform: Rapid computation of simulated neural images," Computer Vision, Graphics, Image Processing, vol. 39, no. 3, 1987, pp. 311–327.

259. Wellig P., Schmid K., Essen H., Kurz A., Schimpf H., and Brehm T., "Clutter analysis of high resolution millimeter wave SAR data in the spatial and wavelet domain," IEEE International Geoscience and Remote Sensing Symposium 2007, IGARSS '07, 2007, pp. 559-562.

260. Weszka J. S., "A survey of threshold selection techniques," Computer Graphics, and Image Processing, vol. 7, 1978, pp. 259-265.

261. Wilkinson G. G., "Results and Implications of a study of fifteen years of satellite image classification experiments," IEEE Transactions on Geoscience and Remote Sensing,   vol. 43, no. 3, 2005, pp. 433-440.

262. Won C. S., and Derin H., "Unsupervised segmentation of noisy and textured images using markov random fields," CVGIP: Graphical Models and Image Processing, vol. 54, no. 4, 1992, pp. 308-328.

263. Wu D., and Linders J., "A new texture approach to discrimination of forest clear cut, canopy, and burned area using airborne C-band SAR," IEEE Transactions on Geoscience and Remote Sensing, vol. 37, no. 1, 1999, pp. 555-563.

264. Wu F., Wang C., Zhang H., and Zhang B., "Change detection and analysis with radarsat-1 SAR image," Geoscience and Remote Sensing Symposium, IEEE International, 2007. IGARSS 2007, 2007, pp. 2601-2604.

265. Xia Z-G., and Henderson F. M., "Understanding the relationships between radar response patterns and the bio- and geophysical parameters of urban areas," IEEE Transactions on Geoscience and Remote Sensing, vol. 35, no. 1, 1997, pp. 93-101.

266. Xiao Y. Q., Li Q. S., Li Z. N., Chow Y. W., and Li G. Q., "Probability distributions of extreme wind speed and its occurrence interval," Engineering Structures, vol. 28, no. 8, 2006, pp. 1173-1181.

267. Yamada H., Yamaguchi Y., Rodriguez E., Kim Y., and Boerner W. M., "Polarimetric SAR interferometry for forest canopy analysis by using the super-resolution method," Geoscience and Remote Sensing Symposium, IEEE International. IGARSS '01, vol. 3, 2001, pp. 1101-1103.

268. Yamaguchi Y., Moriyama T., Ishido M., and Yamada H., "Four-component scattering model for polarimetric SAR image decomposition," IEEE Transactions on Geoscience and Remote Sensing, vol. 43, no. 8, 2005, pp. 1699-1706.

269. Yamaguchi Y., Nagai T., and Yamada H., "JERS-1 SAR image analysis by wavelet transform," IEICE Transactions on Communications, vol. E78-B, no. 12, 1995, pp. 1617-1621.

270. Yamaguchi Y., Takayanagi Y., Boerner W-M., Eom H. J., and Sengoku M., "Polarimetric Enhancement in radar channel imagery," IEICE Transactions on Communications, vol. E78-B, no. 12, 1995, pp.1571-1579.

271. Yamaguchi Y., Yajima Y., and Yamada H., "A four-component decomposition of POLSAR images based on the coherency matrix," IEEE Transactions on Geoscience and Remote Sensing, vol. 3, no. 3, 2006, pp. 292-296.

272. Yang J., Frangi A. F., Yang J-Y., Zhang D., and Jin Z., "KPCA Plus LDA: A Complete Kernel Fisher Discriminant Framework for Feature Extraction and Recognition," IEEE Transactions on Pattern Analysis and Machine Intelligence, vol. 27, no. 2, 2005, pp. 230-244.

273. Yang J., Xiong T., and Ying-Ning P., "Polarimetric SAR image classification by using generalized optimization of polarimetric contrast enhancement," International Journal of Remote Sensing, 2006, vol. 27, no. 15/16, pp. 3413-3424.

274. Yen J-Y., Chen K. S., Chang C. P., and Boerner W. M., "Evaluation of earthquake potential and surface deformation by differential interferometry," Remote Sensing of Environemnt, vol. 112, no. 3, 2008, pp. 782-795.

275. Zebker H. A., and Goldstein R., "Topographic mapping from SAR observation," Journal of Geophysical Research, vol. 91, no. B5, 1986, pp. 4993- 4999.

276. Zhang J. F., Xie L. L., and Tao X. X., "Change detection of earthquake-damaged buildings on remote sensing image and its applications in seismic disaster assessment," Proceedings of IEEE International Geoscience and Remote Sensing Symposium, IGARSS '03, vol. 4, 2003, pp. 2436-2438.

277. Zou H., and Tewfik A. H., "Discrete orthogonal, M-band wavelet decomposition," Proceedings of International Conference on Acoustics, Speech and Signal Processing, vol. 4, 1992, pp. IV-605-IV-608.

Author's Publications

International Journals

1. Chamundeeswari V.V., Singh D., and Singh K., "An adaptive method with integration of multi-wavelet based features for unsupervised classification of SAR images," Journal of Geophysics and Engineering, vol. 4, 2007, pp. 384-393, DOI: 10.1088/1742-2132/4/4/004.

2. Chamundeeswari V.V., Singh D., and Singh K., "An analysis of texture measures in PCA based unsupervised classification of SAR images," IEEE Geoscience and Remote Sensing Letters, Accepted (in Press), 2009.

International Conferences

1. Chamundeeswari V.V., and Singh D., "Computationally efficient extraction and integration of multi-wavelet based features for segmentation of SAR images," International Symposium on "Geospatial Databases for Sustainable Development", Goa, India, September 27-30, 2006, International Archives of Photogrammetry, Remote Sensing and Spatial Information Sciences, vol. 36, Part 4, 2006, pp. 69-74.

2. Chamundeeswari V.V., Singh D., and Singh K., "Unsupervised land cover classification of SAR images using greedy kernel PCA," III International Conference on Microwaves, Antennas, Propagation and Remote Sensing, ICMARS 2006, Jodhpur, India, December 18-22, 2006, pp. 141-142.

3. Chamundeeswari V.V., Singh D., and Singh K., "Unsupervised land cover classification of SAR images by contour tracing," IEEE International Geoscience and Remote Sensing Symposium, IGARSS 2007, July 23-27, Barcelona, Spain, 2007, pp. 547-550, DOI: 10.1109/IGARSS.2007.4422852.

4. Chamundeeswari V.V., Singh D., Singh K., and Wiesbeck W., "A critical analysis to generate change detection map using SAR interferometry for land subsidence monitoring of New Orleans city of USA," IEEE International Geoscience and Remote Sensing Symposium, IGARSS 2008, IGARSS 2008, July 7-11, Boston, USA, 2008.

5. Chamundeeswari V.V., Singh D., Singh K., and Wiesbeck W., "Change detection module for New Orleans city of USA using differential SAR interferometry," 37th COSPAR Scientific Assembly, July 13-20, Montreal, Canada, 2008.

6. Singh D., Chamundeeswari V.V., Sharma S., and Sharma H., "An importance of satellite based radar images to monitor change detection on earth surface,"

International Conference on Radio Sciences ICRS 2008, Jodhpur, India, February 25-29, 2008.

7. Singh D., Chamundeeswari V.V., Singh K., and Wiesbeck W., "Monitoring and change detection of natural disaster (like subsidence) using synthetic aperture radar (SAR) data," International Conference on Recent Advances in Microwave Theory and Applications, MICROWAVE 2008, Jaipur, India, November 21-24, 2008, pp. 419-421, DOI: 10.1109/AMTA.2008.4763244.

National Conferences

1. Chamundeeswari V.V., Singh D., and Singh K., "Unsupervised land cover classification via feature selection and integration using PCA," 13th Symposium in Earthquake Engineering Department, Indian Institute of Technology, Roorkee, India, December 18-20, 2006, vol.2, pp. 163-167.

2. Chamundeeswari V.V., Singh D., Singh K., and Wiesbeck W., "A novel approach to land subsidence with analysis and validation using probability distribution function," National Symposium on Advances in Remote Sensing Technology and Applications with Special Emphasis on Microwave Remote Sensing, Ahmedabad, India, December 18-20, 2008.

3. Singh D., and Chamundeeswari V.V., "A novel approach for disaster monitoring with microwave/SAR images," Symposium on Vaccum electronic devices and Applications, VEDA 2009, Varanasi, India, January 8-10, 2009.

International Journals (to be submitted)

1. Chamundeeswari V.V., Singh D., and Singh K., "Analysis of change detection methodologies for RADARSAT-1 data and validation using weibull distribution," *Communicated to Advances in space research.*

2. Chamundeeswari V.V., Singh D., Singh K., and Wiesbeck W., "Subsidence mapping of New Orleans city of USA: Differential interferometry approach for accurate mapping," *Communicated to IEEE Transactions on Geoscience and Remote sensing.*

3. Chamundeeswari V.V., Singh D., and Singh K.,, "EM modeling and texture information for surface characteristic estimation in SAR images," *Communicated to Remote Sensing of Environment.*

Awards

1. Recipient of "Google India Women in Engineering Award", 2008 for the academic excellence and contribution to computing and technology.